APPLICATIONS OF IMAGE PROCESSING IN COMBUSTION RESEARCH

by

Pal Toth

A dissertation submitted to the faculty of
The University of Utah
in partial fulfillment of the requirements for the degree of

Doctor of Philosophy

Department of Chemical Engineering

The University of Utah

August 2014

The University of Utah Graduate School

STATEMENT OF DISSERTATION APPROVAL

The dissertation of **Pal Toth**

has been approved by the following supervisory committee members:

Eric G. Eddings	, Chair	**3/18/2014** Date Approved
Terry A. Ring	, Member	**3/18/2014** Date Approved
JoAnn S. Lighty	, Member	**3/18/2014** Date Approved
Arpad B. Palotas	, Member	**3/18/2014** Date Approved
Ross T. Whitaker	, Member	**3/18/2014** Date Approved

and by **Milind Deo** , Chair/Dean of

the Department/College/School of **Chemical Engineering**

and by David B. Kieda, Dean of The Graduate School.

ABSTRACT

Digital image processing has wide ranging applications in combustion research. The analysis of digital images is used in practically every scale of studying combustion phenomena from the scale of individual atoms to diagnosing and controlling large-scale combustors. Digital image processing is one of the fastest-growing scientific areas in the world today. From being able to reconstruct low-resolution grayscale images from transmitted signals, the capabilities have grown to enabling machines carrying out tasks that would normally require human vision, perception, and reasoning. Certain applications in combustion science benefit greatly from recent advances in image processing. Unfortunately, since the two fields — combustion and image processing research — stand relatively far from each other, the most recent results are often not known well enough in the areas where they may be applied with great benefits. This work aims to improve the accuracy and reliability of certain measurements in combustion science by selecting, adapting, and implementing the appropriate techniques originally developed in the image processing area. A number of specific applications were chosen that cover a wide range of physical scales of combustion phenomena, and specific image processing methodologies were proposed to improve or enable measurements in studying such phenomena. The selected applications include the description and quantification of combustion-derived carbon nanostructure, the three-dimensional optical diagnostics of combusting pulverized-coal particles and the optical flow velocimetry and quantitative radiation imaging of a pilot-scale oxy-coal flame. In the field of the structural analysis of soot, new structural parameters were derived and the extraction and fidelity of existing ones were improved. In the field of pulverized-coal combustion, the developed methodologies allow for studying the detailed mechanisms of particle combustion in three dimensions. At larger scales, the simultaneous measurement of flame velocity, spectral radiation, and pyrometric properties were realized.

CONTENTS

ACKNOWLEDGMENTS

This material is based upon work supported by the Department of Energy under Award Number DE-NT0005015. The views and opinions of the authors expressed herein do not necessarily state or reflect those of the United States Government or any agency thereof.

The author would like to thank Dana Overacker, David Wagner, Robert Cox, Tom Slowik, Prof. Philip Smith, and Mark Solum for the help they provided throughout this work.

CHAPTER 1

INTRODUCTION TO THE TECHNICAL CONTENT

This dissertation is a compilation of standalone articles. Each following chapter summarizes an approach to a distinct group of problems, along with experiments and experimental results, where applicable. Although it may seem that the problems that are discussed in Chapters 2–10 are at very different spatial scales, there is an underlying concept in the methodologies applied to solve these problems.

The underlying concept in the methodologies is applying digital imaging, image processing and image analysis to study physical phenomena of a very different nature. As digital imaging is a well-defined concept, the methods applied are similar and are based on the same principles. This thesis therefore demonstrates how a mathematical concept can be applied in the study of diverse physical systems.

Another, although more loose underlying similarity is found in the objects of studies themselves. Every chapter describes a specific problem that arose in the general scientific area of combustion research. Chapters 2–6 deal with soot formation in the combustion of liquid fuels (Diesel surrogates), while Chapters 7–10 investigate problems in pulverized-coal combustion.

Chapter 2 is focused on the problem of quantifying soot nanostructure, as it is observed by high-resolution electron microscopy (HRTEM). HRTEM micrographs are two-dimensional intensity arrays (images), that convey information about the molecular structure of soot particles. Interpreting this information in a quantitative fashion is a challenging task as the raw data must be heavily reduced in order to obtain meaningful scalar quantities that describe the three-dimensional structure. Chapter 2 presents an early attempt of this data reduction problem. As a result of this work, structural parameters (scalars) were developed that robustly quantify nanostructure.

Chapters 3 and 4 present an advanced mathematical framework with which the structural descriptors presented in Chapter 2 can be both generalized and their physical meanings

made more intuitive. The novelty of the approach presented in Chapters 3 and 4 lies in the application of filtering theory to the HRTEM micrographs. Image filtering is normally used to enhance, denoise, or reconstruct images or to achieve artistic effects. In these applications, image filtering is employed to extract physical information, like the spatial location and arrangement of molecules from the micrographs. The chapters up to Chapter 4 all deal with studying physical phenomena on the nanoscale, that is, on the scale of individual molecules.

Chapters 5 and 6 build on Chapters 3 and 4, although in different ways. Chapter 5 presents software that applies the theory and implementation developed in Chapters 3 and 4 towards the integrated, automatic control of microscopes. The computational efficiency of the algorithms described in Chapter 4 allows for the utilization of the image filtering technique in real-time applications. In Chapter 6, the methodology presented in Chapters 3 and 4 is applied to extract physical information from "real" HRTEM micrographs and to study the effect of oxidation pressure on soot nanostructure. Chapters 5 and 6 can be viewed as practical applications of the methodology developed in the previous chapters. The methodology presented in Chapter 5 can extend the capability of the techniques described in Chapters 3 and 4 by being able to study physical structure on the microscale, that is, on the scale of soot aggregates.

Chapters 7–10 deal with a different group of problems, namely the combustion of pulverized-coal. There are a number of physical and chemical aspects of coal combustion that have been widely studied in the literature and are important to know in order to be able to efficiently use coal as an energy resource. These aspects include the chemical kinetics of coal particle combustion, the fluid mechanics of pulverized-coal flames, and multiphase, multicomponent mass transfer in such systems. Chapters 7–10 focus on different parts of the problem, but the concept of increasing spatial size scales with each chapter is retained.

Chapters 7 and 8 deal with the study of coal particle combustion, studied at the spatial scale of single particles. This is the scale of millimeters. The methodology described in these chapters allows for the nonintrusive optical measurement of the three-dimensional location, three-component velocity, temperature, and size of individual, combusting coal particles. The method is a combination of stereoscopic imaging, image processing, photometry, and pyrometry. The individual approaches developed in these different fields are combined in a novel way.

Chapters 9 and 10 study pulverized-coal flames on the spatial scale of centimeters and meters. At this scale, it is not possible to observe individual coal particles combusting, but

their behavior can be deduced by observing the macroscopical characteristics of the flame. These characteristics are the radiative emission at different wavelengths and spatio-temporal properties like flame shape, flame length, and the apparent motion of flame structure.

Chapter 9 describes a method with which a descriptor of flame velocity can be extracted from simple (although high-speed) photographs of flames. The method is tested on a 40 kW (nominally 120 kW) pilot-scale pulverized-coal flame.

Chapter 10 utilizes an extension of the velocimetry method presented in Chapter 9, in which the capability of velocity measurement is extended by pyrometric capabilities that allow for the extraction of luminous fluxes in multiple wavebands, along with flame temperature and soot concentration. The combined capability of measuring these properties by using reasonably simple concepts of imaging, image processing, machine vision, and spectroscopy is novel. The method is applied to study the effect of oxygen injection and coal type on the already described 40 kW flame.

A large part of the work (Chapters 2–5 and 9) has been submitted to and accepted by international scientific journals for publication. The remainder of the dissertation consists of manuscripts that are either under peer review or submission procedure at the time of the submission of this dissertation. For this reason, every chapter follows a journal article organization and the original text of the manuscripts is compiled as separate chapters of this dissertation. The following chapters have been published:

- Chapter 2 — Quantitative differentiation of poorly ordered soot nanostructures: a semi-empirical approach. Published in Fuel, volume 99, pages 1-8 (2012),
- Chapter 3 — A novel framework for the quantitative analysis of high resolution transmission electron micrographs of soot I. Improved measurement of interlayer spacing. Published in Combustion and Flame, volume 160, issue 5, pages 909-919 (2013),
- Chapter 4 — A novel framework for the quantitative analysis of high resolution transmission electron micrographs of soot II. Robust multiscale nanostructure quantification. Published in Combustion and Flame, volume 160, issue 5, pages 920-939 (2013),
- Chapter 5 — Automated analysis of heterogeneous carbon nanostructures by high-resolution electron microscopy and on-line image processing. Published in Ultramicroscopy, volume 129, pages 53-62 (2013).
- Chapter 9 — The potential of on-line optical flow measurement in the control and monitoring of oxy-coal flames

CHAPTER 2

QUANTITATIVE DIFFERENTIATION OF POORLY ORDERED SOOT NANOSTRUCTURES: A SEMI-EMPIRICAL APPROACH

Fuel 99 (2012) 1–8

Contents lists available at SciVerse ScienceDirect

Fuel

journal homepage: www.elsevier.com/locate/fuel

Quantitative differentiation of poorly ordered soot nanostructures: A semi-empirical approach

P. Toth [a,*], Á.B. Palotás [a], J. Lighty [b], C.A. Echavarria [b]

[a] Department of Combustion Technology and Thermal Energy, University of Miskolc, H3515 Miskolc-Egyetemvaros, Hungary
[b] Department of Chemical Engineering, University of Utah, 50 S. Central Campus Drive, Salt Lake City, UT 84112-9203, United States

ARTICLE INFO

Article history:
Received 13 July 2010
Received in revised form 11 March 2012
Accepted 5 April 2012
Available online 21 April 2012

Keywords:
Soot
Nanostructure
HRTEM
Image processing

ABSTRACT

A novel, sensitive technique is presented yielding expressive semi-empirical order parameters (distance deviation parameter Ω and junction parameter υ) describing the nanostructure of combustion derived carbonaceous materials. This method is purposively developed to enable the measurement of slight changes in structural properties of young soots originating from the combustion of different fuels – most of which are left undetected by conventional algorithms – by utilizing digital image processing of high resolution transmission electron micrographs (HRTEM images). The study has been motivated by a demand for better understanding the evolution of soot nanostructure. This paper presents the details of the proposed method, along with the comparison with the conventional methodology. Through simulations, the correlation between previously defined order parameters and our new structural indices is demonstrated. As an example of practical utilization, the nanostructural evolution of different fuels with residence time and the extent of oxidation is shown by monitoring changes in Ω and υ. The structural development was analyzed using a specific sampling procedure: soots were collected at various heights above the burner surface.

Published by Elsevier Ltd.

1. Introduction

Dark field lattice fringe imaging techniques utilizing high resolution transmission electron microscopes allow for the observation of soot structure at the atomic levels. Several studies have been published discussing the properties of soot nanostructure based on qualitative [1–4] or quantitative [5–9] image analysis methods.

The atomic-level investigations of combustion-derived carbon structures are generally initiated by either an attempt to determine the source of soot pollution [10,11] or, more universally, a motive to gain a better insight on oxidation and graphite crystal formation. The latter incentive is important from further points of view, since the characteristics of soot nanostructure are believed to be correlated with macroscopic physical properties, e.g. oxidation reactivity and UV–VIS absorption [12] or radiant emissivity and extinction coefficients [13]. Others argue that the short or long range order of lattices has an effect on microstructural properties, porosity and surface area as well [14].

Much effort has been put in the attempts to representatively quantify structural information provided by HRTEM lattice images and several existing methodologies are known that may yield consistent data as a result. While the details of these algorithms are quite different, the basic approaches and main steps of extracting physical information are generally the same. These methods usually consist of the following:

1. the noise filtering of raw, digitized HRTEM images,
2. the classification of pixels as either objects of interest or background,
3. the measurement of some shape properties of these objects and the statistical evaluation of the data collected.

Additionally, several studies utilize cluster or stack analysis in addition to these conventional steps in an attempt to quantify the order of objects and crystallinity of soot structure.

HRTEM images are usually digitized as 8 bit grayscale bitmaps, where the value of each pixel – generally referred to as the gray-scale intensity value (I) – determines the corresponding pixel's probability of belonging to an object. Objects are believed to be graphene layers, also called fringes or lattices.

Noise filtering basically means the removal of regional peaks in images caused by electrostatic effects, not carrying any structural meaning. Because of the characteristics of carbon soot nanostructures – the definite range of fringe spacing and length has already been described by many authors who used different techniques [15–17] – the best results are usually obtained when using frequency domain filtering. Square-profiled bandpass frequency filters (referred to as 'ideal' filters) were the most commonly used

* Corresponding author.
E-mail address: toth.pala@gmail.com (P. Toth).

0016-2361/$ - see front matter Published by Elsevier Ltd.
http://dx.doi.org/10.1016/j.fuel.2012.04.013

filters in initial studies [5]. Sharma and co-workers [6] pointed out that important non-periodically occurring single layers are lost when using bandpass filtering with amorphous soot samples; their study proposed the use of low-pass ideal filters.

For the detection process – the separation of objects and background – basically all authors used binarization methods based on global thresholding. Choosing the appropriate method for the binarization step is crucial for obtaining consistent results, as the detected objects are the inputs of the next steps. Global thresholding means that a single 8 bit threshold value T is set before the detection procedure, and the values $B_{x,y}$ of the output binary image **B** are either 1 if $I_{x,y} \geqslant T$ or 0 otherwise. The outputs of global thresholding algorithms are therefore heavily determined by T, so it is not surprising that the methods used for assigning threshold values have been subjects of debate. Basically, there are authors who set T in order to obtain separated binary fringes in **B** [5] and authors who set T to get equal fractional coverage values for objects and non-objects and used post-processing techniques to separate fringes after binarization [6,7]. These post-processing methods include the skeletonization of fringes, detection of branchpoints, separation and reconnection algorithms based on complex criterion systems [6–8].

From the structural data obtainable from HRTEM images, the most commonly measured parameters by recent studies are the interlayer distance, the fringe length and the fractional coverage of detected objects [5,6,8]. These are also the most easily verifiable by other techniques, such as X-ray diffractometry [18]. For the direct determination of the interlayer distance, to the best of our knowledge, all authors used the approximation proposed by Palotás and coworkers [5]. According to this study, the interlayer distance of two adjacent carbon fringes is the vector–vector distance of the two paralellized orientation vectors, where these vectors are obtained by averaging their orientations but keeping them at their original location, i.e. passing through the centroid of the fringe. Most recent publications place more emphasis on the classification of 'adjacent' and parallel groups of fringes, called 'stacks'. Detailed algorithms for deciding an object's membership to stacks are presented in [6,8]. If considering data describing the stacking of layers, additional parameters arise, such as the diameters of stacks, the number of layers in stacks and other derived indices, e.g. the crystallinity index proposed by Yang et al. [8]. Using whole distribution functions of the interlayer distance and the fringe orientation θ can be expressive, because the amorphity of the texture – the deviation from perfect graphite structure – can be described by the statistical descriptors of these distributions. Shim and coworkers [7] introduced several interesting order parameters, such as the 2D nematic order parameter $S_{2,N}$ and the 2D polar order parameter $S_{2,P}$, defined as

$$S_{2,N} = 2\overline{\cos^2(\theta_i)} - 1 \tag{1}$$

and

$$S_{2,P} = 1 - 2\overline{\cos^2(\theta_i)} \tag{2}$$

where $\vec{\theta}$ is a vector containing the angles between the orientation vectors of each fringe and a directional vector; the overline symbol means the arithmetic mean value of the elements of its argument. The directional vector is the reference vector for $S_{2,N}$ and the vector pointing from the concentric center to the center of mass of fringe i. For a perfectly ordered graphite structure, where all fringes are stacked together and their orientations are the same, the nematic order parameter is 1; for a perfectly concentric, onion-like carbon structure, the polar order parameter is 1.

The aim of this research is to develop a method, with which even slight changes in amorphous soot nanostructures can be monitored. Our previous experiences with conventional algorithms showed that the inherent uncertainty of these methods – mainly coming from the subjectivity of the binarization process and the small sample sizes due to the large amount of excluded data – makes the characterization of very similar structures difficult.

2. Materials and methods

2.1. Sample collection

Soot samples were derived from the flames of ethylene and air, benzene and air and a surrogate fuel consisting of n-dodecane and m-xylene (9:1 V/V) and air. Samples were thermophoretically taken for HRTEM analysis. Ethylene and benzene were burned in air in a flat flame premixed burner under fuel rich conditions for studies of soot formation in aliphatic and aromatic flames [19]. This system consisted of a stainless steel chamber where fuel and air were properly mixed prior to entering the burner. The flame was stabilized over a tube bundle and shielded from atmospheric interference using a nitrogen shroud. A metallic mesh placed 3.5 cm above the burner surface distributed the flame uniformly across the burner.

The surrogate mixture and ethylene were also burned in air in a two stage premixed burner for studies of soot oxidation. In this system, soot was generated in either ethylene/air or surrogate/air fuel rich flames, which served as the first stage. The soot was then burned in a secondary, premixed burner under fuel lean conditions. Details of the premixing systems have been reported earlier [20].

Samples for HRTEM analysis were taken at different heights above the burner surface (HAB) using a thermophoretic probe commonly referred to as a frog tongue. A TEM grid holder was attached to a piston and compressed air at 60 psig was used to quickly insert the TEM grid into the flame. Multiple insertions were necessary to get a representative soot sample on the grid. The grid was oriented with the face parallel to the gas flow, so the disturbance of the flame was minimal. Soot deposits on the grid because of the thermophoretic gradient between the cold grid and the hot flame, allowing freezing some heterogeneous reactions, avoiding changes in the soot morphology after the particles have been impacted upon the cold surface [21].

A summary of the collected samples, heights above burner and flame types is presented in Table 1.

2.2. Image acquisition

HRTEM micrographs were produced using transmission electron microscopes FEI, Models Tecnai F30 and F20 EFTEM operated under 200 keV accelerating potential. The images were digitized as 1024 × 1024 size images. The magnifications of these images were either 760,000× or 1,100,000×.

2.3. Image processing

Our approach is fundamentally different from the previously described ones. Instead of trying to separate fringes based on hypothesized criteria and extract data from bitmaps, we tried to reduce the images to 'networks' that can be topologically characterized. These topological parameters are correlated to the already defined order parameters later.

For noise filtration, Gaussian bandpass filters have been used in the frequency domain. Gaussian filters are better than ideal filters if the harmonic 'ringing' caused by the sharp changes in the transfer function may lead to false fringe detection, as in the case of high resolution soot TEM images. Despite the advantages of using a low-pass filter as proposed by Sharma and coworkers [6], bandpass filters were used, because of the additional intensity homogenizing

Table 1
Summary of collected samples.

Sample name	Fuel type	Burner setup	Heights above burner (mm)
Benzene flame	Benzene/air	Premixed, fuel rich	5, 10, 15
Ethylene flame 1	Ethylene/air	Two stage premixed, fuel rich/fuel lean	0.5, 2, 4
Ethylene flame 2	Ethylene/air	Premixed, fuel rich	10, 15
Surrogate flame	N-dodecane-m-xylene mixture/air	Two stage premixed, fuel rich/fuel lean	1, 3, 5

properties of bandass Fourier filtering (inhomogeneous luminance, e.g. large patches of darker or brighter pixels are considered very low frequency noise). Frequency filters work in the frequency domain of the image, obtained by the Fourier transform. This transformation places the frequency data of the image from the spatial domain x, y into a new coordinate system called the frequency space u, v. This frequency space characterizes the different spatial frequencies of the image. In the following discussion, we use the convenient continuous function notation and we consider a centrally shifted frequency space, meaning that the lowest frequencies appear in the center of the frequency space and frequency increases as one moves further away from this location, proportionally to the Euclidian distance from the central coordinate. In a coordinate system like this, ideal filters can be pictured as cylinders and Gaussian filters can be pictured as two-dimensional Gaussian surfaces, both centered around the origo. The following two equations describe ideal and Gaussian frequency filters, respectively.

$$u^2 + v^2 \leqslant r_{LP} \rightarrow O_{i,LP}(u, v) = 1, \text{ else } 0 \tag{3}$$

$$O_{g,LP}(u, v) = \exp\left(-\frac{u^2 + v^2}{2\sigma_{LP}^2}\right). \tag{4}$$

The index LP refers to low-pass, since the filters allow low frequencies around $u = 0$, $v = 0$. For both filters, there is a parameter controlling the amount of cut frequencies. The ideal filter can be pictured as a cylinder in the frequency space, centered around the $u = 0$, $v = 0$ coordinate, with a radius r_{LP} and a unit height, therefore the amount of frequency cut can be controlled by the radius r_{LP}. In the case of a two-dimensional Gaussian probability distribution function, the parameter σ_{LP} would be the variance, ergo the 'width' of the distribution. Thus it is easy to see by analogy, that σ_{LP} will have the same rule for a Gaussian transfer function as the radius r_{LP} for an ideal filter. In the following we generalize the same idea for bandpass filters. A transfer function for a bandpass Gaussian filter can be generated by superimposing two Gaussian filters similar to the low-pass filter, with one – the high-pass component – being complemented. Thus, the complete function can be defined as follows:

$$O_{g,BP}(u, v) = \exp\left(-\frac{u^2 + v^2}{2\sigma_{LP}^2}\right) \cdot \left[1 - \exp\left(-\frac{u^2 + v^2}{2\sigma_{HP}^2}\right)\right] \tag{5}$$

where the index HP refers to high-pass. The idea behind the determination of σ values is that the same extent of filtering can be achieved by equal 'volume' ideal and Gaussian transfer functions. The ideal bandpass transfer function can be generally pictured as the difference of two cylinders; their radii r_{LP} and r_{HP} correspond to low- and high-pass cut-off frequencies, their heights are 1. Hence, to find the functions $\sigma_{LP} = f(r_{LP})$ and $\sigma_{HP} = f(r_{HP})$ for an $m \times n$ size image, one can write

$$\int_{-n/2}^{n/2}\int_{-m/2}^{m/2} \exp\left(-\frac{u^2 + v^2}{2\sigma_{LP}^2}\right) du\,dv = \pi r_{LP}^2 \tag{6}$$

$$\int_{-n/2}^{n/2}\int_{-m/2}^{m/2} 1 - \exp\left(-\frac{u^2 + v^2}{2\sigma_{HP}^2}\right) du\,dv = m \cdot n - \pi r_{HP}^2 \tag{7}$$

The integration is carried out from $-m/2$ to $m/2$ (or $n/2$), because the Fourier transform will generate a transformed image with the same dimensions as the original image, in a centrally shifted coordinate system. Considering that most HRTEM images are digitized in $m \times m$ sizes, where m is a power of 2 to ease frequency filtering, therefore $m = n$, the integration of the left sides of (6) and (7) yield

$$2\pi\sigma_{LP}^2 \mathrm{erf}^2\left(\frac{m}{2\sqrt{2}\sigma_{LP}}\right) = \pi r_{LP}^2. \tag{8}$$

$$m^2 - 2\pi\sigma_{HP}^2 \mathrm{erf}^2\left(\frac{m}{2\sqrt{2}\sigma_{HP}}\right) = m^2 - \pi r_{HP}^2. \tag{9}$$

It is apparent that the two equations show symmetry, therefore both σ_{LP} and σ_{HP} can be determined by the implicit transcendent equation

$$0 = \frac{r_{XP}}{\sqrt{2}\mathrm{erf}\left(\frac{m}{2\sqrt{2}\sigma_{XP}}\right)} - \sigma_{XP} \tag{10}$$

where XP refers to either low-pass (LP) or high-pass (HP). In practical situations, when r_{XP} is significantly lower than m, Eq. (10) can be simplified to

$$\sigma_{XP} \approx \frac{1}{\sqrt{2}} r_{XP}. \tag{11}$$

The relative error of this assumption is shown in Fig. 1. By choosing adequate values for σ_{LP} and σ_{HP} it is possible to reduce the image only to the information having structural meaning, i.e. both high frequency and low frequency noise can be filtered. In our case, σ_{LP} and σ_{HP} were determined at cut-off frequencies so that the low-pass component filtered out patterns repeating in less than 0.3 nm (the approximate shortest physically meaningful distance between carbon layers) and the high-pass component filtered out large patches with relative frequencies lower than 10.

After frequency filtering, the inverse Fourier transformed image has been re-scaled and saturated to restore the original image format. Since we used an adaptive thresholding technique, further intensity normalization of the restored image was not necessary.

For the detection process, we used a local, adaptive thresholding technique. This method, along with the rest of the techniques are presented in matrix notation for convenience. Adaptive local threshold methods have been widely used in several image

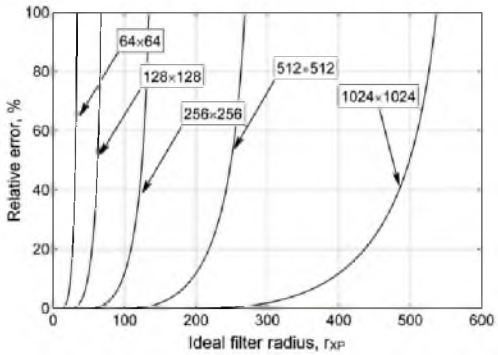

Fig. 1. The relative error of Eq. (11).

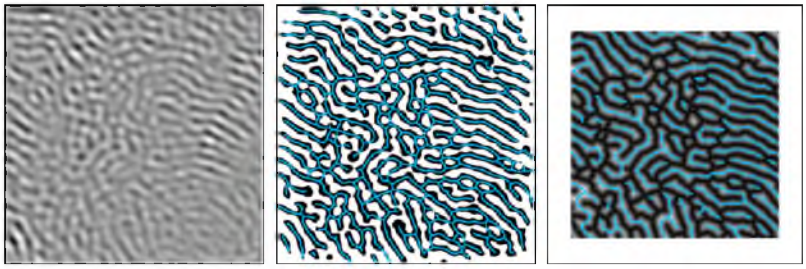

Fig. 2. The main steps of the new algorithm for the determination of Ω. Left: frequency filtered image. Center: binarized image (**B**) with the thinned network indicated by lines (**N**). Right: the grayscale image denotes the distance transform of **N**, $\mathbf{\Delta}$ and the locations of the local maxima in $\mathbf{\Delta}$ are indicated by lines. At these locations, the values of $\mathbf{\Delta}$ will be the members of the set $\mathcal{E}$, from which Ω is computed. The padding in the third image is necessary to eliminate errors caused by the median filter at image edges.

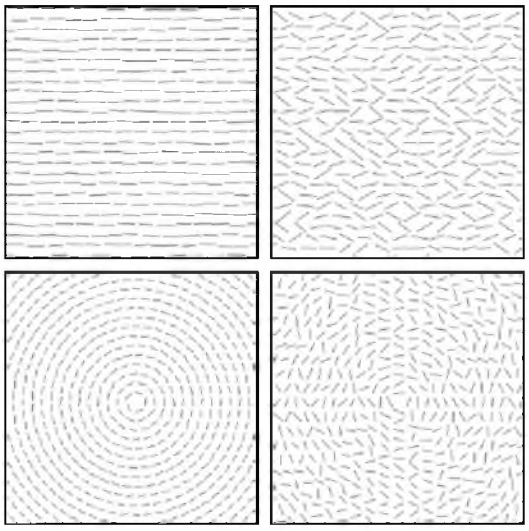

Fig. 3. Examples of artificially created binary fringe skeleton images (artificial versions of **N**). Top left: oriented, axially symmetric set. $S_{2,N} \approx 0.99$. Top right: a shuffled version of the oriented axial set. $S_{2,N} \approx 0.6$. Bottom left: oriented, concentrically symmetric set. $S_{2,P} \approx 0.99$. Bottom right: a shuffled version of the oriented polar set. $S_{2,P} \approx 0.6$.

processing areas, e.g. in document binarization and handwriting recognition [22,23]. 'Local' means that the value of T is not constant for the entire image; instead, T is generalized as a matrix **T** with the same size as the image, thus a variation in the threshold values as a function of the location in the image is allowed. 'Adaptive' means that T (or **T**) is not preliminarily set; its value is dependent on other factors. For an input 8 bit grayscale image **I**, each entry $T_{x,y}$ of the matrix **T** was calculated as the median value of the $\mu \times \nu$ sized neighborhood around the corresponding image pixel $I_{x,y}$, including $I_{x,y}$ itself. As our images were digitized with an aspect ratio of 1, square-shaped median filters were used ($\mu = \nu$). From our point of view, this binarization filter that produces the output binary image **B**, defined in the following way:

$$B_{x,y} = \begin{cases} 0 & \Rightarrow I_{x,y} > T_{x,y}; \\ 1 & \Rightarrow I_{x,y} \leqslant T_{x,y}. \end{cases} \tag{12}$$

has several advantages. First, median filtering has noise-removal effects, making the edges of the detected objects 'smoother', i.e. it

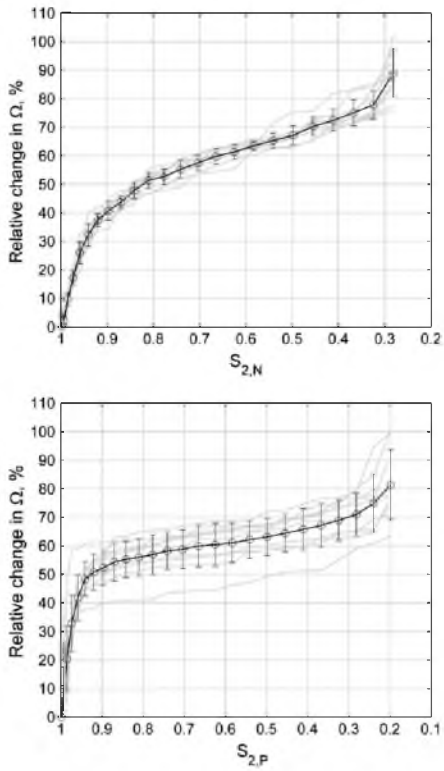

Fig. 4. The results of the stochastic simulations. Top: the correlation of Ω with $S_{2,P}$. Bottom: the correlation of Ω with $S_{2,P}$.

tends to remove spur pixels, which is beneficial in the next step. Second, this method considers regional changes in intensity rather than absolute values, thus less focused or less intense fringes can be detected as well. This feature explains the need for a frequency filter that does not produce harmonic ringing artifacts, thus the usage of Gaussian frequency filters.

In the next step, the detected pattern is skeletonized using the algorithm presented Zhang and Suen [24]. This iterative algorithm removes edge pixels and leaves only the backbone of the structure, but does not tend to leave spurs and diagonal arms. The remaining

lines make a binary network of fringes **N**, which is the input for topological analysis. **N** only contains 1 and 0 values and 1 values form thin connected components.

Two new structural parameters are proposed that can be measured on these connected networks. The distance deviation parameter Ω (nm) is the standard deviation of the Euclidean distance set $\mathcal{E}$, while the junction parameter υ (1/nm) is the average number of branchpoints per network length unit. In the following, we define these parameters and discuss their physical significance.

The calculation of Ω can be achieved in a number of steps. First, the Euclidean distance transform of the binary network $\mathbf{\Delta} = \mathrm{dist}(\mathbf{N})$ is computed. The Euclidean distance transformed value of a point $B_{x,y}$ in a binary set **B** is its Euclidean distance to the nearest point with the value $\neg B_{x,y}$, the negated value. Because **N** is a binary discrete network without blocks of adjacent 1 values, for coordinates (x_0,y_0), where $N_{x_0,y_0} = 1$, Δ_{x_0,y_0} is most likely a regional minimum of $\mathbf{\Delta}$. Note that these are the locations of the 1 valued pixels in **N**, thus it is not surprising that they belong to the regional minima of $\mathbf{\Delta}$ – they denote the skeletons of the fringes in **I**.

From the above mentioned, it is easy to see that points in the regional maxima in $\mathbf{\Delta}$ correspond to half of the shortest distances between the centers of the nearest two objects; the connected lines formed by the adjacent points of the regional maxima of $\mathbf{\Delta}$ are always positioned halfways between objects in **B**. In the second step, values belonging to the set of regional maxima are extracted from $\mathbf{\Delta}$. We denote this set as $\mathcal{E}$. Generally, there are two obvious ways of doing this: one could either use numerical gradient operators to find the locations of regional maxima or apply the same skeletonization routine to $\neg\mathbf{N}$ as one used to obtain **N** itself, so that the 1 valued pixels in the skeleton of $\neg\mathbf{N}$ will indicate the locations of the local maxima in $\mathbf{\Delta}$. Here the latter was used.

Once the set of local maxima of $\mathbf{\Delta}$ has been extracted by the above described method, the distance deviation parameter Ω can be readily computed by computing the standard deviation of the set of local maxima values. Therefore Ω expresses the amount of variation in the generalized interlayer distances. In other words, Ω quantifies how much the fringe distances deviate from the average interlayer distance in an image, in nanometers.

As can be seen, values in $\mathcal{E}$ are simply generalized versions of the already well-known interlayer spacing. The generalization originates in extending the applicability of the interlayer distance to fringes that are not parallel to each other and /or are curved. The advantages of a structural parameter like Ω are the significantly larger sample sizes and the convergent nature of the standard deviation value. By using the original definition of interlayer distances, only one value is obtained from an adjacent pair of fringes – an analogous value in $\mathcal{E}$ can be extracted from every single local maximum in $\mathbf{\Delta}$. If the images are sampled correctly, Ω will converge to a statistically representative value for the image or set of images coming from the same soot sample, thus the uncertainty in Ω will be negligible. The disadvantage is that although Ω is simply the average deviation of the generalized interlayer distances, it is more difficult to grasp its direct physical meaning. Ω characterizes the texture in a complex way, as it is a parameter describing the uniformity of the lattice spacing distribution, the parallelity of the fringes and the order of their orientation as well.[1] Its value is 0 for a perfectly graphitic texture containing only parallel, elongated fringes and increases with decreasing orderliness. A demonstration of the main steps of the algorithm for ease of understanding is presented in Fig. 2.

The calculation of the junction parameter υ is done by counting the branchpoints on the thinned networks and dividing this value by the measured length of the network. The detected branchpoints are filtered so that forks with an arm of length not exceeding a certain threshold are not considered as branches. This way spur pixels and arms that are the results of the binarization of jagged contours are left neglected. The filtering algorithm works by checking the distance of each branchpoint from the nearest endpoint of an arm, and pixels connecting too closely spaced branch-end pairs are removed from the network. Branchpoints too close to each other are merged by binary dilations.

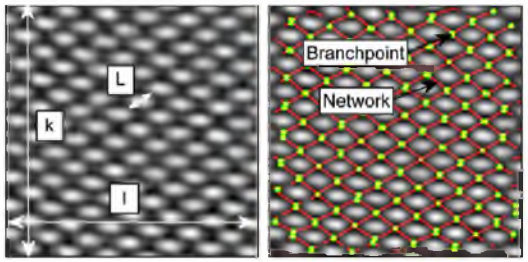

Fig. 5. The verification of the junction-finding algorithm. Left: a detail of a HRTEM micrograph taken of an oriented Si single crystal. Right: The detected network (lines) and branchpoints (dots).

Similar to distance deviation, υ is an empirical parameter of the orderliness of carbon texture as well: higher values indicate a more entangled structure, as the number of branchpoints increase with decreasing fringe lengths and overlapping layers. Its value is 0 for an ideal graphitic crystal with parallel fringes and no overlapping. A more entangled and amorphous structure will exhibit higher values for υ.

3. Results and discussion

To present the correlation of Ω with $S_{2,P}$ and $S_{2,N}$, we have conducted several stochastic simulations by using artificially created fringe skeleton images. For the analysis of $\Omega = f(S_{2,N})$, the images were constructed to contain short fringes with randomly positioned centers of mass, but not allowing overlapping fringe skeletons. Their orientations were also randomized, by using a random generator yielding uniformly distributed numbers in the range $[-q,q]$. For the simulation of concentrically symmetric structures,

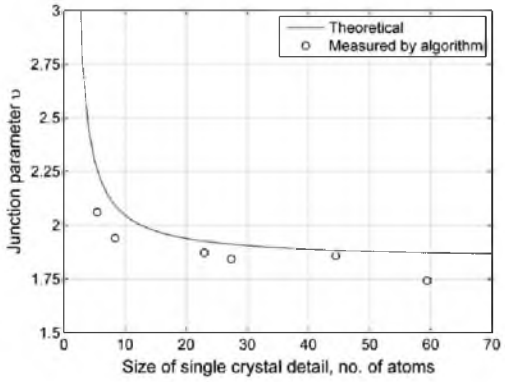

Fig. 6. The verification of the junction-finding algorithm with Si 1 1 0 lattice images. The continuous line shows the theoretical value for Si 1 1 0 images.

[1] Note that the same is true when using the conventional definition of interlayer spacing.

a large number of fringe skeletons were rendered around a concentric center, equally spaced from each other and then perturbing their orientation angle by these random values. In this way, it is possible to observe how Ω changes with the order parameters $S_{2,P}$ and $S_{2,N}$.

Examples of these artificial images are presented in Fig. 3. By simplifying Eq. (2) by only considering concentric symmetry and if the number of fringes on each image is large, both $S_{2,N}$ and $S_{2,P}$ can be estimated by

$$S_{2,X} \approx E(2\cos^2(\Theta) - 1) \tag{13}$$

where Θ is a random variable of uniform distribution with values in the range $[-q,q]$ and $E()$ is the expected value of its argument.

Solving (13) yields

$$S_{2,X} \approx \frac{\sin(2q)}{2q} \tag{14}$$

Fig. 4 presents the results of the stochastic simulations. The tests were conducted with images representing gradually decreasing order parameters in each consecutive test. For each parameter, a total of 10 tests were evaluated, with images containing 400 fringes.

It is apparent that the decrease in the order parameters resulted in an increase in Ω, but the correlation is not linear. The measured values of Ω increased monotonically in both cases, exhibiting steeply increasing periods at both ends of the curves. With our sets, changing the polar order parameter of the concentrically symmetric images induced less predictable changes in the values of the distance deviation parameter and the experimental data was more scattered. The monotonity that can be observed in Fig. 4, along with the fact that Ω responds to many conditions – including these two order parameters – ensures that even slight changes in structure can be representatively monitored. Another advantage is that Ω is sensitive

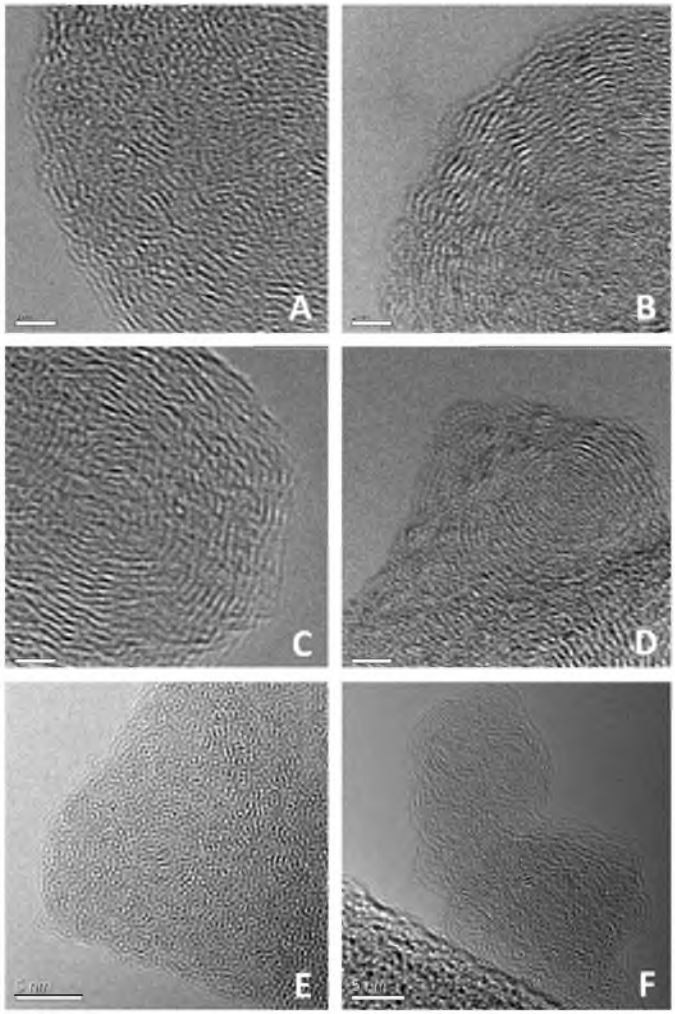

Fig. 7. Some examples of the analyzed images. (A) Ethylene flame 1, HAB = 0.5 mm. (B) Ethylene flame 1, HAB = 4 mm. (C) Surrogate flame, HAB = 1 mm. (D) Surrogate flame, HAB = 5 mm. (E) Benzene flame, HAB = 5 mm. (F) Benzene flame, HAB = 15 mm.

in the range of low $S_{2,P}$ and $S_{2,N}$ values. The downside is that it is impossible to gain information about specific structural parameters solely by observing changes in the value of Ω; it should rather be used as an intuitive empirical parameter of orderliness.

For the verification of the junction finding algorithm, we used HRTEM images of Si lattices. At certain magnifications, Si single crystals look like perfect grids, where intense spots are believed to be Si atoms. For such arrangements and for infinitely large fields of view, the ideal value of υ can be calculated as follows:

$$\upsilon = \lim_{k,l\to\infty}\left[\frac{k\cdot l}{l(k-1)L + k(l-1)L}\right], \tag{15}$$

where k and l are the number of atoms that can be counted on the image horizontally and vertically and $L \approx 0.2715$ nm, half the lattice spacing of Si single crystals [25] (see Fig. 5).

The horizontal axis illustrates the number of atoms ($k \times l$) of the detail that has been cut from a large lattice image. Since the horizontal and vertical dimensions of these details were not the same, an average size of

$$k^* = \sqrt{k\cdot l} \tag{16}$$

is shown.

Fig. 6 shows the results of this verification. The continuous line represents the ideal, calculated value of υ, while the circles mark the measured results. The errors of the algorithm are most commonly caused by duplicate branchpoints, crystal imperfections, inaccurate network extraction and image noise, however the magnitude of errors is in an acceptable range.

The above introduced parameters, Ω and υ were calculated for samples originating from four fuels and with soot samples taken at different heights above burner (HAB). As HAB increases and the soot gets more mature, an increase in orderliness can be expected, as the conventional analysis of [26] could demonstrate a slight shift in fringe lengths in the case of methane soots. An increasing orderliness would suggest a decrease in both Ω and υ. A few examples of the analyzed images can be seen in Fig. 7.

From the real HRTEM images and from each sample, both Ω and υ were computed. Because multiple images had been taken from the same soot sample, for the determination of Ω, images coming from the same sample were processed and sets of $\mathcal{E}$ (containing the generalized interlayer distances) were extracted. These sets were united and Ω was computed from these united sets, thus a single value for Ω was obtained for each soot sample, regardless of multiple images per sample. The number of distances extracted from one 1024 $\times$ 1024 image was between 30,000 and 60,000, and several micrographs were analyzed for each sample. Separate values of υ were calculated for each micrograph, then average values were produced for different samples.

The conventional analysis of these images was also conducted for the sake of comparison, using a methodology based on the technique published by Palotás et al. [5]. The measured parameters of the fringe images were the fringe lengths (nm) – measured as proposed by Vander Wal et al. [11], i.e. the length of the skeleton of the fringe – and interlayer distances (nm), measured as proposed by Palotás et al. [5]. The results of this statistical analysis are presented in Fig. 8.

As it is apparent from Fig. 8, conventional statistical analysis produced results based on which the reliable differentiation of similar structures is difficult. The values of the interlayer distances show insignificant differences between samples and there is no apparent trend in the evolution of fringe lengths. Apart from this, the inherently high standard deviation of the results provided by conventional image analysis makes the differentiation impossible, based on mean values alone.

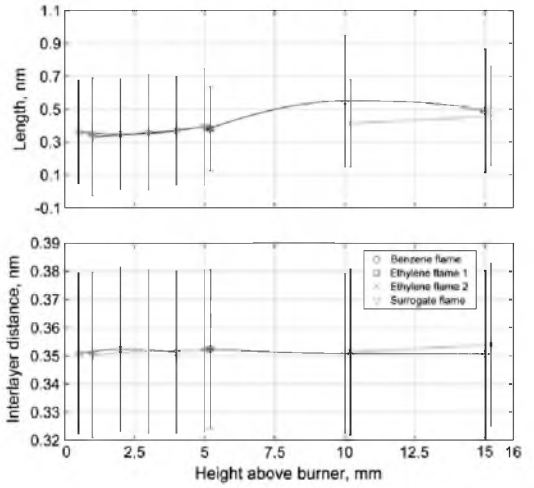

Fig. 8. Results of a conventional statistical image analysis method applied to our samples. Some datapoints were slightly displaced to improve visibility. For exact values regarding HAB see Table 1.

The results for Ω and υ obtained by the proposed method are presented in Fig. 9.

The trends of the two parameters are quite obvious as both decreased with increasing HABs for all four samples, meaning that an increasing magnitude of order could be detected in the soot structures. Interestingly enough, an even stronger correlation was found between Ω and υ. Based on the observation of Ω, the highest degree of structural evolution happened in the soots from the ethylene flames, especially at low HABs. The rather small change in Ω measured in surrogate soots can be explained by the fact that these soots were found to be fairly well ordered even at low HABs (while still being amorphous), however a huge drop in υ indicates some extent of simplification in the texture (notice the highly developed concentric rings in Fig. 7D). Benzene flames showed a slight decrease in Ω and a significant drop in υ as HAB increased, also suggesting a rather evenly spaced population of fringes at all HABs, with fringes getting more elongated. Note that the continuous lines in the plots are just guides to the eye, as soot was only sampled at a few HABs per fuel. The uncertainty bounds on υ were computed as the standard deviation of the separate values for each image. Based on both structural parameters, soot from the surrogate fuel showed the highest structural order. This structural order was still evolving between HABs 1 mm and 5 mm. Ethylene showed the lowest extent of orderliness, however between HABs 0.5 mm and 4 mm its Ω values were quickly decreasing, indicating a very abruptly transforming soot structure. Based on Ω values, the orderliness of soot produced in the second ethylene flame was less than that produced in the first ethylene flame. This can be explained by the premixing system – the first flame was produced by a two-stage premixer, thus a more perfect mixing of the fuel and preliminary oxidation happened, allowing quicker soot structure evolution.

Despite the few sampling locations, it is easy to see trends in the evolution of the structure of soot. Different soots from different fuels start to age at different heights. The data suggests that there are zones of accelerating and decelerating evolution for each fuel and that the location of these zones depend on both the fuel and operating conditions. As an idea for future work we note that by using the above described sensitive structural parameters, it is possible to map these regions in flames.

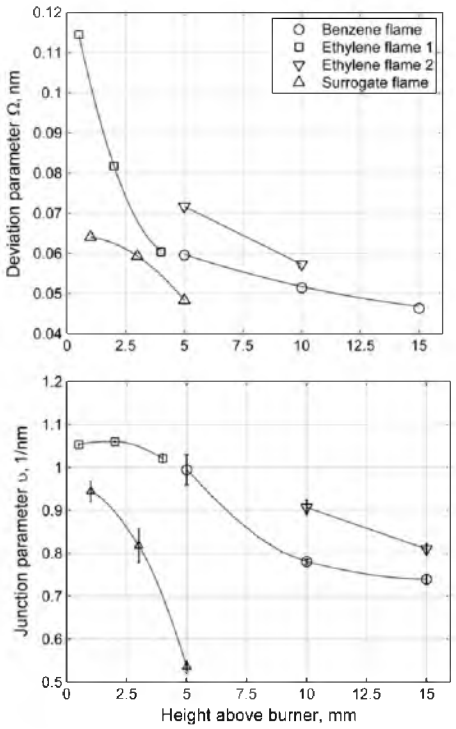

Fig. 9. The measured values of Ω and υ for the fuel samples. Lines are guides to the eye.

4. Conclusions

A sensitive image analysis technique has been developed for the representative quantification of soot nanostructure orderliness utilizing several image processing techniques. The technique proposed here is robust, since the evaluated number of elements in the measured datasets is large, and produces consistently reproducible parameters with a resolution high enough to show differences in soot structure. The method has been applied to soot samples of various fuels, collected from different burner setups at different heights above burner in order to monitor their nanostructural evolution. In all cases, decreasing tendencies were found in the values of the distance deviation and junction parameters as the heights above burner increased, indicating increasing structural orderliness in the soot. The resolute and accurate monitoring of the nanostructural evolution of soot is possible by the described methodology provided that HRTEM images were representative of the sample.

Acknowledgment

This work was partially sponsored by the TAMOP-4.2.1.B-10/2/KONV-2010-0001 project with support by the European Union, co-financed by the European Social Fund.

References

[1] Laurent P, Braekman-Danheux C, Rouzaud JN. Microtextural study of cokes from hydropyrolysis of coals. Fuel 1995;74(2):201–7.
[2] Auguie D, Oberlin M, Oberlin A, Hyvernat P. Microtexture of mesophase spheres as studied by high resolution conventional transmission electron microscopy (CTEM). Carbon 1980;18:337–46.
[3] Ishiguro T, Takatori Y, Akihama K. Microstructure of diesel soot particles probed by electron microscopy: first observation of inner core and outer shell. Combust Flame 1997;108:231–4.
[4] Vander Wal RL, Yezerets A, Currier NW, Kim DH, Wang CM. HRTEM study of diesel soot collected from diesel particulate filters. Carbon 2007;45:70–7.
[5] Palotas AB, Rainey LC, Feldermann CJ, Sarofim AF, Sande JBV. Soot morphology: an application of image analysis in high-resolution transmission electron microscopy. Microsc Res Tech 1996;33:266–78.
[6] Sharma A, Kyotani T, Tomita A. A new quantitative approach for microstructural analysis of coal char using HRTEM images. Fuel 1999;78:1203–12.
[7] Shim HS, Hurta RH, Yang NY. A methodology for analysis of 002 lattice fringe images and its application to combustion-derived carbons. Carbon 2000;38:29–45.
[8] He Yang J, Hui Cheng S, Wang X, Zhang Z, Rong Liu X, Hua Tang G. Quantitative analysis of microstructure of carbon materials by HRTEM. Trans Nonferrous Met Soc China 2006;16:796–803.
[9] Rouzaud JN, Clinard C. Quantitative high-resolution transmission electron microscopy: a promising tool for carbon materials characterization. Fuel Process Technol 2006;77–78:229–35.
[10] Palotas AB, Rainey LC, Sarofim AF, Sande JBV. Where did that soot come from? Chemtech 1998;28:24–30.
[11] Vander Wal RL, Bryg VM, Hays MD. Fingerprinting soot (towards source identification): physical structure and chemical composition. Aerosol Sci 2010;41:108–17.
[12] Alfe M, Apicella B, Barbella R, Rouzaud JN, Tregrossi A, Ciajolo A. Structure–property relationship in nanostructures of young and mature soot in premixed flames. Proc Combust Inst 2009;32:697–704.
[13] Shaddix CR, Palotas AB, Megaridis CM, Choi MY, Yang NY. Soot graphitic order in laminar diffusion flames and a large-scale JP-8 pool fire. Int J Heat Mass Transfer 2005;48:3604–14.
[14] Zhu W, Miser DE, Chan WG, Hajaligol MR. HRTEM investigation of some commercially available furnace carbon blacks. Carbon 2004;42:1841–5.
[15] Henson R, Reynolds W. Lattice parameter changes in irradiated graphite. Carbon 1965;3:277–87.
[16] Tidjani M, Lachter J, Kabre T, Bragg R. Structural disorder induced in graphite by grinding. Carbon 1986;24:447–9.
[17] Aladekomo J, Bragg R. Structural transformations induced in graphite by grinding: analysis of 002 X-ray diffraction line profiles. Carbon 1990;28:897–906.
[18] Aso H, Matsuoka K, Sharma A, Tomita A. Structural analysis of PVC and PFA carbons prepared at 500–1000 °C based on elemental composition, XRD, and HRTEM. Carbon 2004;42:2963–73.
[19] Echavarria CA, Sarofim AF, Lighty JS, D'Anna A. Modeling and measurements of size distributions in premixed ethylene and benzene flames. Proc Combust Inst 2009;32:705–11.
[20] Echavarria CA. Evolution of soot size distribution during soot formation and soot oxidation–fragmentation in premixed flames: experimental and modeling study. PhD Thesis. University of Utah; 2010.
[21] Dobbins RA, Megaridis CM. Morphology of flame-generated soot as determined by thermophoretic sampling. Langmuir 1987;3:254–9.
[22] Sauvola J, Pietikainen M. Adaptive document image binarization. Pattern Recogn 2000;33:225–36.
[23] Gatos B, Pratikakis I, Perantonis S. Adaptive degraded document image binarization. Pattern Recogn 2006;39:317–27.
[24] Zhang TY, Suen CY. A fast parallel algorithm for thinning digital patterns. Image Process Comput Vision 1984;27:236–9.
[25] O'mara WC. Handbook of semiconductor silicon technology. William Andrew Publishing; 1990.
[26] Alfe M, Apicella B, Rouzaud JN, Tregrossi A, Ciajolo A. The effect of temperature on soot properties in premixed methane flames. Combust Flame 2010;157:1959–65.

CHAPTER 3

A NOVEL FRAMEWORK FOR THE QUANTITATIVE ANALYSIS OF HIGH RESOLUTION TRANSMISSION ELECTRON MICROGRAPHS OF SOOT I. IMPROVED MEASUREMENT OF INTERLAYER SPACING

Reprinted from Combustion and Flame, Vol. 160, Pal Toth, Arpad B. Palotas, Eric G. Eddings, Ross T. Whitaker, JoAnn S. Lighty, A novel framework for the quantitative anal- ysis of high resolution transmission electron micrographs of soot I. Improved measurement of interlayer spacing, Pages 909-919, Copyright 2013, with permission from Elsevier.

Combustion and Flame 160 (2013) 909–919

Contents lists available at SciVerse ScienceDirect

Combustion and Flame

journal homepage: www.elsevier.com/locate/combustflame

A novel framework for the quantitative analysis of high resolution transmission electron micrographs of soot I. Improved measurement of interlayer spacing

Pal Toth [a,*], Arpad B. Palotas [b], Eric G. Eddings [a], Ross T. Whitaker [c], JoAnn S. Lighty [a]

[a] Department of Chemical Engineering, University of Utah, 50 S. Central Campus Drive, Salt Lake City, UT 84112-9203, United States
[b] Department of Combustion Technology and Thermal Energy, University of Miskolc, H3515 Miskolc-Egyetemvaros, Hungary
[c] School of Computing, University of Utah, 3893 Warnock Engineering Building, Salt Lake City, UT 841112-9205, United States

ARTICLE INFO

Article history:
Received 27 October 2012
Received in revised form 8 January 2013
Accepted 8 January 2013
Available online 6 February 2013

Keywords:
Soot
Nanostructure
HRTEM

ABSTRACT

The reliable and reproducible quantitative image analysis of digital micrographs from high resolution transmission electron microscopy (HRTEM) of soot has been an area of interest since the early nineties. Since the resolution of HRTEM images is usually sufficient to carry out structural measurements at the atomic level, the information obtained from these images is very valuable as it potentially yields insight into very specific soot oxidation processes; however, extracting physically meaningful, reliable, accurate and statistically robust data from HRTEM images is not an easy process. Data extraction is hindered by the presence of overlapping structures, varying focus, contrast, illumination levels and noise in the images. In this paper a novel image analysis framework is presented to address these issues and explore the possibility of the extraction of high-fidelity structural data from HRTEM soot images. Emphasis is on the analysis of images of mostly amorphous, poorly ordered soot structures, as these are the most difficult to analyze.

Published by Elsevier Inc. on behalf of The Combustion Institute.

1. Introduction

The digital image analysis of high resolution transmission electron microscopy (HRTEM) images of soot allows for the characterization of the carbon structure at the atomic level. The nanoscale observation of soot structure is motivated by either an incentive to determine the source of soot pollution [1,2] or to better understand combustion processes [3]. A typical soot HRTEM micrograph shows an overlapping pattern of periodically occurring dark and bright lines of varying orientation and contrast. These lines are also called fringes and they are understood to be projections of graphene layers formed by phase contrast imaging principles. The meaning of dark and bright fringes are not obvious, as depending on the imaging conditions, they can either indicate carbon atoms or the spaces between them. Although not typical, the meaning of bright and dark fringes can be also dynamically reversed depending on imaging conditions and sample thickness. This phenomenon will be referred to as phase inversion in this paper. Also, it is practically important to satisfy some general conditions for the reliable measurement of geometric properties of fringe images: first, fringe contrast should be maximized and second, image regions where fringe contrast changes abruptly should not be used for geometric analysis [4]. Image processing and analysis methods aiming to extract structural information from HRTEM images of soot have been developed and applied since the mid-nineties [5–10]. These methods differ in details, however the basic procedure consists of the following steps:

1. The pre-filtering of the digital micrograph. This step usually consists of frequency filtering; i.e., the removal of unwanted frequencies in the image. Since carbon layers can only appear in a well-known frequency band determined by physically meaningful values of their interlayer spacing, bandpass frequency filtering is ideal for noise reduction in HRTEM soot images.
2. The detection of separate fringes. This step is usually an image binarization procedure, meaning that the initially gray scale image is transformed to a binary image in which fringes are indicated as 1 values and background is indicated by 0 values. Until lately, in most cases this transformation has been a global, non-adaptive binarization process; i.e., a single pixel intensity threshold has been set to determine whether a particular pixel belongs to a fringe or background. Authors have started to report results obtained by methods utilizing adaptive binarization [10]. The outcome of this step is a binary image in which individual objects (fringes) can be detected and labeled.

* Corresponding author.
E-mail address: toth.pal@uni-miskolc.hu (P. Toth).

0010-2180/$ - see front matter Published by Elsevier Inc. on behalf of The Combustion Institute.
http://dx.doi.org/10.1016/j.combustflame.2013.01.002

3. The postprocessing of binary objects. In this step, the labeled binary fringes are processed further. The postprocessing techniques vary from author to author. Some use geometric criteria for selecting valid fringe candidates [5], some use skeletonization algorithms to reduce fringes to curves or line segments [6–10] and some implement fringe separation/reconnection logic [7].
4. The data extraction step. In this step geometric information is extracted from the postprocessed binary fringe objects. Geometric data can include fringe lengths [6–10], fringe tortuosity [9,10], fringe separation (interlayer distance) [5–10] and fringe orientation [5,8], among others.

The obtained geometrical data is in the form of vectors or sets of the mentioned properties. Each value in each set corresponds to a particular detected fringe in the analyzed micrograph. After extraction, these sets can be statistically described by constructing probability distribution functions (PDFs), specifying mean and standard deviation values and so forth. Structural order can be characterized by quantifying the symmetries and deviations in fringe orientation or fringe spacing values [6,8]. The common drawbacks of methodologies that are based on the steps described above are the usage of subjectively set image processing parameters, results that are sensitive to these parameters and the insufficient amount of structural data extracted due to the oversimplification of images (the detection and artificial separation of individual fringes). Because of all these reasons, it is understood that the quantitative characterization and differentiation of real soot HRTEM images can be a difficult problem, especially when trying to differentiate poorly ordered, highly amorphous and/or only slightly different samples. In fact, the quantitative image analysis of amorphous soot samples has been considered an unsolved problem since the publication of the first papers in this area, especially when on aims to measure interlayer spacing statistics in soot structures (e.g., see insufficient number of data points in [11] or insignificant differences in statistics in [12]). Recently, we have developed an image analysis procedure with which distances can be measured between curved graphene layers as well, thus increasing the fidelity of the obtained distributions; however, this method does not avoid the subjectivity of binarization techniques and can only be used to obtain semi-quantitative descriptors [13].

2. Materials and methods

In this section a detailed description of the proposed image processing and analysis methodology is given along with the details and origins of the image sets used for the validation and verification of the proposed algorithm.

2.1. Image analysis procedure – overview

The image processing methodology proposed in this work is completely different from the methods discussed in Section 1. The proposed method has been developed to address and overcome all the specific issues of the standard methods and it utilizes recent advances and ideas from the image analysis and signal processing literature. Similar algorithms have been applied in HRTEM crystallography [14,15]. While these published algorithms are similar, they are not applicable to images of more complex nanostructures. The basic objectives of the proposed methodology are the following:

1. To extract as much structural data as possible from a single micrograph. A higher number of data points means more accurate and reliable statistical evaluation of the structure. Being able to extract the highest amount of structural information from a single image has significant importance in cases where the availability of samples or micrographs is limited. Since typical procedures for soot sampling deposit abundant quantities of soot particles on TEM grids, the scarcity of samples is usually not a problem when analyzing real soot. However, depending on the heterogeneity of the soot particles, acquiring and analyzing a number of micrographs that is sufficient for obtaining robust statistics can be a time-consuming process. In these cases, being able to extract as much information as possible from each micrograph not only increases the fidelity of the results, but has practical and economic importance as well.
2. To extract information only from reliable image regions in order to minimize measurement uncertainty and errors.
3. To measure structural parameters as accurately as possible.
4. To minimize the number and effect of subjectively chosen and set image processing parameters that are purely technical and do not hold any real physical meaning (e.g., threshold values, filter kernel sizes and parameters for fringe detection logic – see [5] or [11] for typically arising parameters).
5. To be able to handle typical aberrations and artifacts present in HRTEM micrographs; e.g., noise, inhomogeneous illumination and phase inversion.

To achieve these objectives, one must consider a different model for soot HRTEM images than the standard model. By image model we refer to a mindset that is used to interpret these images. The standard model assumes that the micrographs contain identifiable or detectable objects; – i.e., imaged physical bodies (atoms or layers of atoms) with well defined boundaries and the standard methods aim to locate these bodies and their boundaries in the images. Such a model inherently leads to large amounts of eliminated data, as it is only interested in the detected bodies themselves (which are well defined and quantized) and their geometric properties. Instead, our approach interprets the micrographs as continuous (at least at the image level) projections of patterns in electromagnetic fields[1] and tries to analyze the patterns evolved in the projections. This image model is also more realistic from the quantum-physical point of view. Mathematically, images are interpreted as superpositions of two-dimensional patches of sinusoidal patterns with varying phase, frequency, amplitude and orientation corrupted by noise and contrast inhomogeneity. The proposed parameters to use for structural characterization are exactly these (and the maps of these) signal properties. It is easy to see that, following the proposed image model, there is no need for a detection step; – i.e., the labeling of well-defined binary fringes. Information can be extracted at the native resolution of the image, meaning that every single pixel in the image will yield a set of structural parameters. The approach results in an abundant flow of information, which contributes to the statistical robustness of the extracted data. It is also possible to evaluate certain image regions based on their quality (signal strength) and only extract structural information from reliable regions. Since the approach is a spectral technique and is not based on pixel-level manipulations, sub-pixel accuracy can be achieved in the measurement of structural parameters. The upper limit of pointwise accuracy of these measurement is only set by the Nyquist sampling criterion. In the following, a detailed description of the methodology and approach is given.

2.2. Image analysis procedure – development

Three structural parameters are proposed in this study. These are the local orientation θ, local wavelength λ and local modulation

[1] In other words, signals.

strength μ of the signal. These describe the sinusoidal pattern in a specific location in the image, but since the sinusoidal patterns are in fact the interpretations of fringes, the proposed structural properties are simply the continuous generalized versions of the already used and published fringe structural parameters. More precisely, local orientation is a generalized version of fringe orientation and local wavelength is the generalized version of the interlayer spacing. The local modulation strength is a new parameter that describes and quantifies the reliability and local anisotropy of the neighborhood around a specific pixel. To extract these generalized structural parameters, a localized frequency filtering approach is applied based on filtering the images with a set of Gabor filters, also called a Gabor filter bank. Several similar algorithms have been proposed in the field of medical image processing and computer vision for applications like image registration [16,17]. The general approach is a hybrid spatial/frequency domain filtering method and it combines the advantages (sub-pixel resolution, spectral representation and localization) of both [18]. Gabor filters are quadrature filters that can be fine-tuned to specific wavelengths, scales and orientations. Filtering (mathematically realized by two-dimensional convolution) the image with a Gabor filter yields a filtered image, also called a response. In this response, locations where the wavelength and orientation of the sinusoidal pattern in the original image were the closest to the wavelength and orientation of the Gabor filter yield the highest response value. Thus, by repeatedly filtering the image with a set of differently tuned Gabor filters and recording the responses, it is possible to extract local wavelength and orientation values at each image pixel. The term quadrature refers to the phase-independent response magnitudes of Gabor filtering. Since the phase of a sinusoidal pattern is directly connected to its local intensity, it is easy to see that Gabor filtering analysis is immune to the phase inversion phenomenon mentioned in Section 1. In other words, it is not important whether dark or bright pixels indicate atoms or spaces between atoms – the responses will be the same in both dark and bright regions. Gabor filters also achieve the theoretical lowest localization uncertainty, thus they are ideal candidates for applications where one aims to minimize measurement uncertainties [19,20]. The analytical form of a two-dimensional Gabor filter in the spatial domain is the following:

$$g(x,y) = \frac{1}{2\pi\sigma_x\sigma_y}\exp\left(-\frac{x'^2}{2\sigma_x^2}-\frac{y'^2}{2\sigma_y^2}\right)\exp\left(\frac{2\pi i x'}{g_\lambda}\right) = W(x,y)S(x,y) \tag{1}$$

By definition, the two-dimensional (x, y) spatial Gabor filter is a superposition of a Gaussian window $W(x, y)$ and a complex sinusoidal $S(x, y)$. σ_x is the scale parameter of the Gaussian window in the x direction and σ_y is the scale parameter of the Gaussian window in the y direction. i is the complex unit vector and g_λ is the wavelength of the complex sinusoidal (in other words, the wavelength to which the filter is tuned to). The rotated coordinates x' and y' can be expressed as

$$x' = x\cos(g_\theta) + y\sin(g_\theta) \tag{2}$$

$$y' = y\cos(g_\theta) - x\sin(g_\theta) \tag{3}$$

where g_θ is the orientation angle to which the filter is tuned to. g_λ and g_θ are not the same as the local wavelength λ and orientation θ of the image at a particular pixel, thus the different notation. The frequency domain form of the Gabor filter is a Gaussian surface. It can be written as the Fourier transform of $g(x, y)$:

$$G(u,v) = \mathcal{F}[g(x,y)] = \exp\left(\frac{\sigma_x^2(2\pi + g_\lambda u')^2}{2g_\lambda^2 - 0.5(v'\sigma_y)^2}\right) \tag{4}$$

where u and v are the horizontal and vertical frequency coordinates, respectively. u' and v' are rotated frequency coordinates and are obtained similarly to x' and y'. $\mathcal{F}$ denotes Fourier transformation with respect to a centrally shifted frequency domain (u, v). A quadrature Gabor filter pair along with its frequency domain representation is shown in Fig. 1.

The filter demonstrated in Fig. 1 is only a single member of the filter bank that is used to extract wavelengths and orientations from the image. The design of the whole filterbank is the most practical to carry out in the frequency domain. The general idea behind the filter bank design is to cover and sample the relevant frequency bands of the image with Gabor filters. The filter bank is therefore a collection of sets of filter parameters g_θ, g_λ, σ_x, σ_y and by the design of the filter bank, one refers to the determination of these parameters. The determination of g_θ and g_λ is an easier process, since typical HRTEM soot images contain orientations in the full range $[-\pi/2, \pi/2[$[2] and wavelengths corresponding to a well defined frequency band derived from valid interlayer spacing values. One thing to note is that while the orientation scale is linear, the frequency (and therefore wavelength) scale is not, thus one must sample wavelengths exponentially (lower frequencies/higher wavelengths must be sampled more densely). Also note that due to the direction ambiguity of orientation angles, θ values only cover a half circle (a range of π). In other words, an orientation angle value of θ_1 means exactly the same orientation as $\theta_1 \pm l\pi$, where l is an integer. One needs to specify a number of filters n_θ to cover the range of θ and another number n_λ to cover the range of λ. Once these numbers are specified, the orientation and wavelength values to sample can be calculated as

$$g_{\theta,j} = -\frac{\pi}{2} + j\frac{\pi}{n_\theta} \tag{5}$$

$$g_{\lambda,k} = \lambda_{min}q^{k-1} \tag{6}$$

$$q = \left(\frac{\lambda_{min}}{\lambda_{max}}\right)^{\frac{1}{n_\lambda - 1}} \tag{7}$$

where j and k are indices of positive integers between $[1, n_\theta]$ and $[1, n_\lambda]$, respectively; θ_j is the jth orientation, λ_k is the kth wavelength, λ_{min} is the lowest wavelength (highest frequency) of interest and λ_{max} is the highest wavelength (lowest frequency) of interest. The permutation of the sets of $g_{\theta,j}$ and $g_{\lambda,k}$ obtained in this way maps out the filter center frequencies in the frequency domain. After these center frequencies are found, one still needs to specify the scale parameters σ_x and σ_y of each filter. The idea behind the specification of the scale parameters is that the value of adjacent filters can be specified at a point equally far away from their center frequencies. Since there are $n_\theta \times n_\lambda$ possible permutations of sets of $g_{\theta,j}$ and $g_{\lambda,k}$, $n_\theta \times n_\lambda$ values of $\sigma_{x,j,k}$ and $\sigma_{y,j,k}$ must be specified. By fixing the filter values q_θ and p_λ at intermittent points between their central frequencies corresponding to the overlapping values in the θ (angular) and λ (radial) directions in the frequency domain, it is apparent that the scale parameter values can be determined by the following relationships [21]:

$$\sigma_{x,j,k} = \left(2\pi\frac{-i\left(\frac{1}{g_{\lambda,k}} - \frac{q}{g_{\lambda,k}}\right)}{(1+q)(\ln(p_\lambda))^{1/2}}\right)^{-1} \tag{8}$$

$$\sigma_{y,j,k} = \frac{0.5}{2\pi\left[\frac{i\tan\left(\frac{\pi}{2n_\theta}\right)\left(g_{\lambda,k}^{-1}\right)}{2(\ln(p_\theta))^{1/2}}\right]} \tag{9}$$

Note that since the frequency responses of the Gabor filters are normalized, both p_θ and p_λ must be less than 1. If this condition is satisfied, the above equations yield real values for scale parameters.

[2] Here the symbols represent an interval that is open from the left and closed from the right.

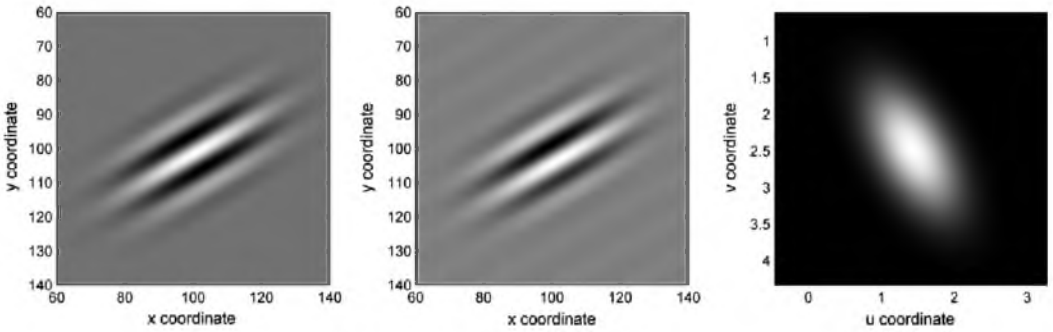

Fig. 1. From left to right: the real component of a Gabor filter in the spatial domain, the imaginary component (quadrature pair) of a Gabor filter in the spatial domain, the Fourier transformed Gabor filter in the frequency domain. The parameters used are: $g_\theta = \pi/3$, $g_\lambda = 0.35$ nm, $\sigma_x = 0.25$, $\sigma_y = 0.5$. This filter would give the highest response at locations where fringes with a spacing of 0.35 nm oriented at $\pi/3$ radians are present in an image with a size of 200 × 200 pixels and a nm per pixel ratio of 5/150. The frequency domain filter is a Gaussian surface centered around frequencies (u_0, v_0). The Euclidean distance of this central point from the origo is exactly $1/g_\lambda$. Note that the filter shown here is enlarged for visualization purposes. Typical filters used for data extraction fit inside a 64 × 64 kernel window.

It is also worth noting that the scale parameters are only functions of $g_{\lambda,k}$ and not $g_{\theta,j}$, which is understandable since the orientation range is sampled linearly. Figure 2 demonstrates the design and construction of a typical Gabor filter bank for soot HRTEM image analysis. Note that while the filter bank essentially contains parameter sets of g_θ, g_λ, σ_x, σ_y, to calculate these sets, the set n_λ, n_θ, p_λ, p_θ must be determined. Therefore, for the balance of this paper the set n_λ, n_θ, p_λ, p_θ will be referred to as the filter bank parameters.

To extract orientations and wavelengths, the HRTEM image is filtered with each filter in the constructed filter bank. The response values for each image pixel are recorded. Intuitively, one can determine the orientation and wavelength at a specific pixel by identifying the filter which gave the highest response at that pixel. The orientation and wavelength of the particular pixel can be estimated as the orientation and wavelength to which the identified best filter is tuned to. While this method is intuitive and graphical, the resulting orientations and wavelengths will be heavily quantized depending on the sampling density of the filter bank. In order to obtain continuous and smooth orientation and wavelength maps, an interpolation method is used in this study. The basic idea of this technique is that the intermediate responses of the filter bank can be approximated by using the individual frequency responses of the filters. The sum of individual filter responses, weighted by the discrete response values obtained by filtering, very closely approximates the continuous response surface one would obtain by filtering with a very densely spaced filter bank. In other words, the ideally high-resolution response surface can be approximated by a finite number of filter responses. The errors introduced by this approximation have been quantified by Perona in 1991 [22]. It has been shown that the error of the approximation quickly approaches zero as the number of filters increases. For our application, the error is practically negligible (approximately 1%) in θ and λ if one uses 15 or more filters per orientation and wavelength range. Mathematically, to find θ and λ at each pixel, one needs to find the global maximum of the interpolated response surface obtained by the following:

$$R_o = \left(Re(I \otimes g_o)^2 + Im(I \otimes g_o)^2\right)^{1/2}\Big|_{x_0,y_0} \tag{10}$$

$$R(u,v) = \sum_{o=1}^{n_\theta \cdot n_\lambda} G_o(u,v) R_o \tag{11}$$

$$(u_{max}, v_{max}) = \arg\max_{u,v}[R(u,v)] \tag{12}$$

$$\theta = \frac{\pi}{2} + \tan^{-1}(v_{max}/u_{max}) \tag{13}$$

$$\lambda = (u_{max}^2 + v_{max}^2)^{-\frac{1}{2}} \tag{14}$$

$$\mu = \frac{R(u_{max}, v_{max})}{R_{ideal}(u_{max}, v_{max})} \tag{15}$$

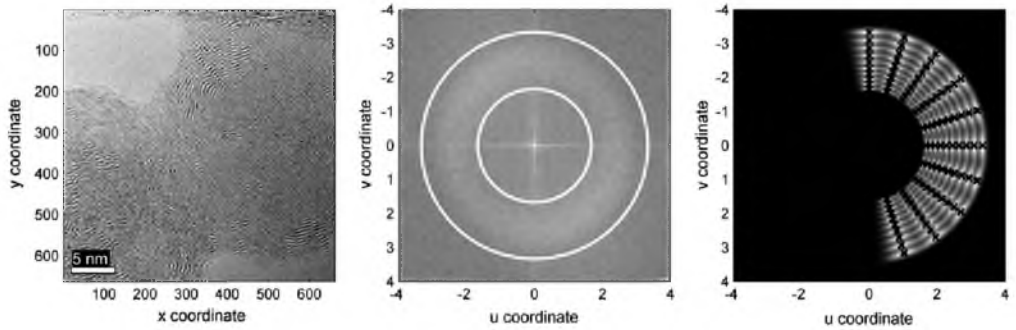

Fig. 2. A demonstration of the design and construction of a Gabor filter bank. Left: HRTEM image of a real soot sample. Middle: the power spectrum (magnitude of Fourier transformation, plotted on a logarithmic scale) of the soot image. Circles denote the selected frequency band for further analysis. This frequency band corresponds to wavelengths between 0.3 and 0.6 nm. These values are chosen based on a priori knowledge of the physically meaningful interlayer spacing values for soot or can be selected automatically by locating the frequency band containing the highest spectral energy (as it is demonstrated by the bright ring around the origo). Right: gray scale values show the superimposed Gabor filters in the frequency domain. Crosses denote the center frequencies of the Gabor filters. The parameters of the filter bank are: $n_\theta = 10$, $n_\lambda = 10$, $p_\theta = 0.05$, $p_\lambda = 0.05$. Note that the filter bank shown in this figure was not the filter bank that was used to extract the data that will be presented in Section 3.3.

where $R(u, v)$ is the interpolated (continuous) response surface at a particular pixel (x_0, y_0), o is the linear index of filters in the filter bank, G_o is the filter frequency response of the oth filter as it is given by Eq. (4), R_o is the discrete response magnitude at a particular pixel (x_0, y_0) of the oth filter and (u_{max}, v_{max}) is the frequency pair which maximizes $R(u, v)$. I refers to the gray scale image itself, $\otimes$ is the symbol of convolution, $Re()$ means the real part of its arguments and $Im()$ means the imaginary part of its argument. The ideal maximum filter response $R_{ideal}(u, v)$ refers to the theoretical maximum response at a location in the continuous interpolated response surface. This value is calculated by convolving an artificial image template containing a sinusoidal pattern oriented and spaced appropriately to a specific filter with maximum contrast and intensity (thus effectively a two-dimensional square-wave signal). This normalization scales the modulation strength between 0 and 1 and therefore makes it a good descriptor for comparing different images taken under similar imaging conditions. Note that it is possible to scale the modulation strength by the maximum modulation strength found in the particular image, making it an intensity-invariant structural parameter and allowing for the comparison of images taken under different imaging conditions. To find the global maximum, a local direct search algorithm has been applied [23]. Global optimization algorithms are usually computationally intensive and difficult to implement, but the global maximum can be reliably found by local maximum search algorithms if the initial guess for the maximum is very close to the global maximum. Assuming a smooth and unimodal response surface, the center frequency of the filter that yielded the highest discrete response is a very good initial guess in this problem. The direct search algorithm has been implemented by using Matlab's *fminsearch* function. Figure 3 demonstrates the maximum search step in the continuous response surface.

Thus the complete algorithm can be summarized as follows:

1. Load the image.
2. Specify the wavelength band of interest either manually or automatically based on the power spectrum.
3. Calculate filter parameters by using Eqs. (5)–(9) and construct the filter bank.
4. Filter the image with each filter in the filter bank and record the discrete responses at each pixel.
5. At each pixel, calculate the frequencies that maximize the continuous interpolated response surface using optimization and store these frequencies using Eqs. (10)–(12).
6. Calculate structural parameters θ, λ and μ at each pixel using Eqs. (13)–(15) and store.

While filtering can be realized by numerical convolution using computationally inexpensive Fast Fourier Transforms (FFTs), the whole algorithm represents a huge computational load due to steps 5 and 6. To overcome this problem and keep the computation times under reasonable limits, steps 5 and 6 have been implemented as parallel algorithms. Under a Matlab environment using a modern quad-core computer computations take 10–60 min, depending on the image and selected filter bank. Processing the typical HRTEM image shown in Fig. 2 took 17 min. If in a specific application computation time is an issue, the algorithm can be further optimized by only using discrete filter responses in the close neighborhood of the filter with the maximum discrete response to compute $R(u, v)$ in the frequency domain, manually specifying regions of interests (ROIs) or outsourcing parts of the computation to graphical processing units (GPUs) that are commonly found in modern personal computers. Figure 4 demonstrates typical extracted fields of the three derived structural parameters.

2.3. Soot sampling

Graphite materials (Union Carbide) from three different fuels (anthracene, bifluorenyl and p-terphenyl) were previously synthesized by high temperature (3000 °C) pyrolysis. The sample preparation procedure has been reported earlier [1]. In brief, the samples were ground in an agate mortar and pestle and then ultrasonically dispersed in ethanol. The suspension was deposited dropwise onto a copper TEM grid coated with a lacey carbon film. HRTEM micrographs of the carbon particles were obtained using a transmission electron microscope operated at 200 keV. Amorphous soot samples were taken using thermophoretic sampling methods previously described in [3]. In brief, benzene was burned in air under fuel rich conditions in a premixed flat flame burner that was initially developed for studying aliphatic and aromatic flames. This system consisted of a stainless steel chamber where fuel and air were properly mixed prior to entering the burner. The flame was stabilized over a tube bundle and was shielded from atmospheric interference using a nitrogen shroud. A metallic mesh placed 3.5 cm above the burner surface stabilized and distributed the flame uniformly across the burner. Samples for HRTEM analysis were taken at different heights above the burner surface (HAB) using a thermophoretic probe commonly referred to as a frog tongue. A TEM grid holder was attached to a piston and compressed air at 60 psig was used to quickly insert and remove the TEM grid from the flame. Multiple insertions were necessary to get a representative soot sample on the grid. The grid was oriented with the face parallel to the gas flow, so that the disturbance of the flame was minimal. Soot deposits on the grid due to the thermophoretic gradient between the cold grid and the hot flame, which also allows freezing of some heterogeneous reactions, as well as avoiding changes in the soot morphology after the particles have impacted upon the cold surface.

3. Results and discussion

To demonstrate the capabilities of the proposed algorithm, tests with both artificial and real images have been carried out. Testing with artificial images is important, since it can achieve what testing with real data cannot: verification of the method by comparison with accurately known ground truth. To demonstrate that the proposed method is capable of reproducing already published results – with higher resolution and accuracy – results from a paper presenting standard structural analysis of different graphites [1] have been compared to results obtained by the method presented here. In addition to demonstrate the methods capability of analyzing and differentiating poorly ordered soot structures, results for images of immature soot obtained by standard image analysis methods and the method proposed here are compared [5].

3.1. Artificial images

Since the method proposed here is practically a signal analysis routine with a number of features specifically designed for soot HRTEM image analysis, artificial images can be constructed to validate the algorithm and quantify its accuracy. Images showing a sinusoidal pattern with varying orientation and wavelength have been generated by taking the sine of an underlying polynomial phase surface. The theoretical wavelength can be calculated as the inverse of the phase gradient magnitude, while the theoretical orientation can be calculated as the orientation angle of the gradient. After generating the images, they have been artificially corrupted by zero-mean Gaussian noise. The standard deviation of the noise has been increased in steps in order to evaluate the algo-

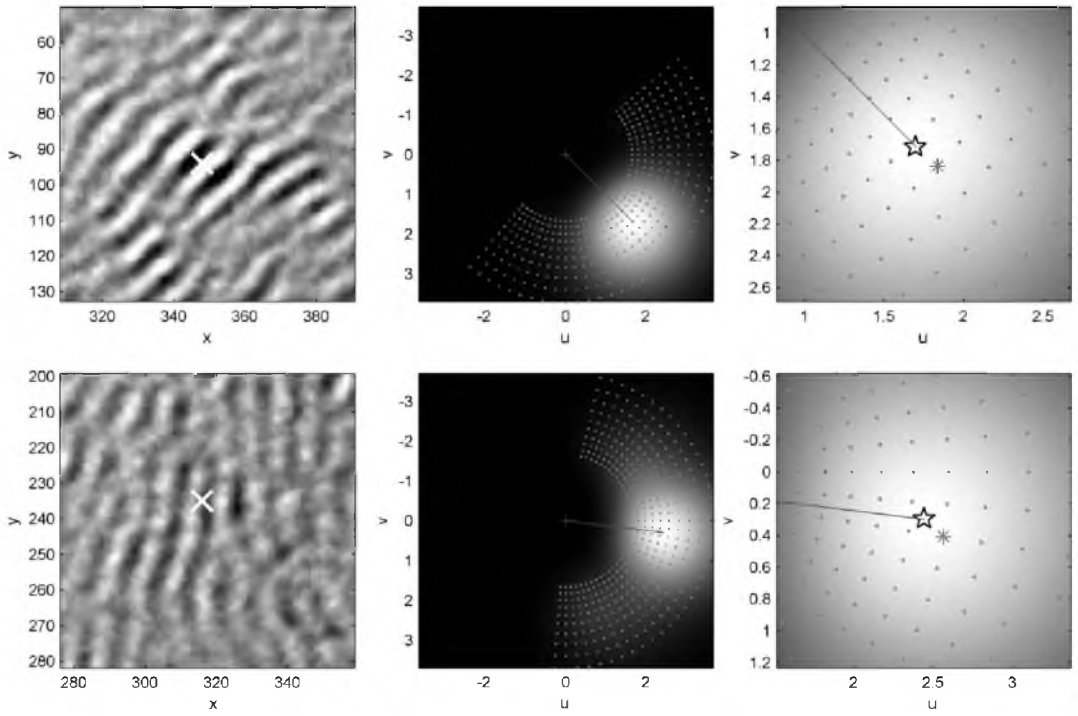

Fig. 3. Two different locations in the real HRTEM soot image shown in full size in Fig. 2 are shown in the first column. White X symbols indicate the analyzed pixel. The second column shows the reconstructed continuous response surfaces for both pixels. Gray dots indicate the center frequencies of the filters. The grayscale values show the values of the response surfaces. The third column shows the results of the maximum search algorithm. These plots show the vicinities of the maximum to improve visibility. The initial guesses for the maximum locations are indicated by the $*$ symbol. The refined maximum found is shown by the $\star$ symbol. Notice that the angular coordinate of the maximum corresponds to a direction normal to the local orientation (see Eq. (13)) and the radial coordinate corresponds to the reciprocal local wavelength (see Eq. (14)).

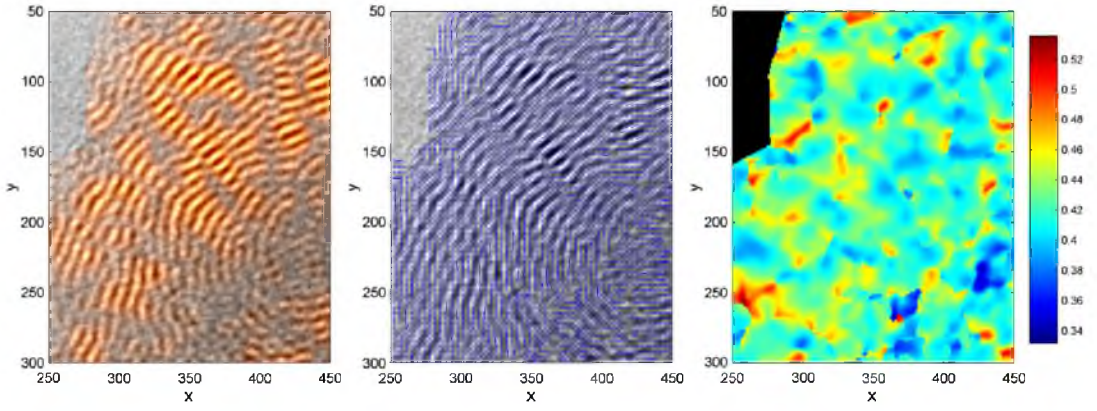

Fig. 4. Extracted modulation strength (μ), orientation (θ) and wavelength (λ) maps from a detail of the real soot HRTEM image shown in Fig. 2, from left to right, respectively. In the first image, hues of orange indicate the value of the modulation strength parameter – the more orange a pixel is, the highest its μ parameter. Notice how the map of μ highlights the best defined and most anisotropic regions. These regions correspond to well-imaged crystalline regions developing short-range order. In the second image, the orientation angles of each pixel are plotted as blue line segments. The orientation of these lines indicate θ. Note that θ is only accurate and meaningful in unimodally oriented areas – these are the areas with high μ values. Other areas return a θ value corresponding to the spectrally strongest orientation angle. The third image shows a color coded plot of λ. The values indicate the distances of fringes at each pixel in the direction that gave the highest response value. If there is only one well defined direction, the value of λ is the generalized interlayer spacing in nanometers at the particular pixel. The visual interpretation of the map of λ of a real soot image is not easy. A more easily understandable representation will be presented in Fig. 5, Section 3.1.

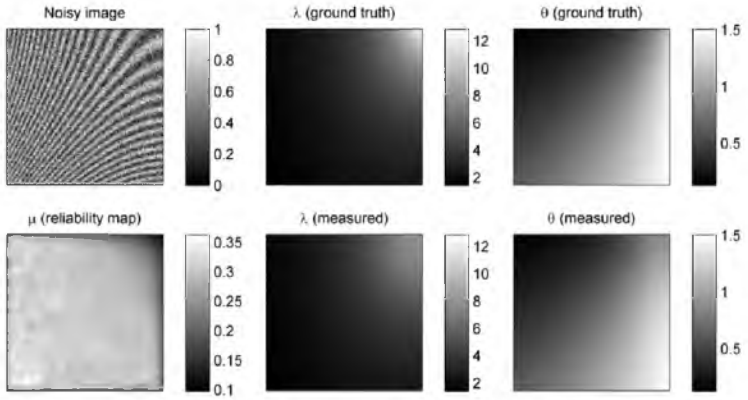

Fig. 5. Top left: an artificial image constructed based on an underlying polynomial phase surface. The image has been corrupted by zero-mean Gaussian noise. The noise level of this particular image is −2.5 decibels. Top middle: ground truth local wavelength map (λ) of the artificial image computed as the gradient magnitude of the noise-free underlying phase. Top right: ground truth local orientation angle map (θ) of the artificial image. Bottom left: extracted modulation strength map (μ). Higher values mean more reliable locations in the image in terms of wavelength and orientation measurement. Bottom middle: measured local wavelength map. Bottom right: measured local orientation angle map. Note that the upper right corner is inaccurate in both the measured λ and θ maps, but the values of μ corresponding to this region are also low, indicating less reliable estimation.

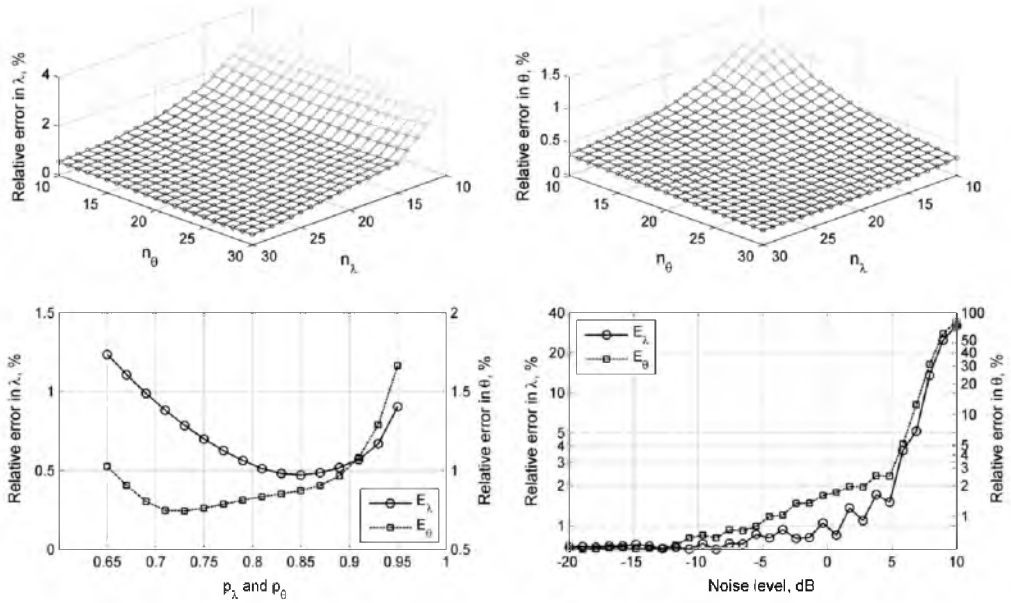

Fig. 6. Results of error quantification tests. Top left: the relative mean error in λ as a function of n_θ and n_λ. Denser sampling in the frequency domain yields lower errors, although it is worth noting that the accuracy of estimations of λ has been found insensitive to n_θ in the tested parameter range. Top right: the relative mean error in θ as a function of n_θ and n_λ. Unlike λ, estimations of θ have been found to be sensitive to both n_θ and n_λ in the tested parameter range. Bottom left: the effect of p_θ and p_λ on the relative mean error in θ and λ. It has been found that there are ideal values for these parameters with which the error is minimal. Overall, the effect of the two p parameters has not effected error values significantly. Bottom right: the effect of noise levels on the accuracy of estimations. The mean error in λ stayed under 1%, while the mean error in θ stayed under 2% for typical noise levels. In the high noise region, noise effected errors the most among the evaluated conditions. Note that in the range of typical noise levels the algorithm is practically immune to noise, as the errors introduced by noise are negligible. Excessive noise levels resulted in inaccurate estimations. It is not advised to use the proposed algorithm for images with noise levels above 5 decibels.

rithm's capability to handle image noise. Noise levels are given in decibels calculated by the following relationship:

$$L_N = 10 \log \left[\frac{\sigma_N}{\max(I)} \right] \tag{16}$$

where L_N is the noise level in decibels, σ_N is the standard deviation of the Gaussian noise and $\max(I)$ is the maximum signal strength (the highest pixel value in the image). A logarithmic noise range between −20 and +10 decibels has been evaluated. Soot HRTEM

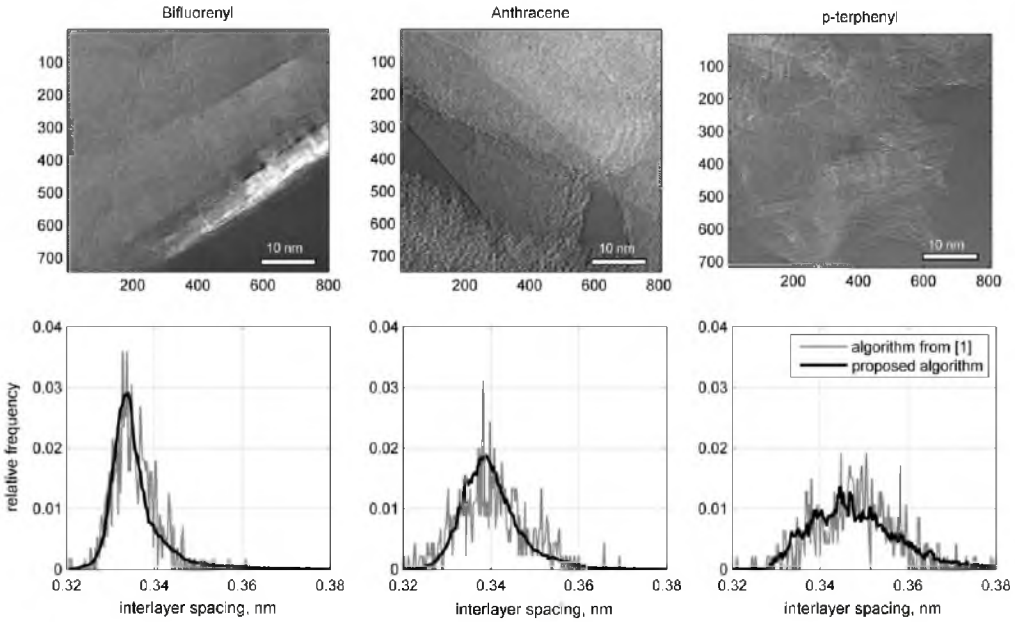

Fig. 7. Results of graphite structure analysis. Top left: HRTEM image of graphite originating from burning bifluorenyl. Top middle: HRTEM image of graphite originating from burning anthracene. Top right: HRTEM image of graphite originating from burning p-terphenyl. Bottom left: interlayer spacing PDF of bifluorenyl graphite. Bottom middle: interlayer spacing PDF of anthracene graphite. Bottom right: interlayer spacing PDF of p-terphenyl graphite. In the PDF graphs the results from Ref. [1] are compared with the results obtained by our proposed algorithm.

images obtained by modern microscopes have noise levels typically between −15 and −5 decibels. Figure 5 shows a generated artificial image along with its wavelength and orientation fields and the results of analysis carried out by the algorithm proposed here.

A series of tests have been conducted to map out the errors and sensitivities of the method. Since the wavelength ranges are approximated based on a priori physical knowledge and the filter scales are dependent on filter spacing, the proposed algorithm has only four independent parameters: n_θ, n_λ, p_θ and p_λ (see Section 2.1). It will be shown that within a reasonably wide range, the results are accurate and insensitive to variations in these parameters. The most important parameters are the number of filters in both the λ and θ direction, as these determine the accuracy of the estimation of the continuous response surface by discrete filter responses (see Section 2.1) at a particular pixel. A set of tests have been carried out by keeping p_θ and p_λ constant (0.9) and trying all combinations of n_θ and n_λ values between 10 and 30. The effect of changing p_θ and p_λ has also been evaluated by keeping n_θ and n_λ constant (both 20) and varying both p_θ and p_λ between 0.65 and 0.97 in steps of 0.02. Since the two p values effect the shape (aspect ratio) of each filter simultaneously, there is no real need to evaluate their different combinations. A noise level of −2.5 decibel has been used to test the algorithms sensitivity to input parameters. To evaluate the algorithms sensitivity to noise, a series of images have been generated by using the same underlying pattern but with increasing noise levels. These images have been processed and analyzed by the following filter bank parameters: $n_\theta = 20$, $n_\lambda = 20$, $p_\theta = 0.9$, $p_\lambda = 0.9$. The algorithm has been evaluated based on error norms. Each resulting θ and λ map has been compared to the theoretical maps and their relative errors have been computed. A single scalar error measure has been computed for each test for both θ and λ by taking the mean of the error matrices. Figure 6 shows the results of these tests.

To summarize the results of validation tests it can be stated that under typical image conditions, the mean error in both θ and λ is under 1%. If the frequency domain is sufficiently densely sampled by filters the results are insensitive to the particular choices in n_θ and n_λ. Our results agree well with the reportings of Perona [22]; namely, it is advised to use at least 15 filters for both θ and λ. It is also worth mentioning that for most soot images, p_θ and p_λ should be set so that the filter bank parameters result in circular filters; i.e., the aspect ratio σ_x/σ_y should be approximately 1 for each filter, as this will result in the lowest error.

3.2. Analysis of graphite

The results presented in this section are reproductions of the results of Palotas et al. published in 1998 [1]. The original study focused on interlayer measurements in HRTEM images of graphites from different sources. The results of interlayer spacing measurements for graphites from bifluorenyl, anthracene and p-terphenyl (among others) were presented and the methodology for generating these graphites can be found in Section 2.3 or in more detail in the original publication. The original image processing algorithm used in [1] is a standard routine based on frequency filtering, global binarization and fringe detection. The interlayer distances were measured as the distances between parallel fringe pairs, with orientations being made equal to the mean of the two orientation values of the fringe pair. Details of this method can be found in [5].

The interlayer spacing values in three graphite HRTEM images have been measured by the algorithm proposed in this paper. Since graphitic structures contain long, parallel carbon layers, measuring

Table 1
Statistics of the measurements of graphite interlayer spacing compared to the statistics of Palotas et al. [1]. Notice the significantly richer datasets obtained by the proposed method.

Sample	# Of data	Mean (nm)	Stddev (nm)	Mode (nm)	Comp. time
Results from Ref. [1]					
Bifluorenyl	557	0.3355	0.0049	0.3322	3 s
Anthracene	451	0.3404	0.0079	0.3316	3 s
p-Terphenyl	468	0.3481	0.0093	0.3479	3 s
Proposed algorithm					
Bifluorenyl	170,274	0.3357	0.0063	0.3316	5 min
Anthracene	74,978	0.3401	0.0066	0.334	5 min
p-Terphenyl	15,320	0.3482	0.0101	0.3443	5 min

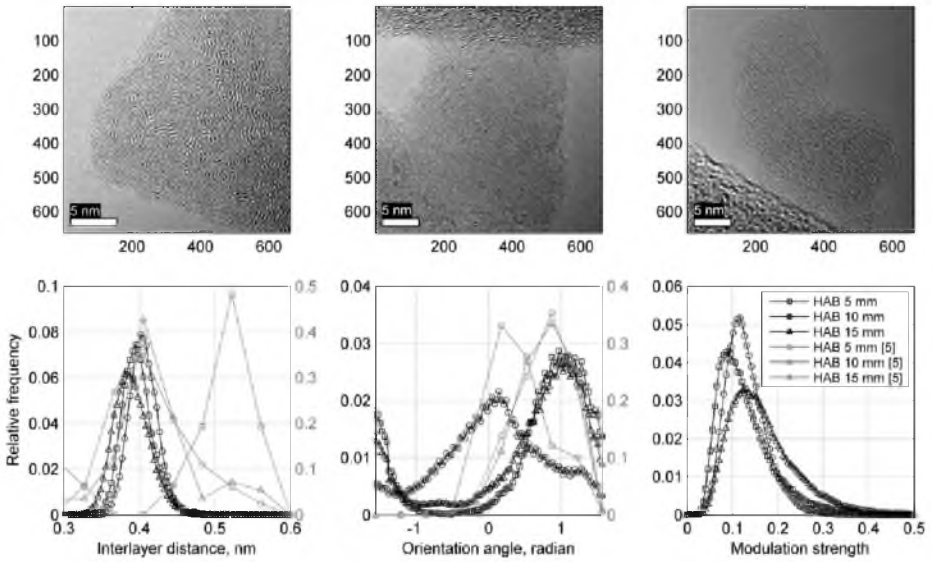

Fig. 8. Top row: HRTEM images of benzene soot sampled at different HABs (5 mm, 10 mm and 15 mm from left to right, respectively). Bottom left: interlayer spacing PDFs obtained by the proposed method and a standard method [5]. Bottom middle: orientation angle PDFs obtained by the proposed method and a standard method [5]. Bottom right: modulation strength PDFs obtained by the proposed method. Notice the high-fidelity, high-resolution interlayer PDFs in the case of the proposed method. The rich datasets allowed for setting the bins by steps of 0.0035 nm in the case of interlayer distances and $pi/100$ radians in the case of orientation angles. For the standard algorithm, ten evenly spaced bins have been defined in the shown ranges.

the orientation maps was not of practical importance. This section aims to demonstrate that the generalized interlayer spacing values (λ) obtained by the method presented in this paper yield practically the same distribution as the interlayer spacing values obtained by the standard basic structural unit analysis algorithm. The following filter bank parameters have been used to obtain the data: $n_\lambda = 15$, $n_\theta = 30$, $p_\lambda = 0.99$, $p_\theta = 0.9$. The values of the obtained maps of μ spanned a range of 0–0.2. Pixels with μ values above 0.06 have been used as reliable pixels for the measurement of λ. Figure 7 shows the analyzed graphite images along with the measured distributions of λ compared to the interlayer distributions first presented in [1].

The information obtained by using the method proposed here implies almost exactly the same physical structures as the information obtained by previous authors. The only difference is in the accuracy and robustness of estimation. Table 1 shows the extracted statistics of the measurements. Our method produced three orders of magnitude richer datasets on average compared to the results of Palotas et al. [1].

Notice that the number of reliable data points was lower for p-terphenyl graphite than for the other two. It is easy to understand why by looking at the image of p-terphenyl graphite – there were less non-overlapping regions with good contrast. Table 1 demonstrates very good agreement between the extracted mean and

Table 2
The statistical evaluation of interlayer distance data obtained from the benzene images. This table compares the results of the proposed method with a standard algorithm described in [5]. Notice the lower standard deviations obtained by our method and the trend in the modes of the interlayer distances. There is no apparent trend in the results obtained by the standard method. On average, the datasets obtained by the proposed methods contained three orders of magnitude more information at a cost in computation time, which was approximately a 100 times longer for the proposed algorithm.

HAB	# Of data	Mean (nm)	Stddev (nm)	Mode (nm)	Comp. time
Algorithm from Ref. [5]					
5 mm	31	0.5273	0.0531	0.5222	12 s
10 mm	56	0.4427	0.0598	0.4056	13 s
15 mm	104	0.4377	0.0751	0.4056	13 s
Proposed algorithm					
5 mm	78,259	0.4071	0.0184	0.402	14 min
10 mm	66,739	0.4001	0.0209	0.3949	15 min
15 mm	168,504	0.4103	0.0243	0.3843	17 min

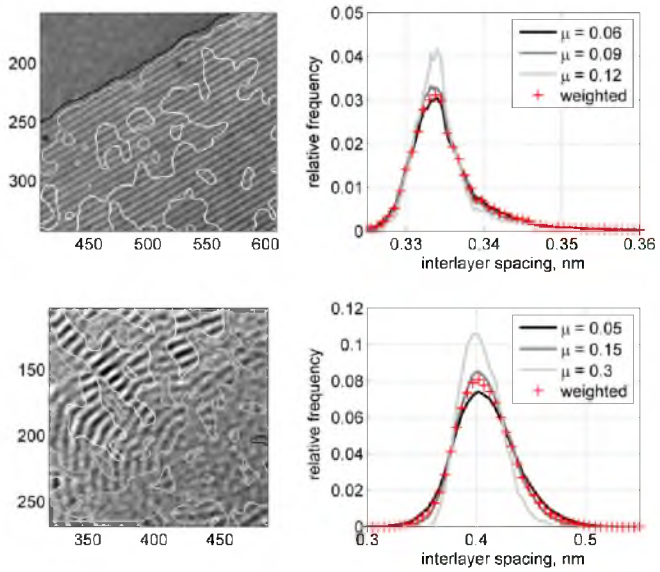

Fig. 9. The effect of different methods for incorporating μ in the obtained interlayer spacing distributions. In the left column, micrographs of the bifluorenyl graphite (top) and benzene soot (bottom) are shown with isocontours of μ overlain. The three shades of gray of the contours correspond to the thresholds shown in the legends of the right column. In the right column, resulting interlayer spacing distributions are shown for the bifluorenyl graphite sample (top) and benzene soot (bottom). Three distributions are shown obtained by thresholding μ by using the threshold values shown in the legends and a fourth one (denoted by red crosses) obtained by weighing λ with μ. (For interpretation of the references to color in this figure legend, the reader is referred to the web version of this article.)

mode values of the interlayer spacing distributions. The slight differences in the obtained standard deviation values can be explained by the inherent volatile nature of variance statistics; in other words, the number of data points extracted by the conventional technique was insufficient for the accurate estimation of the standard deviation of the distributions. Supposedly, introducing additional samples to the conventional measurement would converge the standard deviation estimates toward those obtained by the proposed method.

3.3. Analysis of amorphous soot

To demonstrate the proposed methods applicability to the analysis of highly amorphous soot samples, HRTEM images of benzene soot sampled at different HABs have been processed. Typically, the compaction of the layered structure is expected during the maturation or oxidation of black carbon or soot particles [12,24], resulting in slight shifts in the interlayer spacing distributions towards lower values. Benzene soot images have been processed with the following filter bank parameters: $n_\lambda = 15$, $n_\theta = 30$, $p_\lambda = 0.97$, $p_\theta = 0.97$. The modulation strength values ranged from 0 to 0.6 – a reliability threshold of 0.15 has been selected. Figure 8 shows the results of the measurements.

It is clear from Fig. 8 that the proposed method was able to identify a slight shift in interlayer distances towards shorter distances. This shift corresponds to the maturation and compaction of soot nanostructure. Interestingly, the standard deviation of the interlayer spacing data also increased as HAB/residence time increased. The standard method failed to identify any trends. It is worth noting that in the case of completely amorphous structure, the standard method produced significantly overestimated interlayer distances, which was caused by the lack of truly parallel fringes. As the number of data points extracted by the standard method increased, its results started to get closer to the results obtained by the new method. Orientation angle PDFs obtained by the standard method showed rough consistency with the results of the proposed method. While PDFs of λ and θ can provide physical information on the structure, the PDFs of μ can be used as fingerprinting tools. The PDFs of μ are indicative of the overall crystalline order in the structure – for similar images, the more they are skewed towards higher values, the higher the structural order is. PDFs of μ show a trend of increasing orderliness in benzene soots as HAB increases, as would be expected (notice the increasing fraction of pixels above the threshold μ value – the locations of the peaks are irrelevant, since low μ values represent image background and unreliable image regions; their corresponding pixels are excluded from further calculations). The statistical summary of the results is shown in Table 2.

3.4. Choosing the threshold of μ

Strictly speaking, the modulation strength parameter μ is a descriptor without exact physical meaning. μ is basically a normalized convolution product of an image detail representing a carbon sub-structure with a best-fit filter kernel modeling a structural primitive. In other words, μ is a scalar that represents the similarity between the local structure and the image of an idealized building block of carbon layers. μ therefore carries no absolute quantitative information,[3] but is instead used to classify image regions based on their overall quality. It is easy to understand that actual values of μ depend not only on the local contrast, but on the local morphology of the carbon layers as well. In this section a number of simple strategies are proposed on how to use μ in order to only include high-fidelity information in the obtained interlayer spacing and orientation distributions.

[3] μ can be arbitrarily scaled - only its distribution is important.

The two simplest ways to incorporate μ as a reliability measure are thresholding (used in Sections 3.2 and 3.3) and weighing. As discussed above, thresholding is a procedure that defines a critical value of μ, under which pixels are considered as unreliable and are excluded from further calculations. The threshold values presented in Sections 3.2 and 3.3 were set manually, by overlaying the scalar fields of μ on the micrographs and choosing thresholds that defined and enclosed visually appealing regions. Interestingly, the manually chosen thresholds roughly corresponded to 30% of the highest modulation strength values observed in the analyzed micrographs, although it is expected that this rule of thumb does not generalize very well.

Another method of determining a feasible threshold value is to use a priori information regarding the interlayer statistics and optimize the threshold of μ, such that the obtained interlayer spacing distributions best approximate the expected outcome. This route is only recommended when the a priori information can be regarded as highly accurate; e.g., in the case of graphite. Obviously, a single value should be chosen for a complete set of images, so that the results are comparable.

Instead of setting strict rules on the threshold of μ, the modulation strength can be used as a soft measure of reliability as well. In a Bayesian sense, each interlayer spacing data point (observation) can be given a reliability factor or weight – the value of μ at the same location. Instead of filtering out a number of less reliable pixels and building a distribution of the remaining, one can build weighted distributions, to which less reliable pixels contribute less than more reliable ones. Figure 9 illustrates the strategies discussed in this section.

Since graphite generally has elongated and straight carbon layers, it is understandable that distributions of μ extracted from micrographs of graphite are mostly bimodal – one peak represents the background, where μ is practically zero and the other the structure, where μ is closely maximum. Therefore, in the case of graphite samples it is not surprising that choosing any value of μ as a threshold that is above the value representing the background suffices. In the case of benzene soot, changing the threshold has a greater effect (although not significantly, provided that at least the background is excluded by thresholding), however there are no exact methods of determining the threshold value. Since many factors have an effect on the actual values of μ, using the visual (manual) approach discussed above is recommended. Naturally, for similar structures, the same threshold should be used to facilitate semi-quantitative comparison. Notably, in most practical situations, the modes and means of the interlayer spacing distributions are insensitive to the threshold of μ, provided that the threshold is within a 'reasonable' range – the only effected parameters are usually the variances. If one aims to avoid subjective thresholding completely, using weighted distributions is recommended. In all the cases studied in this paper, the weighted distributions were very close to the ones utilizing manually set thresholds.

4. Conclusion

A novel image processing framework for the analysis of amorphous soot HRTEM images has been designed, developed, tested and evaluated in this paper. The proposed method is completely different from all previously published approaches and is capable of extracting approximately 1000 times more structural information from the same amount of micrographs than standard methods. The method has been purposely developed to be able to extract the most accurate and reliable structural information from soot HRTEM images. To achieve this objective, the method has been designed to be practically immune to image noise, phase inversion phenomena and to yield the lowest localization uncertainty that is theoretically possible. Unlike standard methods, the proposed algorithm provides structural information at native image resolution; i.e., every image pixel yields a set of structural parameters. The method has been tested on artificially created images, real micrographs of graphite and real micrographs of amorphous soot. It has been found that the method provides information consistent with results obtainable by standard algorithms for graphitic structures; however, it is still able to provide high-fidelity data in cases where most standard techniques fail – specifically in the case of amorphous soot samples. As a demonstration of the technique's capabilities, we have applied the methodology to laboratory collected benzene soot. Our analysis revealed an increase in the degree of order (compactness) in soot structure with oxidation (maturation). The finding is consistent with literature data, however the supporting data is orders of magnitude more robust.

Acknowledgments

This work was partially sponsored by the TAMOP-4.2.1.B-10/2/KONV-2010-0001 Project with support by the European Union, co-financed by the European Social Fund. The authors would like to thank Carlos Andres Echavarria at the University of Utah for providing some HRTEM images.

References

[1] A.B. Palotas, L.C. Rainey, A.F. Sarofim, J.B.V. Sande, R.C. Flagan, Chemtech 28 (1998) 24–30.
[2] L.C. Rainey, A.B. Palotas, A.F. Sarofim, J.B.V. Sande, Applied Occupational and Environmental Hygiene 11 (1996) 777–781.
[3] C.A. Echavarria, Evolution of Soot Size Distribution During Soot Formation and Soot Oxidation-Fragmentation in Premixed Flames: Experimental and Modeling Study, Ph.D. Thesis, University of Utah, 2010.
[4] M.J. Hytch, T. Plamann, Ultramicroscopy 87 (2001) 199–212.
[5] A.B. Palotas, L.C. Rainey, C.J. Feldermann, A.F. Sarofim, J.B.V. Sande, Microscopy Research and Technique 33 (1996) 266–278.
[6] J. Yang, S. Cheng, X. Wang, Z. Zhang, X. Liu, G. Tang, Transaction of Nonferrous Metals Society of China 16 (2006) 796–803.
[7] A. Sharma, T. Kyotani, A. Tomita, Fuel 78 (1999) 1203–1212.
[8] H.S. Shim, R.H. Hurt, N.Y.C. Yang, Carbon 38 (2000) 29–45.
[9] J.N. Rouzaud, C. Clinard, Fuel Processing Technology 77–78 (2002) 229–235.
[10] K. Yehliu, R.L.V. der Wal, A.L. Boehman, Combustion and Flame 158 (2011) 1837–1851.
[11] K. Yehliu, R.L.V. der Wal, A.L. Boehman, Carbon 49 (2011) 4256–4268.
[12] C.R. Shaddix, A.B. Palotas, C.M. Megaridis, M.Y. Choi, N.Y.C. Yang, International Journal of Heat and Mass Transfer 48 (2005) 3604–3614.
[13] P. Toth, A.B. Palotas, J. Lighty, C.A. Echavarria, Fuel 99 (2012) 1–8.
[14] M.J. Hytch, Scanning Microscopy 11 (1997) 53–66.
[15] M.J. Hytch, E. Snoeck, R. Kilaas, Ultramicroscopy 74 (1998) 131–146.
[16] M.I. Elbakary, M.K. Sundareshan, Pattern Recognition Letters 26 (2005) 2154–2173.
[17] M.I. Elbakary, M.K. Sundareshan, Image and Vision Computing 25 (2007) 663–670.
[18] N. Bonnet, Micron 35 (2004) 635–653.
[19] D. Gabor, Journal of the Institution of Electrical Engineers III: Radio and Communication Engineering 93 (1946) 429–441.
[20] G.H. Granlund, H. Knutsson, Signal Processing for Computer Vision, first ed., Kluwer Academic Publishers, Dordrecht, Netherlands, 1994.
[21] J. Ilonen, J.K. Kamarainen, H. Kalviainen, Efficient Computation of Gabor Features, Technical Report, Lappeenranta University of Technology, Finland, 2005.
[22] P. Perona, in: IEEE Computer Society Conference on Computer Vision and Pattern Recognition, IEEE Computer Society 1991, pp. 222–227.
[23] J.C. Lagarias, J.A. Reeds, M.H. Wright, P.E. Wright, SIAM Journal of Optimization 9 (1998) 112–147.
[24] X. Zhang, A. Dukhan, I. Kantorovich, E. Bar-Ziv, A.F. Sarofim, in: Twenty-sixth Symposium (International) on Combustion, The Combustion Institute, 1996 pp. 3111–3118.

CHAPTER 4

A NOVEL FRAMEWORK FOR THE QUANTITATIVE ANALYSIS OF HIGH RESOLUTION TRANSMISSION ELECTRON MICROGRAPHS OF SOOT II. ROBUST MULTISCALE NANOSTRUCTURE QUANTIFICATION

Reprinted from Combustion and Flame, Vol. 160, Pal Toth, Arpad B. Palotas, Eric G. Eddings, Ross T. Whitaker, JoAnn S. Lighty, A novel framework for the quantitative analysis of high resolution transmission electron micrographs of soot II. Robust multiscale nanostructure quantification, Pages 920-932, Copyright 2013, with permission from Elsevier.

Combustion and Flame 160 (2013) 920–932

Contents lists available at SciVerse ScienceDirect

Combustion and Flame

journal homepage: www.elsevier.com/locate/combustflame

A novel framework for the quantitative analysis of high resolution transmission electron micrographs of soot II. Robust multiscale nanostructure quantification

Pal Toth [a,*], Arpad B. Palotas [b], Eric G. Eddings [a], Ross T. Whitaker [c], Joann S. Lighty [a]

[a] Department of Chemical Engineering, University of Utah, 50 S. Central Campus Drive, Salt Lake City, UT 84112-9203, United States
[b] Department of Combustion Technology and Thermal Energy, University of Miskolc, H3515 Miskolc-Egyetemvaros, Hungary
[c] School of Computing, University of Utah, 3893 Warnock Engineering Building, Salt Lake City, UT 841112-9205, United States

ARTICLE INFO

Article history:
Available online 12 February 2013

Keywords:
Soot
Nanostructure
HRTEM

ABSTRACT

The quantitative characterization of mostly amorphous soot structures is a difficult problem. High resolution electron microscopy is a tool capable of providing structural information related to the crystalline order in soot; however, well-defined and exhaustive structural parameters are needed for quantification. The typical observable field of view and the insufficient amount of structural information extractable from a single electron micrograph pose another problem in obtaining reliable statistical description. This paper has two objectives: first, to show that the already developed and published structural descriptors can be united by introducing a general model for the characterization of molecular order and second, to extend the general filtering approach presented in Part 1 of this study to allow for the efficient extraction of such general parameters. The computational background is described with automatic, real-time future applications in mind.

Published by Elsevier Inc. on behalf of The Combustion Institute.

1. Introduction

Graphite, an allotrope of carbon has a hexagonal lattice structure with an atom spacing of 0.142 nm and interlayer spacing of 0.335 nm. The layers of the hexagonal carbon structure are referred to as graphene layers. These graphene layers can be imaged and quantified by using high resolution transmission electron microscopy (HRTEM). In a HRTEM micrograph, graphene layers appear as dark or bright linear patterns, also called fringes.

Soot is a product of the pyrolysis of carbonaceous materials and is generally considered as amorphous carbon [1]. Despite being amorphous, in most cases soot nanostructures show some degree of crystalline order typically in the form of graphite microcrystals (mesophasic crystalline units or clusters exhibiting short-range order in the form of parallel graphene layers, also called stacks), partial fullerenic (graphene layers in a concentrically symmetric, onion-like structure) or partial graphitic (longer range parallelity of layers) order [2–4]. Soot nanostructure is effected by combustion conditions, the thermal environment [3] and also by the combusted fuel type [5–7]. Further, in this paper we use the term 'nanostructure' to refer to the degree of crystalline order in soot. Soot nanostructure quantification has been an area of interest since the early nineties [8]. Being able to quantitatively describe soot nanostructure is important from two perspectives.

First, it has been hypothesized that soot nanostructure has an effect on soot reactivity. Correlations are available showing the interdependence of oxidation kinetics and nanostructure [2,3,6–11]. It is understood that the reactivity of edge site carbon atoms (at the edges of graphene layers) is higher than that of carbon atoms in the basal plane (surrounded by other carbon atoms in the graphene layer) [6,12]. Since the transformation of combustion-derived carbon has been found to ultimately lead towards graphitic structure as maturation proceeds (e.g., in the case of biodiesel soot [13] or in large-scale pool fires [14]), the appearance and growth of graphitic clusters can eventually cause passivation. The ordering of the initially amorphous structure also results in the compaction of the carbon structure [15] and decreasing macroscopical surface area for surface reactions. These processes may have an effect of the reactivity of soot formed in high-temperature flames as well. Similar studies are available on coal and coal char nanostructure [16,17] and carbon blacks [18].

Second, since soot nanostructure is affected by the fuel source [5–7], quantitative descriptors may be used as forensic tools [19–21]. Nanostructural parameters from HRTEM micrographs have also been combined with chemical composition information to obtain a dataset more suitable for source identification [21].

Along with X-ray diffractometry (XRD), digital processing and analysis of digitized HRTEM micrographs is a technique capable

* Corresponding author.
E-mail address: toth.pal@uni-miskolc.hu (P. Toth).

0010-2180/$ - see front matter Published by Elsevier Inc. on behalf of The Combustion Institute.
http://dx.doi.org/10.1016/j.combustflame.2013.01.003

of providing quantitative soot nanostructure information. Since XRD structural parameters are derived based on assumed crystal models and are averaging in nature (references to published XRD analysis techniques are given in [22]), and due to the fact that HRTEM allows for the direct observation of the atomic structure, it is suggested that HRTEM image analysis can provide more accurate, more diverse and localized structural data. The drawback of HRTEM analysis is the projected nature of the micrographs, i.e., only two-dimensional information can be extracted. It was first shown by Saltykov [23], that intensive geometric properties measured in projections or two-dimensional segments converge to their three-dimensional analogies, provided that a sufficient amount of samples are gathered. This is the reason behind the consistency between structural information extracted from HRTEM images and those obtained by XRD [22,24]. Sampling and the quantity of available micrographs are also important factors due to the heterogeneity of soot particles, caused by the stochastic nature of soot formation and transformation processes.

The interlayer distance discussed in detail in Part I of this study in itself is a descriptor of crystalline order. It is generally understood that the forming thermal environment, soot maturation and oxidation have an effect on the distribution of interlayer spacing values. Typically, as maturation (either chemical or thermal) proceeds, the distribution gets narrower and the mean value converges to the interlayer spacing of a perfect graphite crystal [14,25]; thus, the standard deviation of interlayer spacing values [26] and the deviation from the interlayer distance of graphite [4] can be good candidates to describe graphitic order. However, there is much more information in HRTEM images than interlayer spacing values alone. The relative distribution of graphene layer orientations is a rich source of structural data when analyzing graphitic order in soot; however, its quantification is not obvious, since the process requires the application of second- or higher-order statistics. The evaluation of graphitic order based on HRTEM fringe orientations of soot loosely resembles the lattice orientation distribution technique applied in mineral or metallurgical crystallography [27].

Many authors have provided many different ways to quantify graphitic order in soot based on fringe orientation measurements. Sharma and co-workers developed an algorithm based on fringe grouping by a system of criteria on relative fringe orientations [16]. Their method finds parallel and neighboring fringes and groups them into stacks. Since maturation happens heterogeneously, starting from multiple locations, the relative amount of stacks is an indicator of graphitic order (complete coverage of a single stack means perfect graphitic structure). This parameter is sometimes referred to as 'apparent crystallinity'. Yang et al. adopted this method and integrated it into their crystallinity index technique [4]. Since the apparent crystallinity describes the size of stacked graphene layers, the distribution of a similar parameter, the fringe length, provides an analogous descriptor of graphitic order as used by Yehliu and co-workers [28]. They also suggest another structural parameter, the tortuosity (or curviness) distribution of fringes. Since a perfect graphite crystal only contains perfectly linear fringes, its tortuosity distribution shows a single peak at unity tortuosity. Note that these parameters are mostly based on first-order statistics, i.e., single mean and standard deviation values describe their distributions. There are far fewer methods providing parameters based on second-order statistics – parameters that simultaneously describe a physical quantity and its spatial distribution.

Shim and co-workers introduced order parameters typically used in liquid crystal theory [29]. Liquid crystal phases can develop different short or long range symmetries, among which only two can be described in two dimensions: nematic (as in the case of graphitic microcrystals) and polar (as in the case of 'onion-like' diesel soot particles) symmetries. In this paper an image processing methodology will be presented with which the order parameters first used by Shim et al. can be efficiently extracted, using the general fringe orientation maps (θ, as described in the Part I). The methodology can be made completely automatic and, due to its computational efficiency, it can work in real-time, allowing for the design and construction of self-contained, artificial intelligence-based imaging robots in the future. It will also be shown that the order parameters introduced by different authors in the past [4,16,29] are special cases of the more general order parameters introduced and predicted [30] by liquid crystal theory.

2. Materials and methods

In this section the modification and extension of the general hybrid spatial/frequency filtering technique presented in Part I is discussed. The main objective of this technique is to speed up the extraction of the maps of the generalized fringe orientation θ from HRTEM images and to quantify the nanostructure by using second-order statistics in a computationally efficient way so that the framework can be the basis of future applications for automatic soot nanostructure analysis. The origins of the HRTEM images that will be used in Section 3 are also discussed here.

2.1. Image analysis

Two similar techniques for two distinct purposes are presented in this section. First, a computationally efficient method is described for the real-time extraction of θ. Second, a robust technique is discussed for the quantification of symmetry and two-dimensional order parameters in soot nanostructures.

2.1.1. The efficient extraction of orientation

In Part I of this study, a Gabor filtering technique was presented with which the reliable extraction of both orientation and interlayer spacing values is possible. The Gabor filtering method is rigorous and yields results with accuracy close to the theoretical limit; however, it is computationally inefficient for real time applications (see the computation times reported in Part I). The two reasons for this inefficiency are the non-orthogonal, non-separable filters used (Gabor filters are less efficient computationally, but are easily tunable and have excellent spectral properties) and the need of pixel-wise evaluation of filter response data (it is not possible to vectorize the pointwise process, thus less efficient FOR loops have to be used). Efforts have been made to make Gabor filter banks orthogonal, but these techniques can only yield approximate results [22,31]. However, the use of Gabor filter banks is only necessary to extract interlayer spacing information.

If the extraction of interlayer spacing values is not needed, orientation and modulation information can be extracted quickly and efficiently using so-called 'exactly steerable filters'. The term 'steerable' refers to the orientation tunability property of the filters and the phrase 'exactly steerable' means that there is no need to approximate the continuous response surface (see Section 2.1 of Part I) with discrete filter responses; instead, the continuous surface can be exactly (with no errors) interpolated by using so-called basis filters and interpolation functions. The design and use of steerable filters have been exhaustively discussed by Freeman and Adelson [32]. They showed that any filter that can be synthesized as the superposition of a rotationally symmetric window function and an even or odd polynomial is exactly steerable; therefore, any derivative of a Gaussian function is exactly steerable; since being the product of a Hermite polynomial and a Gaussian window function. They provided formulae for the design of such filters and the forms of the first four derivatives of a Gaussian with

Table 1
Regression formulae and regression errors to approximate the parameters a, b and c of Eq. (2). The expressions are valid with the shown errors in the range of $\sigma = [2,20]$.

Parameter	Model	q_1	q_2	q_3	Mean error (%)	Max error (%)
a	$a = \exp(q_1 + q_2\sigma^{-q_3})$	−410.423	411.497	0.00492883	0.019	1.82
b	$b = -\exp(q_1 + q_2\sigma^{-q_3})$	−585.425	586.592	0.00696834	0.009	1.23
c	$c = \exp(q_1 + q_2\sigma^{-q_3})$	−694.689	694.044	0.00906858	0.007	1.71

unity scale and their Hilbert transform. An extended version of their methodology is adopted in this paper; therefore, a brief overview is given here.

Among the filters discussed by Freeman and Adelson, the fourth derivative of the Gaussian function (G_4) and its Hilbert transform (H_4) have been chosen for analysis in this study. This choice is explained by the fact that typical HRTEM soot images contain many overlapping areas in which more than one dominant orientation is present (i.e., multimodal orientation regions) and G_4 and H_4 provide sufficient spectral resolution to be able to reliably extract the most dominant from the present orientation modes (an extension to extract multiple dominant orientations is possible, but will not be covered here). Just like in the case of Gabor filter bank analysis, since the net filter response is computed from the responses of quadrature pairs, the extracted orientation values are phase invariant, thus they are insensitive to phase inversion phenomena [33]. G_4 and H_4 can be synthesized from five and six basis filters, respectively, thus the whole orientation map with an arbitrarily fine resolution can be obtained by eleven convolutions. Furthermore, each of the basis filters are given in an x–y separable form, making convolution even more efficient [34].

The filters presented by Freeman and Adelson are for general machine vision tasks; e.g., edge detection and orientation-sensitive filtering [32]. For these general applications, the unscalable formulas they provided are sufficient, since images showing real-life scenes usually contain a wide mixture of frequencies and no *a priori* knowledge is available regarding these. However, since soot HRTEM images contain only a narrow band of frequencies that represent physical information, in order to be able to efficiently adapt these separable steerable filters for soot nanostructure analysis, an extension for scalability is needed.

Omitting derivation, the eleven basis functions (five for the Gaussian term and six for its Hilbert transform) can be written as follows:

$$\begin{bmatrix} G_4^{\theta_{f1}} \\ G_4^{\theta_{f2}} \\ G_4^{\theta_{f3}} \\ G_4^{\theta_{f4}} \\ G_4^{\theta_{f5}} \end{bmatrix} = \frac{4\left(\frac{2}{105\pi}\right)^{1/2}}{\sigma^5} e^{\frac{x^2+y^2}{\sigma^2}} \begin{bmatrix} 4x^4 - 12x^2\sigma^2 + 3\sigma^4 \\ (4x^3 - 6\sigma^2 x)y \\ -(2x^2 - \sigma^2)(\sigma^2 - 2y^2) \\ x(4y^3 - 6\sigma^2 y) \\ 4y^4 - 12y^2\sigma^2 + 3\sigma^4 \end{bmatrix} \tag{1}$$

$$\begin{bmatrix} H_4^{\theta_{f1}} \\ H_4^{\theta_{f2}} \\ H_4^{\theta_{f3}} \\ H_4^{\theta_{f4}} \\ H_4^{\theta_{f5}} \\ H_4^{\theta_{f6}} \end{bmatrix} = \frac{4}{\sigma^8} e^{\frac{x^2+y^2}{\sigma^2}} \begin{bmatrix} ax + bx^3 + cx^5 \\ (0.2a + 0.6bx^2 + cx^4)y \\ x(0.2a + 0.3by^2) + x^3(0.1b + cy^2) \\ y(0.2a + 0.3bx^2) + y^3(0.1b + cx^2) \\ x(0.2a + 0.6by^2 + cy^4) \\ ay + by^3 + cy^5 \end{bmatrix} \tag{2}$$

where $G_4^{\theta_{fi}}$ is the ith Gaussian basis function, $H_4^{\theta_{fi}}$ is the ith Hilbert-transformed basis function, σ is the scale parameter, x and y are the horizontal and vertical coordinates, respectively, and the parameters a, b and c can be determined by using regression models provided in Table 1. The scale parameter σ can be interchangeably used with the image frequency, f, by the following equation:

$$\sigma = \frac{\sqrt{2}}{\pi f} \tag{3}$$

This simple extension for Freeman and Adelson's steerable filter theory provides us with scalable, steerable and separable basis functions for a quadrature filter pair with which the efficient and accurate extraction of the local fringe orientation θ is possible. The scalability extension has been added to the steerable theory for one reason: to provide a theoretical basis for matching filter frequencies with the narrow frequency band present in HRTEM soot images. The matching procedure can be carried out in the simplest case by computing the radial averaged (orientation invariant) power spectrum of the HRTEM image, finding the most dominant frequency $f_{\max}$ (not considering the zero-peak) and setting the filter scale σ to match this frequency by using Eq. (3). Another, more rigorous way is to maximize the normalized filter response function over the whole image:

$$\begin{aligned} \sigma &= \arg\max_{\sigma_f}[\overline{R}(\sigma_f, I)] \\ &= \arg\max_{\sigma_f}\left[\iint_{-\infty}^{+\infty} \frac{\sigma_f^5}{128\pi}\left(e^{-\frac{1}{4}\sigma_f^2(u^2+v^2)}\sigma_f(u^2+v^2)^2\right)\mathcal{F}(I)\,du\,dv\right] \end{aligned} \tag{4}$$

where u and v are the horizontal and vertical frequency coordinates, respectively, and $\mathcal{F}(I)$ denotes the Fourier transform of the HRTEM image I. Note that Eq. (4) will only yield useful values of σ if the image has a well-defined frequency band that can be separated from the zero peak and in those cases Eq. (4) will give the theoretically most efficient filtering. However, for some lower quality images or images of highly amorphous structures, $\overline{R}(\sigma_f, I)$ does not have a local maximum around the frequency band of interest. It is therefore suggested to algorithmically start with Eq. (4) and if no satisfying local maximum is found, proceed with Eq. (3) by substituting $f = f_{\max}$.

After finding the proper value for the scale parameter, the micrograph is filtered by each basis filter. The filter responses at any arbitrary filter orientation σ_f can be computed by using the following interpolation formulae [32]:

$$R^{\theta_f} = \left(\left[\sum_{j=0}^{N=4} k_j^{\theta_{fi}}\left\{I \otimes G_4^{\theta_{fi}}\right\}\right]^2 + \left[\sum_{j=0}^{N=5} k_j^{\theta_{fi}}\left\{I \otimes H_4^{\theta_{fi}}\right\}\right]^2\right)^{1/2} \tag{5}$$

$$k_j^{\theta_{fi}} = (-1)^j \binom{N}{j} \cos^{N-j}(\theta_f)\sin^j(\theta_f) \tag{6}$$

where R^{θ_f} is the filter response at an arbitrary orientation θ_f, $k_j^{\theta_{fi}}$ is the interpolation term and N is either 4, when computing the response of the Gaussian part, or 5, when computing the response of the quadrature component.[1]

After filtering with the eleven basis filters, the quadrature (phase invariant) response can be computed at any filter orientation by using Eq. (5). The local orientation θ and modulation strength μ are then computed in a manner very similar to how they were computed in Part I: a matrix of response values is constructed by using a sufficiently fine set of filter orientation values. At a

[1] The term $\binom{N}{j}$ in Eq. (6) denotes combination.

particular pixel, θ can be approximated by the filter orientation that gives the highest response at that location and μ is simply the normalized filter response. The maps of the two structural parameters (θ and μ) are the inputs for symmetry analysis.

2.1.2. Robust symmetry analysis

Shim et al. [29] proposed the use of two two-dimensional order parameters, namely the nematic and polar order parameters in the following form:

$$S_{2,N} = 2\langle\cos^2(\alpha_i)\rangle - 1 \tag{7}$$

$$S_{2,P} = 1 - 2\langle\cos^2(\alpha_i)\rangle \tag{8}$$

where $S_{2,N}$ is the nematic order parameter, $S_{2,P}$ is the polar order parameter, α_i is the angle between the fringe orientation vector and a so-called director vector and $\langle\rangle$ means mean value. The director vector is approximately the local mean orientation inside an image region in the nematic case; in the polar case, it is a vector pointing from polar symmetry poles to the fringe centroids. It is easy to see that $S_{2,N}$ is 1 for a perfectly ordered structure and 0 for a perfectly disordered structure, while $S_{2,P}$ is 1 for perfect concentric symmetry, 0 for disordered phases and -1 for radial symmetry. Although these properties are two-dimensional, the values of the two-dimensional parameters very closely approximate those of their three-dimensional counterparts, if the assumptions about the overall symmetry of the structure hold (in soot structure, these symmetries can be either polar or nematic; therefore, the assumptions are valid in most cases). $S_{2,N}$ and $S_{2,P}$ can be calculated for every location in the structure or for every pixel in a discretized digital image; therefore, their two-dimensional fields will be the result of structural analysis. The sizes of the environments around a particular location in the structure in which the mean order parameter values are computed are also important factors. It is possible and practical to choose multiple sizes to see how order changes with different scales in the structure. Some structures only exhibit short range order (amorphous carbon, most soot nanostructures), while others show orderliness on longer scales as well (graphite).

The order parameters given by Eqs. (7) and (8) are projected versions of three-dimensional order parameters first defined, used and predicted by liquid crystal theory [35]. It was shown that liquid crystal theory can effectively predict soot equilibrium nanostructure as well [30]. One of the main assumptions of this approach is that graphene layers can be considered as discotic molecules and as such, theories like the Maier–Saupe theory predict their phase behavior [36,37].

Shim et al. suggest a brute force method to compute the order parameters they proposed [29]. This method computes $S_{2,N}$ and $S_{2,P}$ at every pixel by using the orientations of every detected fringe that lie inside the analyzed environment around particular pixels. For high-resolution orientation fields (θ) typically extracted by the technique presented in Section 2.1.1, this method is highly inefficient.

The objectives of this section are the following:

1. To show that nearly every order parameter derived and described by previous works [4,16,29] can be considered as specific cases and representations of the order parameters given by Eqs. (7) and (8).
2. To develop a method with which high-resolution fields of $S_{2,N}$ and $S_{2,P}$ can be computed efficiently at different scales and to show that the proposed method produces the same results as conventional methods.
3. To show that the computational efficiency of the proposed method allows for additional capabilities, such as the automated recognition and analysis of different soot nanostructures by motorized electron microscopes.

2.1.2.1. Extracting the nematic symmetry matrix. By the image model we introduced in Part I, nematic symmetry can be considered as the local similarity of orientation values over different scales. Among the two symmetry parameters, the nematic symmetry parameter is the easier to extract, as its conventional form (Eqs. (7) and (8)) can be implemented almost directly by using convolutions. Mathematically:

$$S_{2,N} = \max_j\left(F_{\sigma N} \otimes \left\{\mu\left[2\cos^2(\mathcal{W}(\theta+\tau_j) - \mathcal{W}(\theta+\tau_j) \otimes F_{\sigma N}) - 1\right]\right\}\right) \tag{9}$$

$$F_{\sigma N} = \frac{1}{\pi\sigma_N^2} e^{-\frac{x^2}{\sigma N^2} - \frac{y^2}{\sigma N^2}} \tag{10}$$

where $F_{\sigma N}$ is a Gaussian kernel with a scale parameter of σ_N. Note that σ_N is not the same scale as σ - instead, it is the scale of the nematic symmetry of the graphene layers, while σ is the scale of adjacent layers. It has to be noted that $F_{\sigma N}$ is scaled such that the results of the convolutions will represent weighted mean operations. The additional weighting introduced by μ adds a reliability measure to the computation, i.e., only the most defined linear patterns will yield the highest symmetry values.

One problem with using orientation values is their directional ambiguity, meaning that due to a modulo π periodicity, an orientation value of $-\pi/2$ means exactly the same physical orientation as $+\pi/2$ (when choosing the reference axis as such). This property leads to erratic $S_{2,N}$ values at locations where the orientation is close to the ambiguous values. To overcome this, one can compute $S_{2,N}$ by using multiple ($n_{\theta N}$) different reference orientation axes. Rotating the reference axis has been implemented by a simple iterative procedure:

1. Add or subtract a small increment τ to or from θ.
2. Find points with orientations q in the modified θ that are either greater than $\pi/2$ or less than $-\pi/2$.
3. Set these points equal to $q - \pi$ and $q + \pi$, respectively.
4. Repeat steps 2 and 3 until no further points are found.

We subsequently refer to this operation as the 'wrapping operation', $\mathcal{W}(\theta+\tau)$, in this paper. By using $n_{\theta N} \geqslant 2$, the correct values for $S_{2,N}$ can be obtained by keeping the highest resulting value for $S_{2,N}$ at each pixel.

The local director of nematic symmetry $\theta \otimes F_{\sigma N}$ is computed based on the assumption that a sufficient number of data points is always available around a particular point in the image. When this assumption fails, the director cannot be approximated by the local mean. In these cases, it has to be computed by an eigenvalue problem [29]. Since when using the generalized orientation maps, θ, the number of data points increase about two orders of magnitude, it is safe to approximate the director with the local mean.

The term 'nematic symmetry matrix' refers to the multiscale nature of symmetry. The nematic symmetry matrix $M_{2,N}$ is simply a matrix storing fields of $S_{2,N}$ at different scales. Conjugate symmetry maps describing overall symmetry can be constructed by using these matrices.

2.1.2.2. Extracting the polar symmetry matrix. Both the polar symmetry matrix $M_{2,P}$ and its extraction technique are very similar to the nematic case. The few differences include different filters used in the process and a different way of summing filter

responses. Maps of the polar order parameter $S_{2,P}$ can be computed by the following equations:

$$S_{2,P} = \frac{1}{n_{\theta P}} \sum_{j=1}^{n_{\theta P}} \mathcal{W}(\theta + \tau_j) \otimes F_{\sigma P} \tag{11}$$

$$F_{\sigma P} = -\frac{16}{\pi \sigma_P^4} x_r y_r e^{-\frac{2(x_r^2 + y_r^2)}{\sigma_P^2}} \tag{12}$$

where x_r and y_r are rotated coordinates and σ_P is the scale of polar symmetry. The filter $F_{\sigma P}$ has four lobes, two positive and two negative, organized in a way so that the filter gives the highest positive response at concentric patterns in θ and the lowest negative response at radial patterns in θ; therefore, its response is analogous to the symmetry parameters of shim et al. [29]. The responses obtained at $n_{\theta P}$ different reference angles can form an aggregate symmetry parameter map by taking their mean value instead of their maximum value, unlike as we did in the nematic case. Again, θ is filtered at $n_{\sigma P}$ polar symmetry scales and the resulting polar symmetry maps are stored in the polar symmetry matrices $M_{2,P}$.

Once the symmetry matrices $M_{2,N}$ and $M_{2,P}$ are extracted, they can be analyzed at each scale level or conjugate symmetry parameter maps can be formed by computing their means or maxima along their scale dimensions. These conjugate parameter maps pinpoint salient structures in the images in an intuitive way. They are discussed in further detail in Section 3.3. Figure 1 shows an example of these conjugate symmetry maps using an artificial test image.

2.2. HRTEM images

Five different images have been chosen to demonstrate the concepts introduced in this paper. These five images show qualitatively different structures; therefore, they are ideal candidates to illustrate the proposed method. Three of the five images are micrographs of real soot; the rest are micrographs of pyrolized graphite. Although typical soot structures never reach perfectly graphitic states in practice, the two micrographs of graphite are ideal images for demonstrating the technique proposed in this paper. Table 2 shows a summary of the properties of the five test images.

The two different sampling procedures have been discussed in detail in Section 2.2 of Part I. Figure 2 shows the five images.

The thermophoretically sampled n-dodecane, m-xylene and ethylene soots have been produced in a premixed flat flame burner under fuel rich conditions (the equivalence ratio was approximately 2 for each of these samples). The details of the sampling procedure and burner can be found in [38]. Graphite samples have been pyrolyzed at 3000 °C and the pyrolysis products have been deposited on a lacey carbon grid dropwise in an ethylene suspension. The details of this sampling technique can be found in [20].

3. Applications – results and discussion

In this section a number of applications will be presented based on the general approach discussed in Section 2.1. These applications mainly employ specific ways of post-processing the symmetry matrices $M_{2,N}$ and $M_{2,P}$ in order to obtain physically meaningful and representative information about the soot structures. Lastly, qualitative comparison between conventional fringe statistics and symmetry parameters and an evaluation of the general performance of the algorithms is given, discussing the feasibility of future real-time applications.

3.1. Frequency matching

A set of experiments have been conducted to check the validity of the frequency matching approach we introduced in Section 2.1.1. Once the frequencies storing the highest powers have been determined by the power spectra of the test images, a range of frequencies around the frequencies of maximum powers have been identified. The images have been filtered by filter sets constructed using σ values computed from the range of frequencies by Eq. (3). Finding an objective, exact method to evaluate the performance of a filter set is a difficult task; however, one can make an empirical evaluation by looking at some norm of the obtained μ values. Ideal filters maximize these localized filter responses, but not necessarily everywhere in the image. Therefore, the mean μ values have been chosen as evaluation measures. Figure 3 shows the results of these experiments.

Based on our results, it is safe to state that using the frequencies in the radially-averaged power spectra that give the highest powers is a relatively robust method to efficiently filter typical HRTEM soot images for orientation extraction. In all cases the obtained modulation values were above 95% of the possible maximum. Image #4 yielded the worst results, in which case the obtained filtering efficiency was approximately 96% of the possible maximum. If the most ideal filters are needed, for high-quality images the use of Eq. (4) gives better results. This approach did not work for images #4 and #5 in our case due to the unseparable zero-peak in their power spectra. Overall, contiguous and reliable orientation maps

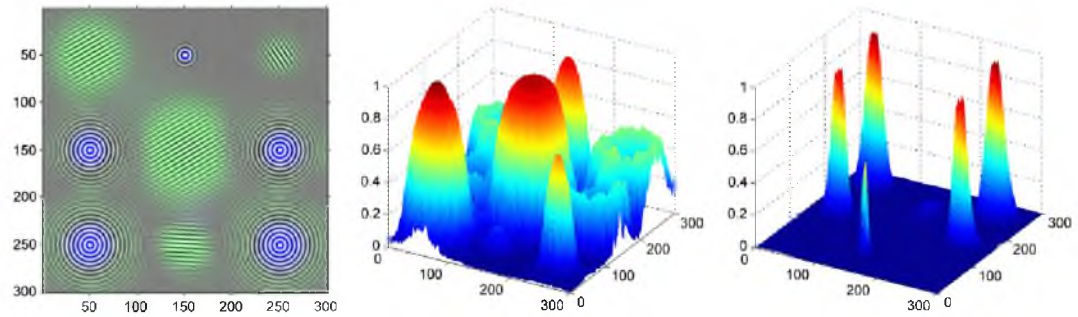

Fig. 1. The illustration of the symmetry detection algorithm. Left: A test artificial image. Colors indicate symmetry saliency: green color means nematic symmetry, blue color means polar symmetry. The image has been prepared by placing linear and polar sinusoidal patterns with a fixed wavelength (which is approximately true for soot HRTEM micrographs) windowed by Gaussian functions. Middle: nematic symmetry saliency map. Right: polar symmetry saliency map. The locations of maxima in the polar saliency map provide the director poles for $S_{2,P}$. Notice how the nematic saliency map covers the concentric fringes with low enough curvature. This is understandable since nematically symmetric regions can be considered as limiting cases – polar symmetric regions with zero curvature. The parameters used to obtain these illustrative results were $n_{\sigma P}$, $n_{\sigma N} = 10$, $n_{\theta P} = 4$, $n_{\theta N} = 2$.

Table 2
Properties of the five test images used for demonstration.

Image	Origin	Structure	Sampling	Magnification	Image size	Notes
#1	n-dodecane	Amorphous	Thermophoretic	430,000×	1024 × 1024	Digital
#2	m-xylene	Short range polar	Thermophoretic	430,000×	1024 × 1024	Digital
#3	ethylene	Long range polar	Thermophoretic	470,000×	1024 × 1024	Digital
#4	p-terpenyl	Short range nematic	Dispersed in ethanol	350,000×	800 × 720	Digitized – low quality
#5	bifluorenyl	Long range nematic	Dispersed in ethanol	350,000×	800 × 740	Digitized – low quality

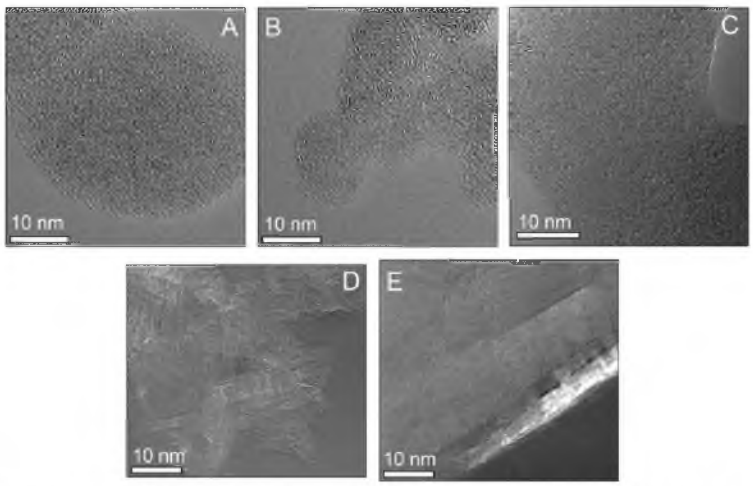

Fig. 2. Test images used to demonstrate the methodology described in this paper. (A) Image #1, amorphous soot from an n-dodecane flame, thermophoretically sampled. (B) Image #2, m-xylene soot exhibiting short range polar symmetry, thermophoretically sampled. (C) Image #3, ethylene soot exhibiting long range polar symmetry, thermophoretically sampled. (D) Image #4, p-terpenyl graphite showing short range nematic symmetry, deposited on the HRTEM grid by dispersing in ethanol. (E) Image #5, bifluorenyl graphite showing long range nematic symmetry, deposited on the HRTEM grid by dispersing in ethanol.

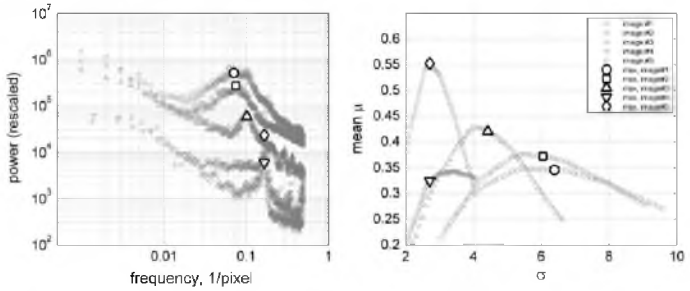

Fig. 3. The results of the frequency matching experiments. In these experiments we constructed filter sets to extract orientation and modulation values from the five test images. The graph to the left shows the power spectra of the test images, along with the determined frequencies that stored the highest powers. These are the dominant frequencies of the HRTEM images and they approximately correspond to the inverse of the lattice spacing of graphite. The graph to the right shows the mean μ values obtained by filtering as a function of the chosen σ filter scale parameter. The results show that selecting σ based on the frequencies of the highest power gives reasonably good filtering efficiency in most cases.

have been extracted from all five test images. The orientation and modulation maps are shown in Fig. 4.

3.2. The validity of the new method

A number of stochastic simulations were carried out to test the validity of the proposed method. By a test of validity we refer to a comparison between order parameter values obtained by the new method and the conventional method [29].

Artificial orientation maps were generated to test the validity of the approximation of both $S_{2,N}$ and $S_{2,P}$. These artificial orientation maps included a circular area with polar or nematic symmetry surrounded by random orientation values. The orientation values in these maps were perturbed slightly in successive steps in order to decrease the expected value of the order parameters. Figure 5 shows $S_{2,N}$ and $S_{2,P}$ values measured by both the proposed and the conventional algorithm.

The results show excellent agreement between the values obtained by the conventional algorithm and the proposed method.

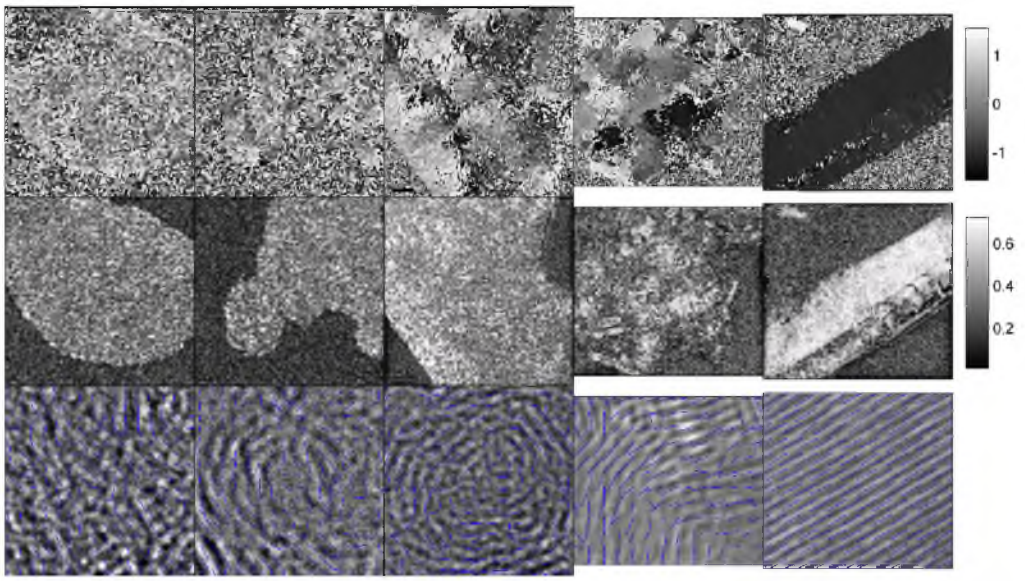

Fig. 4. Extracted orientation (θ) and modulation (μ) maps from the five test images. The top row shows orientation maps, the middle row shows modulation maps and the bottom row shows orientation fields denoted by line segments overlaid on the original images. The columns correspond, from left to right, to test images #1 to #5, respectively.

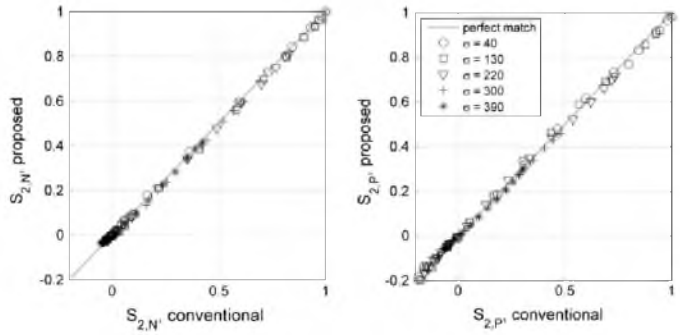

Fig. 5. Validity tests for the proposed algorithm to measure the order parameters $S_{2,N}$ and $S_{2,P}$. The parameters were measured at different scales in a 1 Mpixel artificial orientation map.

3.3. Qualitative analysis – symmetry saliency maps

Saliency maps are obtained for two reasons: to guide imaging automation and to provide a basis for qualitative analysis. High values in the polar or nematic symmetry saliency maps indicate local concentric or nematic order. In both types of saliency maps, points of local maxima always correspond to centers of symmetric regions. Therefore, if the objective of the imaging is to take pictures of nematic or polar structures, the artificial intelligence should focus on areas around maxima in the symmetry saliency maps. The design of these artificial intelligence algorithms is not a subject of this paper – the symmetry saliency maps will be presented for the sake of demonstration of the capabilities of our approach.

Two types of conjugate maps can be formed from the symmetry saliency matrices $M_{2,N}$ and $M_{2,P}$: by summing or averaging along the scale dimension of the matrices, one obtains a conjugate map that shows the overall strength of the symmetry at certain locations, averaged over all scales; while computing the maxima along the scale dimension results in a conjugate map that shows the highly symmetrical regions regardless of the symmetry scale. The former will be referred to as $M_{2,N}^{av}$ or $M_{2,P}^{av}$ and the latter will referred to as $M_{2,N}^{\max}$ or $M_{2,P}^{\max}$. Further differentiation between symmetry scales is possible by computing the maxima or average values only over a certain scale range. The symmetry scales can be converted from σ_N and σ_P to length measures by using the full widths at half maxima of the Gaussian window functions by the following equation:

$$L_X = 2(\ln 2)^{1/2}\sigma_X p \tag{13}$$

where L_X is the length measure of the symmetry scale σ_X in nanometers, the subscript X can either mean nematic (N) or polar (P) symmetry and p is the nm per pixel ratio of the image.

Figures 6 and 7 show symmetry saliency maps. Figure 6 shows images #4 and #5 showing graphitic structures with high nematic symmetry. Image #4 was taken of a p-terpenyl graphite sample which consisted of stacked graphene lamellae. The stacks are not very wide and the long layers broke up into several shorter nematic segments. This sample exhibited very strong short range nematic symmetry, as it can be seen from Fig. 6A (indicated by intense green patches). The symmetry is weaker at larger scales, as it is showed in Fig. 6B. Image #5 was taken of a bifluorenyl graphite sample. This sample exhibited very strong long range nematic symmetry. The symmetry is strong at both short and long scales, as shown by Fig. 6D and E. Figure 6C and F shows the conjugate symmetry saliency maps $M^{av}_{2,N}$ and $M^{av}_{2,P}$ of images #4 and #5. These maps highlight the regions with the strongest symmetries, regardless of the symmetry scale. As it can be seen, polar symmetry is not very dominant in these structures. The few regions having noticable polar symmetry are mostly positioned along the edges of the structure. These regions can be automatically removed from the symmetry maps by introducing a condition on μ, as the lowest values in μ correspond to the background. Such a technique is useful when designing imaging automatons but is not covered in this paper.

Figure 7 shows symmetry saliency maps for images #1, #2 and #3. These images were taken of various soot samples that show different degrees of the so-called onion structure or concentric rings. These rings are most likely the 2D intersections of amorphous cores surrounded by spherical graphene layers. Combustion generated carbon often exhibits this type of structure and when analyzing soot from natural flames one is likely to encounter it. Figure 7A–C shows that both the nematic and polar symmetries are very weak in image #1. A very young soot sample can be seen in image #1, thermophoretically sampled very close to the ignition zone in an n-dodecane flame. These structures are typically amorphous [13,27,38], which is in agreement with the very weak symmetries that were found. At the shortest scale, the distribution of slightly nematic or polar regions in the structure is homogeneous. Figure 7D–F also shows a young soot with a slightly more ordered structure. The next step of structural change is often the formation of small concentric regions [13]. The centers of these regions are highlighted by the polar symmetry saliency map in Fig. 7E and F.

Possibly due to thermodynamic reasons [39], concentric regions can grow and become surrounded by relatively highly crystalline nematic outer shells [13]. Figure 7G–I illustrates this type of structure. The bright red color indicates centers of strong polar symmetry. Notice that these regions are surrounded by green patches, highlighting the crystalline outer shells. In some cases [13,40], the amorphous cores can disappear and the outer nematic regions compose a graphitic structure similar to those shown in Fig. 6.

3.4. Quantitative analysis

In this section a number of ideas will be given on ways of post-processing the extracted symmetry matrices $M_{2,N}$ and $M_{2,P}$ to obtain different representations of the maps of the order parameters. Being equal to the two-dimensional order parameters, the symmetry responses in these matrices themselves can be used for quantitative analysis. Maxima in $M_{2,P}$ can be extracted and can be used as director poles for conventional symmetry analysis. Finally, a multiscale segmentation method will be presented that allows for the analysis of the shapes of the symmetric clusters in soot structure.

3.4.1. The analysis of order versus scale

Analogous to how the symmetry saliency maps are computed, two different types of histograms can be computed from $M_{2,N}$ and $M_{2,P}$. The computation of these histograms are very similar to the computation of $M^{\max}$ and M^{av}, the only difference is the direction of integration or maxima computation. $M^{\max}$ and M^{av} were obtained by integrating $M_{2,N}$ or $M_{2,P}$ with respect to scale – the histograms presented in this section have been computed by spatially integrating over the order parameter maps and storing one conjugate value for each scale.

The histograms obtained in this way show the strength of either the nematic or polar symmetry as a function of symmetry scale. The two types of histograms are the overall symmetry strength histogram S^{av}, which is computed by averaging the symmetry response values over the whole micrograph at certain scales and the location independent symmetry strength histogram $S^{\max}$, which is computed by computing a single maximum symmetry response at a given scale. From the former, one can identify the scale

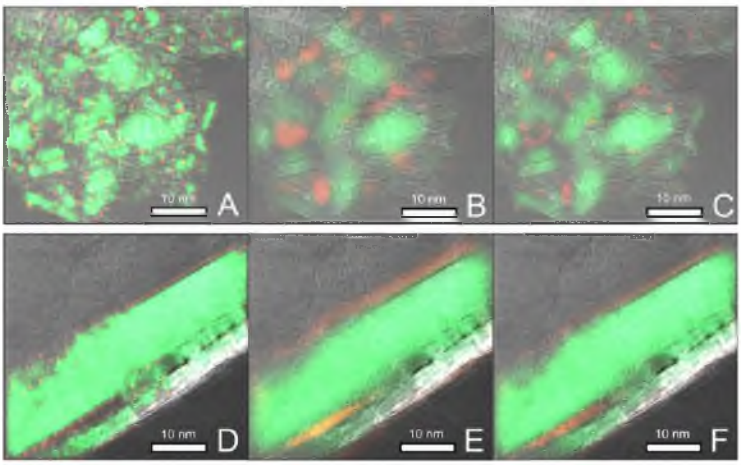

Fig. 6. Symmetry saliency of nematic structures. The saliency maps are laid over the original images. Hues of green indicate the strength of nematic symmetry and hues of red indicate the strength of polar symmetry. (A) Short range symmetry in image #4. (B) Long range symmetry in image #4. (C) Conjugate symmetry maps M^{av} of image #4. (D) Short range symmetry in image #5. (E) Long range symmetry in image #5. (F) Conjugate symmetry maps M^{av} of image #5. The parameters used to obtain these saliency maps were $n_{\sigma P}$, $n_{\sigma N} = 10$, $n_{\theta P} = 4$, $n_{\theta N} = 2$. The limit between the short and long symmetry scales have been set at $L_X = 4$ nm.

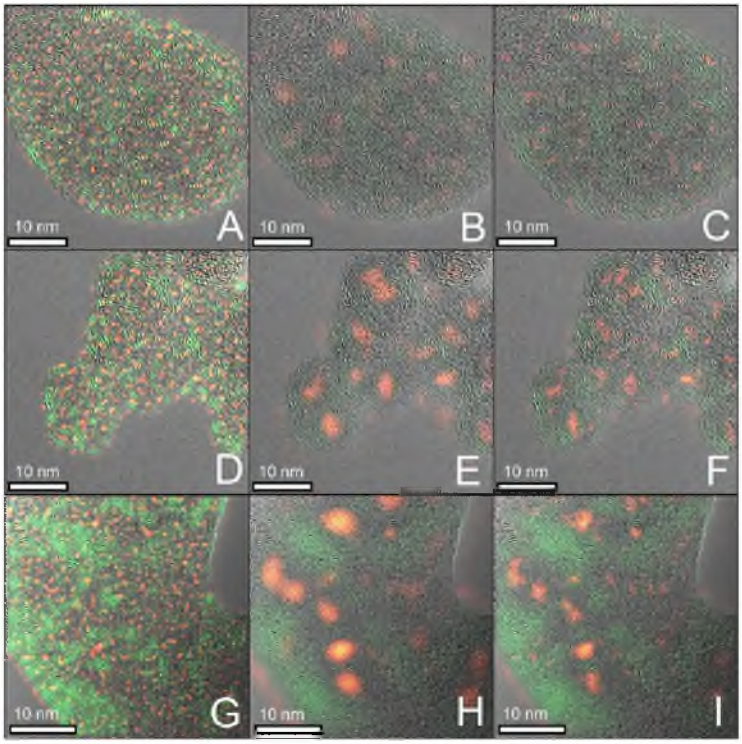

Fig. 7. Symmetry saliency of polar (concentric) structures. The saliency maps are laid over the original images. Hues of green indicate the strength of nematic symmetry and hues of red indicate the strength of polar symmetry. (A) Short range symmetry in image #1. (B) Long range symmetry in image #1. (C) Conjugate symmetry maps M^{av} of image #1. (D) Short range symmetry in image #2. (E) Long range symmetry in image #2. (F) Conjugate symmetry maps M^{av} of image #2. (G) Short range symmetry in image #3. (H) Long range symmetry in image #3. (I) Conjugate symmetry maps M^{av} of image #3. The parameters used to obtain these saliency maps were $n_{\sigma P}$, $n_{\sigma N} = 10$, $n_{\theta P} = 4$, $n_{\theta N} = 2$. The limit between the short and long symmetry scales have been set at $L_X = 4$ nm.

or characteristic length at which the image is the most symmetric and from the latter it is possible to determine which scale carries the single most symmetric sub-structure in an image.

Figure 8 shows the computed symmetry histograms. Due to the nature of the extraction of nematic symmetry, for strong nematic structures the resulting histograms almost always show monotonically decreasing frequency versus scale. This is analogous to the behavior of the nematic symmetry parameters of Shim et al. [29]. From the height, slope and shape of this decreasing profile one can make implications about the nature of nematic symmetry in a structure. As can be seen from row A in Fig. 8, the first two images show very similar nematic distributions. This is due to the low degree of ordering in these soot nanostructures.

A slight increase at short scales can be seen in the nematic symmetry histogram of image #3 corresponding to the more ordered outer shells surrounding the amorphous cores. Images #4 and #5 are structures with dominant nematic symmetry, with the latter being the most ordered. Row B shows similar trends. A thing worth noting is the different shapes of the distributions of images #4 and #5. These trends basically show that the symmetry in image #4 decayed more rapidly as scale increased than in image #5, which agrees well with the physics of these nematic structures. Row C shows the overall polar symmetry strength of the images. Obviously the structure of image #3 is the most symmetric, with the strongest polar symmetry being around 17 nm. This implies that the diameters of concentric particles within this soot are approximately 17 nm. Image #2 exhibits a similar histogram, but with a weaker maximum at approximately 10 nm. The amorphous structure of image #1 shows considerable polar symmetry only at the smallest scales. The histograms of images #4 and #5 are typical for not truly polar structures with a weak short scale symmetry that increases slightly at larger scales. The location independent polar histograms of row D in Fig. 8 implies close to zero polar symmetry in image #1 and the highest polar symmetry in image #3. Notice that the peaks are not overlapping between the overall and location independent polar histograms for the two real polar structures, images #2 and #3. This means that the strongest symmetries are locally present at shorter scales in these images, but those short scales overall do not possess very strong symmetry.

3.4.2. Polar symmetry director poles from $M_{2,P}$

Polar director poles are the coordinates of the centers of concentric regions in the soot structures. These director poles provide reference points to calculate the symmetry parameter $S_{2,P}$ as introduced by Shim et al. [29]. The director poles are easy to find from the symmetry saliency maps $M_{2,P}^{\max}$ and $M_{2,P}^{av}$, since the filters used for polar symmetry extraction give the highest response at these points. Locating the director poles is therefore a problem of finding the local maxima in $M_{2,P}^{\max}$ or $M_{2,P}^{av}$. To extract physically meaningful director poles, it is advised to calculate the symmetry saliency

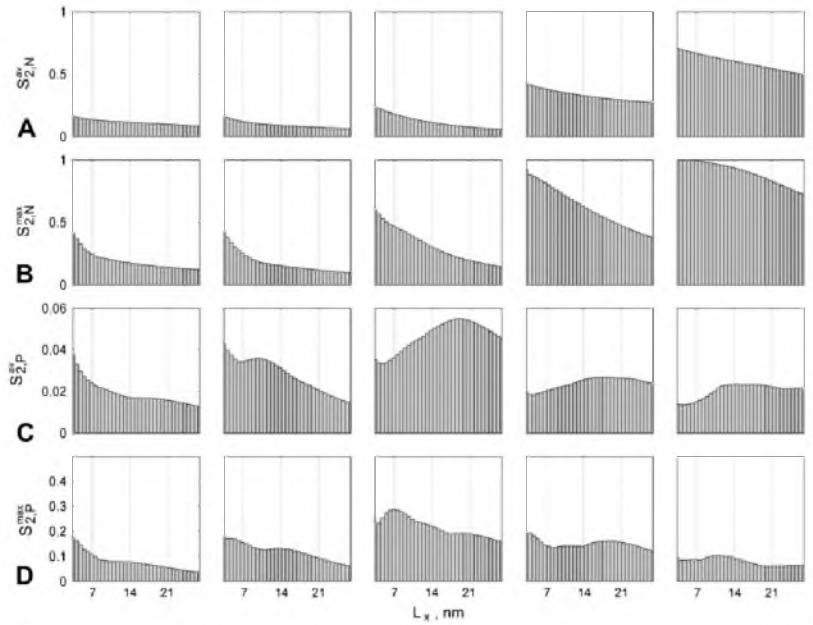

Fig. 8. Histograms of symmetry strength versus scale. Row A: from left to right: nematic symmetry histograms of images #1, #2, #3, #4 and #5. Row B: from left to right: location independent nematic symmetry histograms of images #1, #2, #3, #4 and #5. Row C: from left to right: polar symmetry histograms of images #1, #2, #3, #4 and #5. Row D: from left to right: location independent polar symmetry histograms of images #1, #2, #3, #4 and #5. Note that the maximum ideal value for both symmetry strengths is 1. The parameters used to obtain these results were $n_{\theta P}$, $n_{\theta N} = 35$, $n_{\theta P} = 4$, $n_{\theta N} = 2$. L_x is given by Eq. (13).

maps at longer scales to avoid false detection due to 'noise' caused by short scale symmetries. Setting a threshold on the polar symmetry strength might also be necessary in order to filter out poles with weak symmetry. Figure 9 shows the two structures exhibiting real polar symmetry, along with their director poles and $S_{2,P}$ parameters versus scale.

This kind of utilization of the symmetry analysis technique proposed in this work highlights that primary soot particles or agglomerates of primary particles represent local maxima in the polar symmetry matrices; therefore, they can be treated as special cases of the more general structural order concept.

The calculation of $S_{2,P}$ using maps of θ and μ is similar to the conventional procedure [29]. There are a few subtle differences. First, the angles α_i in Eqs. (8) and (9) are values in θ, the use of which implies a much higher resolution symmetry profile than with conventional analysis. Second, μ can be used as a reliability factor for orientation values, thus the mean operator in Eqs. (8) and (9) can be substituted by the weighted mean, with μ as weight values. As it was shown for interlayer spacing measurement with Gabor filters in Part I, this weighting increases the fidelity of the data extracted, as only those pixels will be used for computation that represent stronger signals.

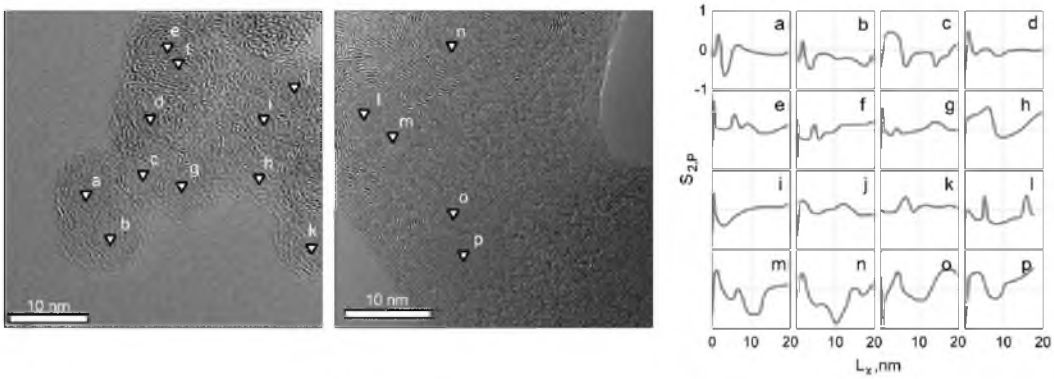

Fig. 9. Conventional polar symmetry analysis using robustly extracted polar director poles (a)–(p). The director poles are centers of concentric regions. Images #2 and #3 and their corresponding symmetry profiles are shown. Symmetry is measured by using the conventional definition for the symmetry parameter $S_{2,P}$ (Eqs. (8) and (9)). The range of the order parameter is $[-1, 1]$ for all plots. The aim of this figure is to illustrate the robust identification of concentric nodes in the structure. L_x is given by Eq. (13).

First, it is worth noting that points a–b, e–f, l–m and o–p are the centers of typical formations consisting of a few amorphous cores surrounded by a more or less crystalline outer shell. Notice the two peaks in the polar symmetry profile of these points – this is the most obvious in the case of point l. The first peak corresponds to the lamellae surrounding the amorphous core and the second peak corresponds to the enwrapping outer shell. The locations of the first peaks in the symmetry profiles provide information about the size of the inner layer around amorphous cores. The diameters are around 4 nm in the case of image #2 and 7 nm in the case of image #3, which is in agreement with row D of Fig. 8. In the case of image #3, these inner shells are also somewhat thicker than those of image #2 (notice stretched-out peaks, e.g., for points o and p).

3.4.3. Multiscale segmentation

Soot structures are agglomerates and as such, they contain many identifiable sub-structures. The distribution of the sizes, shapes and locations of these sub-structures carry information about the origins and formation conditions of the soot.

From the point of symmetry, two main types of these sub-structures can be identified in the aggregate structures: patches with strong common nematic symmetry and regions exhibiting strong polar symmetry. Nematic patches at the smallest scale are crystalline stacks (see the Introduction or [17]) or mesophasic graphite grains; therefore, the concept of 'stacks' [4,16] is also a special case of the general structural order concept presented in this paper. With our method, however, these stacks can be analyzed over longer scales as well. Polar patches at medium to long scales can be remnants of agglomerated primary particles or porous cores wrapped inside crystalline lamellae as well.

Segmentation is a second-order statistical technique, during which a – typically – scalar field is divided into a number of subregions based on some property of the scalar field. In our case this scalar field is one of the conjugate symmetry maps obtained as described in Section 3.3. These conjugate maps can be formed by integrating $M_{2,N}$ or $M_{2,P}$ over a scale range – this scale range determines the scale of the segmentation. For segmenting the conjugate maps, the watershed algorithm has been used [41]. Watershed is a simple algorithm which segments the input scalar map into an unconstrained number of segments based on the gradient of the scalar field. Segments are typically created around local maxima by the watershed routine; therefore, it is ideal to apply on conjugate symmetry maps.

Figures 10 and 11 show the results of the multiscale segmentation approach. The figures have been obtained by segmenting scale-specific $M^{a\ell}$ matrices by watershed and fitting ellipses over the obtained segments. Each of the segments has been analyzed and segments with too weak symmetry have been removed from the segmentation. A single threshold has been used on $M^{a\ell}$ to obtain the figures.

Figure 10 shows the detected nematic segments in a number of images, showing structures dominated by both nematic and polar symmetry. The pure graphitic structure of image #5 produced a single segment, independently of the symmetry scale used. On the other hand, as one may expect, the amorphous structure of image #1 produced no segments with symmetry strength above the used threshold value. Both the nematic structure of image #4 and the polar structure of image #3 produced a plethora of nematic segments at many different scales. The segments of image #4 correspond to the intermediate and outer crystalline shells surrounding the agglomerated primary particles, with more segments next to the edges of the macrostructure (Fig. 10D). On a shorter scale, a host of crystalline stacks have been detected in image #3, typical to the mesophasic structure of not fully graphitized outer layers. Each segment in image #4 corresponds to an orientation change in the wrinkled, layered structure.

After the segments have been obtained, they can be analyzed further to determine the distributions of their size, shape, orientation, etc. For fringe analysis, such techniques have been described in related publications [20] and these can be used to analyze the segments obtained by the method proposed here as well. These methods and the results obtainable by them are not subjects of this paper.

3.5. Comparison with conventional characterization

Most previously published techniques for the characterization of soot or other carbon nanostructure utilize the conventional,

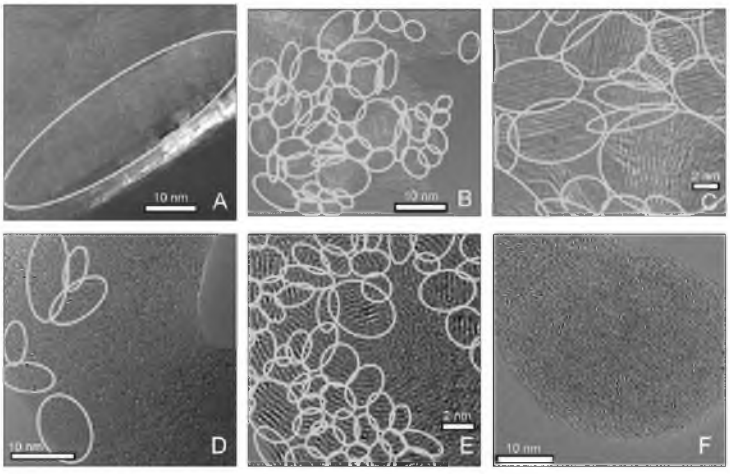

Fig. 10. Demonstration of multiscale segmentation based on nematic symmetry. (A) Segmentation of the graphitic structure of image #5 at any scale. (B) Segmentation of image #4, with allowed scales from the shortest to approximately 4 nm. (C) A zoomed in portion of B. (D) Large scale segmentation of image #3. (E) Short scale segmentation of image #3. The segments closely resemble crystalline stacks. (F) Segmentation of the amorphous structure of image #1. With the same threshold used to obtain Fig. 12A–E, no nematic segments were detected.

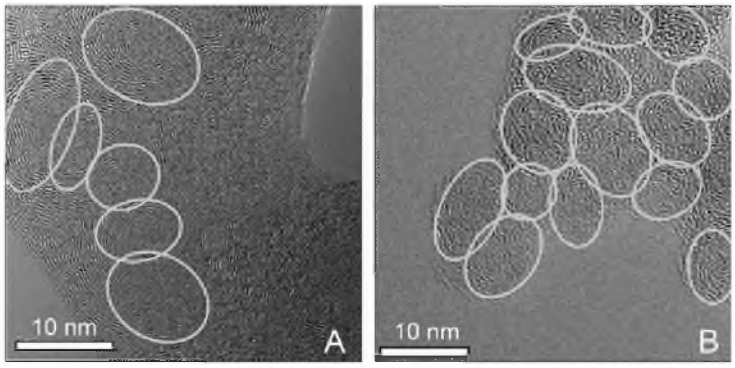

Fig. 11. Polar symmetry segmentation of the polar structures from images #2 and #3. The detected segments closely resemble primary particles in the aggregate structure.

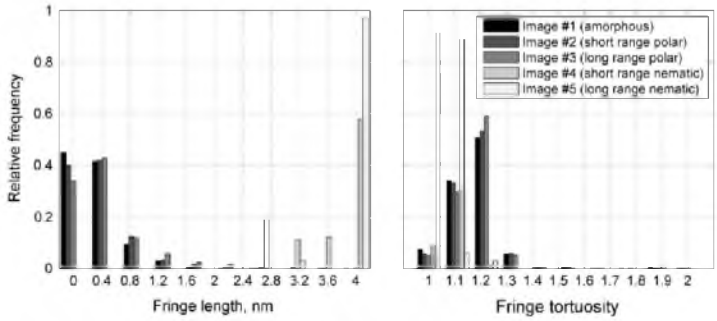

Fig. 12. Conventional, binarization-based fringe statistics. Left: fringe length histograms. Right: fringe tortuosity histograms. Different bar shading represent the five test images. Conventional results are included for the sake of comparison. Note that the last bin of the histograms show the total number of occurrences in bins that are above the last bin as well.

binarization-based procedure.[2] In HRTEM micrographs, carbon layers are identified as individual objects by the standard method and different projected geometric properties of the layers are extracted. Originally, many parameters were defined for structure characterization [20], among which two proved to be the most descriptive: fringe length and fringe tortuosity [16,28,29]. Both parameters were found to be correlated with kinetic parameters [2]. Fringe tortuosity and length affect every property that is a consequence of the electronic structure of soot. Furthermore, fringe length is believed to have an effect on reactivity by affecting the ratio of edge site and basal plane carbon atoms [12].

The relationship between the conventional parameters and the symmetry parameters discussed in this study is difficult to quantify. It is understandable that structures with strong short-scale polar symmetry either consist of relatively small carbon layers (resulting in short observed fringe lengths) or of highly curved ones (resulting in high observed fringe tortuosity). Nematic symmetry is also correlated with fringe length through the scale of symmetry – the longer the fringes, usually the larger the scale of nematic symmetry is. The inverse relationship with tortuosity is obvious: curved fringes cannot contribute to longer scale nematic symmetry. Apart from these trivial statements, the nature of the correlation between conventional and symmetry parameters is not fully understood. Figure 12 shows the results of conventional analysis on the five test images.

[2] For further details on conventional techniques, the reader is referred to Section 1 of Part I of this study.

The fringe length and tortuosity statistics of the three test images of real soot are similar. Overall, among the micrographs of soot, the image of the amorphous soot particle (image #1) contained the shortest, while image #3 (long range polar order) contained the longest fringes. This is consistent with the nematic symmetry strength histograms of Fig. 8. Micrographs of the graphite samples (images #4 and #5) contained much longer fringes. In consistence with the nematic symmetry strength histograms of Fig. 8, image #5 (bifluorenyl graphite) contained the longer fringes of the two graphite images. Tortuosity histograms show very slight differences between the soot samples – the ordering is also consistent with Fig. 8. The fringes in micrographs of graphite (images #4 and #5) were almost perfectly straight – their tortuosities were close to unity.

Overall, it can be stated that although conventional geometric and symmetry parameters are correlated, they describe different aspects of the structure and therefore should be used in conjunction in order to achieve complete characterization. In many cases we found that for the purpose of differentiating similar structures, symmetry parameters exhibit more distinct differences. We will explore further relationships between symmetry and fringe geometry and utilize both to characterize soot structures in future publications.

3.6. General performance and real-time applicability – future work

The flexibility of the algorithms presented in this paper allows for introducing approximations and simplifications in their

implementation to speed up the computation of the symmetry saliency maps. In the form it is presented here, the extraction of orientation and modulation maps does not allow such simplifications, but they are extracted in an already very efficient way. The use of exactly steerable, x–y separable filters allowed for the computation of θ and μ under one second on a typical quad-core workstation for typical 1 Mpixel HRTEM micrographs. Under similar environments, extracting symmetry matrices took approximately 1 min when using a fine sampling of scale – if only symmetry saliency matters, these computations can be sped up to near real-time performance. As a point of comparison, using the conventional algorithm with maps of θ to produce fine maps of the order parameters takes approximately 1 h for 1 Mpixel micrographs. Subsampling generally improves the performance of the extraction of both the polar and the nematic symmetry matrices.

Subsampling is a procedure where the size of a discrete field is reduced by removing elements from the matrix based on subsampling logic [34]. Fortunately, not much information is lost during subsampling the orientation and modulation matrices, due to the fact that symmetries are well conserved during resizing. An item worth noting is that the interpolation method used by the subsampling procedure is critical for resizing matrices of θ. Any type of smoothing interpolation introduces significant errors due to θ being a discontinuous field. This discontinuity is introduced by the modulo π ambiguity of orientation values. Therefore, it is advised to avoid smoothing interpolation and subsample by using the so-called nearest neighbor method [42].

Note that these results have been achieved by simple CPU implementations of the algorithms described in this paper. It is very likely that implementing the framework on a GPU (graphical processing unit) commonly found in most modern computers will result in a truly real-time system.

4. Conclusion

In this paper a novel image analysis method has been presented for the analysis of symmetries in soot nanostructures based on HRTEM micrographs. This method is part of a novel framework developed for the high fidelity, robust analysis of HRTEM soot micrographs. The novelty is based on the use of filter theory to obtain accurate physical information from soot HRTEM micrographs. Two objectives guided the development of the method described in this paper:

1. to be able to obtain accurate information describing the symmetries and order of soot nanostructures and
2. to be able to do this as efficiently as possible.

The latter objective is driven by the incentive of extending our framework to be able to analyze soot structures by driving HRTEMs using artificial intelligence and the symmetry saliency maps that are obtainable by our technique. The techniques presented here have been applied to a test image set showcasing five significantly different carbon structures. It has been demonstrated that the method can efficiently provide robust structural information at high resolution. The structural properties thus obtained are generalized and extended forms of already defined and proposed quantities.

Acknowledgments

This work was partially sponsored by the TAMOP-4.2.1.B-10/2/KONV-2010-0001 Project with support by the European Union, co-financed by the European Social Fund. The authors would like to thank Carlos Andres Echavarria and Joseph Levinthal at the University of Utah for providing HRTEM images.

References

[1] P. Delhaes, Graphite and Precursors, first ed., Gordon and Breach Science Publishers, Amsterdam, 2001.
[2] R.L.V. Wal, A.J. Tomasek, Combust. Flame 134 (2003) 1–9.
[3] R.L.V. Wal, A.J. Tomasek, Combust. Flame 136 (2004) 129–140.
[4] J. Yang, S. Cheng, X. Wang, Z. Zhang, X. Liu, G. Tang, Trans. Nonferrous Met. Soc. China 16 (2006) 796–803.
[5] T. Ishiguro, Y. Takatori, K. Akihama, Combust. Flame 108 (1997) 231–234.
[6] R.L.V. Wal, Soot Nanostructure: Definition, Quantification and Implications, Technical Report 2005-01-0964, SAE, 2005.
[7] A. Santamaria, N. Yang, E. Eddings, F. Mondragon, Combust. Flame 157 (2010) 33–42.
[8] T. Ishiguro, N. Suzuki, Y. Fujitani, H. Morimoto, Combust. Flame 85 (1991) 1–6.
[9] J. Song, C. Song, Y. Tao, G. Lv, S. Dong, Combust. Flame 158 (2011) 446–451.
[10] Z. Li, C. Song, J. Song, S. Dong, Z. Zhao, Combust. Flame 158 (2011) 1624–1630.
[11] A. Strzelec, T.J. Toops, C.S. Daw, in: 7th US National Technical Meeting of the Combustion Institute, The Combustion Institute, 2011.
[12] H. Marsh, Introduction to Carbon Science, 1989.
[13] J. Song, M. Alam, A.L. Boehman, U. Kim, Combust. Flame 146 (2006) 589–604.
[14] C.R. Shaddix, A.B. Palotas, C.M. Megaridis, M.Y. Choi, N.Y.C. Yang, Int. J. Heat Mass Transfer 48 (2005) 3604–3614.
[15] R.H. Hurt, A.F. Sarofim, J.P. Longwell, Combust. Flame 95 (1993) 430–432.
[16] A. Sharma, T. Kyotani, A. Tomita, Fuel 78 (1999) 1203–1212.
[17] A. Sharma, T. Kyotani, A. Tomita, Fuel 80 (2001) 1467–1473.
[18] A.B. Palotas, R.C. Rainey, A.F. Sarofim, J.B.V. Sande, P. Ciambelli, Energy Fuels 10 (1996) 254–259.
[19] A.B. Palotas, L.C. Rainey, A.F. Sarofim, J.B.V. Sande, R.C. Flagan, Chemtech 28 (1998) 24–30.
[20] A.B. Palotas, L.C. Rainey, C.J. Feldermann, A.F. Sarofim, J.B.V. Sande, Microsc. Res. Tech. 33 (1996) 266–278.
[21] R.L.V. Wal, V.M. Bryg, M.D. Hays, Aerosol Sci. 41 (2010) 108–117.
[22] A. Sharma, T. Kyotani, A. Tomita, Carbon 38 (2000) 1977–1984.
[23] S.A. Saltykov, Stereometric Metallography, second ed., Moscow, 1958 (in Russian).
[24] H. Aso, K. Matsuoka, A. Sharma, A. Tomita, Carbon 42 (2004) 2963–2973.
[25] X. Zhang, A. Dukhan, I. Kantorovich, E. Bar-Ziv, A. Kandas, A.F. Sarofim, in: Twenty-Sixth Symposium (International) on Combustion, The Combustion Institute, 1996, pp. 3111–3118.
[26] P. Toth, A.B. Palotas, J. Lighty, C.A. Echavarria, Fuel 99 (2012) 1–8.
[27] W. Massa, Crystal Structure Determination, first ed., Springer-Verlag, Berlin, 2004.
[28] K. Yehliu, L.R.V. Wal, A.L. Boehman, Combust. Flame 158 (2011) 1837–1851.
[29] H.S. Shim, R.H. Hurt, N.Y.C. Yang, Carbon 38 (2000) 29–45.
[30] R.H. Hurt, G.P. Crawford, H.S. Shim, Proc. Combust. Inst. 28 (2000) 2539–2546.
[31] D. Gabor, J. Inst. Electr. Eng. III: Radio Commun. Eng. 93 (1946) 429–441.
[32] T.W. Freeman, E.H. Adelson, IEEE Trans. Pattern Anal. Mach. Intell. 13 (1991) 906–981.
[33] R. Bracewell, The Fourier Transform and its Applications, McGraw-Hill, New York, 1978.
[34] W. Pratt, Digital Image Processing, Wiley, New York, 2001.
[35] S. Chandrasekhar, Liquid Crystals, second ed., The Press Syndicate of the University of Cambridge, Trumpington Street, Cambridge, 1993.
[36] W. Maier, A. Saupe, Z. Naturforsch., A 14 (1959) 882.
[37] W. Maier, A. Saupe, Z. Naturforsch., A 15 (1960) 287.
[38] C.A. Echavarria, Evolution of Soot Size Distribution During Soot Formation and Soot Oxidation-Fragmentation in Premixed Flames: Experimental and Modeling Study, Ph.D. Thesis, University of Utah, 2010.
[39] M. Inagaki, Carbon 35 (1997) 711–713.
[40] R.L.V. Wal, M.Y. Choi, Carbon 37 (1999) 231–239.
[41] L. Vincent, P. Soille, IEEE Trans. Pattern Anal. Mach. Intell. 13 (1991) 583–598.
[42] A. Okabe, B. Boots, K. Sugihara, S.N. Chiu, Spatial Tessellations. Concepts and Applications of Voronoi Diagrams, Wiley, New York, 2000.

CHAPTER 5

AUTOMATED ANALYSIS OF HETEROGENEOUS CARBON NANOSTRUCTURES BY HIGH-RESOLUTION ELECTRON MICROSCOPY AND ON-LINE IMAGE PROCESSING

Reprinted from Ultramicroscopy, Vol. 129, P. Toth, J.K. Farrer, A.B. Palotas, J.S. Lighty, E.G. Eddings, Automated analysis of heterogeneous carbon nanostructures by high- resolution electron microscopy and on-line image processing, Pages 53-62,

Ultramicroscopy 129 (2013) 53–62

Contents lists available at SciVerse ScienceDirect

Ultramicroscopy

journal homepage: www.elsevier.com/locate/ultramic

Automated analysis of heterogeneous carbon nanostructures by high-resolution electron microscopy and on-line image processing

P. Toth [a,*], J.K. Farrer [b], A.B. Palotas [c], J.S. Lighty [a], E.G. Eddings [a]

[a] Department of Chemical Engineering, University of Utah, 50 S. Central Campus Drive, Salt Lake City, UT 84112-9203, United States
[b] Department of Physics and Astronomy, Brigham Young University, N283 ESC, Provo, UT 84602, United States
[c] Department of Combustion Technology and Thermal Energy, University of Miskolc, H3515, Miskolc-Egyetemvaros, Hungary

ARTICLE INFO

Article history:
Received 1 December 2012
Received in revised form
14 February 2013
Accepted 18 February 2013
Available online 28 February 2013

Keywords:
HRTEM
Heterostructure
Automation
Image processing
Soot

ABSTRACT

High-resolution electron microscopy is an efficient tool for characterizing heterogeneous nanostructures; however, currently the analysis is a laborious and time-consuming manual process. In order to be able to accurately and robustly quantify heterostructures, one must obtain a statistically high number of micrographs showing images of the appropriate sub-structures. The second step of analysis is usually the application of digital image processing techniques in order to extract meaningful structural descriptors from the acquired images. In this paper it will be shown that by applying on-line image processing and basic machine vision algorithms, it is possible to fully automate the image acquisition step; therefore, the number of acquired images in a given time can be increased drastically without the need for additional human labor. The proposed automation technique works by computing fields of structural descriptors in situ and thus outputs sets of the desired structural descriptors in real-time. The merits of the method are demonstrated by using combustion-generated black carbon samples.

Published by Elsevier B.V.

1. Introduction

The idea of automating electron microscopes is not new. Computer-controlled scanning electron microscopy has been successfully used to glean mineral intrusions in coal [1], prospect diamonds [2], map the orientation of crystals [3] and study aerosols [4,5] or proteins [6], among other application areas. These methods vary in the extent of automatization—some use on-line image processing to identify regions of interest and focus the electron beam therein; others utilize fully integrated technologies with automatic sample handling and stage positioning.

Solutions for the automation of sample preparation, sample loading, stage positioning and auto-focusing for transmission electron microscopes (TEMs) are readily available on the market. The available software background for on-line image processing can handle magnification down to the so-called square-scale, which refers to fields that contain a single square in a TEM sample holder grid [7]. The scales of the typical carbon nanostructures analyzed in this paper are well below the square-scale—the smallest scale that contains structural information is the atomic scale, at which individual layers of atoms are visible (below 0.1 nm per pixel). Therefore, additional image processing capabilities are needed to be able to automate the process down to the atomic scale. The development and testing of such a method is presented in this work.

Due to the ubiquity of internal combustion engines and the utilization of fossil fuels for energy production, the study of the structure of soot particles has been in the focus of attention [8,9]. Soot can play a favorable role by increasing the radiative heat output of a flame or unfavorable, being a health hazard [10,11], esthetically unpleasant and possibly a contributor to global warming [12]. Controlling soot emissions is possible by designing combustion processes based on the understanding of soot formation mechanisms [13–15]. Soot structure is indicative of the generating combustion environment [16,17]; therefore, by studying the structure, one can deepen one's understanding of the formation processes. Another incentive is pollution source identification [18,19]. High-resolution transmission electron microscopy (HRTEM) was proven to be a reliable tool for the analysis of various carbon structures [20–22] and a number of image analysis techniques have been developed for the quantification of HRTEM micrographs of amorphous carbon [23–25]. All these techniques are for the manual post-processing and analysis of already obtained images.

One of the greatest challenges in the attempt to reliably quantify the structure of amorphous black carbons is posed by its heterogeneity. There are three distinct scales at which these structures can be studied: the scale of aggregates (which grow in length up to the order of 10^3 nm), the scale of primary particles (these make up aggregates and have diameters on the order of

* Corresponding author. Tel.: +1 801 585 1233.
E-mail address: toth.pal@uni-miskolc.hu (P. Toth).

0304-3991/$ - see front matter Published by Elsevier B.V.
http://dx.doi.org/10.1016/j.ultramic.2013.02.017

10^1 nm) and the scale of atomic layers (which are usually considered to be graphene layers—the characteristic lengths are on the order of 10^0 nm, while their separation distance is around 3×10^{-1} nm) [26,27]. The biggest bottleneck for analysis at either of these scales is the number of images available from a particular sample—depending on the extent of heterogeneity of a structure, hundreds or even thousands of images may be necessary for reliable quantification. A system that can locate relevant features at the mentioned three scales and automate image generation will be discussed in this paper.

2. Materials and methods

In this section a general overview is given of the image processing methodology that was used to pinpoint regions of interest (ROIs) in the obtained images. The origins of the soot samples that were used to produce the experimental results are also discussed here.

2.1. Nomenclature

For ease of understanding, a number of definitions will be used throughout this paper. These definitions are explained here.

Image The term 'image' in this context means a digital grayscale image. A digital image is a scalar matrix obtained by the spatial sampling and quantization of an analog signal. In this case, the analogous signal is the two-dimensional (2D) field strength map formed in the focal plane of the imaging assembly in the HRTEM. In this study, the Gatan Digital Micrograph format (DM3) was used.

Pixel Each entry in the image matrix is called a picture element or pixel. Each pixel represents a sampled region of space. The dimensions of this region depend mainly on the applied magnification. Each pixel has a scalar assigned to it—this scalar is quantized (can only take discrete values) and is called an *intensity* value. In the case of DM3 images, being a 16-bit format, intensity values can be whole numbers ranging between 0 to 65,536. The intensity values can be considered as the third dimension of image data; i.e., an image can be portrayed as a surface.

Image neighborhood In this context, an image neighborhood is a square-shaped subimage in an image. By definition, a ROI is an image neighborhood as well.

Image feature An image feature is a subset of pixels in an image. These pixels are grouped so that the subset they form maximizes some local parameter, which we call a *feature descriptor*. Feature descriptors can be of geometric, topological or statistical nature. An image feature is not necessarily a connected component [28,29] in an image. Features can be best detected by detectors that work at the characteristic spatial scale of the features to be detected—this characteristic scale is called the *feature scale*.

Feature detection Features can be found in an image by extracting a scalar matrix from the image in which the value of each entry is correlated with the probability of the pixel's membership to a feature. Usually the higher the scalar value is, the more probable the membership is. If the values in this scalar matrix have no absolute physical meaning (i.e., they are arbitrarily scaled), the scalar matrix is also called a *saliency map*. Features can be detected in many ways. In this paper we mostly deal with morphological detectors [28], thus the saliency maps are extracted by using specially designed 2D *filters*.

Drive The operation in which ROIs are pinpointed based on saliency maps is called drive.

From image acquisition, through saliency map extraction to the final drive step, we refer to this whole process as the decision making procedure.

2.2. The decision making procedure

In general, the decision making procedure needs to be fine-tailored to specific applications. In these applications, the factors that most strongly determine how the decision making procedure has to be set up are the morphology of the samples and the properties of sample holder grids.

In the TEM analysis of soot and aggregate particulate structures, there are two different types of support structures on the same sample holder grid: an irregularly shaped lacey carbon grid and a rectangular metal grid that supports the lacey carbon (navigating over the metallic grids can be done simply by using random sampled ROIs [7]). The particles are deposited onto the lacey film and the best spots for imaging their nanostructure are the locations where they hang over the holes in the lacey carbon grid. Since the aggregate structures have some extent of elasticity, they can behave as pendulums, developing a significant swinging motion. This swinging is more serious further away from the points where the aggregate ends attach to the grid and it degrades the quality of the micrographs by introducing motion blur. Thus the best locations can be defined as: *locations where an aggregate hangs over a hole, but as close as possible to the grid*. Note that this definition is specific to aggregate soot samples deposited on lacey carbon films. Based on the definitions given in Section 2.1, the lacey grid is an image feature—a priori information regarding the properties and dimensions of the lacey carbon grid helps with setting up its feature detector.

Soot aggregates consist of spherical particles with diameters on the order of 10^1 nm, called spherules [27], thus the individual spherules can be detected by looking for spherical image features. There are many different methods of locating spherical structures in an image: one can use convolution- or correlation-based detection, morphological operators, intensity gradient information [30] or the Hough transform [31]. The scalar values returned by these operations are correlated to how similar a local image neighborhood is to a spherical surface. All the mentioned operators require a specified feature scale—in the case of detecting soot spherules, this scale is connected to the diameter of the spherules, thus a priori information regarding spherule sizes is needed to set up the feature detectors.

At the very scale of atoms, all carbon structures look similar. Phase contrast imaging allows for the visualization of layers of graphene, which appear as repeating dark and bright line segments, also called fringes. The ultimate objective of the methodology presented here is to produce many micrographs at the highest magnification, containing structures only from the sample—in this case from the soot, not from the lacey grid. Since the grid is also made of carbon and the atoms that make up the grid look the same as the atoms of the soot, other parameters are needed to differentiate the two. The parameters used in this work are the nematic and polar symmetry parameters. The detailed meaning and computation of these parameters are described elsewhere [23,32]. Briefly, maps of fringe orientations are computed by using so-called steerable filters [33] and the orientation maps are filtered further by specially designed filters. This filtering process returns the polar and nematic symmetry

parameters—the polar symmetry parameter is the highest in the centers of concentric fringe patterns, while the nematic symmetry parameter has the highest values at locations where the fringes are long and parallel to each other. High values of these symmetry parameters correspond to two of the equilibrium structures of carbon–graphitic (nematic) [26] and core–shell (polar) [34,35]. Both symmetry parameters are low at locations where no apparent symmetry is present—which is characteristic of the lacey grid material. Therefore, the saliency maps for finding high-magnification ROIs are the maps of the symmetry parameters, in which high values imply the presence of soot structure.

The choice for the nematic and polar symmetry as spherule-scale saliency is further justified by the nature of typical structural measurements in soot. There are two general types of structural parameters: the geometric properties of fringes (length, curvature and spacing [20,24]) and larger-scale symmetry parameters [23]. Since the parameters belonging to the former group can only be accurately measured in regions that contain well-defined fringes, one should use nematic symmetry saliency in order to locate these regions when the quantification of fringe geometry is the objective. Parameters that belong to the latter group can be the most efficiently quantified in micrographs that contain whole primary particles. Since soot spherules typically have an amorphous core in their center, it is practical to center ROIs around these cores—the polar symmetry saliency map should therefore be used to locate these ROIs. Polar symmetry at the spherule-scale should be used when measuring intensive properties, like apparent crystallinity as well.

Once the saliency maps are obtained, simple algorithms can be used to identify the most salient ROIs and the HRTEM can be driven to those locations. Drive is always a top-down process; i.e., it proceeds from lower magnifications toward higher ones. If the saliency maps are defined and computed properly, the extracted ROIs contain only soot structures. The drive step can be done in different ways—one can visit peaks in the saliency map in an arbitrary order, but it is also possible to return the neighborhoods with the highest mean saliency. The drive step typically returns many ROIs—these can be visited one by one by repeatedly recalling the original field in which they were identified.

The decision making procedure is summarized in Fig. 1.

2.3. Implementation

The scheme outlined in Section 2.2 was implemented in Matlab (Mathworks Inc.) and compiled into a standalone executable application with a graphical interface. The software can load the DM3 format and extract the sensor data and resolution. A number of pre-processing routines were also implemented. The application was designed so that it contained a wide array of different feature detectors and any combinations (additive or multiplicative) of these could be used to compute saliency maps. Feature detection was implemented in a multiscale framework. In a multiscale approach, a range of feature scales can be used to compute saliency values and a conjugate saliency map is extracted based on the responses at each feature scale. The drive operation was implemented as simple peak search (ROIs centered around salient peaks) or neighborhood search (ROIs had the highest average saliency). Table 1 summarizes the capabilities of the software.

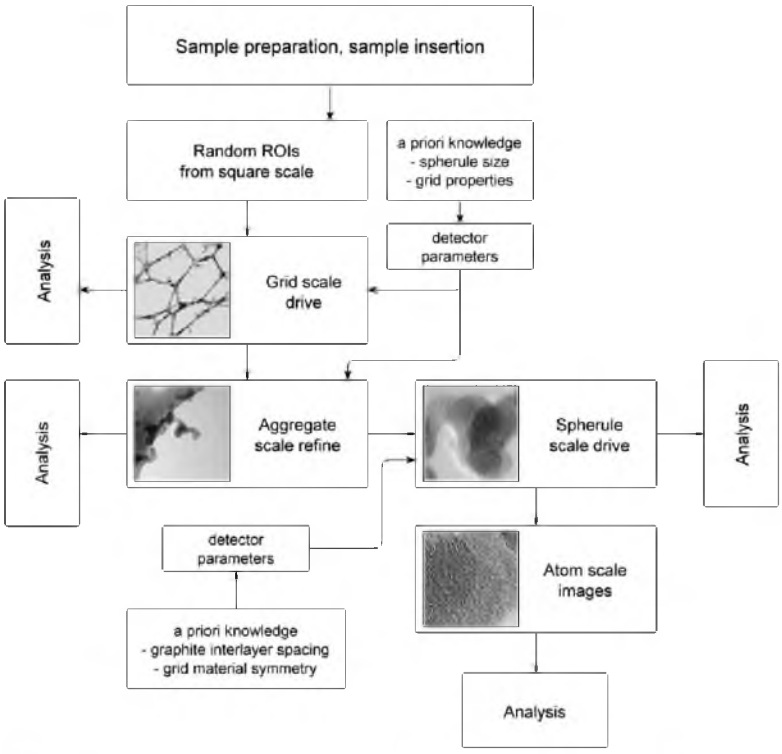

Fig. 1. Schematic of the decision making routine. It is assumed that available software is used to get to the square scale. Analysis can be performed at every distinct scale.

Table 1
Main features of the automation software.

Step	Magnification	Capability
Pre-processing	All	Anisotropic diffusion [36], low-pass filtering [30] Adaptive histogram equalization [37]
Saliency measures	Low-mag	Intensity, gradient [30], divergence [30], entropy [30], variance [30] bottom hat [30], top hat [30], cross-correlation [30], frequency [38]
	High-mag	Polar symmetry [32], nematic symmetry [32]
Drive options	All	Peak detection, peak detection (visit each) Most salient neighborhood, most salient neighborhood (visit each)

For filtering-type feature detectors, the Gaussian function was used as a kernel. For cross-correlation, morphology and template matching type detectors, a spherical surface was used as a template—it was assumed that the intensity surfaces of spherules closely resemble spherical surfaces. Since a multiscale approach was used, the scales of the Gaussian kernels were matched with the scales of the spherical templates—equal energy filtering dictates that $\sigma_G = 3^{-0.5}\sigma_S^{1.5}$, where σ_G and σ_S are the scales of the Gaussian and spherical kernels, respectively. Conjugate saliency maps were generated by keeping the highest responses of the detectors over a scale range, corresponding to the range of expected spherule sizes.

Four different drive schemes were implemented. Peak detection centers ROIs around local maxima in the saliency maps—overlapping ROIs can be accepted (visit each) or rejected by iteratively removing subsets from the saliency maps as the peaks are visited in a descending order of their saliency values. The same concept can be applied to ROIs that maximize the average saliency within them. The average saliency was computed by convolving the saliency maps with a box filter, the size of which matched the ROI size [30]. The ROI size was determined by the ratio of the current and forthcoming magnifications.

2.4. Experiments

A FEI Tecnai F30 HRTEM was used for the experimental evaluation of the automation concept. The operating voltage was 300 kV. Low magnification images (below 230kX magnification) were taken with a large objective aperture and underfocused (Fresnel contrast—bright field imaging). Bright field conditions were used to improve the contrast between the background and absorbing media. For images with magnifications higher than 230kX, the aperture was taken out and overfocused, phase contrast conditions were used to improve fringe contrast. The images were recorded by using a 1 MPixel Gatan Multiscan CCD sensor (Model 794). The highest magnification used was 800kX.

Sample preparation, stage positioning, image shifting and focusing were done manually by the operator, based on the decisions the automation software produced. The decision making and recalling previously visited ROIs happened automatically. Two computers were used in the experiments: one connected to the HRTEM, running the microscope software and one running the automation software. The two computers were communicating via the USB port.

2.5. Sampling and sample preparation

Soot samples were derived from a surrogate fuel consisting of 10 vol% m-xylene and 90 vol% n-dodecane. Samples were thermophoretically taken for HRTEM analysis. The fuel was burned in air in a flat flame premixed burner under fuel rich conditions [39]. This system consisted of a stainless steel chamber where fuel and air were properly mixed prior to entering the burner. The flame was stabilized over a tube bundle and shielded from atmospheric interference using a nitrogen shroud. A metallic mesh placed 3.5 cm above the burner surface distributed the flame uniformly across the burner. The fuel–air equivalence ratio was 2.1. The flame temperature was 1773 K. Details in the premixing systems are reported elsewhere [40].

Samples for HRTEM analysis were taken from a location 5 cm above the burner surface using a thermophoretic probe commonly referred to as a "frog tongue". A TEM grid holder was attached to a piston and compressed air at 500 kPa was used to quickly insert the TEM grid into the flame. Multiple insertions were necessary to get sufficient soot coverage on the grid. The grid was oriented with the face parallel to the gas flow, so the disturbance of the flame was minimal. Soot deposits on the grid because of the thermophoretic gradient between the cold grid and the hot flame, allowing "freezing" some heterogeneous reactions, avoiding changes in the soot morphology, quickly after the particles have impacted upon the cold surface [40,41].

3. Results and discussion

In this section, the general evaluation of the developed procedure is presented and the most successful route among the different feature combinations is described in detail. A set of HRTEM images were obtained using this route and those images are presented also, along with the performance evaluation of the method.

3.1. The evaluation of feature detectors

When using either bright field or mass thickness contrast, the absorbing grid material stands out from the background due to its different average intensity level—the grid is darker than the background. The distinct intensity characteristics of the grid can be used to detect it as a feature. A number of grid detection ideas were implemented in the automation software, but it was found that in most cases, using the intensity level alone produces acceptable results. When using intensity information, a simple binary thresholding routine can find the grid contours. The determination of the intensity threshold value was done by modeling background and grid intensity distributions as normal distributions. The bimodal Gaussian mixtures were fit to the intensity histograms by using direct search optimization [42]. The initial parameters of the normal distributions were computed by using k-means clustering [43]. The soot particles themselves appear as dark features and they are usually indistinguishable from the grid based on intensity alone. Thus after finding the rough outlines of the holes in the grid, their convex hulls were computed to cut off falsely detected particles. Fig. 2 demonstrates this process. This technique assumes that soot aggregates are not long enough to completely reach over holes—if this assumption fails, more sophisticated detectors must be used. Such detectors were implemented by using the local frequency feature descriptor to find grid holes, but were not needed during the experiments. This thresholding operation produced the 'binary grid image', which is a logical array that contains true values at identified holes and false values at the grid.

Soot aggregates can be found by using morphological operations, the intensity gradient or local intensity statistics. Using these methods, particles can be fairly well localized, thus locating the grid may seem redundant; however, the grid must be detected in order to pinpoint particles close to it, to reduce

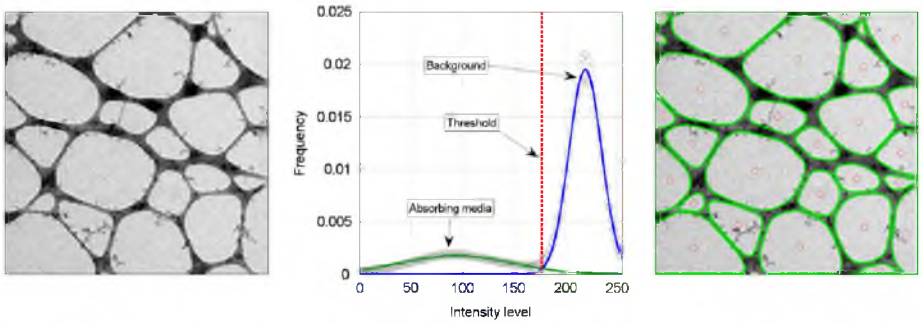

Fig. 2. The grid detection process. Left: Original grid scale micrograph (3900X). Middle: The intensity distribution of the micrograph (circles) and the fit normal distribution (continuous lines). Note that the micrographs were converted to an 8-bit format by the automation software to speed up processing. The dashed line denotes the threshold value, set to be at the intersection of the two modes. Right: Result of thresholding. The circles denote hole centers, the continuous lines denote the grid contour.

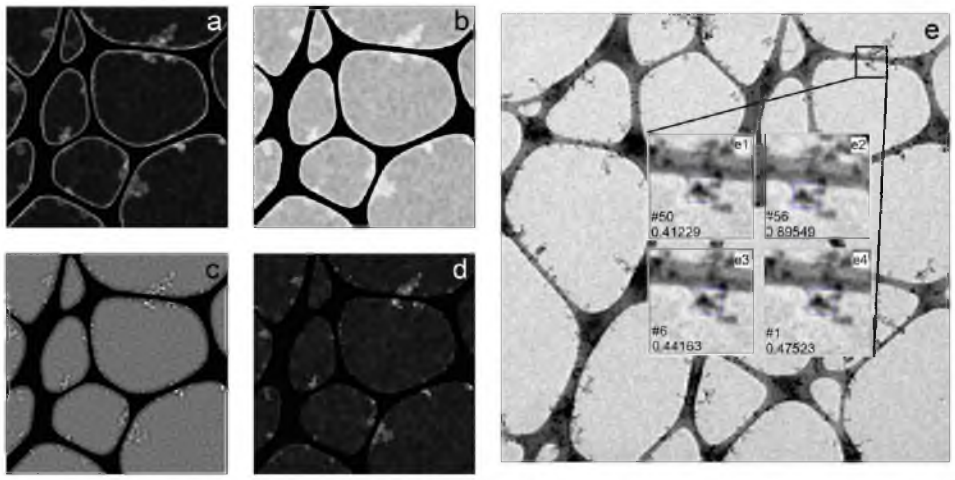

Fig. 3. Saliency maps computed by four different feature detectors and ROI ranking. (a) Local intensity variance, (b) local entropy, (c) intensity divergence, and (d) morphology (the difference of the top hat and bottom hat transforms). The shades of gray denote the saliency value: black is 0 and white is 1. The maps were extracted from the low-mag image shown in Fig. 2. Note that the saliency at pixels corresponding to the grid was set to 0 in order to exclude the grid material from the drive process. The bright areas indicate particle aggregates. (e) ROI ranking. The insets show the results for practically the same ROI (denoted by the black square in the low-mag image) produced by the variance detector (e1), the entropy detector (e2), the divergence detector (e3) and the morphological detector (e4). The sequential numbers denote the placings of the ROIs as proposed by the corresponding detectors and the fractional numbers denote the overall saliency strengths of the ROIs. Note that it is not possible to compare the saliency measures directly to each other, as the distribution of the saliency values in their saliency maps determines the ordering, not the absolute values. The insets show the coarse ROIs and the blue squares inside them indicate the refined decisions (see Fig. 1).

blurring from particle motion (see Section 2.2). Locations close to the grid were found by computing and thresholding the binary distance transform [44] of the binary grid image. The distance threshold was set to be $\sqrt{2}w$, where w denotes the size of the ROIs corresponding to the forthcoming magnification level—this means that locations were included in the ROIs that were not further away from the grid than the diagonal of the ROIs. For the balance of this paper, the thresholded distance transformation of the binary grid image is referred to as the 'grid distance map'.

Different feature detectors respond differently to neighborhoods that contain spherule images. Many feature detectors had been tested in a preliminary study before starting the experiments. Fig. 3a–d demonstrates the differences in the responses of selected feature detectors. When selecting feature descriptors for computing saliency maps, one needs to optimize for the reliability (signal to noise ratio) and localization of saliency. Ideally, the saliency maps contain 1 values at pixels that belong to a feature and 0 values elsewhere.

Once the saliency maps are defined and computed, the drive module of the automation logic defines ROIs that contain the most promising structures. The order of visiting ROIs depends on the value of their overall saliency. We found that a number of feature detectors produce the same ROIs, but in a different order. An example of this is shown in Fig. 3e. To select the best feature detector for detecting soot spherules, a test was conducted in which individuals had been asked to sort a number of proposed ROIs in the order that seemed the most logical to them. These subjective results were then compared to the results of different combinations of feature detectors. It was found that the multiplicative combination (intersection) of the morphological and divergence detectors gave the closest results to those of the human operators. We refer to this combination as the 'particle morphology map'. In the grid scale drive step, the peak detection option was chosen to define the coarse ROIs and within each coarse ROI, the decision was refined by using the maximum

overall saliency option. Note that this step covers three magnification levels—from the lowest (3900X was used in the experiments) to the second highest (310kX), through an intermediate (59kX) magnification.

The spherule scale drive step included the specification of either polar or nematic mode. In polar mode, the automation was looking for core–shell structures, that are characteristic to soot; in nematic mode, ROIs were found which contained many parallel fringes. The extent of symmetry in these sub-structures is strongly correlated with the extent of ordering of the soot structure, which affects its physical, chemical and optical properties. Fig. 4 shows examples of saliency maps obtained by using the polar and nematic symmetry parameters. The final, atomic scale ROIs were identified by the peak detection (visit each) drive option.

3.2. The evaluation of decision making

The efficiency of the decision making procedure was evaluated by conducting experiments with real samples (see Section 2.4). In this section the mechanisms of the low-magnification and high-magnification drive procedures are discussed in detail, along with the presentation of the acquired images.

Fig. 5 illustrates the detailed mechanism of the grid scale drive procedure. First, the overall saliency map is computed as the intersection of the binary grid image (to cut off the grid itself), the particle morphology map and the grid distance map (see Section 3.1). This aggregate saliency map pinpoints spherical image features that hang over holes, but are close to the grid (notice in Fig. 5, that saliency is zero far away from the grid). The aggregate scale ROIs are found by the salient peak detection routine. Refined ROIs at 310kX magnification are also computed in this step—they are identified by using the same saliency map, but by finding the most salient neighborhood around the coarse peak. This refinement process also served to help the operator to find the 310kX ROIs during the tests.

The efficiency and accuracy of the grid scale drive was first tested without the aggregate scale refinement. This low-level procedure is useful for quickly obtaining massive image sets for aggregate sizing. The grid scale was fixed at 3900X magnification and the grid scale drive process identified aggregate scale ROIs at 59kX magnification. Fig. 6 shows example results of grid scale drive.

Note that the resulting magnified ROIs also contain the grid structure. While having the grid in the images hinders aggregate sizing algorithms, it is possible to subtract it by using the binary grid image computed as part of the saliency map (see Fig. 2). The grid coordinates are known at 3900X magnification–using this information the grid can be closely approximated at 59kX magnification by using interpolation techniques. Thus ultimately the ROIs obtained by the unrefined grid scale drive process contain only the aggregate structures that hang over holes.

Fig. 7 demonstrates the mechanism of the high-magnification drive process. By high-magnification, we refer to magnification levels at which the graphene layers are visible. Since the ultimate objective of HRTEM imaging is to measure the structure of materials at the scale of atoms, whenever the carbon fringes are visible, one should use the information contained in them to further refine ROIs and drive the HRTEM. Fig. 7 demonstrates the two operating modes of the high-magnification drive procedure: drive by using the nematic or polar saliency maps.

In the next step, the top-down approach spanning over a magnification range of 59kX (aggregate scale)–800kX (atom scale) was tested. The refinement step was done at 310kX (spherule scale). The test started at 3900X magnification and resulted in images down to 800kX magnification. Note that the high-magnification drive process that was implemented in the automation software can work in different modes when identifying high-magnification ROIs: it can either look for the nematic or polar phases. Alternately, a combined saliency map can be computed, with which the automation defines ROIs that have the most overall symmetry; or, it is possible to look for the amorphous phase by inverting the combined saliency map. Results obtained by the "look for nematic" and "look for polar" modes are presented here. Fig. 8 demonstrates the whole top-down decision making procedure.

Due to the characteristics of the optical assembly in typical HRTEMs, only discrete magnification levels are possible to obtain; furthermore, the acquired images can rotate relative to the stage orientation when changing magnification levels. This phenomenon is especially noticeable when going from 310kX magnification to 800kX—the rotation is approximately 45°. This behavior, however, appears systematically and the transitions where the image orientation changes are known a priori; therefore, the automation software can correct for it. Note that in Fig. 8 the raw (uncorrected) results are shown.

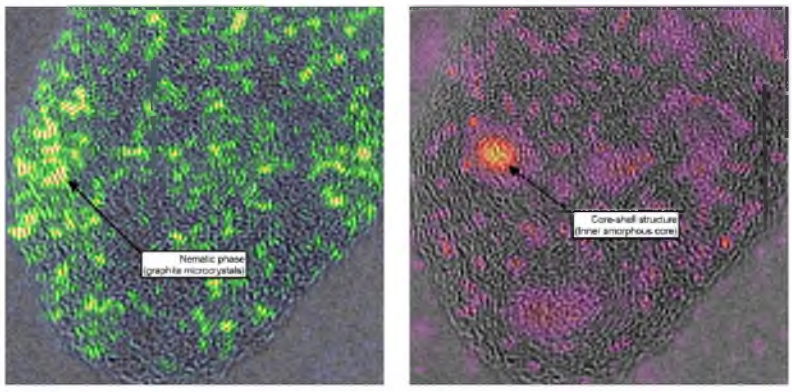

Fig. 4. Examples of spherule scale (310kX) saliency maps. Left: Nematic symmetry saliency map overlaid on the original micrograph (hues from green to yellow indicate increasing saliency strength). Right: Polar symmetry saliency map overlaid on the original micrograph (hues from red to yellow indicate increasing saliency strength). Each symmetry type denotes a particular sub-structure: graphitic microcrystals (nematic) and core–shell structures (polar). (For interpretation of the references to color in this figure caption, the reader is referred to the web version of this article.

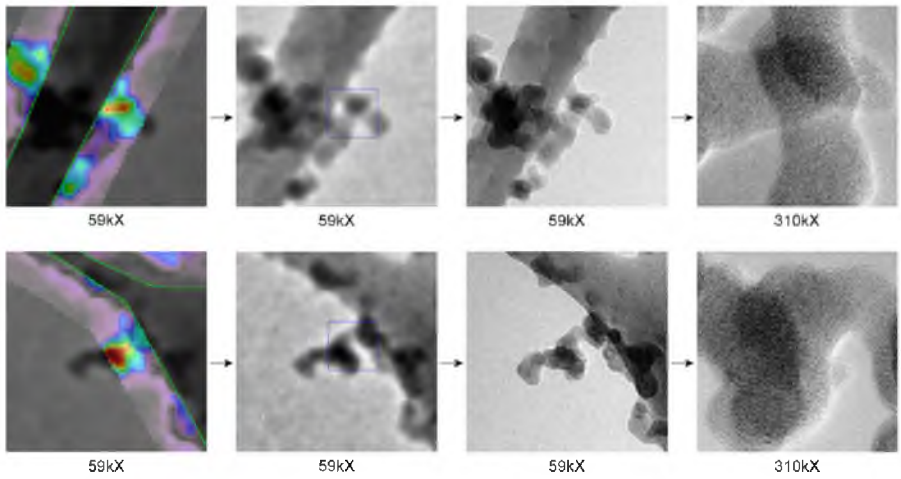

Fig. 5. An illustration of the grid scale drive procedure by two examples. The rows show two different examples. In the columns, from left to right: the computed saliency map overlaid on the original image (colors indicate saliency values—from blue through green to red); the identified ROI as a detail in the original image (the blue rectangle indicates the refined ROI); the identified ROI obtained at its native magnification; the refined ROI at the spherule scale. (For interpretation of the references to color in this figure caption, the reader is referred to the web version of this article.)

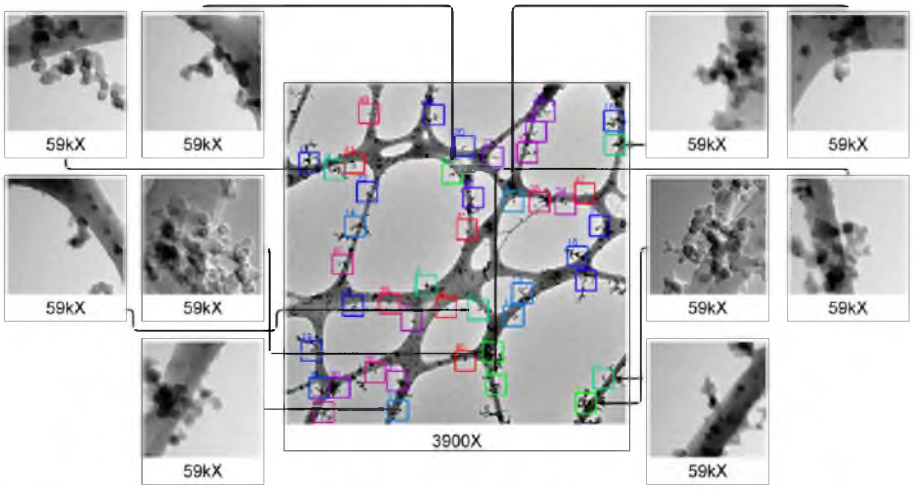

Fig. 6. The grid scale drive process can be used to quickly identify massive numbers of ROIs containing aggregate structures. The ROIs are indicated by colored squares–their numbers show their ranking. The colors indicate the ROI "qualities"; i.e., their overall saliency strength. The qualities decrease as colors go from green through blue to red. The first 10 identified ROI is shown at 59kX magnification as well. Note: ROI # 6 was skipped, due to the disappearance of the spherule inside it (soot structures can move and slightly change under electron beams). (For interpretation of the references to color in this figure caption, the reader is referred to the web version of this article.)

3.3. *Performance*

Overall, the accuracy of the method was found to be very high. The grid scale drive routine was tested with about a dozen low-magnification micrographs. Among the first 10 most salient aggregate scale ROIs, there were usually no false detections. It was found that even when the assumptions of the grid detection routine (see Fig. 2) fail, similarly accurate results can be obtained by using the frequency-based grid detector—the only difference is that the frequency-based detector tends to find less ROIs, than the intensity-based one.

If the aggregate scale decisions of the low-magnification drive step are correct, the high-magnification drive process very rarely gives incorrect results. This is due to the nature of the implemented high-magnification detection method: since it is a correlation-based technique, it only produces reasonable decisions when the fringes are clearly visible—if not, it returns a "reject" decision and the automation moves to the next aggregate scale ROI.

The electron beam can change the imaged sample when too much time is spent at a particular field. In the case of soot, the aggregates can move and vibrate due to the external

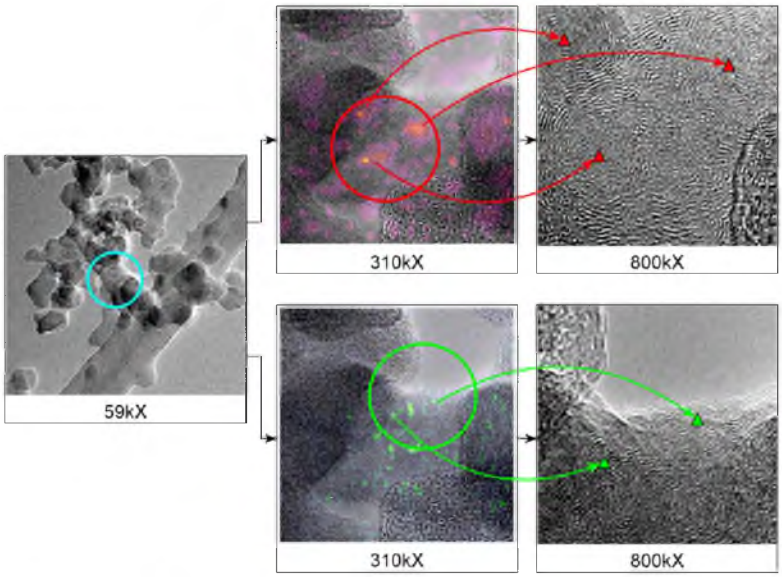

Fig. 7. An illustration of the high-magnification drive procedure. Left: Aggregate scale ROI. Top middle: Spherule scale ROI with the polar saliency map overlaid. Hues from red to yellow indicate the strength of polar symmetry. Top right: Final, high-magnification image. Triangles indicate the salient peaks corresponding to core–shell structures. Bottom middle: Spherule scale ROI with the nematic saliency map overlaid. Hues from green to yellow indicate the strength of nematic symmetry. Bottom right: Final, high-magnification image. Triangles indicate the salient peaks corresponding to graphite microcrystals. (For interpretation of the references to color in this figure caption, the reader is referred to the web version of this article.)

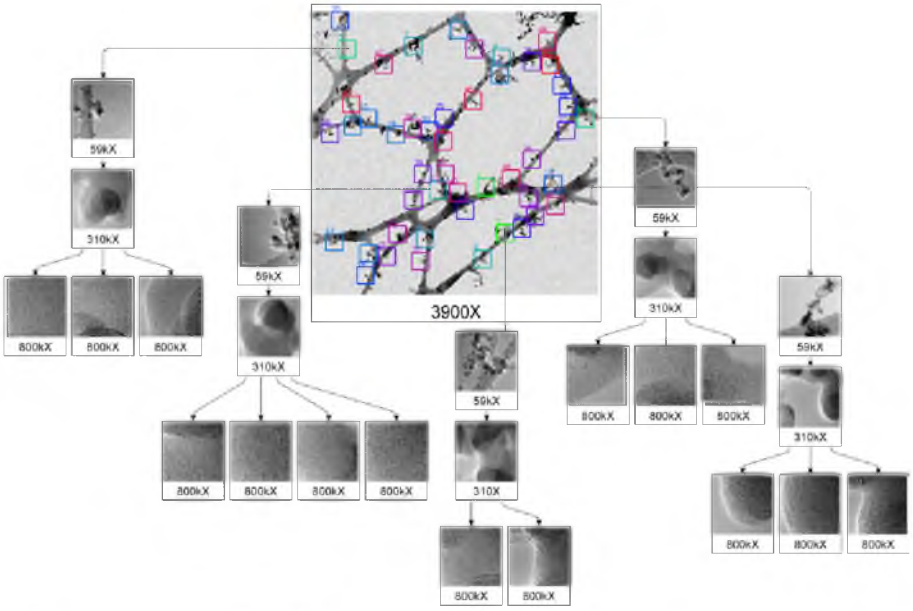

Fig. 8. A demonstration of the whole top-down decision making process. The procedure starts at 3900X and defines ROIs at 59kX. It then refines these ROIs by zooming in further to 310kX magnification. Graphene layers are visible at this scale, thus the algorithm proceeds by computing either the polar or nematic symmetry saliency maps and driving to 800kX by finding regions with strong symmetry. The first five identified aggregate scale ROIs are shown, along with their nested ROIs. Note that the HRTEM images can rotate at certain magnification levels—this is due to the characteristics of the imaging assembly.

electromagnetic force or the radiation can change the nanostructure of carbon as well. We encountered one case in which a previously detected spherule disappeared during the drive process—these cases can be automatically detected by recomputing the saliency maps before the aggregate scale refinement step, and "reject" decisions can be returned to the main automation.

With manual stage positioning, we were able to produce around 20 high-magnification micrographs per hour. When using robotic positioning and automatic focusing, the upper limit of this rate only depends on the capabilities of the applied robotics, which, in the worst case are comparable to those of human operators [6]. A similar previous study [6] identified the decision making procedure as the bottleneck of automated processing. In this work, we demonstrated that the computations required for decision making are relatively simple and they can be done in real-time by utilizing a dedicated CPU or an on-board graphical processing unit (GPU)—thus the decision making is practically instantaneous. Speed is a definite advantage of the method, which further helps with minimizing the extent of sample transformation under the electron beam.

The applicability of the method for other types of samples was not tested. It is generally expected though, that the concept works for all kind of materials that develop relatively simple large scale symmetries (i.e., the spherical aggregate structure of soot).

4. Conclusion

A method for the automation of decision making during the HRTEM analysis of an amorphous, particulate carbon material (soot) was developed. The concept of this method is based on visual saliency, the maps of which are computed by analyzing the digital micrographs acquired on-the-go. The proof of this concept is presented in this paper, including results from real samples. The merits of the method are the following:

1. It can increase the number of obtained micrographs per unit time. High numbers of carefully chosen and high quality micrographs are necessary for the reliable analysis and quantification of materials with heterogeneous structures.
2. By automating the decision making process during imaging, the need for human labor can be eliminated. Large datasets can be obtained without human supervision; however, setting up the method based on a priori information is still needed prior to measurements.
3. By reducing the time needed for decision making and thus the exposure time of the samples to radiation, samples are possibly better preserved under the electron beam. Better preserving samples results in better quality and more representative structural data.

Acknowledgments

The authors are thankful to Joseph Levinthal (University of Utah) for providing soot samples. This work was partially sponsored by the TAMOP-4.2.1.B-10/2/KONV-2010-0001 project with support by the European Union, co-financed by the European Social Fund.

References

[1] O. Charon, A.F. Sarofim, J.M. Beer, Distribution of mineral matter in pulverized coal, Progress in Energy and Combustion Science 16 (4) (1990) 319–326.
[2] N. Keulen, M.T. Hutchison, D. Frei, Computer-controlled scanning electron microscopy: a fast and reliable tool for diamond prospecting, Journal of Geochemical Exploration 103 (2009) 1–5.
[3] R.A. Schwarzer, Automated crystal lattice orientation mapping using a computer-controlled SEM, Micron 28 (3) (1997) 249–265.
[4] V.V. Kindratenko, P.J.M.V. Espen, B.A. Treiger, R.E.V. Grieken, Fractal dimensional classification of aerosol particles by computer-controlled scanning electron microscopy, Environmental Science and Technology 28 (1994) 2197–2202.
[5] G.P. Huffman, N. Shah, N. Cprek, F.E. Huggins, G. Casuccio, E. Ramer, CCSEM investigation of respirable quartz in air samples collected during power plant maintenance activities, Fuel 95 (2012) 365–370.
[6] H. Minghui, M. Vink, C. Kim, K.D. Derr, J. Koss, K. D'amico, A. Cheng, J. Pulokas, I. Ubarratxena-Belandia, D. Stokes, Automated electron microscopy for evaluating two-dimensional crystallization of membrane proteins, Journal of Structural Biology 171 (1) (2010) 102–110.
[7] A. Cheng, A. Leung, D. Fellmann, J. Quispe, C. Suloway, J. Pulokas, Towards automated screening of two-dimensional crystals, Journal of Structural Biology 160 (2007) 324–331.
[8] T.H. Fletcher, J. Ma, J.R. Rigby, A.L. Brown, B.W. Webb, Soot in coal combustion systems, Progress in Energy and Combustion Science 23 (1997) 283–301.
[9] D.R. Tree, K.I. Svensson, Soot processes in compression ignition engines, Progress in Energy and Combustion Science 33 (2007) 272–309.
[10] A. Seaton, W. MacNee, K. Donaldson, D. Godden, Particulate air pollution and acute health effects, The Lancet 345 (1995) 176–178.
[11] U. Pöschl, Atmospheric aerosols: composition, transformation, climate and health effects, Angewandte Chemie International Edition 44 (2005) 7520–7540.
[12] V.R.G. Carmichael, Global and regional climate changes due to black carbon, Nature Geoscience 1 (2008) 221–227.
[13] B.S. Haynes, H.G. Wagner, Soot formation, Progress in Energy and Combustion Science 7 (4) (1981) 229–273.
[14] I.M. Kennedy, Models of soot formation and oxidation, Progress in Energy and Combustion Science 23 (1997) 95–132.
[15] H. Richter, J.B. Howard, Formation of polycyclic aromatic hydrocarbons and their growth to soot – a review of chemical reaction pathways, Progress in Energy and Combustion Science 26 (2000) 565–608.
[16] R.L.V. Wal, A.J. Tomasek, Soot oxidation: dependence upon initial nanostructure, Combustion and Flame 134 (1–2) (2003) 1–9.
[17] R.L.V. Wal, A.J. Tomasek, Soot oxidation: dependence upon synthesis conditions, Combustion and Flame 136 (1–2) (2004) 129–140.
[18] A.B. Palotas, L.C. Rainey, A.F. Sarofim, J.B.V. Sande, R.C. Flagan, Where did that soot come from? Chemtech 28 (7) (1998) 24–30.
[19] R.L.V. Wal, V.M. Bryg, M.D. Hays, Fingerprinting soot (towards source identification): physical structure and chemical composition, Aerosol Science 41 (2010) 108–117.
[20] A.B. Palotas, L.C. Rainey, C.J. Feldermann, A.F. Sarofim, J.B.V. Sande, Soot morphology: an application of image analysis in high-resolution transmission electron microscopy, Microscopy Research and Technique 33 (3) (1996) 266–278.
[21] A. Sharma, T. Kyotani, A. Tomita, A new quantitative approach for microstructural analysis of coal char using HRTEM images, Fuel 78 (1999) 1203–1212.
[22] T. Ishiguro, Y. Takatori, K. Akihama, Microstructure of diesel soot particles probed by electron microscopy: first observation of inner core and outer shell, Combustion and Flame 108 (1–2) (1997) 231–234.
[23] H.S. Shim, R.H. Hurt, N.Y.C. Yang, A methodology for analysis of 002 lattice fringe images and its application to combustion-derived carbons, Carbon 38 (2000) 29–45.
[24] K. Yehliu, L.R.V. Wal, A.L. Boehman, Development of an HRTEM image analysis method to quantify carbon nanostructure, Combustion and Flame 158 (2011) 1837–1851.
[25] P. Toth, A.B. Palotas, J. Lighty, C.A. Echavarria, Quantitative differentiation of poorly ordered soot nanostructures: a semi-empirical approach, Fuel 99 (2012) 1–8.
[26] P. Delhaes, Graphite and Precursors, 1st Ed, Gordon and Breach Science Publishers, Amsterdam, 2001.
[27] W. Merchan-Merchan, S.G. Sanmiguel, S. McCollam, Analysis of soot particles derived from biodiesel and diesel fuel air-flames, Fuel 102 (2012) 525–535.
[28] W. Pratt, Digital Image Processing, Wiley, New York, 2001.
[29] G.F. Simmons, Introduction to Topology and Modern Analysis, McGraw-Hill Education, 2004.
[30] R.C. Gonzalez, R.E. Woods, Digital Image Processing, 2nd Ed, Prentice Hall, 2001.
[31] I. Grishin, K. Thomson, F. Migliorini, J.J. Sloan, Application of the Hough transform for the automatic determination of soot aggregate morphology, Applied Optics 51 (5) (2012) 610–620.
[32] P. Toth, A.B. Palotas, E.G. Eddings, R.T. Whitaker, J.S. Lighty, A novel framework for the quantitative analysis of high resolution transmission electron micrographs of soot II. – robust multiscale nanostructure quantification. (Combustion and Flame. In review), http://dx.doi.org/10.1016/j.combustflame.2013.01.003.
[33] T.W. Freeman, E.H. Adelson, The design and use of steerable filters, IEEE Transaction on Pattern Analysis and Machine Intelligence 13 (9) (1991) 906–981.

[34] J. Song, M. Alam, A.L. Boehman, U. Kim, Examination of the oxidation behavior of biodiesel soot, Combustion and Flame 146 (2006) 589–604.
[35] T. Ishiguro, Y. Takatori, K. Akihama, Microstructure of diesel soot particles probed by electron microscopy: first observation of inner core and outer shell, Combustion and Flame 108 (1–2) (1997) 231–234.
[36] P. Perona, J. Malik, Scale-space and edge detection using anisotropic diffusion, in: Proceedings of IEEE Computer Society Workshop on Computer Vision, IEEE, 1987, pp. 16–22.
[37] K. Zuiderveld, Contrast limited adaptive histogram equalization, in: Graphics Gems IV, Academic Press Professional Inc., 1994, pp. 474–485.
[38] P. Kovesi, Image features from phase congruency, Videre: A Journal of Computer Vision Research 1(3).
[39] C.A. Echavarria, A.F. Sarofim, J.S. Lighty, A. D'Anna, Modeling and measurements of size distributions in premixed ethylene and benzene flames, Proceedings of the Combustion Institute 32 (2009) 705–711.
[40] C.A. Echavarria, Evolution of Soot Size Distribution During Soot Formation and Soot Oxidation-Fragmentation in Premixed Flames: Experimental and Modeling Study, Ph.D. Thesis, University of Utah, 2010.
[41] R.A. Dobbins, C.M. Megaridis, Morphology of flame-generated soot as determined by thermophoretic sampling, Langmuir 3 (1987) 254–259.
[42] J.C. Lagarias, J.A. Reeds, M.H. Wright, P.E. Wright, Convergence properties of the nelder-mead simplex method in low dimensions, SIAM Journal of Optimization 9 (1) (1998) 112–147.
[43] H. Spath, Cluster Dissection and Analysis: Theory, FORTRAN Programs, Examples, Prentice Hall, 1985.
[44] D. Paglieroni, Distance transforms: properties and machine vision applications, Computer Vision, Graphics, and Image Processing: Graphical Models and Image Processing 54 (1) (1992) 57–58.

CHAPTER 6

DETAILED INVESTIGATION OF SOOT NANOSTRUCTURE: EFFECT OF PRESSURE

6.1 Abstract

Soot nanostructure has an effect on soot reactivity and therefore may be included in intrinsic oxidation kinetic models. Diesel and jet engines often operate at elevated pressures, thus the investigation of the effect of pressure on soot nanostructure may contribute to the understanding of real-world systems as well. In this paper soot nanostructure is investigated and the effects of the pressure of the oxidizing environment are identified. The analyzed soot was generated in premixed flames of liquid fuels: n-dodecane, m-xylene, and n-butanol and oxidized under elevated pressures. Nanostructure is described via differentiating between the isotropic and nematic phases of soot particles. These phases are characterized by the polar and nematic order parameters. Along with the order parameters, the nematic phase is further characterized by graphene layer spacing and length. The structural parameters were measured by utilizing high-resolution electron microscopy and digital image analysis. The image analysis framework used in this paper is a recent development, which provided us with high-fidelity structural data. This refined methodology made drawing our conclusions possible. A significant effect of pressure was observed on soot nanostructure—increasing pressure reduced interlayer spacing and increased the average length of layers. The isotropic particle cores grew as pressure was increased. The observations regarding graphene layer odering were interpreted via the thermodynamic model of Hurt et al. Reasonable consistency was found between experimental and numerical results—which drove us to the conclusion that soot nanostructure can possibly be accurately predicted by models and the predicted nanostructure can be used to derive intrinsic kinetic parameters.

6.2 Introduction

Soot is a product of the pyrolysis of carbonaceous materials and is generally considered as amorphous carbon [1]. Despite being amorphous, in most cases soot nanostructures show some degree of crystalline order typically in the form of graphite microcrystals (mesophasic crystalline units or clusters exhibiting short-range order in the form of parallel graphene layers, also called 'stacks'), partial fullerenic (graphene layers in a concentrically symmetric, 'onion-like' structure), or partial graphitic (longer range parallelity of layers) order [2–5]. Soot particles are composed of amorphous and crystalline fractions. For the balance of this paper, the amorphous fraction is referred to as the "isotropic phase" and the crystalline fraction is called "nematic phase." Soot nanostructure is affected by the thermal environment and combustion conditions [3] and also by the combusted fuel type—different fuels may produce different nanostructures [5–7].

The importance of soot nanostructure can be summarized as follows. Current soot models account for nucleation, growth, coagulation, and oxidation processes [8–10], among which all except the first are affected by the molecular structure of soot—either through the density and distribution of active surface sites determining the rate of chemical processes [11, 12] or via affecting van der Waals forces and therefore physical interactions [13, 14]. Experiments demonstrated [15] that the rate of surface growth is not exclusively determined by surface area, which further supports the importance of the arrangement of surface sites. Similarly, discrepancies exist between observed oxidation rates [2] and the rates predicted by the Nagle-Strickland-Constable equation [16], which is applicable to describe the high-temperature oxidation of carbon blacks—these discrepancies are possibly caused by peculiarities of soot structure.

Hurt et al. showed that soot nanostructure can be qualitatively modeled by thermodynamic principles [17]. Their model described the typical core-shell nanostructure [5] as an equilibrium arrangement between the competing isotropic-nematic transformation and the free energy contribution of the splay deformation of graphene layers. They argued that the core-shell structure is a configuration that is simultaneously optimal for layer growth and aromatization and the Van der Waals forces acting between layers. According to their model, the equilibrium diameter of the isotropic core is affected by the splay deformation constant, the free energy change of the isotropic-nematic transformation, and properties of the nematic phase—molecular weight and density.

The quantities of interest in the model of Hurt et al. can be estimated by analyzing the high-resolution electron micrographs (HRTEM) of soot. In HRTEM images, individual

graphene layers are made visible by phase-contrast imaging. Since typical HRTEM images contain hundreds of imaged graphene layers, in most practical cases, their representative and accurate characterization can only be carried out by using automated digital image analysis. Many automatic [18–20] and semi-automatic [21] algorithms are known that can extract structural information characterizing graphene lamellae and their arrangement. It was pointed out [22] that the heaviest drawback of these algorithms is the usage of subjectively set parameters in the implementations of image processing techniques and the sensitivity of the obtained results to these parameters. Recently, we addressed this issue and developed a novel image analysis framework by which the robust extraction of representative structural information is possible [23, 24]. If such robust techniques are available—despite being a two-dimensional technique [25]—HRTEM analysis can provide results that are consistent with X-ray diffractometry [26, 27].

Although practical combustion systems either for energy generation or transportation often operate at elevated pressures, there is a general lack of models describing the effects of elevated pressure on soot nanostructure [28]. Also, observations regarding the structure of soot as a function of the pressure of the oxidizing environment have not been reported before. In this study, we present results of HRTEM observations of the effect of pressure on soot nanostructure.

6.3 Materials and methods

In this section the conditions and equipment used for soot generation, oxidation, and characterization are discussed. For the reader's convenience, a brief overview is given on the recently developed image analysis framework and the meaning and significance of the extracted structural parameters.

6.3.1 Soot generation

A premixed burner was used to create the soot samples from different liquid fuels. The soot was generated in a flat-flame, premixed burner under heavily sooting conditions and captured on a water-cooled stabilization plate that was located 50 mm above the burner surface.

The burner system consisted of a stainless steel chamber (50 mm inner diameter, Schedule 80, 127 mm long), where fuel and air were injected and mixed prior to entering the burner. The flame was stabilized over a tube bundle (1.578 mm inner diameter, 31.75 mm long) through which the mixture passed in laminar flow. A nitrogen shroud was utilized to shield the premixed flame from atmospheric interference. Air and the liquid mixture

were fed to the burner using a commercial vaporizer (Mesoscopic Devices Inc.) coupled to a syringe pump and temperature control system. The vaporizer allowed for effective fuel vaporization before being mixed with the air.

The temperature in the vaporizer was controlled depending on the fuel used, and the compositions of the fuel fed and vaporized fuel were analyzed by using gas chromatography to verify the performance of the vaporizer. The objective was to vaporize and deliver the mixture without distilling it. The vaporized fuel was trapped into a cold dichloromethane trap.

Soot was generated from n-dodecane, m-xylene, and n-butanol. The soot generated was collected on the stabilization plate and then crushed into a powder. Flame temperatures were measured using a type-B thermocouple (wire diameter 0.02032 mm) at 50 mm above the burner surface, which corresponded to the distance where the soot is collected. The temperatures were corrected by radiation effects. Table 6.1 summarizes the conditions for each flame studied.

6.3.2 Soot oxidation

A high-pressure thermogravimetric analyzer (HTGA), type Cahn TherMax 500, was used to oxidize soot under controlled pressurized conditions. All tests were performed isothermally. 10 mg soot were placed in a quartz crucible (18 mm diameter and 20 mm height). The crucible was suspended from a ceramic coil attached to a microbalance. The furnace and balance were purged with nitrogen prior to each experiment. An inert material (silicon-carbide beads) was used in all of the runs to minimize thermal and mass transfer effects by decreasing the stagnant atmosphere between the surface of the soot and the entrance of the container. Isothermal tests were performed at 575 ^{o}C. A heating rate of 10 K/min was used to reach the oxidation temperature in nitrogen. Nitrogen flowed at 0.55 l/min through the microbalance to protect it. The oxidizer, a mixture of oxygen and nitrogen, flowed at 1 l/min. Mass data were recorded approximately every second, and the experiments were terminated when the mass loss surpassed 50%. After termination, the

Table 6.1: Experimental conditions for soot generation

Fuel	Equivalence ratio	C/O ratio	Velocity, cm/s	Flame temperature, K
n-dodecane	1.7	0.65	4.6	1705
m-xylene	2.15	0.7	4.6	1725
n-butanol	2.8	1.21	4.3	1723

samples were quenched in nitrogen at 20 K/min. Soot was oxidized under different pressures to study the effect of pressure on the soot nanostructure. In order to represent conditions from atmospheric pressure to environments in typical aircraft engines [28], 1 atm, 10 atm, and 40 atm atmospheres were used.

6.3.3 HRTEM imaging

Soot was placed in vials with ethanol (200 proof). This mixture was filtered in a BHS Sonthofen pressurized filtration system. The remaining soot was then suspended in the ethanol and sonicated for 15 minutes. Upon completion one drop from a glass micropipette was placed on a coated lacey carbon grid (Ted Pella 200-mesh Formvar). The grids were allowed to dry completely prior to being stored in the grid holder. HRTEM micrographs were produced using two FEI HRTEMs: a Tecnai F30 and an F20 EFTEM, both operating under 200 keV accelerating potential. The micrographs used for further quantification were produced at 500,000X magnification under slightly overfocused phase contrast conditions.

6.3.4 Image analysis

HRTEM images were processed by a novel image analysis framework specifically designed for analyzing HRTEM micrographs of soot. The details of the framework can be found in [23,24]. In brief, the framework is based on filtering theory—the micrographs are filtered with special two-dimensional filters in order to extract interlayer spacing and symmetry parameters. Gabor filters [29] tuned to frequencies present in soot HRTEM micrographs were used to extract interlayer spacing distributions. In a previous study [23], we showed that the filtering method produces datasets that are two orders of magnitude more robust than datasets produced by conventional fringe analysis algorithms [18]. Nematic and polar order parameters (S_{2N} and S_{2P}, respectively) were extracted by the orientation-filtering technique described in [24]. These parameters were first used to describe soot nanostructure by Shim et al. [20] and are defined as follows:

$$S_{2N} = 2\left\langle \cos^2(\alpha_i) \right\rangle - 1 \tag{6.1}$$

$$S_{2P} = 1 - 2\left\langle \cos^2(\alpha_i) \right\rangle \tag{6.2}$$

where S_{2N} is the nematic order parameter, S_{2P} is the polar order parameter, α_i is the angle between the fringe orientation vector and a so-called director vector, and <> means mean value. The director vector is approximately the local mean orientation inside an image region in the nematic case; in the polar case, it is a vector pointing from polar symmetry poles (amorphous particle cores) to the fringe centroids. It is easy to see that S_{2N} is 1

for a perfectly ordered structure and 0 for a perfectly disordered structure, while S_{2P} is 1 for perfect concentric symmetry, 0 for disordered phases, and -1 for radial symmetry. For further details about S_{2N} S_{2P}, the reader is referred to [20]. These parameters are also defined and computed in regions of specific size—the size of these regions is called the scale of the symmetry, σ. The term "long-scale symmetry" therefore refers to cases in which a high value of either symmetry parameter is retained over long distances.

For the extraction of fringe length and fringe tortuosity, an extended version of the algorithm of Palotas et al. [18] was used. The image binarization scheme of Palotas et al. was extended by introducing locally varying thresholds values for fringe separation. After fringe detection, the extraction of geometric properties (length and tortuosity) was done as described in [21].

6.4 Results and discussion

In this section, results from both qualitative and quantitative structural analysis are presented. The quantitative discussion consists of four parts. First, results from conventional fringe analysis are shown, demonstrating the differences between fringe length and tortuosity statistics between samples. High-fidelity interlayer spacing distributions are presented next, followed by the quantification of overall structural symmetry.

6.4.1 Qualitative analysis

Between 10 and 20 micrographs were acquired from each sample in a representative manner. Examples of the micrographs are shown in Figure 6.1.

Increasing pressure under which the soot had been oxidized apparently affected the nanostructure of soot from all three fuel sources. However, the effect of pressure is not obvious at first sight. The micrographs shown in Figure 6.1 were selected subjectively for demonstration purposes, based on how well they represented the qualitative trends found in the different structures—note that the quantitative trends presented in Section 3.2 are averaged over all micrographs within the respective samples.

All samples developed structures typical to combustion-generated carbonaceous residues. Core-shell structures [5,30] were predominantly found in the samples. Hollowed-out particles previously observed in diesel and biodiesel soot [30], and soot heated by pulsed lasers [31] were not found amongst the analyzed samples.

N-butanol soot generally showed increased ordering with pressure. The atmospheric sample contained mostly amorphous soot particles and although the spherules were found to be relatively large—their diameters were about 30–40 nm—in a significant fraction of the

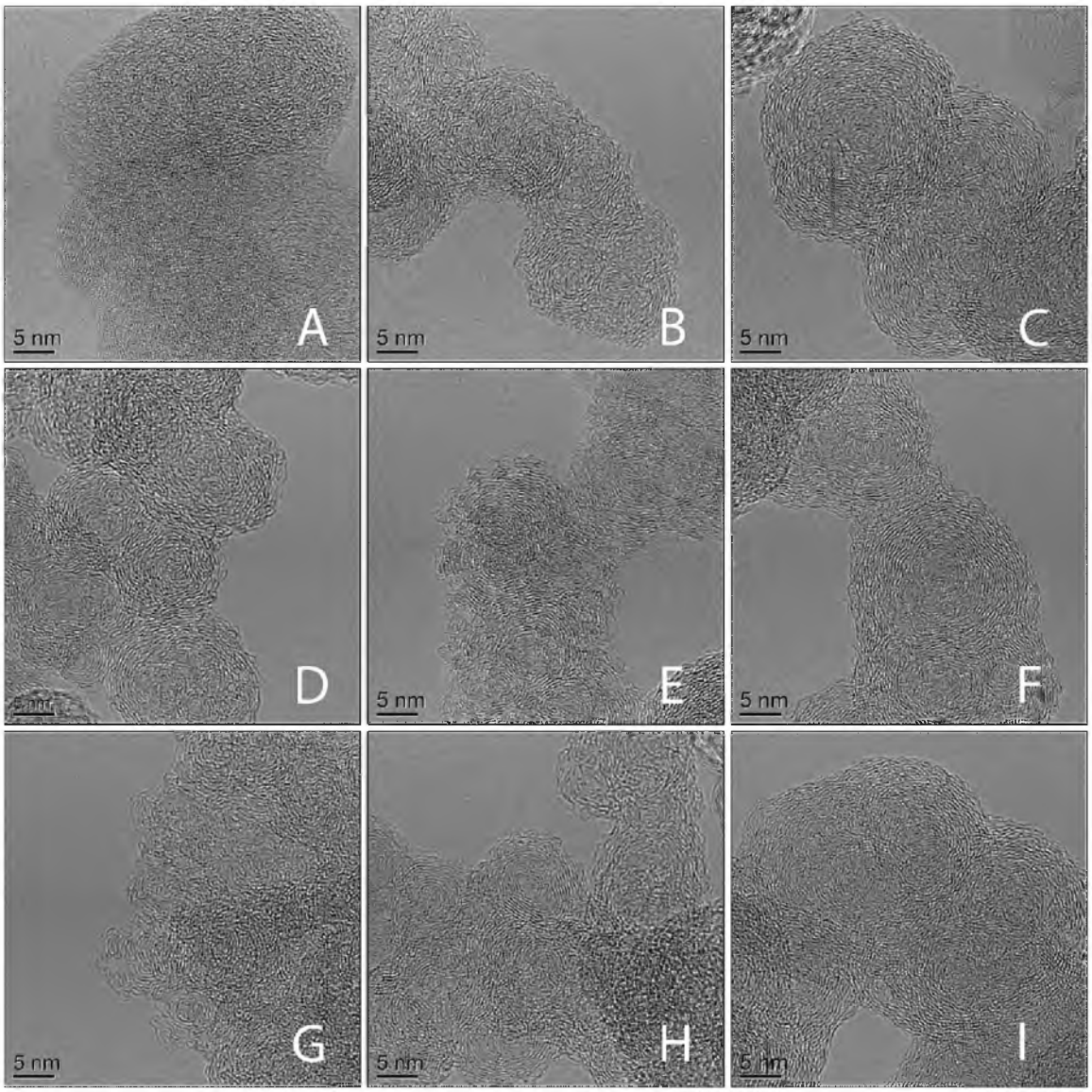

Figure 6.1: Examples of the acquired micrographs. (A) n-butanol sample, oxidized at 1 atm. (B) n-butanol sample, oxidized at 10 atm. (C) n-butanol sample, oxidized at 40 aftm. (D) n-dodecane sample, oxidized at 1 atm. (E) n-dodecane sample, oxidized at 10 atm. (F) n-dodecane sample, oxidized at 40 atm. (G) m-xylene sample, oxidized at 1 atm. (H) m-xylene sample, oxidized at 10 atm. (I) m-xylene sample, oxidized at 40 atm.

spherules, little to no apparent crystalline order was found. Another fraction of particles from the same sample showed reasonably well developed core-shell structures.

An interesting observation in the case of n-dodecane and m-xylene soots was the appearance of concentric rings at the boundaries of particles. These rings had diameters between 1 and 3 nanometers and were apparently single or multilayered fullerene structures. In the case of n-dodecane oxidized under 10 atm, these small fullerenic substructures dominated the nanostructure and caused qualitative differences between the appearance of the 10 atm sample and the 1 and 40 atm samples. The fullerenic rings were observed in some particles of the soot produced in an m-xylene flame oxidized under 1 and 10 atm as well, although they were much less dominant in these structures. The 40 atm samples showed ordered structures free from small-scale fullerenic substructures.

Fullerenic carbon in soot has been a known phenomenon [32–35]—most previous studies focused on the formation of fullerenes in flames. In this study, however, the appearing of small fullerene molecules is associated with the reordering of the carbon structure induced by oxidation under moderate pressures.

6.4.2 Quantitative analysis

Since being a projected length measure, the arclength of a fringe visible in a HRTEM image is indicative of the size of the graphene layer that produced the fringe in the image. Because soot structure is primarily composed of carbon atoms, and the bond length of these atoms is known in graphene, a statistical measure of fringe length is proportional to the average molecular weight of graphene layers in the structure. Detecting individual fringes in micrographs and measuring their lengths therefore yields quantitative information regarding the molecular weight distribution of the graphene sheets that compose a soot particle.

Another descriptor of individual graphene layers, fringe tortuosity is the measure of the curviness of graphene layer projections. Since being a projected measure, fringe tortuosity only qualitatively describes the three-dimensional structure of graphene sheets. Graphene layers can become curved due to irregularities in their lattice structure and as a result of the splay deformation described in [17]. The former case represents the effect of 5- and 7-membered rings being present in graphene and typically results in high curvature; the latter case can deform regular graphene sheets consisting of 6-membered aromatic rings as well, but the deformation results in lower curvature.

Fringe length and tortuosity data were extracted from every micrograph acquired from each sample. The extracted information was averaged over the micrographs representing a particular sample. Figure 6.2 shows the obtained histograms and fit probability density

functions (PDFs). The parameters of the skewed Gaussian PDFs were found by using nonlinear optimization. After optimization, the PDFs were renormalized and scaled for visualization purposes. Since only very slight differences were found between the distributions, in order to present a better visualization, the differences between the pressurized and atmospheric PDFs were computed and plotted in Figure 6.2. The slight differences observed suggest that increased oxidation pressure increases the size of graphene layers. This trend was found to be true for the n-butanol and m-xylene samples; however, soot from the n-dodecane flame behaved differently: n-dodecane soot oxidized under 10 atm contained shorter fringes than the atmospheric sample, while the soot oxidized under 40 atm contained longer ones. Tortuosity distributions followed a similar trend: in the case of n-butanol and m-xylene soots, fringes became less curved as pressure increased, while in the case of n-dodecane, they became more curved. The anomalous observations regarding

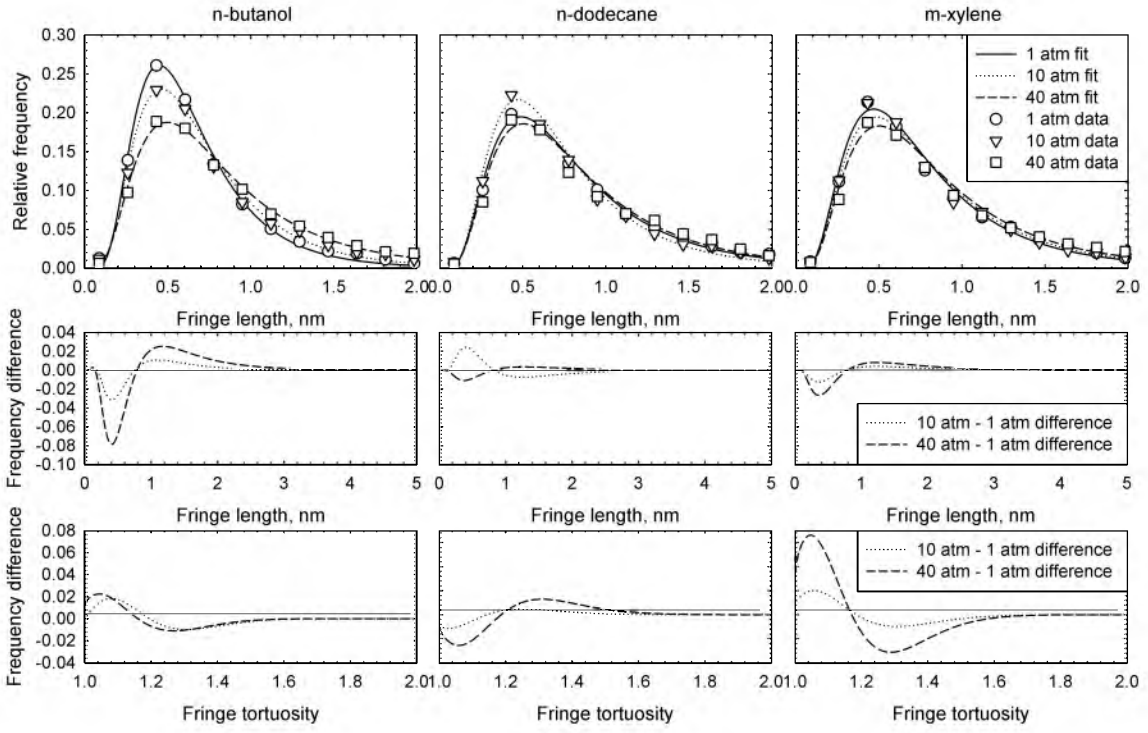

Figure 6.2: Extracted fringe length and fringe tortuosity histograms. The top row shows fringe length histograms with fit PDFs. The PDFs are skewed Gaussian distributions. The middle row shows the differences between the fit PDFs relative to the 1 atm cases. A negative difference means that there were fewer occurrences in a given length bin relative to the 1 atm case. The bottom row shows the differences in the fit tortuosity PDFs. Note that the scales of the horizontal axes of the top row are different than those of the middle and bottom rows.

soot from the n-dodecane flame are possibly caused by the appearance of small fullerenes in the structure as described in Section 6.4.1. Fringe length statistics were used to compute the molecular weight of the nematic phase, used in Section 6.4.3.

Figure 6.3 shows extracted interlayer spacing distributions. Interlayer spacing is the distance between neighboring graphene layers. As a number of previous studies have shown [30,36], as the maturation of soot proceeds, stacked layers of graphene become more similar to graphite crystals. This similarity is expressed in terms of the length, linearity, and spacing of the layers composing the microcrystals. Besides being an indicator for graphitic order, interlayer spacing supposedly affects the diffusivity of oxygen inside the microcrystals and thus the overall reactivity of soot. As Figure 6.3 demonstrates, the general trend is that increased oxidation pressure decreases the mode of the interlayer spacing distributions. The spacing of graphene layers in the atmospheric samples was found to be the longest and increasing pressure generally shifted spacing distributions toward the 0.335 nm value, which corresponds to the spacing of regular graphite crystals. In the case of n-dodecane soot oxidized under 10 atm, again, an anomalous distribution was found as a slightly increasing mean spacing was observed. However, in this case, the difference between the 10 atm and 1 atm distributions was very slight, and this difference was within the uncertainty limits of the algorithm used to extract spacing values. In the other cases, the measurements showed a definite shift in the interlayer spacing distributions toward shorter distances. It is worth noting at this point, that the slight compaction of the nematic phase caused by elevated pressures is most likely an indirect effect; that is to say, the uniaxial force of external compression is orders of magnitude weaker than the short-range forces acting between graphene layers. Thus, the compaction is more likely caused by changes in the chemical structure induced by increased pressure—these changes may include the removal of 5- and 7-membered rings and intercalations. Interlayer spacing statistics were used to compute the density of the nematic phase, used in Section 6.4.3.

Besides fringe statistics and interlayer spacing distributions, symmetries in graphene layer arrangement can be measured and used to describe soot nanostructure. The term "symmetry" refers to regularities in the relative position and orientation of fringes in HRTEM micrographs. Symmetry can be characterized by order parameters—the two used here is the polar (S_{2P}) and nematic order parameter (S_{2P}) introduced by Shim et al. (see Section 6.3.4 or [20]). Maps of the symmetry parameters were computed by the algorithm described in [24]. The extracted maps of S_{2N} and S_{2P} were integrated over the analyzed areas to obtain an aggregate measure of symmetry strength in the samples.

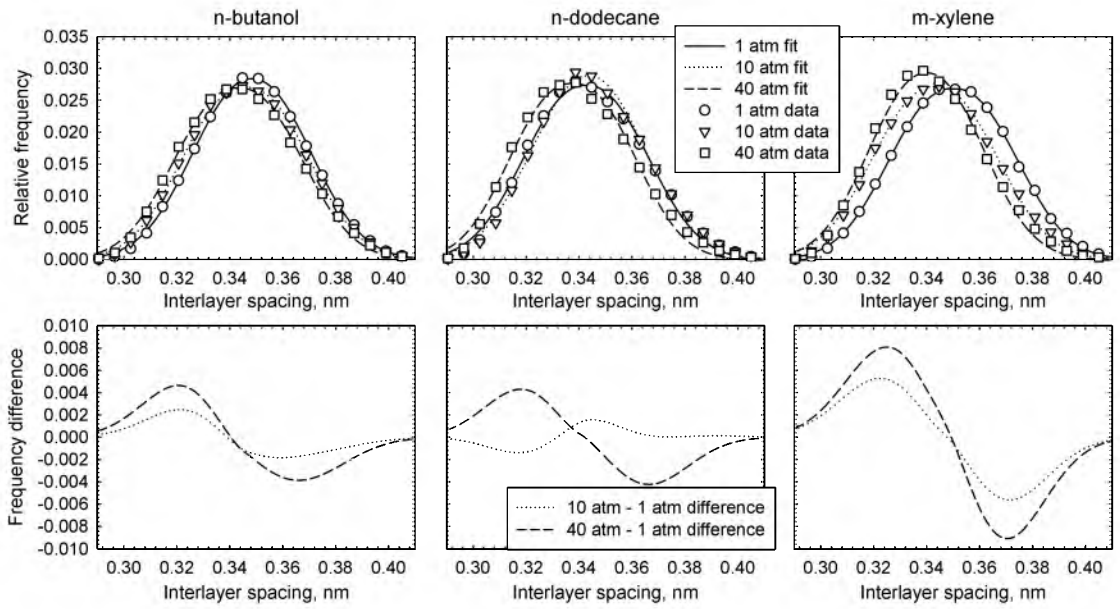

Figure 6.3: Extracted interlayer spacing histograms. The top row shows interlayer spacing histograms with fit PDFs. The PDFs are generalized Gaussian distributions. The bottom row shows the differences between the fit PDFs relative to the 1 atm cases. A negative difference means that there were less occurrences in a given bin relative to the 1 atm case.

The results are shown in Figure 6.4. Figure 6.4 visualizes the overall symmetry present at particular scales—certain scales are characteristic to certain structural primitives, e.g., strong polar symmetry at short scales represents small fullerenes. The symmetry-scale distributions shown in Figure 6.4 can therefore be interpreted as indicators that show the relative frequency of occurrences of particular structural primitives in the nanostructure.

The polar symmetry distributions of all samples were found to be bimodal. The first peak appeared below a scale of 2 nm. This peak indicates the presence of small fullerenic rings—as the insets show, the overall symmetry at this scale was the highest in the n-dodecane soot oxidized under 10 atm, which is consistent with the observation regarding small fullerenic rings described in Section 6.4.1. The second peak was found at varying scales above 6 nm—this peak represents the larger onion-like fullerenes or core-shell structures. Peak locations at this scale roughly correspond to the average size of the onion fullerenes. Large-scale polar symmetry generally got more dominant as pressure was increased—again, soots from the n-dodecane flame were exceptions. In the case of n-butanol, the structure got more symmetric at higher oxidation pressures, with the peak shifting slightly towards lower values. This shift was found in the case of n-dodecane soot as well, although the symmetry became weaker. M-xylene soot showed a consistent increase in both symmetry strength

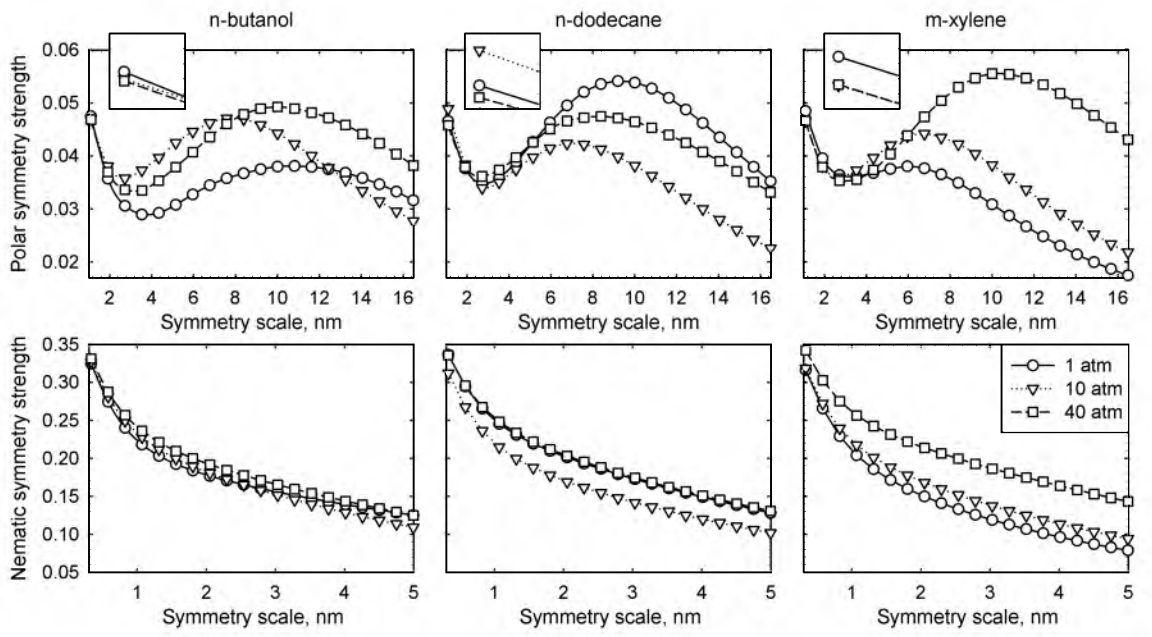

Figure 6.4: Overall polar and nematic symmetry of the analyzed structures. The top row shows overall polar symmetry strength versus scale. The bottom row shows overall nematic symmetry strength versus scale. Insets show magnified portions of the graphs at the shortest scale. Inset axes have the same scales.

and dominant scale with pressure. Nematic symmetry distributions are indicative to the distribution of stacked graphene layers, namely, the number of graphene sheets in each identified microcrystal. Consistent with the results of [19], nematic symmetry distributions that decreased with symmetry scale were observed. The smallest scale for the extraction of nematic symmetry was chosen to be approximately 0.4 nm, which is the scale of 2-membered graphene stacks. Monotonically decreasing profiles indicate that the relative frequency of the occurrence of stacked layers is inversely proportional to the number of graphene layers in them. All samples developed similar monotonically decreasing nematic symmetry distributions. Generally, elevated pressures increased the nematic symmetry strength of the samples, with the exception of the 10 atm n-dodecane sample. M-xylene soot showed the most significant ordering with pressure. Polar symmetry was used to compute the diameters of isotropic cores, and nematic symmetry was used to locate fringes in the nematic phase, used in Section 6.4.3.

Figure 6.5 shows material properties derived from HRTEM structural data. The results shown in Figure 6.5 refer to the nematic phase only. The nematic phase was located by setting a threshold on the nematic order parameter and identifying image regions that fell over the threshold. The threshold limit was the theoretical limit set by the Maier–Saupe

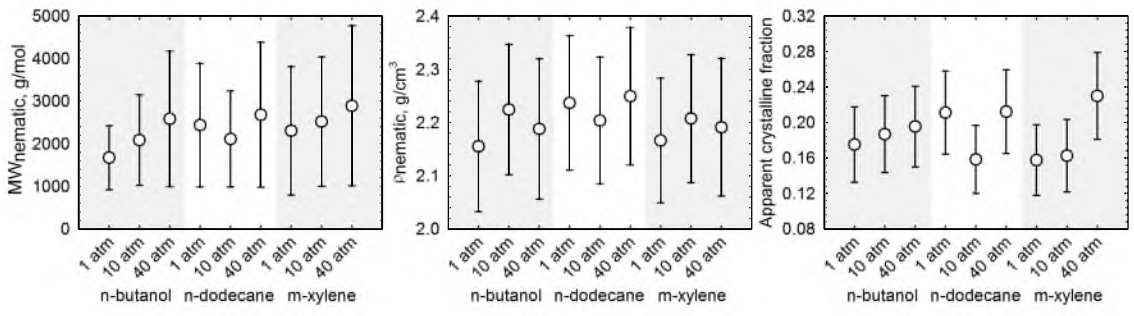

Figure 6.5: Derived properties from structural parameters extracted by HRTEM image analysis. Molecular weight was estimated by assuming a circular catenation mechanism for carbon atoms. Density was estimated by assuming graphite lattice structure. The apparent crystalline fraction is the fraction of the nematic phase in the nanostructure. All material properties pertain to the nematic phase. Circles denote mean values.

theory, $S_{2N} = 0.43$ [37, 38]. This threshold was varied over a $\pm 10\%$ range and along with the standard deviation of the structural parameters, the uncertainty resulting from the threshold variation was included in the error bars in Figure 6.5. The molecular weight of the nematic phase was estimated by assuming a circular catenation mechanism of carbon atoms as described in [39]. Assuming circular catenation, fringe length is directly proportional to the diameter of circular graphene layers, which, with some uncertainty, can be converted to molecular weight. The density of the nematic phase was estimated by assuming the geometry of a graphite lattice with slightly variable interlayer spacing. The density is then given by $\rho = 4m_C / \left(2a^2 d_{002} \sin 120^\circ\right)$, where m_C is the mass of a carbon atom, $a = 0.142$ nm, and d_{002} is the interlayer spacing in nm. The apparent crystallinity was defined as the volume fraction of the nematic phase in the soot structure. The three-dimensional volume fraction was approximated with the two-dimensional area fraction [25].

Both the mean molecular weight and apparent crystallinity of n-butanol and m-xylene samples increased at elevated oxidation pressures. The anomalous behavior of the 10 atm n-dodecane sample was possibly caused by the factors described above. The mean density values were affected by the mean interlayer spacing. Note that although the distributions and modes of the interlayer spacing showed clear trends with pressure, density did not. It is safe to state that within the uncertainties of the estimations, the density values did not show any significant trends or differences. Mean values and uncertainty ranges of the derived properties are shown in Figure 6.5 since they were used in model predictions as described in Section 6.4.3.

6.4.3 The interpretation of the results

Although the detailed modeling of soot nanostructure is not yet possible, we asked the question whether the structural changes we observed were consistent with the thermodynamic model of Hurt et al. [17]. In this model, the equilibrium diameter of the isotropic (amorphous) particle cores is computed as

$$d_{core} = 2\sqrt{\frac{2K_{11}}{(\rho/MW)\,\Delta G_{N\to I}}} \tag{6.3}$$

where K_{11} is the splay elastic constant, ρ is the density and MW is the molecular weight of the nematic phase and $\Delta G_{N\to I}$ is the Gibbs free energy change of the nematic-isotropic phase transition [17]. $\Delta G_{N\to I}$, which is given by

$$\Delta G_{N\to I}/T = -\int_{T_c}^{T} \frac{\Delta U + p\Delta V}{T^2}\mathrm{d}T \tag{6.4}$$

where ΔU is the internal energy change of the transition, p is pressure, T is temperature, T_c is the clearing temperature and ΔV is the molar volume change during the transition. ΔU is estimated by the Maier–Saupe mean field theory [37, 38] by averaging the orientational potential energy function of single molecules over an orientation distribution obtained by solving a self-consistent equation for the mean nematic order parameter [40]. The constants of the model are K_{11}, ρ, MW, T_c, ΔV and p, among which T_c, ΔV and K_{11} cannot be directly measured by HRTEM techniques. However, d_{core} shows an asymptotic behavior as a function of the reduced temperature T/T_c; thus the asymptotic values were considered in this section. ΔV depends on the molar mass and the density of the nematic phase, from which the molar mass is assumed to stay constant during the transition, and density change is limited by the densities of graphite (2.1 g/cm^3) and amorphous carbon (1.8 g/cm^3). Hurt et al. identified a meaningful value for K_{11} to be on the order of 10^{-12} N. Model results were fit to experimental data by varying ΔV and K_{11} within the realistic bounds. The model results are shown in Figure 6.6.

The experimental measurement of the isotropic core diameter is possible by recording S_{2P} as a function of the symmetry scale σ at distinct symmetry poles. This was done automatically as described in Section 3.4.2 of [24]. In brief, profiles of S_{2P} were measured at symmetry poles and averaged over the identified poles. Core diameters were defined as the peaks in these mean profiles (the highest peak locations are denoted by circles in Figure 6.6). In some cases the profiles of S_{2P} showed bimodal trends, which indicate multiple preferred core diameters. In these cases the uncertainty of the measurement was determined as the range between the peaks, along with their standard deviation; in unimodal cases the

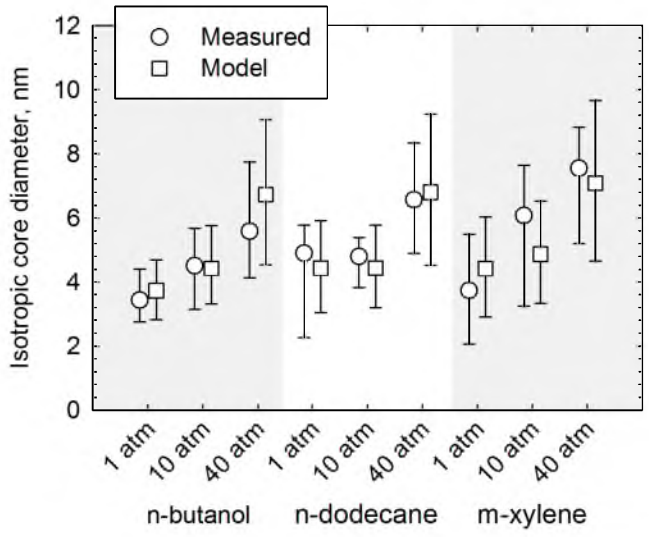

Figure 6.6: Measured isotropic core diameters versus model predictions. Circles denote the most probable core diameters measured by HRTEM image analysis. Squares denote mean model predictions. Error bars indicate the uncertainty on measurements or predictions caused by either algorithmic uncertainty or the variance of the input parameters. Fit model parameters are $K_{11} = 7.5 \times 10^{-12}$ N, $\Delta V = 0.09\%$.

uncertainty was estimated simply by the standard deviation of the Gaussian distribution fit to the identified peak in $S_{2P}(\sigma)$. This is the reason for the asymmetric error bars on the experimental results.

As Figure 6.6 shows, the predictions of the simple thermodynamic model were in good agreement with the experimental results. Core diameters generally grew as pressure increased. In the case of n-dodecane, both model and experimental results indicate a very slight shrinkage. The fact that modeling results support the anomalous behavior of n-dodecane indicate that our observations have physical basis and are not simple outliers. Note that the results of this section only indicate that the lattice structure we observed and quantified is consistent with the polar order and isotropic core diameters. The parameter that contributed most to model sensitivity was the molecular weight, which suggests that a simplified prediction of soot particle nanostructure may be possible by simply tracking the graphene layer growth.

6.4.4 Future work

As Section 6.4.3 demonstrated, simple models can well predict the equilibrium nanostructure of soot primary particles oxidized under elevated pressure. However, there are many assumptions and simplifications in the model used. The first is the application of

the mean field theory to predict the Gibbs free energy change of the phase transition. Although this theory has been proven to give surprisingly good predictions for a number of problems [41], it lacks the implementation of a number of phenomena important from the point of soot nanostructure evolution. The most important is the transient growth of graphene layers happening simultaneously with layer reordering.

Should a simple but reasonably accurate model be available for soot nanostructure prediction, the bottom-up synthesis of intrinsic reactivity constants may be possible. Based on predicted values for S_{2N} and S_{2P}, a virtual soot nanostructure can be reconstructed in a Monte-Carlo fashion that may allow for the extraction of intrinsic reaction rates. At this point it seems that by simply predicting the mean molar mass of the nematic phase by chain-growth models it is possible to accurately reconstruct virtual nanostructure. Figure 6.7 presents a proposed workflow for intrinsic soot reactivity modeling.

The loop shown in Figure 6.7 depicts a single iteration cycle of a proposed intrinsic reactivity model. The thermal and chemical environment (i.e., as an output of a CFD code) along with the time-history of soot particles determine the molecular weight of the nematic phase. This, along with temperature and pressure determine S_{2N} and S_{2P}, which subsequently determine the virtual soot structure. This virtual structure is the representation of the apparent crystallinity and overall symmetry of soot nanostructure and as such is a very simplified description. The next step is the bottom-up synthesis of the reaction rate along with particle and aggregate distributions, which are then fed back to the first step.

As future work, we plan to identify and develop the missing links in this framework

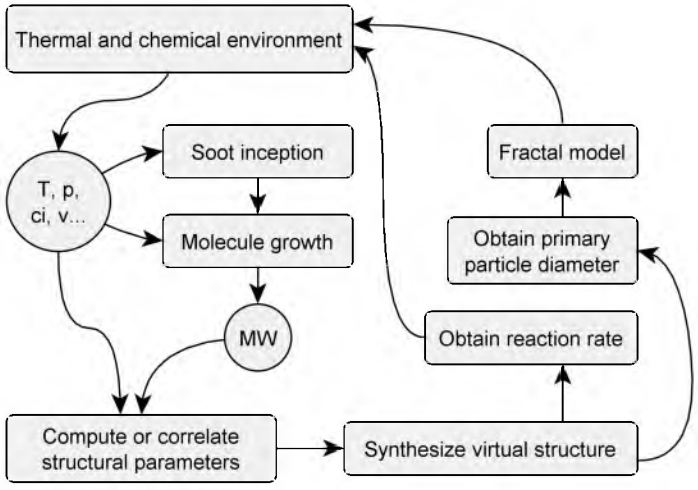

Figure 6.7: A possible method for intrinsic soot reactivity modeling.

related to soot nanostructure. These missing links are the inclusion of transient molecule growth in the prediction of order parameters and thus the Gibbs free energy change of the isotropic-nematic phase transition, the prediction of S_{2N} as a function of the model parameters described in Section 6.4.3, the synthesis of the virtual soot nanostructure, and the bottom-up extraction of intrinsic reaction rates. Current models also need to be extended to allow for using distributions or moments of structural properties instead of single mean values.

6.5 Conclusion

In this study we investigated the effects of elevated oxidation pressure on soot nanostructure. Soot from the flames of three surrogate liquid fuels, n-butanol, n-dodecane, and m-xylene were oxidized in controlled, high-pressure environments. HRTEM images were acquired of the obtained soot samples. The lattice structure of soot was investigated by utilizing state-of-the-art automated image analysis. Elevated oxidation pressure had an effect on the fringe length distribution and thus molecular weight of the analyzed soot—higher pressures were found to produce structures consisting of larger graphene layers. Elevated oxidation pressure also reduced the spacing between graphene sheets. Pressure significantly affected the symmetry of soot nanostructure. Results from symmetry measurements were interpreted by using the thermodynamic model of Hurt et al. It was shown that increasing pressure generally increases the radii of isotropic particle cores, consistently with model predictions.

CHAPTER 7

THREE-DIMENSIONAL STREAK IMAGING OF COMBUSTING COAL PARTICLES I. VELOCIMETRY

7.1 Abstract

Knowledge of the in situ temperature, size, velocity, and number density of a population of burning coal particles yields insight into the chemical and aerodynamic behavior of a pulverized coal flame, e.g., through means of combustion model validation. Sophisticated and reasonably accurate methods are available for the simultaneous measurement of particle velocity and temperature; however, these methods typically produce single particle measurements in small analyzed volumes and require extensive instrumentation. We present a simple and inexpensive method for the simultaneous, in situ, three-dimensional (3D) measurement of particle velocity, number density, size, and temperature. The proposed method utilizes a combination of stereo imaging, 3D reconstruction, multicolor pyrometry and digital image processing techniques. The details of theoretical and algorithmic backgrounds are presented, along with examples and validation experiments. By utilizing numerical simulations, rigorous uncertainty quantification is performed in order to estimate the accuracy of the method and explore how different parameters affect measurement uncertainty. The method is described in two parts. The first part, presented in this paper, describes particle velocity and population density mapping by stereo streaking velocimetry on overexposed emission images.

7.2 Introduction

The combustion of pulverized coal particles in typical flames is a complex process, affected by properties both intrinsic and extrinsic to the coal itself. Understanding and modeling coal combustion phenomena is carried out by the separation of interacting effects

attributed to mass and energy transport, chemical kinetics, and thermodynamics. Predictive models integrate the separated contributing factors and typically describe the behavior of a flame through variables like temperature, velocity, and species concentration [42, 43]. For model validation purposes, the ability to nonintrusively measure these variables in flames is valuable. Also, as past studies show [44], in-situ measurements in practical flames are of importance. Optical diagnostic techniques have been predominantly employed [45] for both laboratory-scale and industrial nonintrusive measurements.

Particle velocity enters the combustion models via the kinetic energy term and subsequently affects particle behavior through energy conservation. Particle velocity, often simultaneously with other properties of interest, has been measured by laser Doppler velocimetry or similar techniques (LDV, [46–49]), methods utilizing coded apertures for acquiring time-delay signals [50, 51], dual-pulse laser probes [52], or high-speed video observation [53]. The distribution and local number density of particles affect the radiative output of a pulverized coal flame [43]. Previous studies have used laser-based probing techniques [52] or holography [54–56] for studying particle distributions in pulverized coal flames.

Previous studies reported achievable measurement accuracies in velocity between ±2 and ±10% [48,51]. The common drawbacks of the previous methods are very small measurement volumes [48, 51], the requirement of lasers or other sensitive instrumentation [48, 49, 51, 54–59], low data rate [51, 57–59], or applying planar imaging to measure generally three-dimensional particle velocities [53]. Dual-pulse or time-delay type velocity measurements also implicitly assume the negligible z-motion of analyzed particles. With the exception of holography [54], these methods can either be classified as one-dimensional [48,49,51,52,57–59], or planar two-dimensional [53].

This paper is Part I of a two-part study presenting a simple and inexpensive stereo imaging method, which simultaneously measures particle temperature, size, velocity, and number density in three dimensions (3D). In the first part, the 3D mapping of particle velocity and number density by stereo particle streaking velocimetry (SPSV) is discussed.

SPSV was developed in the late eighties [60,61] and since has been used for the measurement of 3D vorticity fields [62], among others. The adaptation of SPSV for the diagnostics of pulverized-coal flames includes the following:

1. The flow is imaged by recording the emission of burning coal and char particles in an overexposed image instead of capturing light scattered by specially designed injected tracer particles. Due to differences in aerodynamic and optical properties of coal particles versus those of tracer particles, typical imaging conditions are also likely

different than in conventional SPSV. Particle streaks generally have unknown intensity profiles when using pulverized-coal instead of tracers, which may increase localization uncertainty in the measurements. Also, a luminous detection limit is introduced (i.e., the method is only able to analyze particles that emit enough light).

2. Since there is no control over the local density of imaged particles in a flame (in fact particle density is a measured unknown), resulting velocity data may be sparser than what is normally desired in SPSV measurements. This may affect the required post-processing.

The main objectives of this paper are the following: first, to describe the method and assess the expected aerodynamic behavior of burning coal and char particles, second, to assess localization uncertainty caused by irregular particle streaks and propagate these uncertainties through the stereoscopic system, and third, to demonstrate the method by presenting a post-processed validation data set.

7.3 Method description

In this section, the imaging, image processing, and 3D reconstruction methodologies are presented.

7.3.1 Imaging

For acquiring stereo images, a single lens, three-mirror stereo setup was used. A schematic representation of the setup can be seen in Figure 7.1. The camera sensor was split in half by positioning a right angle mirror in front of the lens—the left half of the sensor recorded the left view and the right half of the sensor recorded the right view. Virtually, the flame was imaged by two cameras, forming a cross-eyed stereo arrangement.

The positions of the flat mirrors were carefully set so that the zones of acceptable sharpness in both images covered approximately the same regions in space. The focal length and aperture size of the real camera lens were set so that the full thickness of the flame remained in focus during experiments. In fact, the stereo setup shown in Figure 7.1 was chosen instead of a two-mirror setup in order to be able to obtain fully focused images in both views, without having to use very large f-numbers. Setting up such a system for the stereo imaging of radiating particles should be optimal in terms of resolving power, depths of acceptable sharpness and the amount of transmitted light. A telephoto lens with a focal length of 110 mm and f-number of 14 was used.

For recording stereoscopic images, an inexpensive, commercially available digital single-lens reflex camera (DSLR) was used. The CMOS camera sensor allowed for acquiring 12

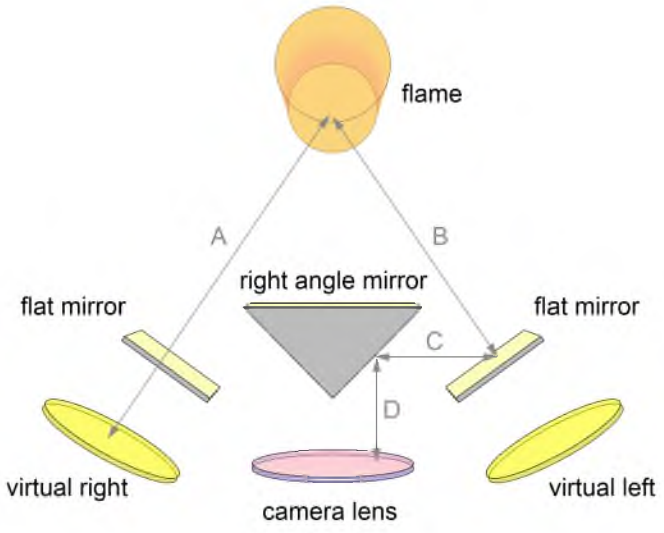

Figure 7.1: Single lens, three-mirror stereo setup used in this study (top view of schematic). Ideally, the distances of virtual cameras from the flame are the same. In this case, A = B + C + D.

MPixel (6 MPixel stereoscopic) images at 24-bit color depth. During experiments, the camera operated with a vertically traveling focal-plane shutter. The shutter speed was 1/1000 second. It is important to note that for this particular application, the type of shutter has a significant effect on the accuracy of the obtained results. CMOS sensors with rolling electronic shutters are typically not applicable without correction in postprocessing for velocity measurement since the shutter effect causes a systematic underestimation or overestimation of velocities, depending on scan direction. CCD sensors and CMOS sensors with global release or mechanical shutters are applicable—the latter only if the gating mechanical shutter is fast enough so that the integration of neighboring rows of pixels starts and ends approximately simultaneously. The exact meaning of "neighboring" depends on the apparent length of recorded particle streaks, which is a function of particle velocities and effective integration time. Focal plane shutters in commercial DLSRs are usually fast enough not to introduce any significant velocity measurement errors under typical combustion conditions. For the purpose of this method, the usefulness of a sensor can be evaluated by checking if the extracted velocity vectors are affected by sensor orientation. In other words, the apparent velocities must remain the same if the sensor is turned upside-down or to one side, for example. We were unable to quantify any differences in velocities obtained with different sensor orientations with the DSLR that was used in this study. The light sensitivity of the sensor was ISO 6400.

The method presented here measures particle velocities by acquiring overexposed images

of the moving particles, thus recording the trajectories of their motion. Due to the nature of imaging, these recorded trajectories are two-dimensional projections of three-dimensional paths. Since within a single exposure no time-resolved information is available, the three-dimensional particle trajectories and velocity history of particles cannot be reconstructed in general. However, instantaeous velocities can be estimated if one assumes that within a single exposure, particle velocities are constant.

In turbulent flows, the motion of the particles is affected by the velocity gradients and thus viscous shear the particles experience in a Lagrangian sense. Due to their inertia, however, there is usually a slip between particle velocities and gas velocities. The time it takes for a particle to respond to the changing surrounding gas velocities is called the characteristic response time of a particle, τ_p, or Stokes-time and is on the order of

$$\tau_p = \frac{\rho_p d_p^2}{\rho_0 18 \mu} \tag{7.1}$$

where ρ_p is particle density, ρ_0 is the density of the surrounding medium, d_p is particle diameter, and μ is dynamic viscosity. Note that Equation 7.1 is valid for spherical particles; however, aspherical particles can be satisfactorily treated as spheres with an equivalent diameter d_{eq} [63].

In order to make the assumption of constant particle velocities over a single exposure valid, the exposure time t_{exp} must be less than τ_p, the smallest turbulent time scale still affecting the particles. It is not part of the scope of this study to accurately assess the analytical determination of t_{exp}. However, Equation 7.1 provides a rough estimate in most practical cases. For the experimental part of this paper, τ_p was predicted to vary between 2/1000 and 8/1000 seconds; thus the chosen 1/1000 exposure time appeared to be an appropriate value. For unknown τ_p, the validity of the constant velocity assumption can be experimentally verified considering that when using low-distortion lenses, the projections of constant velocity 3D paths are two-dimensional (2D) linear segments.

If $t_{exp} < \tau_p$, then within a single exposure, a three-dimensional linear particle trajectory can be reconstructed and resolved in time by modeling it with a three-dimensional line segment $\vec{S}$. This line segment is defined by its three-dimensional start point $p_0 = \{x_0, y_0, z_0\}$ and endpoint,

$$p_1 = \{x_1, y_1, z_1\} = \{x_0 + v_x t_{exp}, y_0 + v_y t_{exp}, z_0 + v_z t_{exp}\} \tag{7.2}$$

with velocities $\vec{v} = \{v_x, v_y, v_z\}$.

The unknown z-components of particle endpoints can be computed from a stereo image pair. Omitting detailed derivation, stereo imaging allows for computing the scaled depth,

given that the fundamental matrix relating the two camera coordinate systems is known. The scaled coordinates can be renormalized to absolute world coordinates in either left or right reference coordinate system by using the extrinsic matrices of the cameras [64]. The fundamental matrix and extrinsic camera matrices can be determined by a calibration procedure. For this purpose, we used the Matlab implementation of the camera calibration toolbox of Jean-Yves Bouguet [65–68].

Three-dimensional linear particle trajectories, $\vec{S}$, are therefore reconstructed by finding corresponding start and endpoints of particle streaks in stereo image pairs. After computing the three-dimensional trajectory, the instantaneous velocity $\vec{v}$ can be estimated by

$$\vec{v} = \frac{d\vec{s}}{dt} \approx \frac{\vec{S}}{t_{exp}} \approx \frac{\{x_1, y_1, z_1\} - \{x_0, y_0, z_0\}}{t_{exp}} \tag{7.3}$$

We expect this approximation to give negligible error when $t_{exp} < \tau_p$.

It is important to point out that the particle streaking approach yields ambiguous velocity directions. In most practical cases, however, at least one component of the velocities has a preferred direction based on which the trajectories can be reliably reconstructed. In our case the preferred direction was $+y$. In very turbulent flows, direction ambiguity might cause unreliable velocity estimation, and the utilization of regularization techniques (e.g., [69]) may become necessary.

The stereoscopic particle streaking aspect of the presented method allows for the measurement of three-dimensional particle velocities, particle position and derived quantities (e.g., particle concentration over the whole thickness of the studied flame).

7.3.2 Image processing

A simple image processing framework was developed to facilitate the extraction of three-dimensional position, velocity, temperature, and size data from stereo image pairs. The velocimetry module of this framework is presented in this section. This module extracts streak location, identifies corresponding streaks in stereo image pairs, and reconstructs velocity and number density maps. A significant part of the image processing algorithm has been described previously [70, 71]; thus only the differences are discussed here.

Typical stereo images showed high noise levels, caused by the relatively high light sensitivity of the sensor and the low intensity light emitted by the particles. This high noise level, the occasional occurrance of overlapping streaks, and inhomogeneous streak intensity made intensity thresholding [71] and conventional line segment detectors (the Hough transform and its variants [72]) impractical for streak detection. Thus, a template matching routine, based on Gabor-filtering [29] was adapted. A Gabor filter bank was

constructed based on the power spectrum (the magnitude of the discrete Fourier transform) of an image, one view at a time. The region that contained most of the energy in the power spectrum was identified, and the filter bank was constructed by specifying a resolution in the Θ' (tangential coordinate of the spectrum, representing orientation) direction and the amount of overlapping between filters (for the details of filter bank construction, the reader is referred to [23]). The filter bank contained filters of a single central frequency, and the aggregate filter response was constructed by taking only the even component of filter responses. The central frequency was set so that the Gabor-like wavelets well approximated streak shapes. Local maxima in the aggregate response were considered as candidates for detected streaks.

In the next step, streak detections were refined by an energy minimization scheme similar to that used in the implementation of active contour models [73]. At this point, the streaks were considered to be one-dimensional objects, only characterized by their centroid coordinates, lengths, and orientations. Thus, line segments were initialized centered at the maxima in the aggregate filter response with initial orientations given by the orientations of the wavelets that produced the highest response at the maxima in the aggregate response and initial lengths set by the user. The position and orientation of these lines were optimized by applying an optimization procedure similar to the one described in [74].

For subpixel streak detection, we adapted a model fitting approach similar to that described in [70]. Streak images can generally be modeled as motion-blurred particle images [75, 76]:

$$g(x', y') = f(x', y') \otimes PSF(x', y') \otimes h(x', y') + n(x', y') \tag{7.4}$$

where $f(x', y')$ is the crisp, stationary particle image, $PSF(x', y')$ is the point spread function, $h(x', y')$ is the motion blur function, and $n(x', y')$ is additive, zero-mean Gaussian noise. The x' and y' coordinates are image-frame (pixel) horizontal and vertical coordinates. For the balance of this work, the apostrophe symbol is used to denote image-frame objects and coordinates. The simplest form of the motion blur function is

$$h(x', y') \begin{cases} 1/L' & \text{if } \sqrt{(x')^2 + (y')^2} \leq \frac{L'}{2},\ \frac{(x')}{(y')} = -\tan(\theta') \\ 0 & \text{otherwise} \end{cases} \tag{7.5}$$

where L' is the length of blur and θ' is the orientation of blur (or projected particle trajectory). Note that Equations 7.4 and 7.5 describe image formation (i.e., L' and θ' are projected two-dimensional parameters); thus, the differentiation of image-frame coordinates x' and y' is necessary from world coordinates x, y, z. This motion blur function is consistent with the assumptions regarding linearity discussed in Section 7.3.1.

Conventionally, subpixel particle detection is achieved by fitting Gaussian surfaces over the intensity data attributed to particles [77]. When the imaged particles are small, $f(x', y')$ can be modeled with the 2D Dirac function—thus $f(x', y') \otimes PSF(x', y') = PSF(x', y')$. The Airy function, the analytical form of the PSF, is often approximated by a Gaussian surface. Thus, fitting a Gaussian surface over the particle image is expected to have negligible error. When particles are not small, as in the case of our application, $f(x', y') \otimes PSF(x', y') \neq PSF(x', y')$. Thus, a Gaussian surface fit over the intensity data of pulverized coal particles will not fit as closely, which increases the uncertainty of the detection.

For the balance of this work, the model fit over projected particle trajectories is referred to as the streak model. The streak model can be written as follows.

$$g_s(x', y') = A \left[h(x', y') \otimes \exp\left(\frac{-x'^2 - y'^2}{\sigma'^2} \right) \right] \tag{7.6}$$

where A is the height of the streak model (approximately the peak intensity) and σ is the spread of the Gaussian kernel. The scaling factor A expresses the nonuniformity of streak intensities. A is a function of particle temperature, size and velocity.

The streak model has six degrees of freedom: parameters A and σ' and the endpoints $\{x'_0, y'_0\}$ and $\{x'_1, y'_1\}$. The values of these parameters are found by nonlinear regression over the streak image. The initial guesses for σ' are provided by the user as a representative average value for a given experiment. The initial value for A is set to be the mean intensity over the optimized line segment. The initial values for the endpoints are the endpoints of the optimized line segment. Figure 7.2 demonstrates the image processing procedure up to the step of streak model fitting.

The stereo matching of streaks was performed by scanning the views and collecting streaks that started and ended at the same epipolar lines defined by start and endpoints of the other view. The possible matches were filtered based on their intensity (streak pairs with highly differing intensities were discarded). From those remaining, the pair with start and endpoints closest to the epipolar lines was kept. Each pair's start and end coordinates were triangulated and streak position and velocity (along with temperature and size) values were stored as vector data. Figure 7.3 shows an example stereo image pair, detected streaks, and reconstructed 3D models.

Although the investigated experimental cases allowed for fuel-lean conditions in the flame, some soot was formed. Soot forming from the volatiles leaving coal particles initially surrounds the particles as envelopes [78]. Later, larger-scale, more diffuse soot clouds can form. From the perspective of streak localization, the former case may produce significant

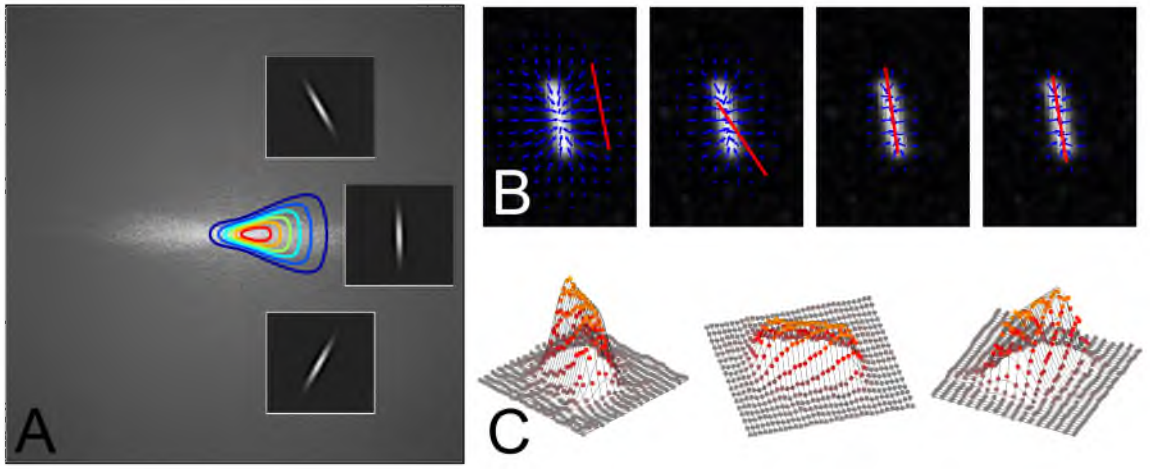

Figure 7.2: The first step in processing stereo streak images. (A) constructing the even-parity Gabor filter bank based on the power spectrum. The insets show three members of the filter bank. Contour lines show the aggregate frequency response of the filter bank. (B) Optimizing detected line orientation and location by energy minimization. Note that initial guesses produced by Gabor filtering were much more accurate than the shown initial position of the line. The four images show iterations 1, 60, 120, and 180 (final iteration). The optimized line segment is shown in red; the gradient direction is superimposed with blue arrows. (C) fit models over streak images. The wireframes show the models; the dots show the raw intensity values. The three images show the same streak from three different view points.

errors by altering the appearance of streaks and thus making the fit streak models inaccurate. As long as the particle streaks are clearly visible, the latter case only contributes to the uncertainty of temperature measurement and sizing. Although this paper discusses velocity and particle concentration measurements, it should be noted that radiation from diffuse soot clouds was subtracted from streak images by modeling background radiation as the low-pass filtered intensity image. This was done in order to calculate the temperature and size of the particles but did not affect the particle velocity and location measurements presented in this paper. For further details, the reader is referred to Chapter 8.

7.4 Uncertainty in streak localization

This section aims to elaborate on the second objective declared in section 7.1, namely, to assess uncertainties caused by irregular streak profiles and propagate these uncertainties through the stereo imaging model.

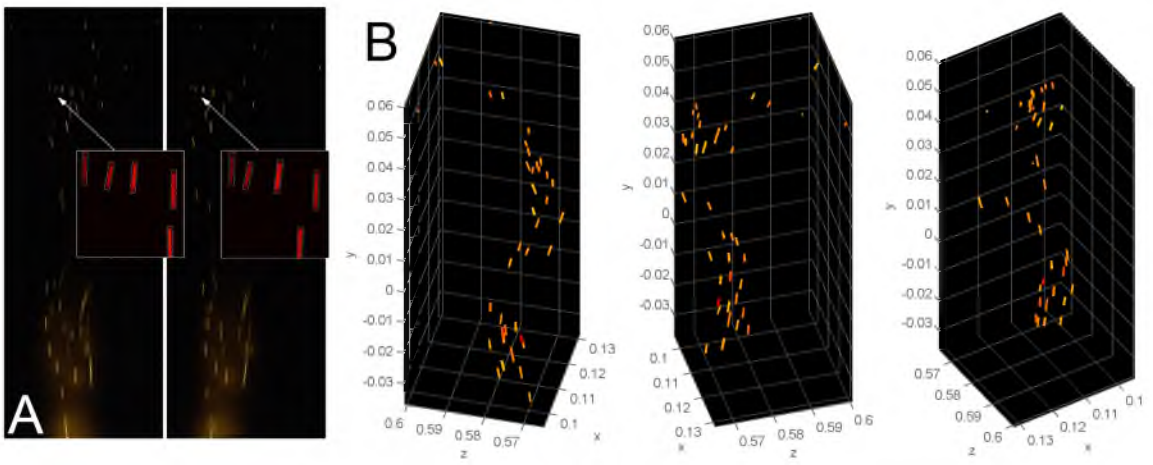

Figure 7.3: Stereoscopic reconstruction of three-dimensional particle trajectories. (A) an example stereo image pair (left and right, respectively). The insets show details of the images with streak bounding boxes. (B) the reconstructed 3D scene from three different view points. The coordinate system is centered at the left virtual sensor. The values are in meters. Streak colors indicate particle temperatures (red – coldest, yellow – hottest). Note the apparent smoothness of the extracted particle motion. To demonstrate the spatial location of virtual sensors, the reference frame used in this example is that of the left virtual sensor.

7.4.1 Streak image simulation

In particle imaging velocimetry, flow velocity is typically visualized by tracer particles injected into the flowing media. In these applications, the experimenter has the freedom to choose or even design the tracers so that the resulting particle images are easy to process and the extracted velocity is accurate. In typical applications, tracer particles are usually very fine and have fairly spherical shapes. Using fine particles reduces τ_p (see Equation 7.1), thus allowing for better tracking the velocity of the studied flow. Also, the use of spherical particles may be beneficial in terms of their scattering properties [63]. In the application described in this paper, however, neither of these parameters is freely adjustable.

For small, spherical particles, the streak model proposed by [70] and adapted here (Equation 7.6) has insignificant error since the most dominant factor in determining the final appearance of particles in the images is the PSF of the optical system. However, in a pulverized coal flame, particles can be much larger than typical tracers. Coal particle diameters are on the order of 10^0–10^2 μm. This, along with the aspherical shapes of pulverized coal particles, leads to less accurate fits of the streak model to streak intensities. These differences increase detection uncertainty, which propagates through the stereo reconstruction procedure into the uncertainty of extracted particle location and velocity.

Since coal particle shape cannot be determined visually by the method presented in this paper, instead of the modification of the streak model, one can treat the effect of irregular streak profiles as an additional uncertainty term in localization.

We define detection uncertainty as the size of the confidence regions around measured endpoints. These regions are defined to be 95% likely to contain the actual endpoint of a streak. The endpoints extracted by the image processing methodology described in Section 7.3.2 are called nominal values. The coordinate system for uncertainty quantification is chosen to be oriented the same as the streak in question. Defining the coordinate system this way transforms the x' and y' components of the endpoints to lateral and longitudinal components. Figure 7.4 helps illustrate the definitions used in this section. It is important to note that the uncertainty inherent in streak model parameters is solely caused by the residual of the fit and is computed in the nonlinear regression procedure. The confidence regions computed from the variance-covariance matrix of the fit model may not include the real streak endpoints. The signal-to-noise ratio SNR is defined as follows:

$$SNR = A/\sigma_n \tag{7.7}$$

where σ_n is the standard deviation of the noise. The parameter σ_n was measured in weak textured regions of the experimentally obtained images [79].

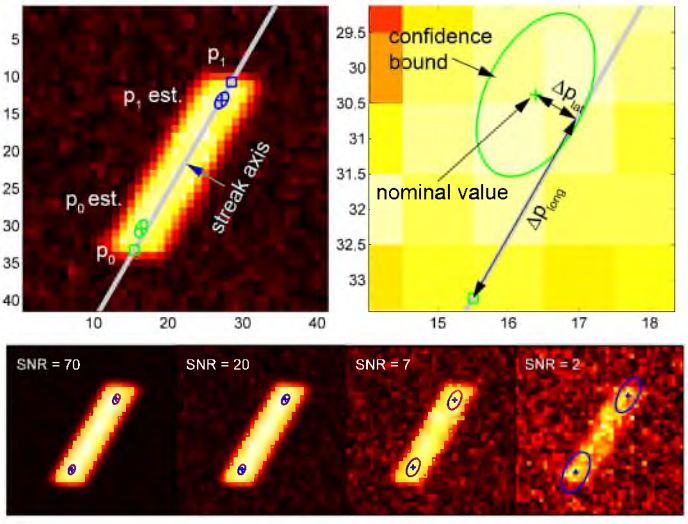

Figure 7.4: The definitions used in quantifying detection uncertainty. The ground truth streak endpoints are p_0 and p_1. The extracted endpoints are p_0 est. and p_1 est. The uncertainty attributed to the fit parameters are shown by the ellipses around nominal values. The top right figure is a zoomed in portion of the top left figure. The bottom row shows the effect of image noise on the uncertainties in fit parameters.

To quantify the uncertainty caused by irregular streak profiles, simulated streak images $f(x', y')$ were created and the image processing routine (see Section 7.3.2) was applied to these simulated images. Measurement uncertainty was quantified in an inverse fashion by comparing extracted streak location with ground truth, which was available from simulation geometry.

The simulated geometries were created to best match the experimental setup described in Section 7.5. Sensor dimensions, position, and resolution were set to be the same as the sensor of the camera used in the experiments. Spherical lens elements closely approximating the arrangement of the used telephoto lens were chosen. The exit aperture was sized based on the effective focal length and f-number (see Section 7.3.1). As in the experiments, the standoff between the entrance aperture and simulated particles was varied between 500 and 600 mm. By assuming no significant field distrortion when using telephoto lenses, particles were placed in the principal axis of the optical system.

To study the effect of particle shape and size on streak profiles, particle geometries were created in an attempt to mimic pulverized coal particles. The created models were triangulated polyhedra consisting of a random number of polygons between 200 and 600. Particles were modeled as polyhedra generally characterizable by the three principal axis lengths of their bounding ellipsoid. The bounding ellipsoids can be of any type (i.e., spherical, oblate, prolate, or tri-axial). Pulverized bituminous coal particles tend to fall into the quasi-spherical, prolate (needle-like) and oblate (plate-like) categories [80]. Two parameters are used in the literature for coal particle shape characterization: the equivalent diameter d_{eq} and sphericity factor ϕ [80–82]. The d_{eq} is the diameter of a sphere with the same surface area as the particle and sphericity is defined as the ratio of the surface area of a sphere with the same volume as the particle and the particle surface area

$$\phi = \pi^{1/3} (6V_p)^{2/3} A_p^{-1}. \tag{7.8}$$

From the definition above, it is apparent that $\phi = 1$ for a sphere and ϕ tends to zero for very aspherical particles. Coal sphericity factors of 0.78 [80], 0.73 [81, 82] and 0.6–0.8 [47] were previously reported. Simulated particles had sphericity values between 0.5 and 1 and equivalent diameters between 10 and 200 μm.

Particles were treated as ideal black bodies; therefore, their transmittance and reflectance were set to 0. Rays leaving particle surface elements were treated as monochromatic light at 600 nm. This wavelength roughly corresponds to the observable peak wavelength in the red channel. Normalized ray intensities were proportional to $1/\cos\omega$, where ω is the angle between the normal of the particle surface element and the direction

of the ray. The sensor was assumed to have uniform efficiency as a function of angle of incidence. This assumption seemed realistic with converging rays caused by the relatively small exit aperture. The optical setup only contained refractive elements.

Simulated images formed on the sensor were computed by the ray tracing method [83]. For each simulation, 5×10^4 rays were traced to the sensor plane. The starting points and direction vectors of rays were drawn randomly from a uniform distribution; however, some constraints were applied. First, the number of rays leaving each side of the triangulated particle geometry was proportional to the area of the corresponding side. The physical meaning of this constraint is homogeneous temperature distribution over the particle surface, an assumption routinely made in the analysis of coal combustion [51]. Second, only rays that actually reached the sensor were traced. The second constraint was implemented by precomputing limits on ray direction, and its purpose was to make simulations more efficient. Without this constraint, in order to obtain the same ray density on the sensor with similar geometries, at least 10^7 rays would be needed.

Each virtual pixel of the sensor was a surface element accumulating ray intensities. Sensor response was not modeled—the sensor was assumed to have unity efficiency. Obtained simulated images were made comparable to experimentally obtained streaks by rescaling the intensities of the simulated images and adding Gaussian zero-mean noise. Rescaling intensities and determining noise standard deviation was carried out so that the resulting signal-to-noise-ratio (SNR) values stayed in the range of the SNR values observed in the experiments. Figure 7.5 illustrates the streak simulation process.

After computing $f(x', y')$, streak images $g(x', y')$ were created by using Equation 7.4. Note that this process inherently assumes insignificant particle rotation during t_{exp}. The lengths and orientations of $h(x', y')$ had no significant effect on detection uncertainty, partly due to the choice of coordinate system (see Figure 7.4).

A total of 4×10^4 particles were simulated. For each particle, 10 random orientations were computed. The principal axis lengths of the bounding ellipsoids were set randomly in each case; thus, the population represented a uniform distribution of prolate, oblate, and quasi-spherical particles.

The simulated quantities of interest were the image-frame streak endpoints $\{x'_0, y'_0\}$ and $\{x'_1, y'_1\}$ extracted by fitting the streak model to the simulated intensity profiles. For this reason, the simulation only covered one side of the stereoscopic system, and the projected 2D locations of streak endpoints were considered as ground truth.

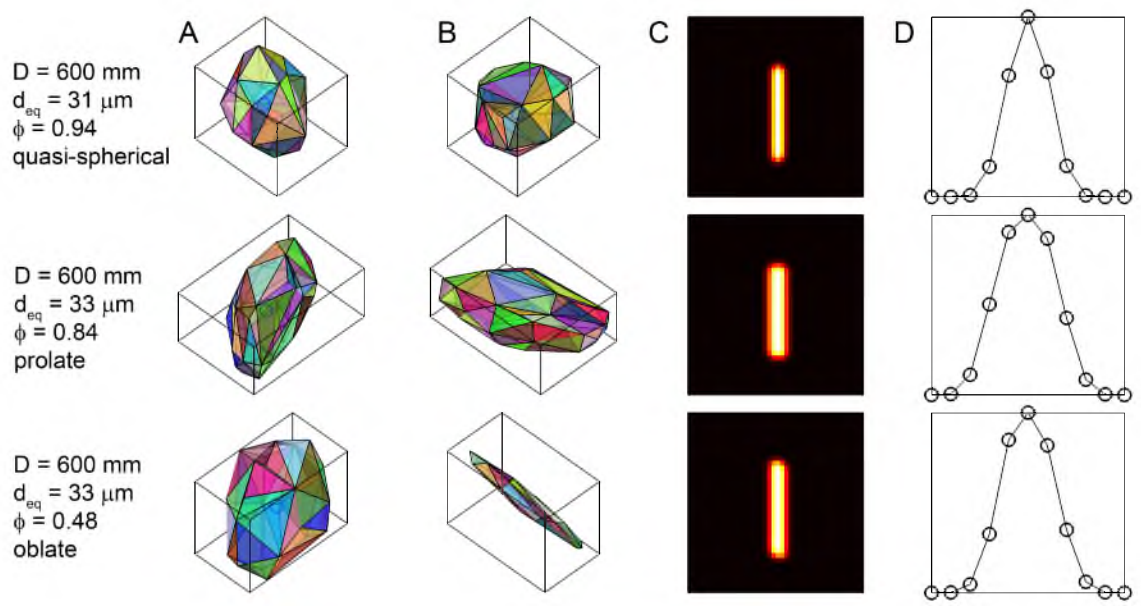

Figure 7.5: A demonstration of particle streak image simulations. Column A: particle models. Column B: particle models from a different view. Column C: simulated streaks. For visibility, noise is not shown in this figure. The images shown in this Figure are false color—only the red channel was simulated. Column D: streak cross-section (perpendicular to motion) profiles. Rows show, from top to bottom: a quasi-spherical particle, a prolate-shaped particle and an oblate-shaped particle. D is the distance between the particle and the center of the sensor.

7.4.2 Simulation results

Along with the sphericity factor, the nondimensional particle size d_{eq}/D was used for exploring how size and shape affects detection uncertainty in two dimensions. D is the distance of the particle from the image plane; thus, d_{eq}/D is an approximate measure of angular diameter using the equivalent diameter and small angle approximation.

The purpose of the quantification of detection uncertainty is ultimately to provide confidence bounds on extracted streak endpoints. In order to achieve this, the error between known simulated streak endpoints and extracted model parameters $\{x'_0, y'_0\}$ and $\{x'_1, y'_1\}$ was quantified.

For ease of understanding, detection uncertainty can be implicitly modeled as follows.

$$p_n = p_{n,est.} + \mu\Delta p + \epsilon \tag{7.9}$$

where p_n is the true location of endpoint n, $p_{n,est.}$ is the estimated location of endpoint n (see Figure 7.4), $\mu\Delta p$ is a bias term and ϵ is the measurement uncertainty. The term ϵ can be treated as a zero-mean random variable with standard deviation $\sigma\Delta p = \{\sigma\Delta p_{lat}, \sigma\Delta p_{long}\}$.

As mentioned in Section 7.4.1, ϵ follows an elliptical bivariate normal distribution, which becomes uncorrelated if described in a rotated coordinate system, as shown in Figure 7.4.

Nonlinear regression yielded fit parameters $\{x'_0, y'_0\}$ and $\{x'_1, y'_1\}$ as random variables described by their probability distributions. Since the fit model had six degrees of freedom, the obtained variance-covariance matrices were 6×6. By observing the variance-covariance matrices, it was found that the endpoints are uncorrelated with A and σ, but x'_0 is slightly correlated to x'_1 and y'_0 to y'_1. The values of the off-diagonal terms in the covariance matrices were on the order of one-fifth of the diagonal terms. The sign of the off-diagonal terms did not correlate with measurable parameters in real images; thus, it was not possible to estimate their values a posteriori. For this reason, this slight correlation between estimated endpoint coordinates was ignored in further calculations.

Figure 7.6 reveals that the norm of error between estimated and ground truth endpoint coordinates. The norm of the error ($|\Delta p|$) generally increases as particle size increases and sphericity decreases. The highest discrepancies are produced by particles that have line-like projections. The probability of a particle orienting itself such that its projection is line-like is higher in the case of prolate geometries than in the case of oblate geometries. This explains the higher error associated with the detection of large, aspherical, prolate particles.

The confidence bound can be readily quantified for simulated streaks since the ground truth is known; however, in real images, due to the lack of ground truth knowledge, uncertainty needs to be estimated based on measurable quantities. One cannot measure particle shape directly from real images; however, it was found that there is a strong correlation between the statistics of Δp and the normalized mean squared error (MSE) of the fit and SNR of the image—both of which can be measured in real images. The correlation is shown in Figure 7.7. Apparently, using this correlation to estimate endpoint uncertainty also bootstraps the problem of particle shape, meaning that error statistics become independent of particles being oblate, prolate, or quasi-spherical. In other words, the sphericity and size distribution of the simulated particles becomes irrelevant in terms of a posteriori uncertainty quantification.

By using Equation 7.9, the posteriori distributions of p_n can be estimated based on the bias $\mu\Delta p$ and random error term $\sigma\Delta p$. This is done for every detected streak by correlating error statistics to the measured MSE and SNR parameters of the streak. Confidence bounds on the predicted real endpoints can be constructed based on the estimated error statistics.

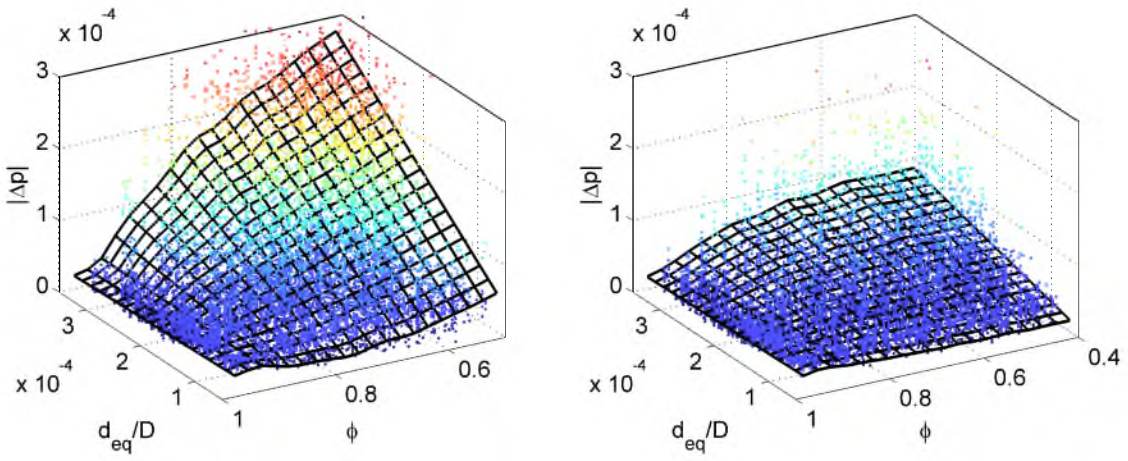

Figure 7.6: Typical behavior of $|\Delta p|$ as a function of particle size and shape. Two populations are shown here: Left – prolate shaped particles, Right – oblate shaped particles. The error in extracted streak coordinates is higher with prolate-shaped particles. The probability of oblate shapes to be oriented such that the projections appear linear is much lower than that of prolate shapes. Line-like apparent shapes give the highest deviation from the Gaussian streak model (see Equation 7.6). Surfaces are LOWESS fits to simulation data (every tenth point shown).

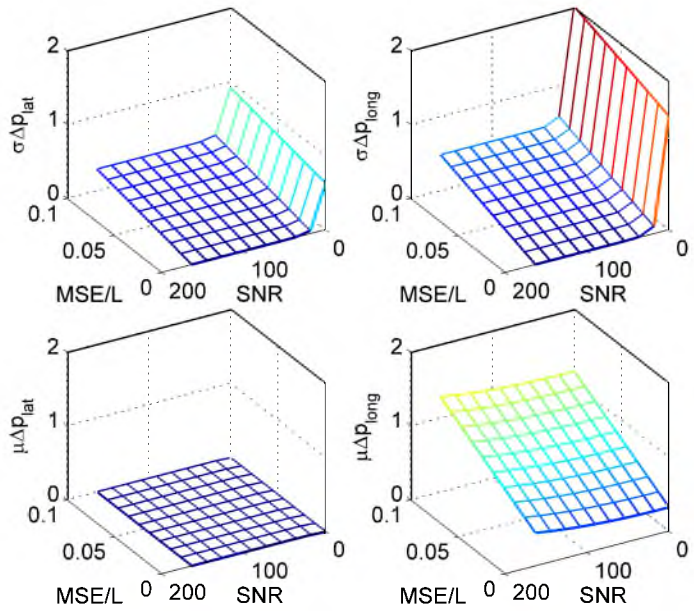

Figure 7.7: The correlation between MSE, SNR and the statistics of Δp. These relationships can be used to estimate detection uncertainty in real images. Surfaces are parametric fits to simulation data. Note that the lateral component of the bias is 0.

7.4.3 Propagation of uncertainty

The purpose of this section is to incorporate the previously described 2D detection uncertainty term into the total localization uncertainty of 3D streak coordinates $\{x_0, y_0, z_0\}$ and $\{x_1, y_1, z_1\}$. The total localization uncertainty of a streak in three dimensions therefore contains the following terms:

1. The two-dimensional (image-frame) detection uncertainty described in the previous section,
2. The uncertainty in calibration parameters.

The probability distributions of input variables $\{x_0', y_0'\}$, $\{x_1', y_1'\}$ and calibration parameters were collected for each experimental streak in each run. Image-frame detection uncertainty was used to determine the distribution of $\{x_0', y_0'\}$, $\{x_1', y_1'\}$, as presented in Figure 7.7. As described in [67, 84], we used 8 intrinsic camera calibration parameters (4 pairs, left and right – focal length, principal point, skew and distortion) and 2 extrinsic parameters (rotation and translation matrices). Uncertainties in these parameters were determined in the calibration procedure. Figure 7.8 shows localization uncertainties caused by calibration parameter variation alone.

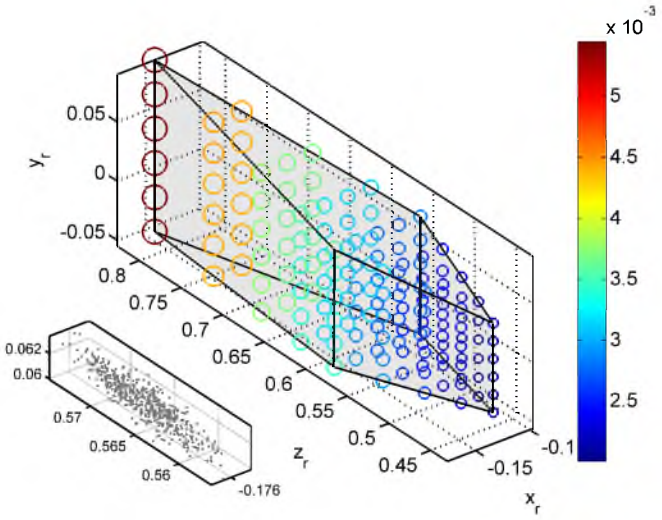

Figure 7.8: The spatial variation of localization uncertainty caused by uncertain calibration parameters. This figure also demonstrates the region of space seen by the stereo system. Marker sizes and colors are proportional to localization uncertainty. Units are in meters. The right virtual camera reference frame is used. The inset shows the asymmetric distribution of 500 3D points obtained by a Monte-Carlo simulation taking calibration parameter uncertainty and a single stereo point pair as input.

The distribution of calibration parameters was assumed to be uniform around the nominal values. The distribution of the output variables $\{x_0, y_0, z_0\}$ and $\{x_1, y_1, z_1\}$, the 3D start and endpoint coordinates, was determined by propagating input uncertainties by the Monte-Carlo method [85]. The uncertainty propagation algorithm was vectorized; thus the efficiency of the implementation allowed for running at least 10^5 Monte-Carlo trials per streak. Confidence bounds on the outputs were computed from the final distribution of output variables.

From 3D spatial coordinates, particle density can be computed. For computing velocity, localization uncertainty propagates into the uncertainty of streak lengths; however, an additional uncertainty term is introduced by the shutter speed (see Equation 7.3). Shutter speed uncertainty is expected to be on the order of 10% for mechanical shutters and below 1% for electronic shutters. In the current study, a normal distribution of shutter speed values around the nominal value 1/1000 second with a standard deviation of 1% was used. It should be noted that the precision of shutter speed depends heavily on the camera used. The 1% uncertainty is included for comparison with the other uncertainty terms. For fully electronic cameras, the shutter speed uncertainty term is most likely negligible.

7.5 Experimental

Experiments were run in order to demonstrate the described method and to study the magnitude of uncertainties propagated through a real system.

Coal was fed into the tube-in-a-tube type pulverized coal burner shown in Figure 7.9 by a coal feeder unit. This unit consisted of a quartz tube that is slowly raised into a stainless steel tube by an electric motor. Inside the stainless steel tube, another smaller stainless steel tube extended into the quartz tube. Carrier gas (CO_2) was injected into the annulus between the two steel tubes. The gas turned inside the quartz tube and carried coal into the smaller steel tube, which was connected to the central port of the burner. The motor speed and carrier gas flow rate were adjustable, so that the coal feed rate was precisely set to 0.1 g/min.

Pulverized coal particles leaving through the central hole of the burner were ignited by a primary pilot ethylene flame. The premixed ethylene-oxygen mixture was flowing out through the annular hole pattern surrounding the central hole. The flow velocity of the premixed gas was reasonably high (around 2 m/s at the burner surface), which facilitated early contact with the coal particles. Additional CO_2 and/or O_2 was optionally added through the annulus surrounding the primary pilot hole pattern. The purpose of this stream was to introduce additional oxygen for more complete burnout further away from the burner

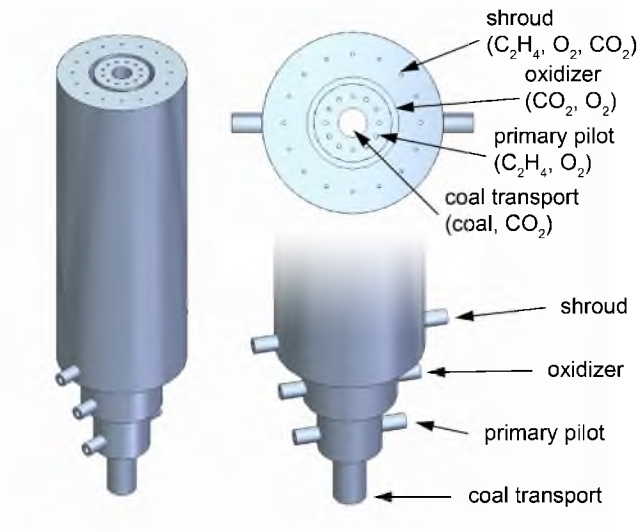

Figure 7.9: A rendering of the laboratory-scale pulverized coal burner used in the experiments.

or to cool the flame by adding CO_2 (this stream is referred to as the "oxidizer stream"). The outermost hole pattern was used for a stabilizing and shrouding ethylene-oxygen flame, which reduced the heat loss of the flame and prevented air intrusion in the studied region of the flame. This shrouding flame also increased overall flame length and thus extended the region where luminous particles appeared. Table 7.1 gives the relevant dimensions of the burner.

The burner was enclosed by an acrylic glass box. Flue gas left the box through the top, which was connected to a flue gas disposal system. Air was entrained into the encasing box from below the burner, which was positioned in a circular opening on the bottom side of the encasement. The whole setup was mounted on one end of an optical table, which also served as a basis for mounting the stereo system (see Section 7.3.1). There were two additional openings on the encasing acrylic box: one on the side from where the camera looked at the flame and one on the opposite side. The sizes of these openings were adjustable so that additional air flow could be introduced into the box from both sides. This allowed for

Table 7.1: Burner dimensions.

	no. of holes	ID, mm	OD, mm
coal transport	1	7.94	-
primary pilot	12	1.18	-
oxidizer (annulus)	1	21.18	24.89
shroud	16	1.016	-

creating asymmetric flame shapes.

Utah Skyline bituminous coal was used for the experiments. Coal was sieved into different size fractions.

Five experiments were run. The experimental conditions of these runs were set so that each run demonstrated a different aspect of the measurement capabilities. Most of the runs were done in pairs, in which each run represented one extreme in the varied parameters. The runs were given codenames that are summarized below:

- Runs "Cold" and "Hot" – These runs were primarily carried out to compare particle temperatures in flames with very different equivalence ratios. A large amount of excess oxygen was added to the flame of the Hot set compared to that of the Cold set. Also, additional CO_2 was added to quench the flame of the Cold set. The 88–105 μm size fraction of coal was used for these runs.
- Runs "Small" and "Large" – These runs were carried out to study the capabilities of the method to measure particle size. The flow rates for these two runs were identical. The particle size fraction used for the Small set was 53–74 μm, while the size fraction used for the Large set was 125–150 μm.
- Run "Asymmetric" – This run aimed to illustrate the effect of asymmetric air co-flow on the flame. From one side, additional airflow was introduced into the acrylic encasement, which made the flame lean towards the positive z_b direction. The size fraction used for this run was 88–105 μm.

The exact conditions for the five runs are summarized in Table 7.2.

For the balance of the discussion and for the sake of simplicitiy, the experimental cases will be called by their above given code names.

Table 7.2: Operating conditions for the five runs. Flow rates are in g/min.

		cold	hot	small	large	asym.
coal transport	CO_2	1.58	1.58	1.58	1.58	1.58
	coal	0.1	0.1	0.1	0.1	0.1
primary pilot	C_2H_4	0.38	0.38	0.38	0.38	0.38
	O2	1.33	1.33	1.33	1.33	1.33
oxidizer	CO_2	2.96	0	0	0	1.48
	O2	0	2	1	1	1
shroud	C_2H_4	0.38	0.38	0.38	0.38	0.38
	CO_2	2.81	2.81	2.81	2.81	2.81
	O_2	0.67	0.67	0.67	0.67	0.67
Φ (without shroud)		0.97	0.39	0.55	0.55	0.55
Φ (with shroud)		1.3	0.65	0.86	0.86	0.86
d_p, μm		88-105	88-105	53-74	125-150	88-105

7.6 Results of laboratory-scale experiments

In this section, experimental results using this modified SPSV technique on a lab-scale, pulverized-coal flame are presented in order to preliminarily assess the applicability of this method. Experimental results at five different test conditions are discussed and qualitatively compared against intuitive physical understanding. Due to the sparse nature of data, three dimensional constructions are potentially less meaningful than probability density functions. However, both representations of the data are presented in this section.

Figure 7.10 shows the velocity probability distributions for each case as well as the corresponding mean velocity and standard deviation of the Gaussian fit. It should first be noted that the oxidizer stream did not have the same velocity across all five conditions. As seen in Table 7.2, every other stream remained constant over each condition. The Hot, Cold, and Asymmetric sets had oxidizer stream velocities of approximately twice those in the Large and Small sets. However, it appears that this disparity between oxidizer stream velocities does not have a large effect on particle velocities. If it did, we would expect to see the Hot, Cold, and Asymmetric sets at a similar velocity to each other and a higher velocity than the other two sets. This is not seen. In fact, the Small set has a mean velocity significantly higher than the Hot set despite having half the velocity in the oxidizer stream.

It appears that particle size has a much stronger effect on velocity than the oxidizer stream flow rates. The Small case has the fastest mean velocity, and the Large case is the second only to Asymmetric as the slowest. The Hot and Cold sets have similar mean velocities that fall in between the Small and Large sets. Thus, we see in these data, as may be intuited, that the smaller the particle, the faster the average velocity. The Asymmetric case actually has lower velocities than the Large case despite having smaller particles.

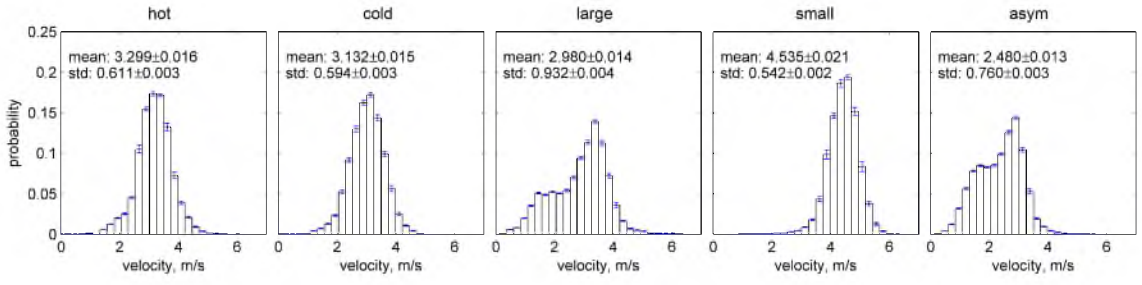

Figure 7.10: Particle velocity magnitude probability distributions of the five experimental cases. Error bars on the distributions include both particle localization and velocity uncertainty terms. The heights of the error bars signify 95% confidence bounds on the probabities.

However, it is difficult to compare the two cases due to the introduction of a large current of perpendicular airflow in the Asymmetric case.

The Small run has the smallest standard deviation of particle velocities, while the Large run has the largest. The Large set can be argued to have the largest array of particle sizes, due to the inherent imprecision in the sieving process and also due to particle devolitilization and fragmentation once in the reactor. Thus, if particle size has a strong influence on velocity, it seems reasonable that the Large set would have the largest spread of velocities. The Hot and Cold sets, with the same initial particle size distributions, have very similar standard deviations. The Asymmetric case, which also has the same particle size distributions as Hot and Cold, has a standard deviation significantly higher. This is to be expected since the velocity field of the Asymmetric set is tilted, which gives a more distributed set of velocities.

Another, albeit weaker, effect on particle velocity seems to be the occurrence of devolatilization. The Hot case is, on average, slightly faster than the Cold case. The particles in the Hot case have more immediate access to oxygen and are not quenched by CO_2. Thus, the Hot case particles begin devolatilizing faster. During devolatilization, hot gases from the particle often surround the particle and cause a buoyant effect; thus, the particle may rise faster. The Small case has inhibited devolatilization from lack of O_2 and increased CO_2 and thus has slightly smaller mean velocities.

Figure 7.11 shows the information in Figure 7.10 subdivided into three height bins. These bands are from 5–8.5 cm, 8.5–12 cm, and 12–15.5 cm above the burner (in the y_b direction). It appears that a major effect on particle velocity as a function of height is the initial particle size. The Large set slows the most with height, the Asymmetric slows less, the Hot set slows still less, and the Small set slows the least. Possibly, larger particle sizes have more drag and therefore have more reduced velocities as a function of height. The Asymmetric case slows down slightly more than the Hot set despite having the same initial particle size distribution. This may be due to the tilted flame, which can cause the particles to shear more with the stagnant air while moving upwards. The Cold set does not fit into this trend. In fact, the Cold set velocities increase slightly with height. As previously discussed, the particles in the Cold set have delayed devolitilization. Thus, it is possible that as the particles move upward in the flame and begin to devolatilize, the buoyant force of the released hot gases counteracts the drag force on the particles.

In Figure 7.10, the Large and Cold sets have similar mean velocities, despite having different initial conditions. Figure 7.11 demonstrates the differences between the two sets.

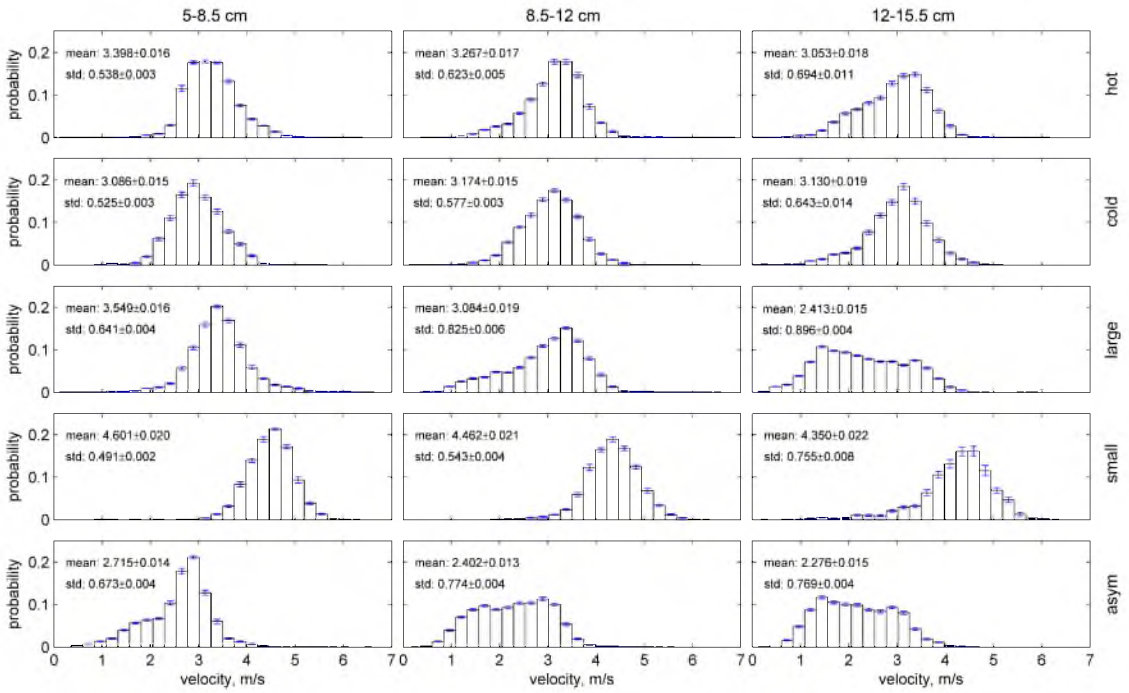

Figure 7.11: Particle velocity magnitude probability distributions shown as a function of the height above the burner, or the vertical coordinate, y_b. The obtained particle velocity maps were subdivided into three height bins. The error bars contain both the velocity and localization uncertainty terms (since particles close to a boundary between bins may be in one bin or the other depending on the localization uncertainty). The error bars signify a 95% confidence bound on the probability.

The Large case initially has a higher mean velocity than the Cold. However, the mean velocity of the Large case decreases substantially, while the Cold set mean velocities stay fairly steady with height. Thus, the two sets happen to average to a similar global velocity, but when height is taken into account, it is obvious that different phenomena are occuring.

The standard deviation of velocity in each case increases as a function of height. This is intuitive since the flame spreads as height increases. This causes the particle velocities to become more disparate, as particles in the center of the flow maintain a fairly high velocity and particles on the outside of the flow shear with the stagnant air and decrease in velocity. The standard deviations of the Asymmetric case actually change the least. The perpendicular coflow air is introduced during the lowest height bin. This airflow spreads out the distribution of velocities at the base of the flame. Thus, there is not as much of a contrast between the velocity distribution in the bottom and top height bins.

The top row of Figure 7.12 shows both particle number density contour slices as a function of height from the burner (y_b axis) and the interpolated, 3D, velocity vector field.

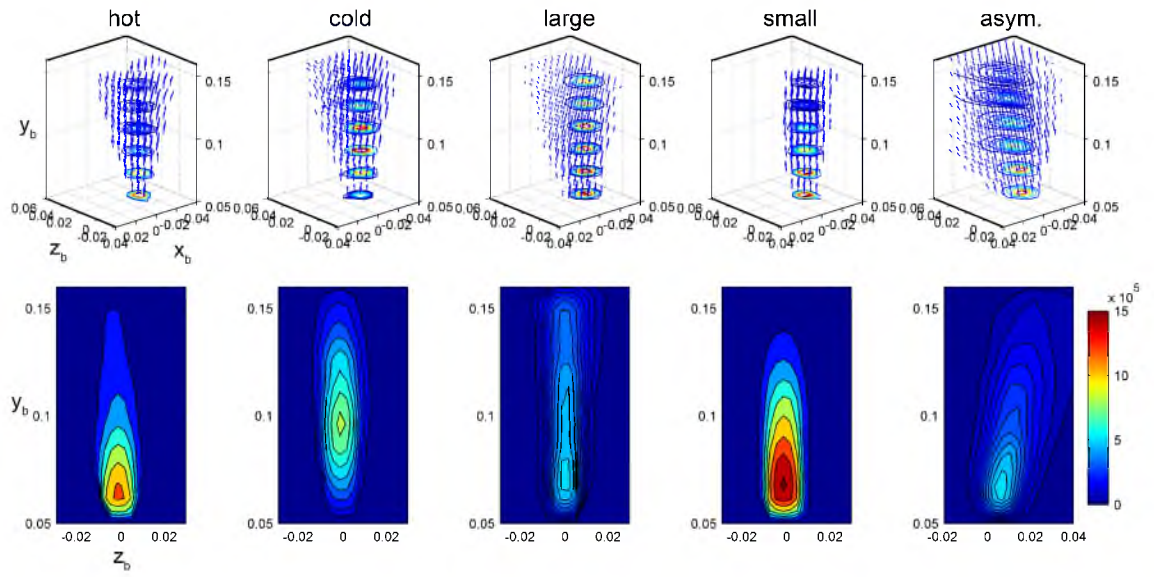

Figure 7.12: The visualization of three-dimensional particle velocity and number density maps. The top row shows interpolated velocity maps as quiver plots. Contour slices of particle number density are overlaid on vector plots. The bottom row shows contour slices of particle density maps along the z_b direction at $x_b = 0$. Vector lengths are proportional to velocity magnitude. Spatial dimensions are in meters. The contour plots of the bottom row are color-coded respective to the colorbar shown in the right, which displays particle number density valuesunits of $1/\mathrm{m}^3$.

The bottom row shows the particle number density contour sliced through $\mathrm{x}_b = 0$.

The 3D velocity vector fields tend to look unevenly distributed; however, the Asymmetric case is the only uneven flame, as seen by the contour slices on the bottom row of the figure. The apparent asymmetry is due to the visualization method: the particle velocity maps were interpolated by Gaussian kernel interpolation [86] inside the convex hull of detected particle locations. Thus, the shapes of the 3D velocity fields include space where any particle was found, even if a vast majority of the particles were found in a smaller, symmetric volume. The particle density maps shown by contour slices better describe flame shape in terms of particle locations.

From the 3D velocity field map, it is seen that the Asymmetric case is clearly tilted with the majority of the velocity vectors containing a large component in the positive z_b direction, which is the direction of the coflow air introduced at the base of the flame. It also has the widest spatial particle distribution, which is to be expected from the introduction of the coflow air. The Small case has the smallest spatial particle distribution as the smaller particles remain more entrained in the upward flow and are also consumed more quickly

than in other conditions. This increased entrainment is seen in the 3D velocity map since the velocity vectors have the largest upward (y_b) component compared to the other conditions.

Examining the bottom row of Figure 7.12, the tilt in the flame is again clearly seen in the Asymmetric case. The flame is also significantly wider than the other sets. The Large case has rectangle-like contours, while the other cases have wavy, flame-like contours. The larger particles in this case have a longer Stokes-time and thus do not follow the gas velocities as closely as in the other cases. The Small and Hot cases have the shortest flames. Both cases also have small regions of dense particles near the base of the flame. The Hot case has immediate access to oxygen and no quenching CO_2 in the oxidizer stream, so the particles tend to be consumed quickly. This quick consumption of particles is seen as well in the Small set since the smaller particles are more easily devolitilized.

The Small case has the largest amount of particles (since mass flow rate remained constant for each case), and the Large set has the smallest. Thus, the stark difference in particle number densities seen between the two cases is expected. The Asymmetric case has the smallest particle number density since the flame is larger than the others.

For every case, the densest region of particles should be at the base of the flame—where the particles are introduced. However, a certain amount of liftoff is seen in each case, especially in the Cold set—despite there being no liftoff present in the actual flame. Due to the nature of this technique, the particles must be radiating with an intensity above a certain threshold in order to be detected in the images. Thus, cold particles newly introduced into the flame have a certain residence time before they have heated enough to be detected. The Hot, Small, and Asymmetric cases all have similar distances before detection. The Large case takes slightly longer due to the increased time it takes to heat larger particles. As expected, the Cold case—with limited oxygen and increased CO_2—has the longest residence time for particle detection. For this reason, although the uncertainty of particle localization can be accurately assessed (Section 7.4), particle density mapping remains semiqualitative with this technique.

Figure 7.13 shows the uncertainty quantifications for 3D particle location (defined as the start point of each streak) and the magnitude of each particles velocity. The plain bars represent the uncertainty in respective units and the hashed bars represent relative uncertainty. The percent uncertainty for particle location was calculated by normalizing the uncertainty in millimeters by each particles standoff distance from the virtual camera ($\sim$55 cm). The percent uncertainty for velocity magnitude were obtained by normalizing the uncertainty in m/s by the velocity magnitude of each particle. As previously mentioned,

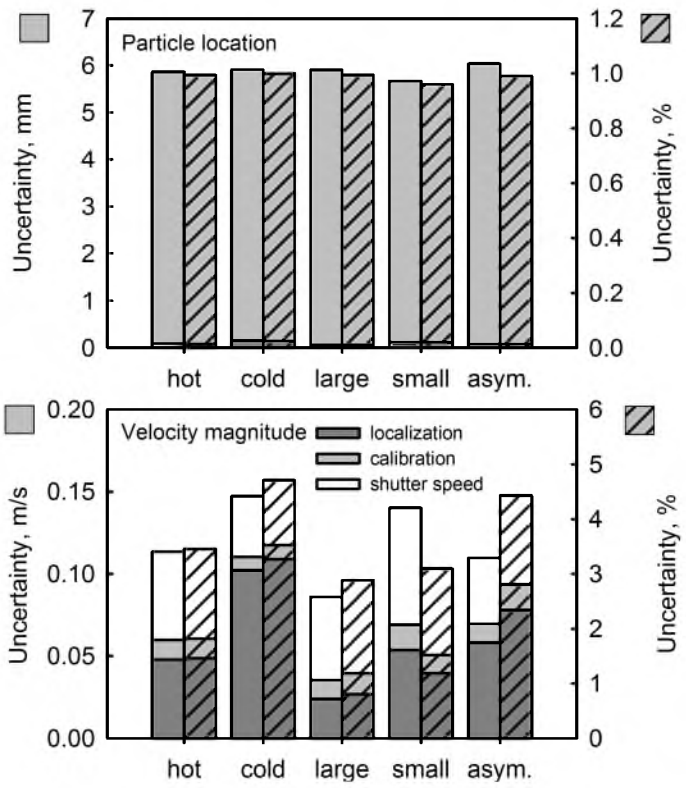

Figure 7.13: Uncertainties in particle localization (top) and particle velocity magnitude (bottom) measurements. The bars show total uncertainties in either their respective physical units (left vertical axes) or as normalized measures (right axes). The bars are subdivided based on the ratios of total effect indices (S_{Ti}) of input parameters. Thus, the subdivisions illustrate the relative contribution of each term to the total output uncertainty. All five experimental cases are investigated separately to explore effects of particle intensity, number density, spatial distribution, and velocity on the uncertainty.

uncertainty is defined as the 95% confidence bound. Each bar is subdivided into the uncertainty contribution of different parameters: detection uncertainty, calibration uncertainty, and—in the case of velocity magnitude—shutter speed. These subdivisions are proportional to the ratios of the total effect indices (S_{Ti}), or Sobol-indices. The Sobol-indices express the effect of one parameter to the total output uncertainty, including higher-order cross interaction terms (for details, see [87] and [88]).

As discussed in Section 7.4, the calibration uncertainty is caused by uncertainty in a collection of calibration parameters, and the detection uncertainty is caused by uncertainties during image processing. The calibration uncertainty dominates the total uncertainty for particle location. Referring back to Figure 7.7, the largest error due to particle detection uncertainty is $\sim$2 pixels, or a fraction of a millimeter once propagated through triangulation. The uncertainty of the calibration parameters is much higher than this. The largest

calibration uncertainty—and thus the largest total particle location uncertainty—is in the z direction as can be seen in the inset of Figure 7.8.

The overall magnitude of particle location uncertainty is similar over all the cases (~6 mm). The Small case has the smallest uncertainty. It also has the most vertical velocity profile, and thus the least variation in the z-direction, which leads to a smaller calibration uncertainty. The largest particle location uncertainty occurs in the Asymmetric case, which has the largest z-component in the velocity field. The Asymmetric case also has the largest change between the uncertainty in millimeters and its normalized percentage. The uncertainty is normalized by the z-axis distance from the camera to the particle and the cross-flow air blew particles further from the camera.

The detection uncertainty term becomes a more substantial contribution than the calibration term in regards to the velocity magnitude uncertainty. The detection uncertainty remains very small; however, in the calibration uncertainty, the endpoints are correlated. In other words, the distance between the first and last point of a particular streak stays almost constant despite variation in the calibration parameters. As seen in Figure 7.8, the calibration uncertainty varies as a function of position within the reactor. Since the beginning and end points are at different positions, the calibration uncertainty can change at each point. However, since the streaks are so small, this difference in uncertainty between the two points is also very small. Thus, the length of each streak does not change significantly with calibration uncertainty and therefore contributes less to the total velocity magnitude uncertainty than in the total particle location uncertainty. The detection uncertainty, while small in magnitude (~2 pixels), does not correlate the two endpoints of a streak. Thus, it has a substantial contribution to total velocity magnitude uncertainty. Since calculating the velocity depends on both streak length and shutter speed, an uncertainty with a 1% standard deviation in shutter speed was included to demonstrate the magnitude of its effect and for comparison. When using electronic shutters, this term is most likely negligible. The Cold set has the highest uncertainty for velocity magnitude because it has the lowest signal to noise ratio, yielding the largest detection error.

7.7 Conclusion

This paper is Part I of a two-part study describing a novel method for measuring particle location, velocity, size, and temperature in pulverized-coal flames. In this paper, particle location and velocity measurements are discussed along with rigorous uncertainty quantification and validation experiments. The proposed method is a combination of

stereoscopic particle streaking velocimetry, particle emission imaging, and digital image processing. The main objectives of this paper were to 1) describe the general concept and optical setup of the technique, 2) assess uncertainty caused by irregular particle streaks due to the size and shape of coal particles, and 3) present post-processed data to demonstrate the capabilities of the method. Uncertainty in particle location measurements was caused by uncertain stereoscopic calibration parameters and image processing errors. Via ray-tracing simulations, it was found that larger and more aspherical coal particles can only be localized in three dimensions with increased uncertainty, which is affected by particle size and shape. This detection uncertainty can be estimated a posteriori from image statistics. By propagating both these uncertainty terms through the imaging model, it was found that three-dimensional particle location can be extracted with an accuracy of $\pm 1\%$ when the standoff distance from particles to camera lens is $\sim$50–60 cm. Similarly, particle velocity—with a third uncertainty term of shutter speed also propagated through the model—can be extracted with an accuracy of $\pm 4\%$. It should be noted that—due to the nature of emission imaging—a lower luminous detection limit is introduced. This limit makes particle density mapping semiquantitative in practical cases. However, the method is capable of extracting and mapping the aforementioned parameters in three dimensions with uncertainties comparable to (or better than) other current two-dimensional or point-measurement methods.

CHAPTER 8

THREE-DIMENSIONAL STREAK IMAGING OF COMBUSTING COAL PARTICLES II. PYROMETRY

8.1 Abstract

Knowledge of the in situ temperature, size, velocity, and number density of a population of burning coal particles yields insight into the chemical and aerodynamic behavior of a pulverized coal flame (e.g., through means of combustion model validation). Sophisticated and reasonably accurate methods are available for the simultaneous measurement of particle velocity and temperature; however, these methods typically produce single particle measurements in small analyzed volumes and require extensive instrumentation. We present a simple and inexpensive method for the simultaneous, in situ, three-dimensional (3D) measurement of particle velocity, number density, size, and temperature. The proposed method utilizes a combination of stereo imaging, 3D reconstruction, multicolor pyrometry and digital image processing techniques. The details of theoretical and algorithmic backgrounds are presented, along with examples and validation experiments. By utilizing numerical simulations, rigorous uncertainty quantification is performed in order to estimate the accuracy of the method and explore how different parameters affect measurement uncertainty. The method is described in two parts. The second part, presented in this paper, describes particle temperature and size measurement in overexposed emission images.

8.2 Introduction

Particle temperature and size are key properties in the description of pulverized coal combustion [42,43]. Accurately measuring particle temperature and size is critical from the perspective of testing chemical kinetics models [89].

Particle temperature is affected by radiative and convective heat transfer and the chem-

istry of the particle and surrounding media. Typically, particle temperature is measured by narrow-band, two-color pyrometry [90–94]. The selection of infrared channels is advised due to the lower infrared emissivity of soot, which often surrounds burning coal particles, biasing the results towards higher temperatures [95]. Nevertheless, many studies utilized partly [96] or fully [97] visible measurements or even single-color visible pyrometry [98], indicating that these are also valid techniques for temperature measurement. The filter bandwidths (full width at half maximum, FWHM) used for two-color measurements are typically between 10 and 25 nm, with some exceptions of up to 75 nm [96]. More widely separated and narrower bands improve the reliability of measurements by making the numerical solutions of the irradiance equations (e.g., Equation (6) in [99]) more stable and very narrow bands allow for the assumption of single wavelengths, simplifying the irradiance equations. Based on past studies, two-color pyrometry can be a reasonably accurate tool for temperature measurement even when using wider [96], closely spaced [97], or overlapping [100,101] bands, such as the bands Bayer filters on color sensors [102] produce. Current state-of-the-art methods claim to be able to measure coal particle temperature at an accuracy of $\pm 1\%$ [51] in laboratory-scale flames.

The size of individual coal and char particles affects their aerodynamic properties and the mass and heat transfer to and from the particles. Tracking the size distribution of particles in a flame allows one to infer statements on reaction kinetics [51]. Since the properties of the particle population in a flame may affect larger-scale flame behavior in an entangled manner, knowledge of particle size distributions is important from the point of char fragmentation as well [103–105]. Current in-situ methods for coal particle size measurement utilize coded aperture [50, 51, 106], quasi-imaging [47–49], holographic [54, 55], or pyrometric [107–109] principles. Reported accuracies are around $\pm 20\%$ for coded aperture sizing [51] or $\pm 15\%$ for holographic techniques, although the latter has only been applied to nonreacting flows.

Similarly to the techniques cited in Chapter 7, apart from digital holography, all the above mentioned methods operate in small measurement volumes, typically analyzing a single particle at a time. Even with digital holography, the measurement volume is not larger than 10 cm^3 [56]. The stereo particle streaking approach described in Chapter 7 is extended in this paper by adding pyrometric temperature and sizing capabilities. The three-dimensional (3D) aspect of the measurement method is fully retained.

8.3 Method description

In this section, the theoretical and practical details behind the combined pyrometric sizing aspect of the proposed method is are described. Temperature and size measurements are both done pyrometrically. Temperature is measured by means of two-color pyrometry (i.e., by comparing the signal levels in two color channels in the images). Particle size can be estimated when the temperature and spatial location of a particle become known. Following the notation of Chapter 7, an equivalent particle diameter (d_{eq}, the diameter of a sphere with the same surface area as the particle) is defined and used throughout this paper. For both temperature and size calibration, the sensor response of the camera must be calibrated against known emission sources. In the second half of Section 8.3, the calibration procedure is described.

8.3.1 Pyrometry of moving objects

Typical multicolor pyrometry correlates the pixel counts C of a single pixel with the incident irradiance by using the following equation:

$$C_\lambda = K_\lambda E_\lambda(\lambda, T, \epsilon) \tag{8.1}$$

where C_λ is the pixel counts as the response to radiation at wavelength λ, K_λ is a gain-like term determined by sensor calibration, and $E_\lambda(\lambda, T, \epsilon)$ is the spectral irradiance at wavelength λ. The irradiance term depends on the temperature T and emissivity ϵ of the imaged, radiating object.

Equation 8.1 is valid when—among others—the following assumptions hold:

1. The interference filter used to separate the wavelength λ has a very narrow passband—in this case, the spectral irradiance E_λ can be used instead of the band-integrated irradiance $\int_\lambda R_{filter}(\lambda)E(\lambda)\,\mathrm{d}\lambda$, where R_{filter} is the transmittance of the interference filter.
2. The sensor response is a linear function of irradiance at the wavelength λ.
3. Every pixel in the sensor is being irradiated for approximately the same amount of time. In other words, the integration or exposure time of the sensor is very small compared to the velocity of the imaged object. If this condition is satisfied, the sensor response can be correlated with the irradiance E_λ instead of the total radiant energy $Q_\lambda = \int_{t_0}^{t_0+t_{exp}} E_\lambda(t)\,\mathrm{d}t$.

Equation 8.1 does not hold when either of the above listed assumptions fail. A more general form of Equation 8.1 can be written as the following.

$$\int_{A_s} f_{cal}\left(C_\lambda\right)\,\mathrm{d}A_s = \int_{t_0}^{t_0+t_{exp}} A_p(t)F_{p\to s}(t)\int_\Omega\int_\lambda R_s(\lambda)\prod_{i=i}^{2}\left\{R_m(\lambda)\right\}\epsilon(\lambda)P(\lambda,T,t)\,\mathrm{d}\lambda\,\mathrm{d}\Omega\,\mathrm{d}t \tag{8.2}$$

where A_s and A_p are the area of the sensor and surface area of the particle, respectively; f_{cal} is a monotonic function relating incident radiant energy to pixel counts, determined by calibration; $F_{p\to s}$ is the radiation view factor specifying the ratio of radiant energy incident on the sensor and the total radiant energy emitted by the particle in all directions, and R_s is the normalized spectral response curve of the sensor for a specific color. In the current formulation, the term R_m refers to an aggregate spectral transfer function of all optical elements between the sensor and imaged object. Following section 7.2, it is easy to understand that R_m most importantly describes the mirrors used in the optical setup. ϵ is the emissivity of the particle and $P(\lambda,T,t)$ is the Planck radiation emitted by the particle at temperature T, wavelength λ and time instant t.

Equation 8.2 assumes Lambertian char or coal particle surfaces and can be simplified further by introducing the following additional assumptions:

1. The emissivity of the particles follows the gray-body model. This assumption, or even the blackbody model, has been routinely used in the literature [51,98,107].
2. The char particles can be modeled as spherical. Previous studies [51, 107] assume spherical particles and derive equivalent particle diameters for particle characterization. In the current study, the assumption of spherical particles also allows for the analytical determination of $F_{p\to s}$.
3. Radiation from individual char particles can be closely localized in the obtained images. In other words, A_s can be substituted with sensor area in the close vicinity of identified particle streaks (see Chapter 7) and with a typical setup, the size of the neighborhood depends mainly on the point spread function (PSF) of the imaging system and the size and shape of the imaged particle. More specifically, the integral $\int_{A_s} f_{cal}\left(C_\lambda\right)\,\mathrm{d}A_s$ in Equation 8.2 becomes the volume under the particle streak model $g_s(x',y')$. The assumption of close localization is expected to be valid for fully focused images, which are subsequently preferred with the proposed method (see section 7.2).
4. Assuming no energy loss between the planar mirror and the sensor, the particle-sensor view factor $F_{p\to s}$ can be approximated by the view factor of the particle to the first planar mirror $F_{p\to m}$ (on one side of the stereo system). Intuitively, this assumption seems reasonable whenever the whole area of the planar mirrors are visible in the stereo images. Multiple reflections between the particle and mirrors are neglected,

which is reasonable as carbon particles are generally opaque.

5. Neither particle temperature, nor size change considerably during the exposure time t_{exp}. By doing a simple heat transfer calculation [80], a characteristic heating time for coal particles can be defined as

$$\tau_h = \frac{d_p^2 \rho_p C_p}{6 N u k} \tag{8.3}$$

where C_p is the heat capacity of the particle, Nu is the Nusselt number, and k is the thermal conductance of the surrounding gas. Assuming pure CO_2 as surrounding medium at temperatures around 1700 K, and $Nu = 2$, the characteristic heating time is on the order of 10^1 ms for typical pulverized coal particles. Equation 8.3 holds for spherical particles—for aspherical particles, τ_h is typically higher than that predicted for spheres. The exposure time used in this study (1 ms, see Chapter 7) seems appropriate for assuming constant particle temperature during exposures. A characteristic time for particle size change is more difficult to derive, but it seems intuitive that, unless a singular event (particle breakup) happens, particle size remains fairly constant during such short times in typical pulverized coal flames.

Making the above listed assumptions, Equation 8.2 reduces to the following:

$$h_{cal}\left(\int_{\mathbb{K}} g_s(x', y')\,\mathrm{d}\Gamma|_\lambda\right) = t_{exp}\pi d_{eq}^2 F_{p\to m}\epsilon \int_{\mathbb{K}} R_s(\lambda) P(\lambda, T)\,\mathrm{d}\lambda \tag{8.4}$$

where Γ is a local sensor area around the image of the particle streak (see Section 8.3.3) and h_{cal} is a different calibration function incorporating the mirror reflecticity term $\prod R_m(\lambda)$ and the integration over all directions $\int_\Omega ...\mathrm{d}\Omega$. The function h_{cal} can be applied to the integral instead of the streak model function g_s since h_{cal} is a linear function. This is practical in terms of computational efficiency.

Using the gray-body assumption allows one to factor out the particle emissivity ϵ from the integration $\int_\lambda ...\mathrm{d}\lambda$ and precompute the radiant intensity $\int_\lambda R_s(\lambda)P(\lambda, T, t)\,\mathrm{d}\lambda$ over all realistic temperatures, given that the normalized spectral response of the sensor $R_s(\lambda)$ is known. When using the gray-body assumption, if the $R_s(\lambda)$ of the sensor are not too overlapping, the ratio of the radiant intensities at any two colors uniquely determines the temperature of the imaged object. Thus, T can be computed by using a calibrated lookup table that relates the ratios of radiant intensities to temperatures, thereby bootstrapping the computation of the absolute radiant energies. Furthermore, when $g_{cal}(C_\lambda)$ is a linear function, as it is routinely assumed, even the radiant intensities are not necessary to compute—it is sufficient to construct a calibration function $RG(T)$ that relates the ratio

of pixel counts in two channels to temperature (previous studies that used this concept are [100, 110]). The ratio of pixel counts, C_r/C_g, is the mean of intensity values measured along the streak centerline.

When T is known, the particle surface area A_p can be computed from the total measured radiant energy at any color, given that $F_{p\to m}$ and ϵ are known. Using the streak model presented in Chapter 7, an analytic expression can be used to compute the total radiant energy E_i of a streak in channel i:

$$E_i = \pi A_i' \left(L' \pi^{-0.5} \sigma' + \sigma'^2 \right) \tag{8.5}$$

where σ' is the spread of the streak model, L' is the streak length, and A_i' is the height of the streak model (see Chapter 7 for further details). The apostrophes signify image-frame (pixel) coordinates.

The radiation view factor $F_{p\to m}$ was computed analytically by assuming rectangular, known mirror dimensions and known mirror location. When computing $F_{p\to m}$, the particles were assumed to be completely spherical—the asphericity of coal particles was handled as an uncertainty term (see Section 8.4). Mirror size was provided by the manufacturer by a known precision; however, the variation in $F_{p\to m}$ caused by the uncertain mirror dimensions was so small, that it was neglected in the computations. The location of the mirror was obtained from the spatial calibration procedure (see Chapter 7, Section 2.B).

The following expression was used to compute $F_{p\to s}$ [111]:

$$F_{p\to m} = \frac{d}{4\pi} \iint_{A_m} \frac{1}{(x^2+y^2+z^2)^{3/2}} \, \mathrm{d}A_s. \tag{8.6}$$

where A_m is the mirror surface. The expression was integrated numerically. The coordinates x, y, and z are the coordinates of the particle in a reference frame centered on the flat mirror.

It is important to point out that particle size measurements are made possible by the knowledge of their 3D location. Within the measurement volume used in this study, mostly depending on the z coordinate, $F_{p\to m}$ varies within $\pm 50\%$. When using a larger measurement volume, this variation is even more significant. Thus, without explicitely computing particle location, if only a single constant was used in computing the total radiative energy from a single particle, the obtained particle size would be uncertain within at least $\pm 50\%$ as well (probably much more uncertain than this—see Section 8.4.2), which would comromise data quality greatly. Therefore, $F_{p\to m}$ is the link between the pyrometric sizing procedure and the 3D localization method presented in Chapter 7

The emissivity ϵ must have an assumed value because ϵ and A_p are not independent variables in the system of equations as formulated here. In the calculations, we used the value 0.9, following previous work [107].

For temperature and size measurements, the red and green channels of the sensor were used. The reason behind this was the much higher signal-to-noise ratio obtainable by using these channels. At temperatures typical to pulverized coal combustion, particles radiate very weakly in the blue channel. Around 90% of the imaged particles produced unusable sensor response in the blue channel. In the green channel, this ratio was much better, around 20%.

8.3.2 Intensity calibration

The uniqueness of the calibration procedure required in the presented method, compared to calibration used in conventional two-color pyrometry (e.g., [99]), is that a function that relates pixel counts to incident radiative energy is obtained, as opposed to a function that relates counts to incident irradiance.

For the determination of g_{cal}, we carried out a calibration procedure of the optical system by using a NIST-calibrated tungsten ribbon filament lamp. In the visible range, tungsten is not a blackbody emitter, but the emissivity of tungsten ribbon is fairly well known from literature [112].

The tungsten ribbon was masked by a black anodized aluminum slit in order to restrict the radiating area to a known area and crop the nonuniformly radiating edges of the ribbon. As the slit was positioned close to the ribbon, the visible part of the ribbon was treated as a rectangle with dimensions determined by the ribbon and slit dimensions. The masked ribbon was placed carefully so that the surface of the ribbon was in a parallel plane with the virtual sensor surface, with edges being parallel to the x or y axis. This positioning was validated by computing the position of the ribbon with stereo triangulation similarly to how the location of coal particles are computed. Once the location of the radiating rectangular surface was known, its view factor was computed as [113]

$$F_{r\to m} = \frac{1}{A_r}\sum_{l=1}^{2}\sum_{k=1}^{2}\sum_{j=1}^{2}\sum_{i=1}^{2}\left\{(-1)^{i+j+k+l}G(x_{s,i}, y_{s,j}, x_{r,k}, y_{r,l}, z_r)\right\}$$

$$G(x_s, y_s, x_r, y_r, z_r) = \frac{1}{2\pi}\left((y_r - y_s)\sqrt{(x_r - x_s)^2 + z_r^2}\tan^{-1}\left\{\frac{y_r - y_s}{\sqrt{(y_r - y_s)^2 + z_r^2}}\right\} + \right.$$
$$+ (x_r - x_s)\sqrt{(y_r - y_s)^2 + z_r^2}\tan^{-1}\left\{\frac{x_r - x_s}{\sqrt{(x_r - x_s)^2 + z_r^2}}\right\} -$$
$$\left. - \left\{\frac{d^2}{2}\ln\left\{(x_r - x_s)^2 + (y_r - y_s)^2 + z_r^2\right\}\right\}\right) \tag{8.7}$$

where $x_r = [x_{r,c} - w_r/2, x_{r,c} + w_r/2]$ and $y_r = [y_{r,c} - h_r/2, y_{r,c} + h_r/2]$ are the coordinates of ribbon edges in the plane parallel to the virtual sensor surface, $x_{r,c}$, $y_{r,c}$, and z_r being the centroid coordinates, and w_r and h_r being the width and height of the ribbon, respectively. Similarly, $x_s = [-w_s/2, +w_s/2]$ and $y_s = [-h_s/2, +h_s/2]$ are the coordinates of the mirror edges, with w_s and h_s being the width and height of the mirror, respectively. Coordinates were measured by stereo triangulation by centering the coordinate system at the planar mirror.

Incident total radiant energy was correlated with pixel counts by performing a calibration over the temperature range of 1400 K–2000 K by increments of 100 K. Since the tungsten ribbon was stationary relative to the sensor during calibration, a neutral density (ND) filter with a transmittance of 1.563% was used to maintain the same dynamic range of pixel counts as was observed in the particle streaking images. The transmittance term of the ND filter was included in the calibration equation, which was analogous to Equation 8.4. Total incident radiant energy per pixel was correlated to the mean pixel count measured over the irradiated area of the sensor. Simultaneously, the assumption of uniformly radiating tungsten surface was validated by noting that the nonuniformity of the pixel counts over the irradiated area was below the thermal noise level of the sensor. Figure 8.1 demonstrates the calibration procedure.

By taking a closer look at Figure 8.1, it becomes apparent that the measured sensor response is not a perfectly linear function or incident photon flux. Especially at lower intensities, the nonlinearity in the response causes problems when trying to compute either temperature or size from pyrometric data. Specifically, nonlinear sensor response may cause the normally monotonic function $RG(T)$ to become nonmonotonic. Theoretically [110], the ideal form of $RG(T)$ can be written as

$$RG(T) = \frac{\int_0^\infty \epsilon(\lambda, T) R_{s,r}(\lambda) P(\lambda, T)\,\mathrm{d}\lambda}{\int_0^\infty \epsilon(\lambda, T) R_{s,g}(\lambda) P(\lambda, T)\,\mathrm{d}\lambda} \tag{8.8}$$

thus, for a black body, the ratio of pixel counts in two channels (red and green in Equation 8.8) is fully determined by the spectral response curves of the sensor. The spectral response curves were measured by using a tunable acousto-optical filter (AOTF) and the tungsten

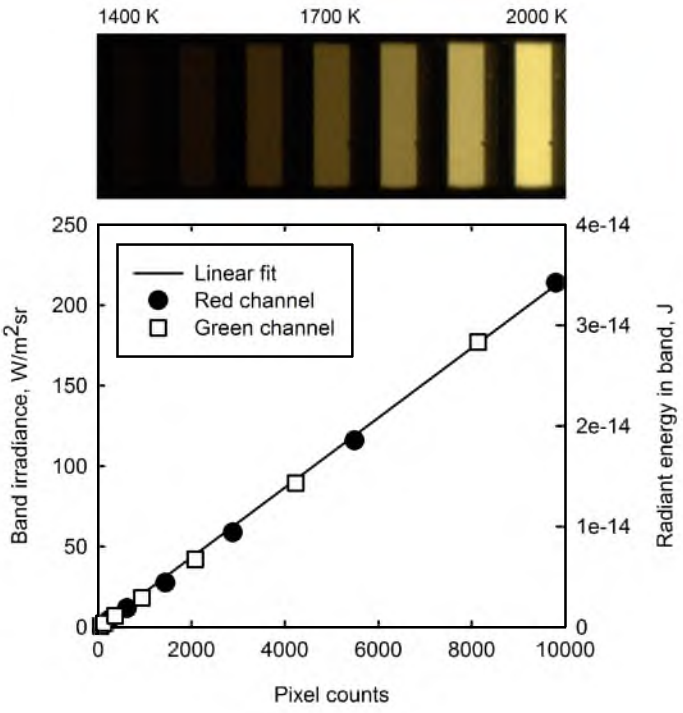

Figure 8.1: The linear relationship between pixel counts in two channels and incident band irradiance and band radiant energy. The top row shows examples of calibration images taken of the tungsten ribbon at different temperatures.

ribbon lamp as a standard light source. For nonblack bodies (like tungsten ribbon), the emissivities must be taken into account as well. Unfortunately, due to sensor nonlinearity, the measured values deviate from the ideal behavior. In such cases, it is practical to introduce an adjustment function that corrects for the nonlinear sensor behavior and alters pixel counts in postprocessing so that the altered pixel counts display a perfectly linear trend. The details of this procedure are given in the literature [114]—briefly, the procedure consists of subtracting a bias and gain term from each measured pixel count in calibration such that the obtained pixel count values form a linear function of incident photon flux. After the correction, the measured pixel count ratios should well approximate the function $RG(T)$. This is shown in Figure 8.2.

The intensity calibration procedure described in this section was done with the same optical setup as described in section 7.2. This setup was also used in the experiments.

8.3.3 Image processing

As discussed in Chapter 7, under fuel-rich conditions, a local envelope of radiating soot can form around coal particles. When the particle concentration is high, these soot

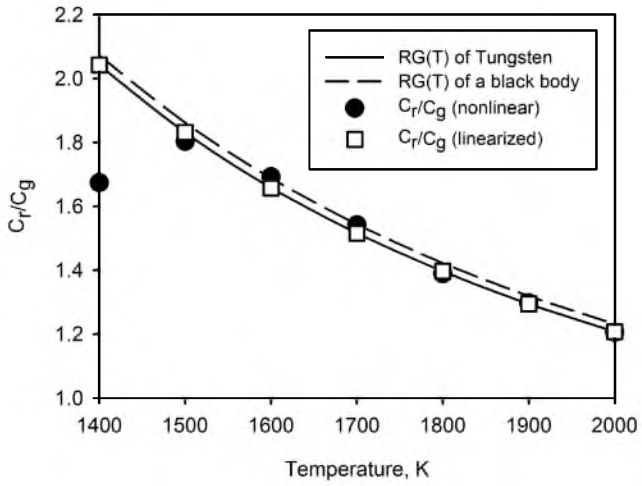

Figure 8.2: The theoretical function $RG(T)$ for black bodies and tungsten ribbon (continuous and dashed lines, respectively) and measured raw pixel count ratios (full circle) and pixel count ratios after nonlinearity correction. The deviation from $RG(T)$ was corrected by the adjustment procedure. After correction, the measured pixel count ratios C_r/C_g are consistent with $RG(T)$ and thus can be used for the estimation of temperature.

envelopes can unite and form a radiating soot cloud. It has been shown previously [95] that the presence of soot around coal particles can bias temperature measurement towards higher values. In our case, the presence of soot also causes additional radiation that is being picked up by the camera sensor. Thus, when computing particle size using Equation 8.4, the obtained size values are positively biased as well. With the methodology presented here, there is no exact way to deal with this additional, unwanted radiation as soot also emits over a continuous spectrum; however, one can exploit the fact that the amount of soot radiation can be estimated by observing the close vicinity of an imaged particle. When soot is present around particles, the obtained streak images will also be surrounded by a diffuse patch of high intensity values that stand out from the background. The intensity of the diffuse patches is proportional to the amount of radiation coming from soot, assuming homogeneous soot concentration and temperature over the analyzed scales (the scale of a particle, 10^1 μm).

Assuming a simple additive relationship between soot and particle radiation is not completely unreasonable due to the small size of soot and coal particles relative to the z-distance of the sensor and scene, but the assumption ignores the attenuation and absorption of particle radiation through volumes of soot. For the present study, the optical thickness of soot clouds was negligible; thus the error corresponding to this assumption is expected to be acceptable. In practical (industrial-scale) situations, the bias caused by soot radiation

is rarely negligible. We propose a number of solutions to this problem in Section 8.7.

The radiation from the particle surrounded by a soot cloud can be estimated by subtracting the local "background" around the streak image from the streak image itself before fitting the streak model (see Section 2, Chapter 7). Subsequently, the background can be estimated by using a moving minimum filter, such as the one described in [115] over the low-pass filtered [116] intensity image. The scale of the moving filters must be set so that over a streak image, the filter registers the intensity of the background and not the intensity of the streak itself. For low-pass filtering, we used kernels of the Gaussian type [116].

This procedure was applied to all five of the experimental sets described in Chapter 7, but the effect it had was only significant with the Small set. Images in this set displayed a high density of streaks with highly overlapping soot envelopes. The overestimation of particle size was around 30% (based on the input sieved size fraction) without background subtraction.

8.4 Uncertainty analysis

In this section, the uncertainty in all reported quantities are assessed via a bottom-to-top approach. Similarly to section 7.3, first the sources of uncertainty are listed, then the methodology of uncertainty quantification is presented and lastly, notes on uncertainty propagation are given.

8.4.1 Sources of uncertainty

Due to the nature of the pyrometric sizing procedure used in our method, particle diamter can only be computed if the particle temperature is known—temperature is computed from the color ratio C_r/C_g (see Section 8.3.1) and size is a function of temperature, particle location, and the total radiant energy of the streak. While in theory temperature and size can vary independently, since size is computed based on temperature, the uncertainty of temperature measurement propagates into sizing. For this reason, it is practical to discuss the uncertainties of the two (temperature and size) separately.

During the calibration procedure, the adjustment function to achieve linear sensor behavior is constructed and the function $h_{cal}(C)$ is established to relate pixel counts to incident radiant energy. The parameters affecting both functions are the following:

1. sensor noise, as it causes the pixel counts measured during calibration to be uncertain,
2. the uncertainty in sensor spectral response data, as $R_s(\lambda)$ is used to compute both the total incident radiant energy and $RG(T)$,

3. the uncertainty in tungsten emissivity data, as it is used to compute incident total radiant energy,
4. the uncertainty in tungsten ribbon temperature, as it is used in setting up $RG(T)$ and computing incident radiant energy,
5. localization uncertainty, as the spatial location of the tungsten ribbon, as measured by stereo triangulation, affects $F_{r\to m}$, which is used to compute the total incident radiant energy,
6. the uncertainty in the transmittance of the ND filter, as a constant in the equation used to compute the total incident energy in the calibration,
7. the uncertainty of tungsten ribbon dimensions, for affecting $F_{r\to m}$ and for appearing in Equation 8.4 and
8. the uncertain exposure time (see Equation 8.4).

In further calculations all these items except the uncertainty in ribbon dimensions and the transmittance uncertainty of the ND filter are considered. As mentioned previously, the output variance caused by ribbon dimensions was so low that it was neglected in sensitivity analysis for efficiency considerations. The variance in ND filter transmittance was neglected for similar reasons.

Among the listed items, measured temperature values are affected by items 1, 2, and 4. Extracted equivalent diameter values are affected by every item.

On the measurement side, the following items contribute to the total uncertainty in measured parameters:

1. sensor noise, as it causes the measured pixel ratios to be uncertain,
2. the uncertainty in fitting the streak model, as it affects the measured total radiant energy values,
3. the uncertainty in the 2D localization of streaks, as it affects both the measured spatial location and streak length, and
4. the uncertainty in background subtraction.

As it is apparent, these items are fairly interdependent as they are all ultimately related to image noise. Temperature is only affected by the first item, while size is affected by all of them.

There is an additional source of uncertainty in size extraction that cannot be categorized as either clearly calibration- or measurement-related. This term is the uncertainty in the particle-mirror view factor $F_{p\to m}$ caused by particle asphericity. Recall that $F_{p\to m}$ is

computed analytically assuming a spherical particle, which means that particle asphericity introduces error in the computation of $F_{p\to m}$ that ultimately propagates into the total uncertainty of the extracted equivalent diameter values.

8.4.2 Uncertainty quantification

The objective of this section is to describe the quantification of each item listed in the previous section.

Sensor noise was treated as a source that makes extracted mean values uncertain. The uncertainty caused by noise was quantified as the sample standard deviation of the mean:

$$\sigma_\mu = \sigma_{int}/\sqrt{N} \tag{8.9}$$

where σ_μ is the standard deviation of the mean μ, σ_{int} is the population standard deviation of the obtained intensity values, and N is the number of intensity values. In other words, in the Monte Carlo simulations used to propagate uncertainty (see Section 8.4.3), the mean intensities were treated as random variables following a normal distribution with standard deviation σ_μ and mean μ. It is clear that the amount of data N has a significant effect on the uncertainty.

Sensor spectral response was measured by using an acousto-optical tunable filter (AOTF). The uncertainty in these measurements was quantified by taking into account the quantum efficiency of the sensor, the emissivity uncertainty of the standard light source used, and sensor noise. By taking these factors into account, the uncertain points of R_s were treated as uncorrelated random variables following a normal distribution with a standard deviation of approximately 5%. This value was obtained by using Equation 8.9.

The uncertainty of tungsten ribbon emissivity was given in [112]. Again, the normal distribution was assumed.

The quantification of localization uncertainty and exposure time is given in section 7.3 of this dissertation.

For the quantification of uncertainty caused by particle asphericity, a number of numerical simulations were carried out. These simulations are analogous to those presented in Chapter 7, where the purpose of the simulations was the quantification of localization uncertainty. Particle geometries were created by following the same scheme as described in Chapter 7, but here the objective was to study the effect of asphericity on $F_{p\to m}$. Ultimately, for the Monte Carlo uncertainty propagation, the probability distribution of $F_{p\to m}$ is needed.

$F_{p\to m}$ is uncertain due to two factors: the localization uncertainty and particle asphericity. The total variation of $F_{p\to m}$ was treated as a product of the two factors. In uncertainty

propagation and sensitivity analysis, the two factors can be handled separately by exploiting the fact that they are independent of each other. Being able to study the sensitivity of the two factors individually makes this separation practical.

Given a known polygonal particle geometry, $F_{p\to m}$ can be estimated by computing the sum of the view factor of the mirror surface to each unobstructed polygon, summing the obtained values and inverting it using the reciprocal rule [117]. The particle geometries were triangulated and the individual view factors between the triangles and the mirror surface were computed numerically by using the contour integral method [118]. The particles were assumed to be diffuse emitters. A total number of 4×10^4 particles were simulated. This simulated population represented a uniform distribution of different oblate and prolate geometries (see section 7.3).

It was found that with the geometry of the optical setup (see section 7.2), the relative variation caused by asphericity is not affected by the location of the particle significantly. This finding allows for treating the two sources independently, as mentioned previously. Figure 8.3 shows simulation results for particles at a distance of 600 mm from the mirror.

Unfortunately, no clear correlations were found between the particle-mirror view factor and other quantities measurable in real images. For this reason, a distribution of sphericity

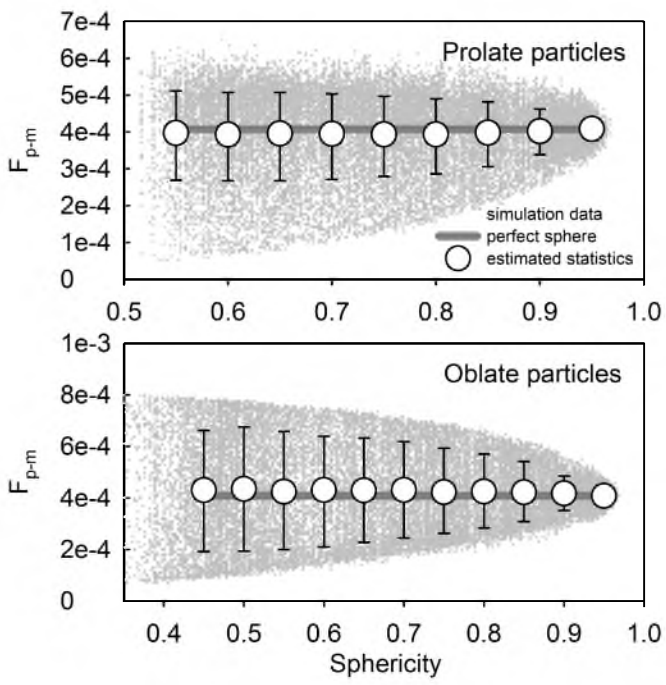

Figure 8.3: Numerical results for the particle-mirror view factor $F_{p\to m}$ with different aspherical particle geometries.

values in the fired coal population was assumed. Based on literature data [80–82], a single sphericity value of 0.74 was assumed. The distribution of $F_{p\to m}$ was set up for Monte Carlo simulations by computing the already perturbed value that did not contain variation caused by asphericity and multiplying this value by a normally distributed random variable determined by the relative standard deviation obtained in the view factor simulations at the sphericity value of 0.74. This standard deviation was estimated to be 30%, based on the results shown in Figure 8.3. A 50–50% mixture of prolate and oblate geometries was assumed in the fired population.

8.4.3 Uncertainty propagation and sensitivity

Similarly to the estimation of localization uncertainty (see Chapter 7), the Monte Carlo method was predominantly used for propagating different uncertainty terms into final uncertainty measures. A total number of 10^4 Monte Carlo trials were run per streak for estimating the uncertainty of particle temperature and size. For characterizing sensitivity, the Sobol-indices were used [87, 88].

8.5 Experimental

The details of the experimental runs can be found in Table 7.1, section 7.4. In brief, the five different test scenarios ("Hot," "Cold," "Large," "Small," and "Asymmetric") aimed to cover a matrix of combustion parameters to demonstrate the sensitivity of the presented method. The names of the cases are indicative to their expected outcome—for example, the pair of sets "Hot" and "Cold" illustrate the difference of particle temperatures in the two flames while keeping the initial particle size distribution constant.

8.6 Experimental results

Figure 8.4 shows the overall distributions of particle temperatures and equivalent diameters for each case, averaged over the entire observation volume (see Section 7.3). The two parameters are interdependent, and different trends can be observed in different locations in the flame; however, the overall trends are well illustrated by the histograms of Figure 8.4. Particle temperatures in the Cold set are the lowest. This set also has the highest amount of diluent (CO_2) added to the flame. The second coldest flame is observed in the Asymmetric case. While the flame has some CO_2 added to the oxidizer stream, the dominant cooling effect more likely comes from the cold coflow air introduced at the base of the flame. The added air flow results in slightly oscillatory flame behavior and significantly spreads the particles spatially (see Section 7.5). The overall equivalence ratios of the Large and Small

sets are the same. Thus, the striking difference in measured particle temperatures is most likely caused by the difference in the initial particle size distributions. The Hot set has twice the oxygen in the oxidizer stream than the Small set, yet has lower particle temperatures. Again, this is most likely caused by the difference in the initial particle size distributions. The observed particle temperatures are between 1400 and 2200 K in all cases, which is in agreement with literature data [51, 107, 108] when considering that the flames studied in this work were small-scale, loosely confined systems.

The mean values of the equivalent diameter measurements show reasonable agreement with the mesh sizes of the initial particle populations. The equivalent diameter means from Figure 8.4 of the Cold, Asymmetric, and Large sets are all within their respective initial particle size distributions (see Table 7.1). The equivalent diameter means for the Hot and Small sets are very slightly beneath the lowest value of their respective initial particle size distributions. Thus, the mean measured particle sizes appear to be well correlated to the initial particle sizes of each case. However, the high variance of the measured particle size distributions in Figure 8.4 do not correlate to the inital particle size distributions well. In order to understand the causes of this apparent discrepancy, one should consider the following:

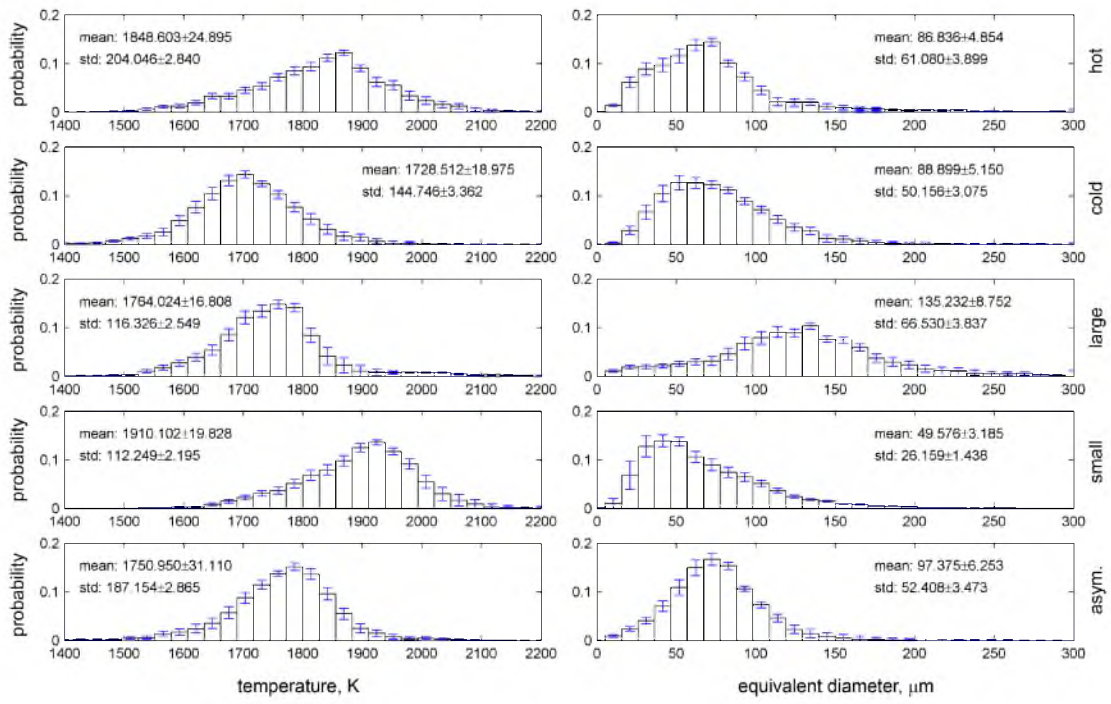

Figure 8.4: Overall probability distribution functions of particle temperature and equivalent diameter for each case.

1. There are a number of different definitions of particle size for pulverized coal particles. Equivalent diameter is one of these definitions. However, sieving does not separate particles based on their equivalent diameters but rather based on their breadth diameters. Elongated, prolate-type particlese can have significantly larger equivalent diameters than the breadth diameter allowed to pass through sieves. Thus, one must be cautious in comparing particle distributions based on sieving and particle distributions based on equivalent diameter.
2. During combustion, the size and shape of a single particle can change drastically. Fragmentation and shrinking core-type burnout decrease the observed size, while swelling increases it. Soot aggregates and tar particles often form from secondary combustion products. The sizes of these secondary particles may be uncorrelated to the initial particle size distribution.

Under these considerations, the variances of the measured particle size distributions shown in Figure 8.4 seem reasonable. Similar apparent discrepancies between mesh sizes and pyrometrically determined equivalent diameters were reported previously [109]. In order to better explain the differences between sets, it is practical to examine trends in particle temperature and size as a function of height above the burner. Figures 8.5 and 8.6 show these trends.

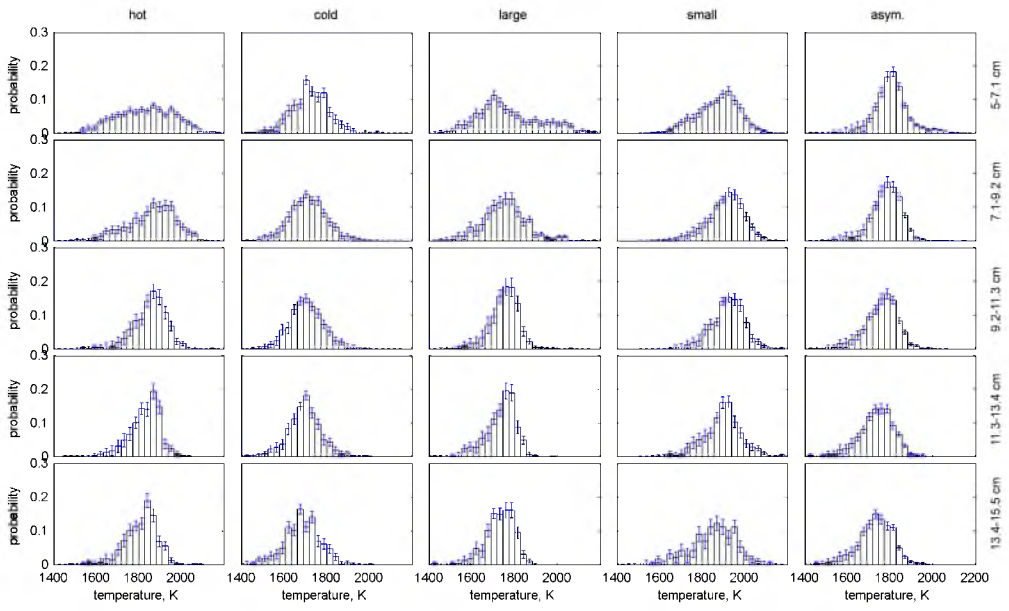

Figure 8.5: Probability distributions of particle temperature at five different height bands above the burner for each of the five cases.

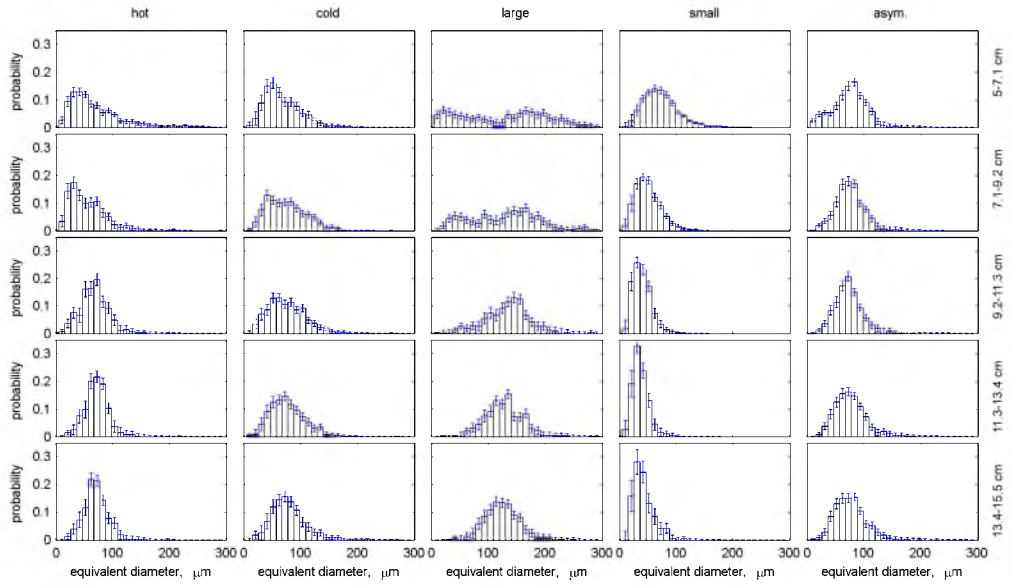

Figure 8.6: Probability distributions of particle equivalent diameter at five different height bands above the burner for each of the five cases.

Figure 8.5 shows the probability distributions of temperature for each case at five different height bins (2.1 cm each) above the burner. The top row is the height bin closest to the burner and the bottom row is the bin furthest from the burner. In the Hot, Large and Small cases, the mean temperatures first increase then decrease slightly. This is a trend one might see in a typical flame. The particles are cold when first introduced into the flame, they are heated, they ignite, and they begin to cool as they travel upwards and lose heat to the surroundings. The Asymmetric set only decreases in temperature as a function of height. The particles in this flame are increasingly dispersed in space with height; thus, as the particles travel upward, they experience more heat loss. The Cold set has almost no change in temperature between the five height bins. Due to the increased CO_2 and decreased O_2 in the flame, these particles do not devolitilize as quickly as in other cases. Thus, an increase in particle temperature in the lower height bins is not seen. The particles' lower temperatures also cause less of a driving force for heat loss. Thus, particle cooling is not seen in the upper height bins.

Figure 8.6 is very similar to Figure 8.5 and shows the probability distributions of the equivalent diameter for each case at the same five height bins above the burner. In general, the mean value of each set is fairly constant. Thus, any fragmentation and shrinking core-type burning must be counterbalanced by swelling in other particles; otherwise, a shift in the mean value would be seen. However, the distribution of particle sizes still

changes with height. This is most clearly seen in the Large set. Initially, particles are fairly evenly distributed over a large spectrum of diameters. As height increases, the smallest and largest particles disappear, creating a fairly normal distribution at the bin furthest from the burner. The Small set is the only set where the mean particle size does not remain constant with height. The set's probability distribution narrows and shifts to the left as a function of height. Thus, these particles must be fragmenting and burning more than they are swelling.

In Figure 8.6, it is seen that the smaller particles in the Hot set are consumed more quickly than in the Cold set. The Hot set particles have more access to oxygen. The Cold set distribution changes the least as a function of height, which may indicate less devolitilization than in the other cases. In the Asymmetric set, many small particles disappear between the first and second height bands. Since the coflow air is introduced at the base of the flame, many of the smaller particles are blown out of the flame. Thus, in the Asymmetric case, the disappearance of those small particles is not fully due to complete devolitilization or swelling. The shape of the Asymmetric profiles—like the Cold set—does not change drastically as a function of height. This is most likely due to cooling from the coflow air, which causes the less devolitilization and thus less change in size.

Figure 8.7 shows bivariate plots comparing particle temperature to equivalent diameter for each case. This figure demonstrates that, in general, particle size and temperature are inversely related, which is intuitive. The gray region represents the detection limit of the camera for these tests. It is a function of particle temperature, size, spatial location, and velocity. Large, high temperature particles are the easiest to detect since they are the brightest. However, particles that are closer to the camera, are slow moving, or are moving perpendicular to the camera lens will appear brighter in the images than otherwise. Thus, even a particle identical to a detected neighbor may be below the detection limit if it is further away from the camera, traveling faster, or traveling in a different direction. Because of these considerations, a detection limit band was calculated for each case. Any particle size and temperature combination above the band is detected, while no particle size and temperature combination below the band can be detected. Within the band, some particles can still be detected—if the particle location and velocity conditions are favorable. Thus, some particles within the band are detected for each case.

In section 7.5, particle velocity results were presented for each of the five cases. Despite being split between the two papers, the particle velocity, temperature, and size data are simultaneously taken. Figure 8.8 compares these three parameters. The top row of Figure 8.8

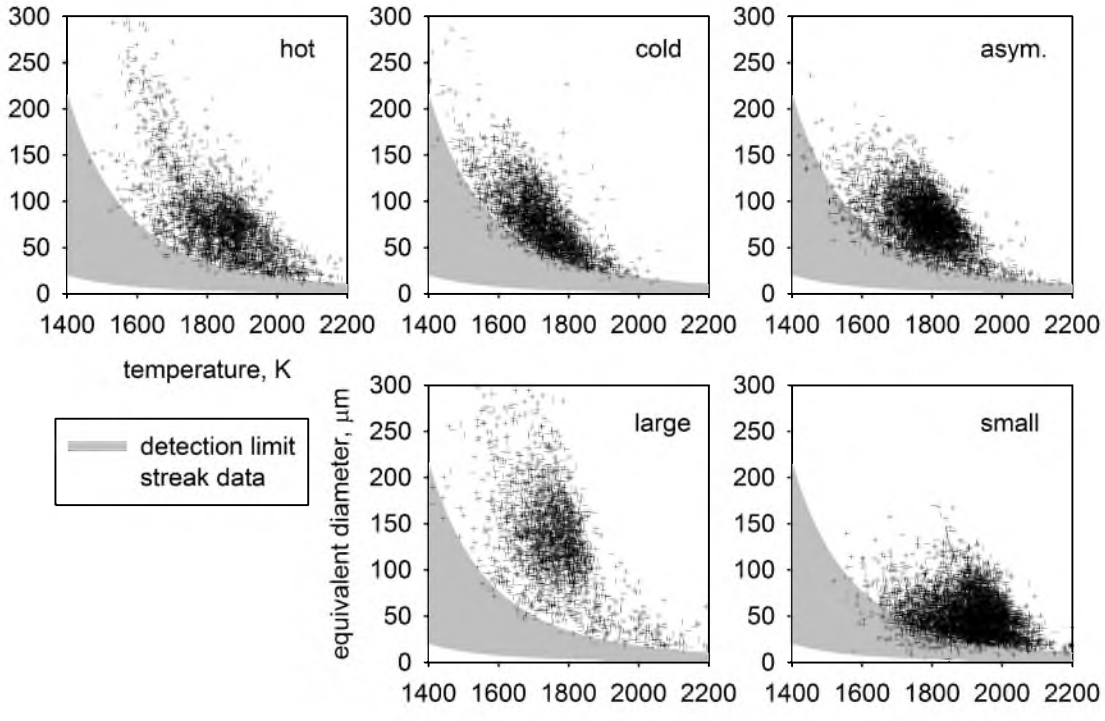

Figure 8.7: Bivariate plots of particle temperature and equivalent diameter for each case. The gray region represents the detection limit of the camera.

compares each particle's equivalent diameter to its velocity for each case. Correlating with intuition, the Small set has the smallest particles and the fastest velocities. Likewise, the Large set has the largest range of particle sizes with a wide range of velocities. The Hot and Cold sets have the same initial particle size, and their plots of equivalent diameter versus velocity look fairly similar. The Hot set has slightly higher velocities, most likely due to increased devolitilization. On close inspection, the Asymmetric set is composed of two distinct clusters overlapping vertically. This led to further analysis of the Asymmetric case in Figure 8.9. While this will be discussed in greater detail following that figure, one cluster is primarily composed of particles within the flame, while the other is primarily composed of particles blown outside of the flame by the coflow air. In general, the particles within the flame are at a higher velocity than those blown out of the flame. The Asymmetric case is seen to have smaller velocities on average than the Large case—despite having smaller initial particles, which is most likely due to the introduction of the coflow air.

The bottom row of Figure 8.8 compares each particle's temperature to its velocity for each case. Within most cases it is possible to see a slight positive correlation between temperature and velocity. The Hot set has a wider range of temperatures than the Cold

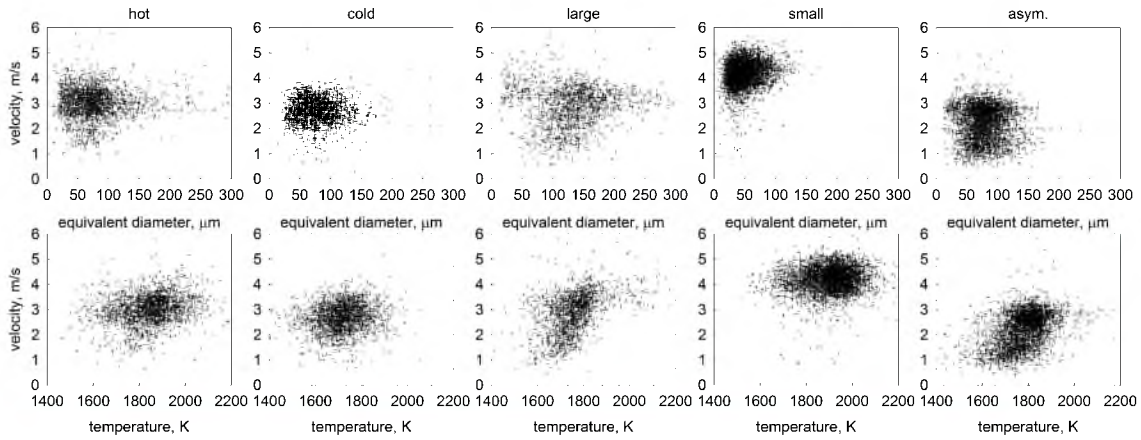

Figure 8.8: Bivariate plots of particle equivalent diameter versus velocity and particle temperature versus velocity for each case.

set, since more oxygen is available to heat the particles as they leave the burner. The Large set has the most obvious correlation between temperature and velocity, while the Small case has the weakest correlation. This may indicate that particle temperature has a stronger effect on the velocity of larger particles. With respect to the Asymmetric case, two distinct clusters are again seen stacked diagonally and to the right. As will be shown in Figure 8.9, generally, the particles within the flame are at higher temperatures than those blown out of the flame, as may be intuited.

Figure 8.9 shows the probability distributions of particle temperature, equivalent diameter and velocity for the Asymmetric case for two different depth bins in the z-direction. The blue dots in the first bin represent streaks closer to the camera, and the pink dots represent streaks further from the camera. The two bins were split at the middle of the burner. The bins have an uneven number of particles since the flame is asymmetric. Moving from the

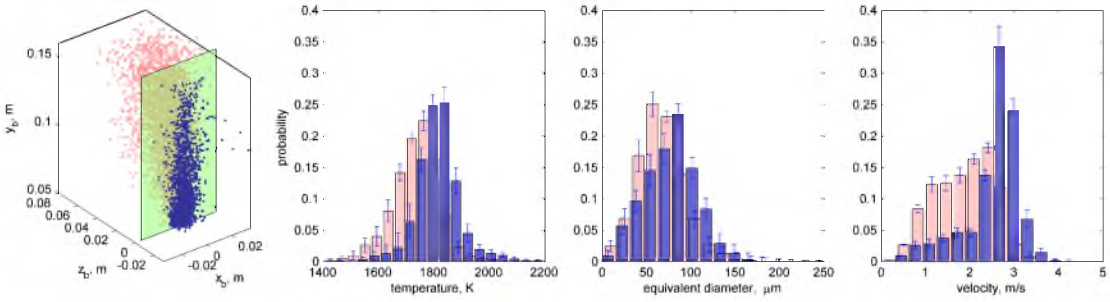

Figure 8.9: Probability distribution histograms of particle temperature, equivalent diameter, and velocity for two depth bands for the Asymmetric case. The two bands are shown on the left of the histograms. The coflow air introduced at the base of the flame blows the flame in the positive z-direction.

blue to the pink band—in the direction of the coflow air—the particle temperature, size, and velocity decreases. The temperature decreases since these particles have been blown out of the warmer flame area. Smaller particles are more easily blown into the second bin by the coflow air. Thus, there is a higher percentage of small particles present in the second bin. The particles blown into the second bin are not propelled upward as directly by the gases exiting the burner; thus, these particles have smaller velocities than those in the first bin.

Figure 8.10 shows the uncertainty contributions of various parameters for the temperature (in K and %) and equivalent diameter (in μm and %) measurements. Both uncertainties were normalized using the temperature or equivalent diameter of each streak to give each respective percentage. The spectral response and image sensor noise dominates the temperature uncertainty. The lamp temperature, calibration sensor noise and background subtraction have less of an effect. The background subtraction uncertainty values are at their highest for the Cold and Small sets. The Cold set has more radiating soot in the background than the other conditions. The Small set has more particles than the other conditions. This causes an increase in overlapping streaks, which creates additional background noise. Sensor noise in the image is more extreme than sensor noise in calibration, because the uncertainty is inversely proportional to the number of data points (see Equation 8.9). Twenty calibration images were taken of the lamp at each temperature, as opposed to the one image taken during data collection. Thus, during calibration, the number of data points is higher and the associated sensor noise uncertainty decreases. As previously discussed, the spectral response was assumed to have a normal distribution with a standard deviation of 5%.

The equivalent diameter uncertainty is much higher than the temperature uncertainty. The diameter is calculated using the temperature; thus, all the temperature measurement

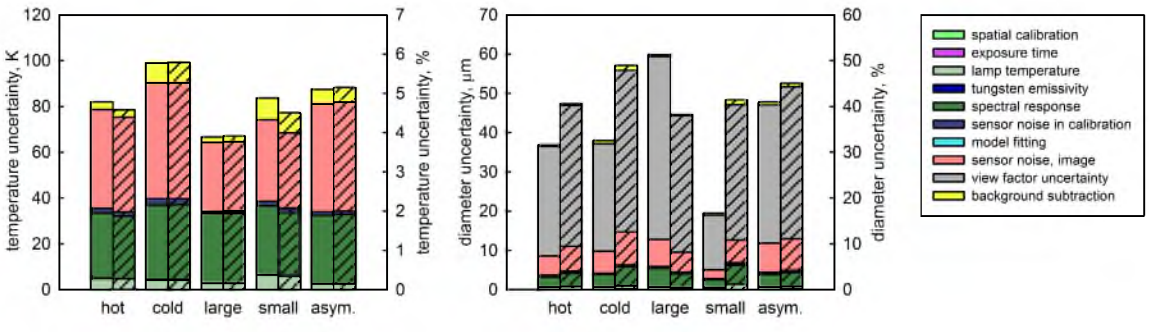

Figure 8.10: Uncertainty contributions for particle temperature and equivalent diameter.

uncertainties are propogated into the size uncertainty. The particle size uncertainty is dominated by the view factor uncertainty. This high uncertainty comes from the unknown shape of the burning particles and is illustrated in Figure 8.3.

8.7 Possible improvements

Among the uncertainty contributors shown in Figure 8.3, the term caused by background subtraction can be suppressed and the problem of luminous detection limit (see Figure 7.12) can be more or less solved by shifting the measurement wavelength range towards the infrared end of the spectrum. It is well known that soot radiation can be satisfactorily described by the Hottel–Broughton relation [119]:

$$\epsilon_{soot} = 1 - \exp \frac{-KL}{\lambda^{\alpha}}. \tag{8.10}$$

As seen, the emittance of soot is inversely proportional to wavelength, meaning that with a high enough wavelength, soot emission is expected to become negligible or less interfering. Preliminary tests were carried out by imaging the same flame (the Cold set, which was the most prone to obstructions caused by soot clouds) in both the visible and midwave infrared regions (centered at 3900 nm, with a full width at half maximum of 150 nm) of the spectrum. A resulting image pair from these tests can be seen in Figure 8.11.

As shown in Figure 8.11, particle streaks in the infrared appear more defined. Furthermore, more streaks can be detected as their intensities stand out from the background better. The benefits of midwave infrared imaging are clear in this application; however, it has to be noted that utilizing stereo infrared optics possibly increases the cost of the method by orders of magnitude. It is also expected that in practical situations, where particles are imaged within a radiating, refractory-lined chamber, wall radiation is more significant in the infrared than in the visible region.

8.8 Conclusion

This paper is Part II of a two-part study describing a novel method for measuring particle location, velocity, size, and temperature in pulverized-coal flames. In this paper, particle temperature and size measurements are discussed along with rigorous uncertainty quantification and validation experiments, building on the localization measurements described in the previous part. The proposed method is a combination of stereoscopic particle streaking velocimetry, particle emission imaging, and digital image processing. The main objectives of this paper were to 1) describe the concept of pyrometric sizing measurements in overexposed particle streak images, 2) assess the uncertainties inherent in the method

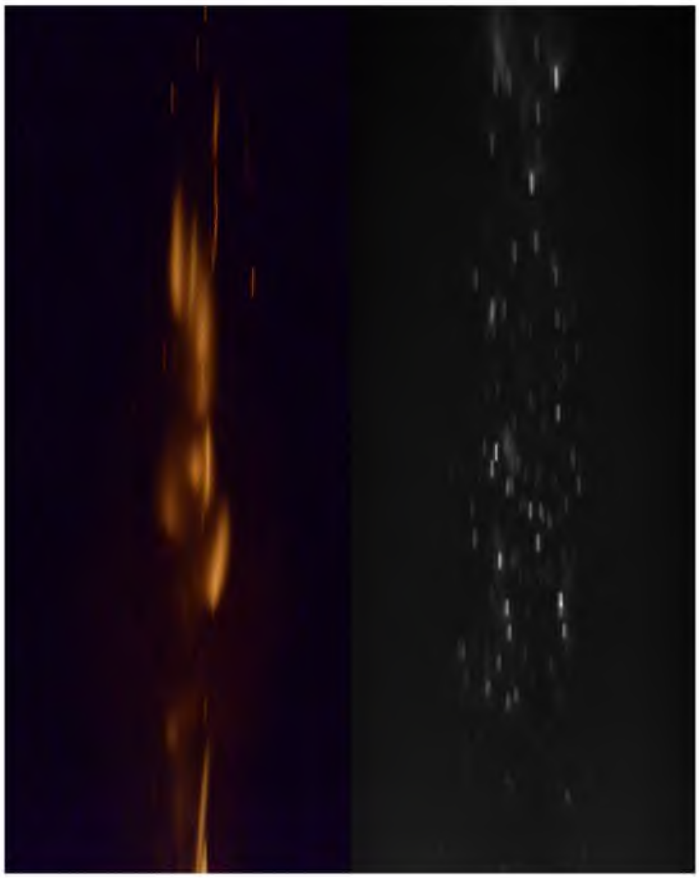

Figure 8.11: A comparison of typical particle images acquired in the visible range of the spectrum (left) and in midwave infrared (right). Particle streaks are much clearer in the infrared due to the reduced emittance of soot.

by identifying factors that contribute to total measurement uncertainty while propagating localization uncertainty quantified in Sedction 7, and 3) present postprocessed data of a laboratory-scale dataset to demonstrate the capabilities of the method. The sources of uncertainty inherent in particle temperature measurement were identified as the uncertainty in spatial calibration, exposure time, intensity calibration parameters, such as emissivity data, sensor noise, uncertainty in the image processing algorithms, and terms related to the underlying physics, such as the unknown particle shape and radiating background and other unwanted luminosity. Each term was rigorously assessed via either calibration, literature data, additional measurements, or numerical simulations. Uncertainty terms were propagated through the measurement model and total uncertainty values, along with their sensitivity indices, were obtained. It was found that under typical laboratory conditions, particle temperature can be measured up to a $\pm 5\%$ accuracy, while particle size can be measured by a $\pm 45\%$ accuracy, on average. Temperature measurements are most sensitive to

the sensor spectral response data and sensor noise, among which the former can be addressed by increasing the fidelity of spectral response measurements. By far, the most significant contributor to particle size uncertainty is the unknown particle shape, which cannot be addressed without significantly altering the method. Overall, the presented method is capable of measuring particle temperatures with accuracies comparable to already existing methods and measuring particle sizes with higher uncertainty than what is achievable with other methods. However, the technique presented in this paper has the benefit of being able to carry out these measurements along with simultaneous particle localization and velocimetry in three dimensions.

CHAPTER 9

THE POTENTIAL OF ON-LINE OPTICAL FLOW MEASUREMENT IN THE CONTROL AND MONITORING OF OXY-COAL FLAMES

Exp Fluids (2014) 55:1727
DOI 10.1007/s00348-014-1727-3

RESEARCH ARTICLE

The potential of on-line optical flow measurement in the control and monitoring of pilot-scale oxy-coal flames

Pal Toth · Zhonghua Zhan · Zhisong Fu · Arpad B. Palotas · Eric G. Eddings · Terry A. Ring

Received: 10 July 2013 / Revised: 29 March 2014 / Accepted: 10 April 2014

Abstract Digital image processing techniques offer a wide array of tools capable of extracting apparent displacement or velocity information from sequences of images of moving objects. Optical flow algorithms have been widely used in areas such as traffic monitoring and surveillance. The knowledge of instantaneous apparent flame velocities (however, they are defined) may prove to be valuable during the operation and control of industrial-scale burners. Optical diagnostics techniques, coupled with on-line image processing, have been applied in the optimization of coal-fired power plants; however, regardless of the available technology, the current methods do not apply optical flow measurement. Some optical flow algorithms have the potential of real-time applicability and are thus possible candidates for on-line apparent flame velocity extraction. In this paper, the potential of optical flow measurement in on-line flame monitoring and control is explored.

1 Introduction

The applicability of digital image processing-based techniques for monitoring, controlling and optimizing industrial-scale pulverized-coal burners has been widely studied. Digital imaging is an attractive approach to achieve these objectives because of its flexibility and high data rate. Previous studies managed to obtain information regarding flame luminosity or brightness (Shimoda et al. 1990; Lu et al. 2004, 2005), temperature, based on two-color pyrometric concepts (Jiang et al. 2009; Smart et al. 2010; Xiangyu et al. 2011; Lou et al. 2011; Gonzalez-Cencerrado et al. 2012), flame geometry (Baldini et al. 2000), flame stability and flicker frequency (Zhang et al. 2011; Sun et al. 2011; Gonzalez-Cencerrado et al. 2012) and flame spectra (Baeg et al. 2005; Sun et al. 2011), among others. The key incentive behind advanced, vision-based on-line flame monitoring are the "increasingly stringent standards on energy saving and pollutant emission" (Lu et al. 2005). Water (Lu et al. 2004; Gonzalez-Cencerrado et al. 2012) or air-cooled (Jiang et al. 2009; Lou et al. 2011), ruggedized camera assemblies with optical guides, have been used for flame monitoring in systems larger than laboratory scale.

Optical flow is a general term referring to the apparent (projected) motion of brightness patterns in a sequence of scalar (intensity) images. Computer algorithms that can extract optical flow (OF) from video data are used in off-line combustion diagnostics, such as in particle image velocimetry (PIV) or particle tracking velocimetry (PTV). By the term "off-line," we refer to the typical procedure by which combustion diagnostics are performed: The imaging is done prior to the batch processing of image data. In contrast, by "on-line" measurements, we refer to techniques that can provide information simultaneously with imaging at a sufficient data rate so that the extracted information can be used a in control loop.

In an industrial environment, typical optical combustion diagnostics methods are rarely applied because of their sensitivity to dust, vibrations, temperature and due to their equipment cost. Although efficient software allows for on-line data acquisition (Arik and Carr 1997; Roberts 2012) in industrial settings, the standard method for flow visualization and velocity measurement, PIV, is impractical due to the need to operate lasers. In PIV, lasers are used to

P. Toth (✉) · Z. Zhan · Z. Fu · A. B. Palotas · E. G. Eddings · T. A. Ring
Department of Chemical Engineering, University of Utah, 50 S. Central Campus Drive, Salt Lake City, UT 84112-9203, USA
e-mail: toth.pala@gmail.com; toth.pal@uni-miskolc.hu

Published online: 04 May 2014

make velocity measurements planar, i.e., motion only in the plane of the illuminating laser sheet is registered. By omitting the use of laser sheets, the acquired flame image sequences contain out-of-plane motion as well. Nevertheless, this motion, if extracted, might prove to be useful information from the perspective of flame monitoring and control. None of the previously listed studies (Kurihara et al. 1986; Baek et al. 2001; Lu et al. 2008) apply optical flow extraction.

In contrast with the typical cross-correlation-based PIV algorithms, optical flow algorithms extract apparent motion based on the brightness constancy assumption, expressed as

$$I(x, y, t) = I(x + u, y + v, t + 1), \tag{1}$$

where $I(x, y, t)$ is the intensity in an image sequence at a pixel location (x, y) and time t and (u, v) are the two components of the apparent displacement. Note that for notation purposes, the interframe time Δt is chosen to be unity, but when computing OF velocity, (u, v) must be divided by the real value of Δt. Optical flow algorithms aim to solve the inverse problem of obtaining (u, v) by satisfying Eq. (1). More refined methods apply multi-scale frameworks (Bouguet 2000), image segmentation (Farneback 2001), approaches that can handle discontinuous flow fields (Deriche et al. 1995) or balance the resulting flow to also account for the gradient constancy assumption:

$$\nabla I(x, y, t) = \nabla I(x + u, y + v, t + 1) \tag{2}$$

Similar algorithms were used to perform unseeded, planar, laser velocimetry on small-scale flames (Fielding and Long 2000; Fielding et al. 2001) or to study mixture formation (Scholz et al. 2008).

The optical flow algorithm implemented in this study (Brox et al. 2004) solves Eqs. (1) and (2) by minimizing the energy functional

$$E(\mathbf{w}) = \mathbf{E}_{\text{data}} + \alpha \mathbf{E}_{\text{smooth}}, \tag{3}$$

where

$$E_{\text{data}}(\mathbf{w}) = \int_{\Omega} \left(|I(\mathbf{x} + \mathbf{w}) - \mathbf{I}(\mathbf{x})|^2 + \gamma |\nabla I(\mathbf{x} + \mathbf{w}) - \nabla \mathbf{I}(\mathbf{x})|^2 \right) \mathbf{dx} \tag{4}$$

$$E_{\text{smooth}}(u, v) = \int_{\Omega} \psi \left(|\nabla_3 u|^2 + |\nabla_3 v|^2 \right) \mathbf{dx} \tag{5}$$

Here, $\psi(s^2) = \sqrt{s^2 + \epsilon}$, with ϵ being set to 0.001, $\nabla_3 = (\partial_x, \partial_y, \partial_t)^T$[1] is the spatiotemporal intensity gradient, $\mathbf{w} = (\mathbf{u}, \mathbf{v}, \mathbf{1})^{\mathbf{T}}$ is the vector of interframe displacement, $\mathbf{x} = (\mathbf{x}, \mathbf{y}, \mathbf{t})^{\mathbf{T}}$ is the vector of spatiotemporal location in the video, Ω is a local image region and the parameters γ and α are free parameters. The parameter γ is the relative importance of the gradient constancy assumption in solving the inverse problem and α is the importance of the smoothness criterion of the OF velocity field $\mathbf{w}$. The algorithm of Brox et al. was chosen due to its high accuracy and computational efficiency.

In this paper, the potential of an optical flow velocimetry (OFV) technique that does not require seeding particles or lasers, that can operate at safe distances from a pulverized-coal flame and that can be made efficient enough for on-line data acquisition in flame monitoring and control is demonstrated. An oxy-coal flame with a nominal thermal output of 120 kW was studied by the OFV method. The responsiveness and sensitivity of OFV measurements are demonstrated by monitoring changes in OF velocities following perturbations in combustion conditions.

2 Materials and methods

In this section, the relevant details of the experiments are presented. This section includes a description of the combustion system, imaging equipment and image processing.

2.1 The combustion system

The combustion system used in this study was a pilot-scale oxy-coal combustor burning Utah Sufco bituminous coal with a nominal heat output of 120 kW. Oxy-firing is a promising new technology with the objective of reducing global CO_2 emissions by facilitating the more complete capture of flue gas CO_2. In oxy-coal firing, coal is fired in a stream of relatively pure O_2 with CO_2 that has been recycled from the combustion products (Buhre et al. 2005). In these experiments, pure CO_2 was utilized without flue gas recycle.

The details of the construction of the oxy-coal combustor have been reported previously (Zhang et al. 2007). In brief, the combustion system consists of a refractory-lined, cylindrical combustion chamber with an inner diameter of 0.61 m, a cylindrical radiative section with an inner diameter of 0.27 m and a convective zone with installed heat exchangers (0.15 × 0.15 m, square cross-section). The flue gas leaving the convective zone passes through a bag filter before being emitted. The furnace is controlled by an automated digital system that takes gas concentration, flow rate and temperature information as the input in its control loop. The combustion chamber ("burner section") of the system has built-in electric wall heaters

[1] T denotes vector transpose.

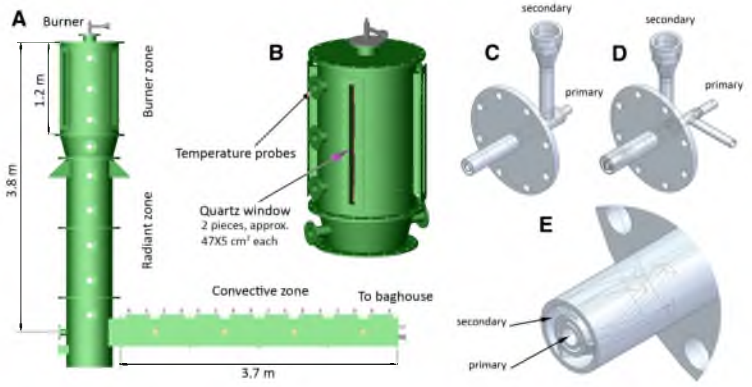

Fig. 1 A schematic of the combustion system used in the experiments. **a** Side view of the oxy-coal combustor with the combustion chamber and flue gas disposal system. **b** A rendering of the combustion chamber. **c** A rendering of the co-axial burner. **d** A rendering of the swirl burner. **e** A close-up view of the head of the swirl burner with the swirling vanes in the secondary stream shown. The middle stream of the swirl burner was not used

Table 1 Burner dimensions, mm (ID–inner diameter, OD–outer diameter)

	Inner tube ID	Inner tube OD	Outer tube ID	Outer tube OD	Remarks
Co-axial burner	15.8	21.34	35.05	42.16	–
Swirl burner	12.52	26.67	40.89	48.26	3 turning vanes, 15°

(each 800 W) that allow for keeping wall temperature constant during experiments. This section also has 4 quartz windows set at 90 degree orientations (approximately 5×100 cm^2) as optical access ports. Figure 1a, b shows the combustion system schematically.

Two types of burners were used in the experiments: a co-axial zero-swirl burner and a swirl burner. Both burners were tube-in-a-tube constructions (with pulverized coal and the primary gas stream in the inner tube and the secondary gas stream in the outer annulus). The two types of burners produced significantly different flame geometries. From the perspective of computing optical flow from flame images, the co-axial burner was expected to produce flames with more homogeneous velocity fields dominated by the axial velocity component, while the swirl burner was thought to produce flames with a wider range of arising instantaneous velocities and higher tangential velocities. For this reason, we chose to evaluate the optical flow method with both types of burners. The dimensions of the burners can be seen in Table 1. Isometric views of the burners are shown in Fig. 1c–e.

2.2 Imaging

A Photron APS-RX type visible, high-speed camera was used to acquire most of the flame image sequences presented in this paper. The camera captured 1 Mpixel, grayscale images at a bit depth of 10 bits. A telephoto lens (Tamron, 18–270 mm) was used in conjunction with the camera. The focal length of the camera was set to 50 mm. The spectral sensitivity range of the camera was 300–700 nm. The magnification of the system was approximately 0.05. The overall lateral resolution of the system was approximately 2 mm in the center plane of the imaged flame, at a standoff of 1.5 m from the quartz window.

The camera captured a field of view (FOV) of approximately 50×50 cm^2. This FOV contained about half of the total height of the quartz window. The whole window was not captured in order to obtain sufficient image resolution over the flame image. The region 0–50 cm downstream of the burner was captured in cases where the co-axial burner was used, while the region approximately 10–60 cm downstream of the burner was imaged in the cases done with the swirl burner. This choice of regions of interest is justified by the different flame liftoff for the two burners: flames produced by the co-axial burner were usually attached to the burner surface, while swirled flames were detached and their luminous region started downstream of the burner. Each recording was approximately 5 min long. As the luminous intensities of the flames produced by the two burners were different, the aperture setting of the lens was set to best fit the dynamic range of the camera. In every case, the entire thickness of the flame was within the zone of acceptable sharpness. Imaging parameters during runs were not changed.

The camera was triggered such that the timing simulated the double-framing mode of typical PIV cameras. In this timing scheme, frames are acquired in pairs and the time between subsequent pairs is longer than the time between frames within pairs. The interframe time between frames within pairs for the camera was 333 μs. Fifty frame pairs were acquired each second. The integration time of each frame was 80 μs.

For triggering the camera, a Stanford Research DG535 type digital delay generator was used. The generated TTL pulses were 1 μs long. Each pulse reset the internal clocks of the camera. The second frames in dual-frame pairs were triggered by the reset 3 kHz internal frequency generator, thus the interframe time of 333 μs was realized inside dual-frame pairs.

2.3 Image processing

In the first step of image processing, the acquired images were registered. The registration step included cropping and rotating the images to a vertical orientation, i.e., the burner axis pointed downwards.

The processing of the OFV images utilized the optical flow algorithm of Brox et al. (2004). There was no preliminary normalization necessary before running the optical flow routine on the acquired luminosity images. A standard library (OpenCV) was used to implement the CUDA variant of the OFV routine on a graphical processing unit (GPU). There are a number of free parameters in this algorithm (see Sect. 1).

Omitting further details, one needs to set a high value of α when the underlying displacement field is assumed to be smooth, a high value of γ when one wants to balance the extracted motion field to favor edges over brightness patterns in tracking and a high value of n_p when a large spatial variation of displacement is expected. Increasing both n_l and n_o typically results in higher precision at the cost of increased computation time. In our implementation, the remaining parameter, r_f, was used in conjunction with n_p for fully determining the image pyramid. For computing the OF velocity fields presented in Sects. 3 and 4.3, the following parameter values were used: $\alpha = 100, \gamma = 3$, $\eta = 0.5. n_p = 2. n_l = 7, n_o = 50$[2]. The parameters were set by inspecting the obtained displacement fields and visually comparing them to overlaid double frames. An example of overlaid frames and extracted displacement fields are shown in Fig. 2.

Note that the spatiotemporal gradient (see Eq. (5)) was replaced with the spatial gradient, since the two-frame implementation of the optical flow algorithm was used. The spatial gradient was computed by the Sobel operator on every scale of the image pyramid (Gonzalez and Woods 2001).

3 Flame monitoring by OFV

In this section, the potential of OFV in practical applications as an input provider for control loops is demonstrated. In these tests, image sequences were produced that captured transient flame behavior during scenarios in which furnace operating conditions were abruptly changed. These sequences of images were processed by the OFV algorithm and transient OF velocity maps were computed.

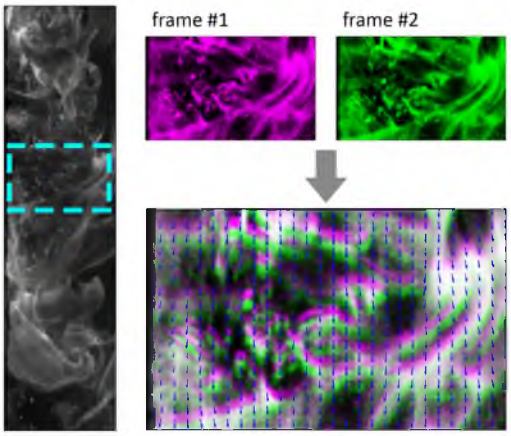

Fig. 2 An example OF velocity field obtained from a frame pair. *Left* frame #1 of a flame image pair. The *rectangle* shows a detail that was enlarged. *Top right* the marked detail in frames #1 (*magenta*) and #2 (*green*). *Bottom right* overlaid frames and extracted displacement field. The purpose of this montage is to illustrate how the flame image moves between two consecutive frames. The images were contrast-enhanced to improve visibility

The test scenarios simulated unexpected pressure fluctuations in the secondary gas inlet stream and abrupt changes in the coal feeding rate. Each of these scenarios started from the same base conditions, which were altered during operation and the transient behavior of the flame was captured by the OFV technique. By these scenarios, we studied the effect of decreasing or increasing the secondary CO_2 flow and decreasing the coal feed rate. A total of 6 runs were done: the three test scenarios (CO_2 drop, CO_2 increase and coal feed rate decrease) were run with both the co-axial and swirl burners. The absolute change in the total gas flow rate studied during the scenarios was approximately 15 %, while the decrease in coal feed rate was about 40 %.

The operating conditions are shown in Table 2. Characteristic flame images shown in Fig. 3 illustrate the visible changes caused by the perturbations. As can be seen, changing the operating conditions altered flame appearance in every case. The most drastic changes were caused by decreasing the coal feed rate, which de-stabilized the flames and resulted in a flickering behavior.

The simplest way to illustrate the velocity tracking capabilities of the OFV method is the visualization of the

[2] These parameter values are consistent with the original paper of Brox et al. (2004). η is the reduction factor between subsequent pyramid levels.

transient OF velocity. Since the visualization of transient two-dimensional fields is difficult, it is practical to present results as transient point measurements. Note that OFV is capable of extracting velocities within the whole region of interest, thus reducing the data to point measurements involves defining "points," in which OF velocity magnitude is tracked as a simple scalar parameter. Figure 4 serves to illustrate this concept. The "point measurements" shown in Fig. 4 are in fact spatial averages of OF velocity magnitude within small interrogation areas defined within image frames. These small subregions are shown as green (position #1, far-burner) and blue (position #2, near-burner) rectangles. The interrogation areas were approximately 0.4 and 0.2 m downstream of the burner for the runs done with the co-axial burner. The camera was repositioned for runs with the swirl burner to best capture the luminous zones of the swirled flames. For those runs, the interrogation areas were placed at approximately 0.5 and 0.3 m downstream of the burner.

Table 2 Operating conditions during the test scenarios

Parameter	Unit	CO_2 flow rate drop	CO_2 flow rate rise	Coal flow rate drop
Coal feed rate	kg/h	4.7	4.7	4.7→2.7
Primary O_2	kg/h	1.1	1.1	1.1
Primary CO_2	kg/h	6.8	6.8	6.8
Secondary O_2	kg/h	10.4	10.4	10.4
Secondary CO_2	kg/h	10.4→5.9	10.4→14.9	10.4
Wall temperature	°C	1010	1010	1010
Flue gas exit temperature	°C	200	200	200
Flue gas O_2 concentration	vol%	3→varying	3→varying	3→varying

The table lists three different scenarios. These three scenarios were run with both the co-axial and swirl burners; thus, the total number of experiments run was 6. *Arrows* denote the abruptly changed parameters from base operation. The base settings were the same in each scenario

As seen in Fig. 4, the obtained OFV velocities were responsive to changes in operating conditions. In the first test scenario shown in Fig. 4, the flow rate of secondary CO_2 was decreased by 15 %. Shortly after the transient event, OFV indicated a drop of apparent velocity in both interrogation areas. The measurements of the flue gas analyzers slowly followed the trend detected by OFV. The time lag between the optical method and the gas analyzers was approximately 2 min. Note that this time lag was due to the travel time of the sampled gas from the combustor to the flue gas analyzers installed in a control room. The length of the gas transport tubes was on the order of 10 m. Even with this time delay subtracted, the flue gas analyzers showed a much slower response (around 3 min) in terms of reaching the new steady state. This slow response is specific to the gas analyzers that were used; however, the response time reported here most likely well represents the expected responsiveness of conventional gas analyzers. In

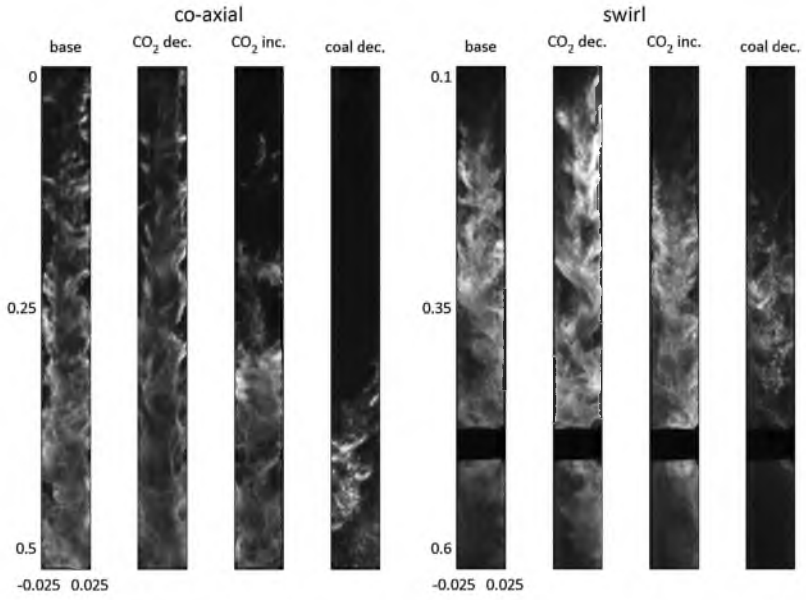

Fig. 3 Characteristic flame images of the different experimental cases. The differences in appearance are caused by changing aerodynamic, chemical and thermal conditions. The images were slightly contrast-enhanced to improve visibility. Intensities are normalized (Pizer et al. 1987). The dimensions are in meters. The gaps in the swirled flame images are gaps between the two parts of the quartz window

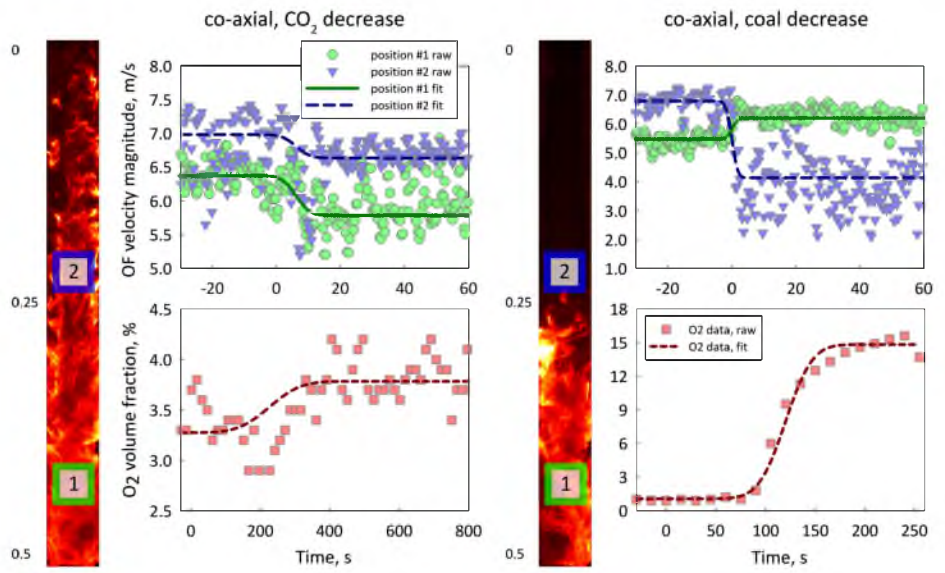

Fig. 4 A demonstration of transient OF velocity magnitudes measured during two scenarios: decreasing CO_2 and decreasing coal feed rate. Both tests were done with the co-axial burner. The flame images show the locations of subregions in which the displayed transient velocities were measured and illustrate flame detachment. Axial coordinates are given in meters. The *top row* shows the OF velocity measurements collected within the two subregions. Note that the shown raw OF velocity data are subsampled to improve visibility—the original measurements produced 50 velocity maps per second. The *bottom row* shows the response in the O_2 concentration of the flue gas, measured by infrared gas analyzers. The first column shows the data collected during the CO_2 drop scenario and the second column shows results of the coal decrease scenario. Trend lines are best fits of the generalized logistic function (Richards 1959) computed by nonlinear regression. The time scale shown has the origin at the transient event, i.e., at the instant when the operating conditions were changed. The time delay in the gas analyzer system was not subtracted from the *x*-axis coordinates in figures of the bottom row in order to illustrate the typical delay of gas analyzers compared with OFV measurements

the test in which the secondary CO_2 was decreased, apparent velocity most likely decreased due to reduced volumetric gas flow. Flame stability was not affected by this change. Flue gas O_2 concentration increased due to the reduced dilution of the flue gas by CO_2.

Interpreting the results shown in the second column of Fig. 4 is more difficult as flame stability was significantly affected by decreasing the coal feed rate. Under such conditions, the interpretation of the results is only possible by considering thermal, chemical and aerodynamic effects simultaneously. The high rise in flue gas O_2 concentration was caused by the massively changed stoichiometric ratio in the flame. The decreased velocities measured in position #2 (closer to the burner head) showed significantly increased variation and reduced data rate. The change in data rate was caused by flame detachment—in other words, the luminous zone of the flame shifted downstream, away from the burner surface. Flickering flame behavior may cause insufficient luminosity at certain instances in the interrogated area, which in turn results in missing OFV data. The change of mean OF velocity in both positions was possibly caused by the downstream shifting of the ignition and devolatilization zones of the flame. In these zones, due to high rate of heat generation and the release and expansion of volatiles, flame velocity is expected to have a local maximum.

Figure 5 shows the transient velocities obtained in the rest of the transient test scenarios. In most cases, OFV produced useful responses in the transient apparent velocity signals. In some cases, e.g., in the case of decreasing CO_2 with the swirl burner, even the oscillatory behavior of velocity caused by the abrupt change in flow rates was captured. Note that some trends are not obvious in Fig. 5, such as the increasing velocities that followed the decrease in the secondary CO_2 in the case of the swirl flame. For a satisfying explanation of this observation, it is useful to study the joint behavior of apparent flame velocity and intensity. Further trends seen in Fig. 5 are explained in conjunction with the joint intensity-velocity data. Figure 6 shows extracted axial profiles of flame intensity and OF velocity magnitude. The presented profiles are ensemble-averages of the two "steady" states in each experiment: the

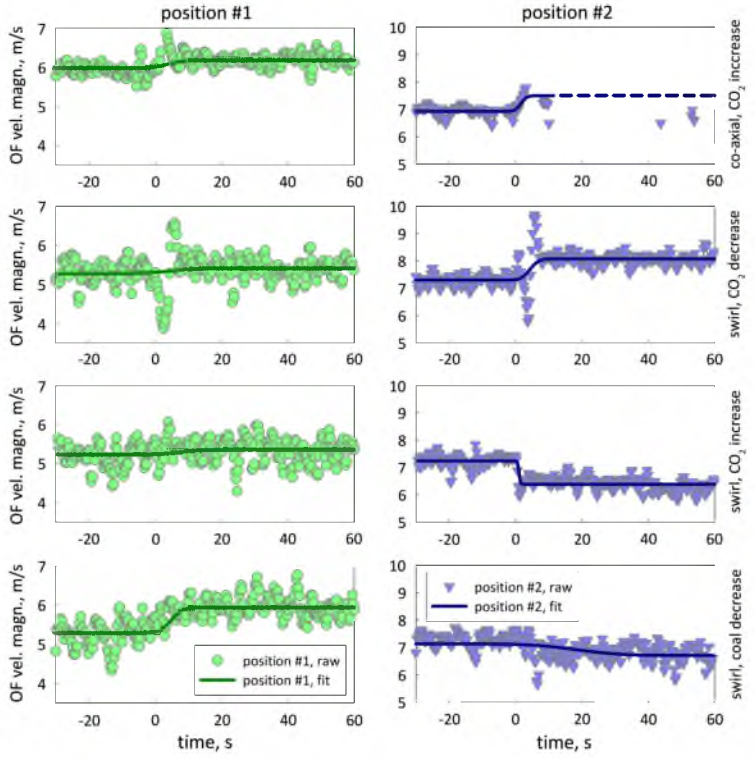

Fig. 5 Transient time-apparent velocity plots showing the response in OF velocity values obtained by OFV to changes in operating conditions. The *horizontal axis* shows time in seconds, the *vertical axis* is OF velocity magnitude in m/s. Labels indicate the interrogated subregion in the flame and the test scenarios. Fit functions are of the logistic form

base starting operation and the operation after the varied parameter were changed. Note that by steady states we simply refer to the operation before and after the perturbation—by this term, we do not intend to characterize the "steadiness" of each state, as in some cases (e.g., the coal flow rate drop scenarios), the flame remained unstable after the transient event.

As mentioned previously, decreasing the CO_2 co-flow in the flames produced by the co-axial burner decreased OF velocity magnitudes in most of the observed region of interest. This can be explained by the lower volumetric flow rate of gas. At the same time, as seen in Fig. 6, flame intensity increased, possibly due to the decreased amount of diluting CO_2. In the case of the co-axial burner, increasing CO_2 co-flow did not clearly produce the opposite effect, as this change destabilized the flame. For this reason, OF velocity and intensity data were only available in the lower portion of the imaged region (below 0.25 m downstream from the burner). In this region, apparent flame velocity showed an increasing trend with axial location and the perturbed OF velocity exceeded the base velocity at approximately 0.4 m downstream of the burner. The low OF velocity in more upstream regions of the flame was due to flame detachment. A similar trend is seen in the scenario in which coal feed rate was decreased, indicating that in both cases, the co-axial burner produced a detached flame. Notice the higher variance in both apparent flame velocity and intensity in this scenario, which suggests an unstable flame.

The scenarios varying CO_2 co-flow with the swirl burner are illustrative of the joint effect of thermal, chemical and aerodynamic factors. With the swirl burner, in contrast with the co-axial cases, decreasing CO_2 increased both velocities and flame intensity, while increasing CO_2 co-flow decreased them. The trends in flame intensity profiles can be explained by thermal and chemical principles. Decreasing CO_2 flow rate decreases the dilution of the flame, which affects the total thermal inertia of the flame, possibly along with reaction rates. Trends in OF velocity profiles are more difficult to interpret, due to the significance of aerodynamic factors. Referring back to part E of Fig. 1, the varied CO_2 flow rate affects only the secondary stream of the swirl burner—this is the swirled stream. Therefore, if the momenta of the secondary and primary streams are comparable (they were in these cases), it is expected that changing the flow in the secondary stream

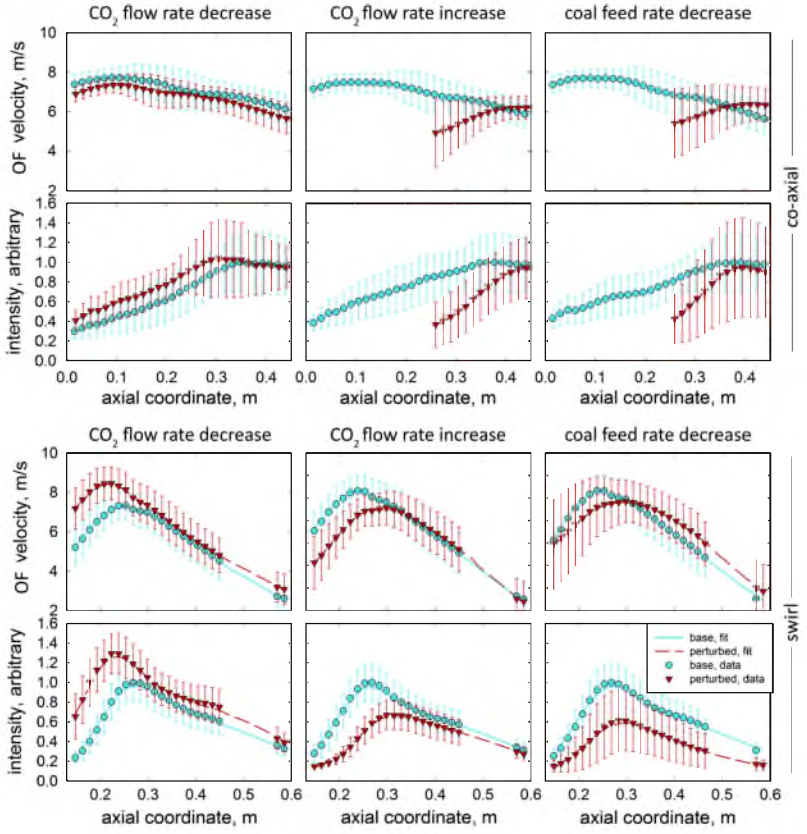

Fig. 6 Extracted axial profiles of apparent flame velocity magnitude and intensity. The profiles are ensemble-averages of "base" and "perturbed" operation. The averages were computed in subsets before and after the transient events. The *error bars* indicate one standard deviation of the collected measurements. *Top row* OF velocity profiles of the cases run with the co-axial burner. *Second row from the top* flame intensity profiles of flames produced by the co-axial burner. *Third row* OF velocity profiles of the cases run with the swirl burner. *Second row from the top* flame intensity profiles of flames produced by the swirl burner. The gaps in the swirl case profiles were caused by the blocked optical access between the two parts of the quartz window. Trend lines and interpolation over missing data were computed by the LOESS method (Cleveland 1979)

affects the overall swirl of the flame. When flow rate is increased in the secondary stream, a higher tangential velocity is attained throughout the flame, which increases the jet-like spread of the flame, resulting in lower velocity magnitudes. This is a possible explanation for the reversed trends in OF velocity in the swirled flames relative to the zero-swirl flames seen in Figs. 6 and 5. Further proof is provided for this idea in Fig. 7. In the coal decreasing scenario, the swirl flame also showed an unstable behavior—this is visible in the high variation of OF velocity in regions above 0.3 m downstream of the burner (this is the zone of detachment) and in the high variation of intensity values. The shifted OF velocity profile is also indicative of downstream shifted ignition and devolatilization zones. Due to the significantly reduced thermal output of the flame, intensity decreased over the whole imaged area compared with the base state.

Apart from apparent velocity magnitude, the direction information in the extracted OF velocity fields can also be considered for utilization in control loops. The direction of apparent velocity vectors itself lacks generality for direct use, but a scalar property characterizing the directions in the vector fields can be a useful candidate. Such a scalar property can be a measure analogous to the swirl number of a flame The swirl number is defined as

$$S = \frac{\int_0^R wur\mathrm{d}r}{\int_0^R uur\mathrm{d}r}, \tag{6}$$

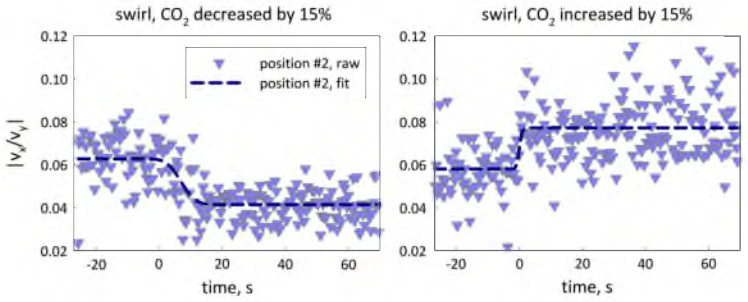

Fig. 7 The transient behavior of the simplified indicator of flame swirl, S_v, for the scenarios in which flame swirl was expected to change. The change of swirl was only significant in the upstream regions of the flames, therefore only the transient signals extracted in position #2 are shown. As expected, decreasing CO_2 co-flow decreased swirl, while increasing CO_2 co-flow increased swirl. Fit functions are of the logistic form

where w and u are tangential and axial velocity components, respectively, r is the radial coordinate and R is some characteristic radius of the system. Customarily, S is computed by using mean velocities and burner geometries, but it can also be computed locally, using local means of velocity. Unfortunately, r is not measured by the OFV method; thus, the local version of S cannot be directly computed from OFV data. Since S expresses the ratio of tangential and axial momenta, an analogous, simplified descriptor can be defined as the ratio of x and y projected velocity components, where x is the projected radial coordinate and y is the axial coordinate. Thus, the simplified measure of flame swirl analogous to the swirl number is computed as follows.

$$S_v = \left|\frac{v_x}{v_y}\right|. \tag{7}$$

S_v was also computed in the interrogation areas shown in Fig. 4 as the ratio of local mean x and y velocities. Figure 7 shows the extracted results for the swirl, CO_2 decreasing and increasing scenarios.

As is apparent from Fig. 7, decreasing CO_2 co-flow decreased the swirl of the flame, while increasing CO_2 increased it. This is in agreement with the OF velocity data (see Fig. 6). Note that the flame spread caused by the increased tangential pull is not directly visible in the images due to the limited optical access. However, by looking at Fig. 3, some widening is visible in the case of the CO_2 increasing scenario. This is most apparent when comparing the flame images of the CO_2 increase case with the CO_2 decrease case.

4 Remarks

In this section, various issues regarding the physical meaning of OF velocities and the practical applicability of the method are addressed.

4.1 Interpreting OF velocities

Section 3 demonstrated the responsiveness of OFV measurements to changes in operating conditions. However, it is important to point out that OF velocity, as it is extracted from typical line-of-sight images, is not equivalent to either flame front velocity, gas velocity or particle velocity. It is practical to consider OF velocity as a quantifier of the apparent, projected motion of scalar fields. The practicality of this consideration lies within the terms used to describe OF velocities:

1. The apparent nature of the motion suggests some subjectivity in OF velocity extraction. The most well-known cause of this subjectivity is the aperture problem—in other words, flow patterns close to occlusions and within bounded regions cannot be exactly determined. More generally, OF motion is always an approximation of the projected physical motion, as physical motion is not necessarily correlated to image intensity. Other difficulties contributing to the subjectivity of OF velocity are summarized in (Beauchemin and Barron 1995).
2. The nature of the projection responsible for image formation is a significant factor contributing to the uncertainty in the definition of OF velocities. When monitoring combustion systems, the image formation process typically includes emission, absorption and refraction. The emission of photons happens in a volume. The emitted photons interact with parts of the flame and some are absorbed. Since turbulent flames often exhibit steep gradients in their corresponding physical fields, the effect of absorption through flame layers is not constant over an image. This results in images in which it is unclear which layer of the flame is visible at a particular location; thus, OF velocity maps are heavily convoluted by the effects of unknown

observed depth. OF velocities may be more meaningful in the case of certain flame geometries than in others. Refraction plays a role in bending light rays that travel within the flame and through lenses. Image distortion caused by either excessively high gradients in the refractive index field of a flame or lens distortion affects the fidelity of obtained OF velocity values.

3. The emitting scalar field itself heavily determines what becomes apparent in images. When studying luminous flames, the scalar field is typically a function of local temperatures and the concentration of gaseous species and soot. In images of complex flame geometries, particularly of hollow flames surrounded by strongly absorbing layers, the extracted OF velocities mostly express the projected motion of the surface of the flame, possibly convoluted by a significant z-component of the velocity. It is thus important to know the practical limitations of OFV monitoring in terms of flame sizes and geometries. As the scalar field is a function of temperature and concentration, in some cases, insufficient signal levels cause regions of missing data in OF velocity maps.

4.2 Sensitivity to input parameters

One way to assess the uncertainty caused by the subjectivity inherent in OF velocity extraction is measuring the sensitivity of the obtained data to the variation of the input parameters of the OF algorithm. The effect of input parameter variation was assessed by Monte-Carlo simulations. The simulations consisted of running the OF algorithm over a subset of flame images with input parameters drawn randomly from uniform probability distributions. The varied parameters were α, the relative importance of image intensity and γ, the relative importance of image gradients. The ranges of variation were 80–120 and 1–5, respectively. These ranges were determined empirically, by observing the extremes of the parameter combinations that still produced meaningful apparent motion fields. Each image was processed with a 10^3 combinations of α and γ drawn from the ranges given above. The sensitivity of OF velocities to input parameter variation is expressed as the standard deviations of the populations of the 10^3 OF velocity values obtained at every pixel. The averages of these standard deviations over every image are shown in Fig. 8. The subsets of images were picked from image sets of steady operation (see Table 2). A subset of 100 images was selected from cases with the co-axial burner and the swirl burner (total of 200 images).

As seen in Fig. 8, the variation caused by OF velocities by the input parameter variation was generally higher in the case of images of the swirled flame. This alone does not tell much about the geometry of the flame—it merely implies that the motion of visual patterns arising in the swirled flame was more ambiguous than of those in the co-axial flame. The relative sensitivity of the y-component (vertical component) of OF velocities stayed under 5 % in both the co-axial and swirl cases. The horizontal component showed a higher relative sensitivity, possibly because of the lower and zero-mean projected tangential velocities. The relative sensitivity of the vertical (projected axial) velocity component is promising.

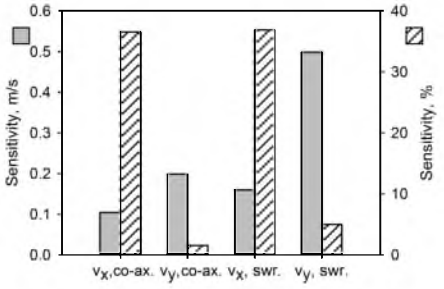

Fig. 8 The sensitivity of OF velocities to variations in parameters α and γ. Sensitivity is expressed as the standard deviation of OF velocity values computed in Monte-Carlo sets varying α and γ. The *left vertical axis* shows sensitivity in m/s units, while the *right vertical axis* shows sensitivity values relative to mean OF velocities

4.3 Handling missing data

As mentioned in Sect. 4.1, the peculiarities of the emitting scalar field may yield insufficient image intensity (signal strength) either locally or globally in a flame image used to extract OF velocity. Images of inherently non-luminous or lifted flames, such as the ones shown in Fig. 3, may contain featureless regions. "Holes" in intensity images can be treated statistically via forms of temporal averaging and missing data handling. Another method is to shift the range of imaged wavelengths to regions in which the monitored flames show sufficient luminosity. Sooting flames typically emit in the visible band, as demonstrated in Sect. 4. Non-sooting flames may still be monitored by the OFV technique in the infrared. Figure 9 shows synchronized pairs of visible and mid-wave infrared (MWIR) flame images along with axial profiles of OF velocity extracted from both visible and infrared image sequences.

For acquiring the infrared images shown in Fig. 9, a FLIR SC6703 type MWIR camera was used. This camera responded to infrared light in the 3,800–4,000 nm wavelength range and was equipped with a 50 mm focal length MWIR lens. At a standoff of approximately 4 m, the system realized a magnification of 0.015 and a lateral

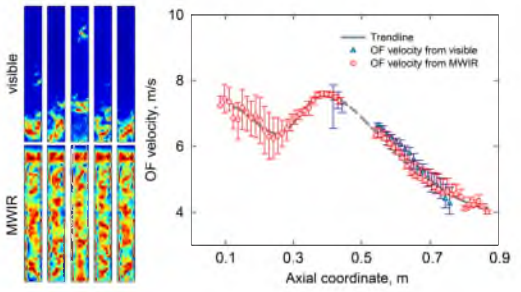

Fig. 9 Shifting the imaged wavelength band from the visible to the infrared may solve the problem of dark or partly featureless images in certain cases. The *left side* shows synchronized pairs of visible and MWIR images. Each column of two images is a synchronized pair—correspondence may be easier to recognize in regions where there is visible emission. The images were enhanced by adaptive histogram equalization (Pizer et al. 1987) to improve the visibility of features. The *right side* shows axial profiles of OF velocity extracted from both the visible and MWIR image sequences. *Error bars* indicate the sensitivity of OF velocity values as described in Sect. 4.2. Uncertainty is increased in regions with lower contrast and/or less defined visual patterns. The *dashed* part of the trend line is interpolation between image areas which are occluded by the gap between the two pieces of the quartz window (see Sect. 2.2)

resolution of 5 mm in the center plane of the flame. The size of the acquired MWIR images was 576 × 52, which roughly corresponded to a FOV of 9 × 100 cm^2. This camera was used in conjunction with the high-speed visible camera described in Sect. 2.2 in order to acquire synchronized pairs of visible and infrared images. The image pairs were spatially referenced by using multi-modal intensity registration that maximized the cross-correlation metric.

The cameras were triggered using the same dual-framing timing scheme as described in Sect. 2.2. The interframe time between frames within pairs was 1 ms. Ten frame pairs were acquired each second. The integration time of each frame was 60 μs.

Figure 9 demonstrates that by shifting the imaged spectral region, it is possible in certain cases to extract information from image regions that are featureless in the visible range. Imaging in MWIR may provide better OFV data in cases of non-sooting flames or flames with non-sooting regions, provided that in these regions, there is a sufficient concentration of hot hydrocarbons that emit in the infrared. The detached flames studied in this paper fall in this category. Figure 9 shows results obtained from images of a detached, unstable flame produced in the oxy-coal combustor described in Sect. 2.1. The axial velocity profile shows a local minimum of OF velocity around 0.27 m downstream of the burner. The location of this minimum approximately corresponds to the zone of ignition.

4.4 Performance

Performance was studied by profiling the GPU implementation of the OFV algorithm (Brox et al. 2004) with the acquired flame images. The computational platform was an inexpensive personal computer with a CUDA-capable GPU. The obtained frame rates for typical flame images when computing the full OF velocity field were between 20 and 60 frames per second. When subsampling the images to define specific interrogation areas, the processing speed was up to two orders of magnitude faster. This performance is possibly sufficient for on-line applications. The time needed for image acquisition or the communication overhead between the camera and GPU was not included in the computation. At typical bus speeds of 100 MB/s and typical bitmap sizes of 0.05–1 MB (8-bit grayscale), the performance drop can be estimated to be 5–10 % due to data transfer relative to the reported values, assuming direct copying to/from host memory.

4.5 Practical considerations

As shown, the performance of the OFV method suggests potential in industrial applications. With regard to the achievable physical robustness of the system, we point out that a dedicated high-speed camera is not an absolute necessity for optical flow measurements under typical industrial conditions. First, less expensive dual-framing CCD cameras can be used to capture subsequent image pairs. If such a camera is not available, it is also possible to synchronize two regular (synchronizable) video cameras so that their combination practically realizes dual-frame imaging. In terms of rugged and heat-resistant imaging optics, the large number of previous studies (Kurihara et al. 1986; Shimoda et al. 1990; Baldini et al. 2000; Baek et al. 2001; Lu et al. 2004, 2005, 2008; Baeg et al. 2005; Jiang et al. 2009; Smart et al. 2010; Zhang et al. 2011; Xiangyu et al. 2011; Sun et al. 2011; Lou et al. 2011) suggests that such hardware is available. Soot blowers, rugged optics and cooling are potentially required for safe operation. Naturally, implementing an on-line version of the OFV setup described in this paper might cause some drop of thermal efficiency in the operated combustion system due to the required cooling and cleaning of the optics. On the other hand, in contrast with conventional industrial methods for velocity measurement in pulverized-coal combustion systems (e.g., electrostatic correlation probes (Xu et al. 2009) or pitot-tubes), the OFV technique is comparatively non-intrusive and can provide a characterization of apparent velocities in the full FOV, while being more robust than existing optical diagnostics methods that are conventionally used for velocimetry. Analyzing the economic feasibility of the technique is not part of the scope of this paper.

5 Conclusion

In this study, we examined the potential of utilizing the optical flow velocimetry (OFV) technique in the field of pilot-scale oxy-coal combustion and burner control. The main focus of this study was the assessment of the responsiveness and usefulness of optical flow velocity information in potential control and flame monitoring applications. A small, pilot-scale, oxy-coal combustion system was used to demonstrate the capabilities of the OFV technique. The transient velocity signals obtained during furnace operation showed promise in terms of responsiveness to system inputs. The obtained transient velocity data were consistent with physical intuition and the data of gas analyzers. The possible shortcomings of OFV, including the subjectivity and uncertainty in the extracted information, were listed. Mid-wave infrared imaging was proposed as a possible method for solving the problem of insufficient image intensity or signal strength that may be present in certain images. Lastly, based on off-line performance tests, it was found that the computational efficiency of the OF algorithm used in this work was sufficient for the suggested applications.

Acknowledgments The authors are thankful to Taylor Geisler (University of Utah) for assistance in pilot-scale tests and to Prof. Philip Smith (University of Utah) for his insights on interpreting the results. This material is based upon work supported by the Department of Energy under Award Number DE-NT0005015. The views and opinions of authors expressed herein do not necessarily state or reflect those of the United States Government or any agency thereof. This work was partially sponsored by the TAMOP-4.2.1.B-10/2/KONV-2010-0001 project with support by the European Union, co-financed by the European Social Fund. This research was carried out in the framework of the Center of Excellence of Sustainable Resource Management of the University of Miskolc.

References

Arik EB, Carr J (1997) Digital particle image velocimetry system for real-time wind tunnel measurements. In: International congress on instrumentation in aerospace simulation facilities, pp 267–277

Baeg SY, Kim SM, Cho CH (2005) Development of flame monitoring system with optical receiver for pulverized coal firing boilers. In: Proceedings of SPIE 6041, ICMIT 2005: information systems and signal processing, pp 1–5

Baek WB, Lee SJ, Baeg SY, Cho CH (2001) Flame image processing and analysis for optimal coal firing of thermal power plant. Proc Int Symp Ind Electron 2:928–931

Baldini G, Campadelli P, Lanzarotti R (2000) Combustion analysis by image processing of premixed flames. Proc Int Conf Image Process 2:708–711

Beauchemin SS, Barron JL (1995) The computation of optical flow. ACM Comput Surv 27(3):433–467

Bouguet JY (2000) Pyramidal implementation of the Lucas Kanade feature tracker—description of the algorithm. Intel Corporation, Tech. rep.

Brox T, Bruhn A, Papenberg N, Weickert J (2004) High accuracy optical flow estimation based on a theory for warping. In: Proceedings of the eighth European conference on computer vision, pp 25–36

Buhre BJP, Elliott LK, Sheng CD, Gupta RP, Wall TF (2005) Oxy-fuel combustion technology for coal-fired power generation. Prog Energy Combust Sci 31(4):283–307

Cleveland WS (1979) Robust locally weighted regression and smoothing scatterplots. J Am Stat Assoc 74(368):829–836

Deriche R, Kornprobst P, Aubert G (1995) Optical-flow estimation while preserving its dis-continuities: a variational approach. In: Proceedings of the second Asian conference on computer vision vol 2, pp 290–295

Farneback G (2001) Very high accuracy velocity estimation using orientation tensors, parametric motion, and simultaneous segmentation of the motion field. In: Proceedings of the eighth international conference on computer vision vol 1, pp 171–177

Fielding J, Long MB (2000) Comparison of particle image velocimetry and optical flow velocimetry for turbulent flows and flames. In: Laser applications to chemical and environmental analysis–combustion diagnostics II

Fielding J, Long MB, Fielding G, Komiyama M (2001) Systematic errors in optical-flow velocimetry for turbulent flows and flames. Appl Opt 40(6):757–764

Gonzalez RC, Woods RE (2001) Digital image processing, 2nd edn. Prentice Hall, Englewood Clifs

Gonzalez-Cencerrado A, Pena B, Gil A (2012) Coal flame characterization by means of digital image processing in a semi-industrial scale pf swirl burner. Appl Energy 94:375–384

Jiang ZW, Luo ZX, Zhou HC (2009) A simple measurement method of temperature and emissivity of coal-fired flames from visible radiation image and its application in a cfb boiler furnace. Fuel 88:980–987

Kurihara N, Nishikawa M, Watanabe A, Satoh Y, Ohtsuka K, Miyagaki M, Highashi T, Masai T (1986) A combustion diagnosis method for pulverized coal boilers using flame-image recognition technology. IEEE Trans Energy Convers 1(2): 99–103

Lou C, Li WH, Zhou HC, Salinas CT (2011) Experimental investigation on simultaneous measurement of temperature distributions and radiative properties in an oil-fired tunnel furnace by radiation analysis. Int J Heat Mass Transf 54:1–8

Lu G, Yan Y, Colechin M (2004) A digital imaging based multifunctional flame monitoring system. IEEE Trans Instrum Meas 53(4):1152–1158

Lu G, Gilabert G, Yan Y (2005) Vision based monitoring and characterisation of combustion flames. J Phys Conf Ser 15:194–200

Lu G, Yan Y, Cornwell S, Whitehouse M, Riley G (2008) Impact of co-firing coal and biomass on flame characteristics and stability. Fuel 87:1133–1140

Pizer SM, Amburn EP, Austin JD, Cromartie R, Geselowitz A, Greer T, Zimmerman JB, Zuiderveld K (1987) Adaptive histogram equalization and its variations. Comput Vis Graph Image Process 39:355–368

Richards FJ (1959) A flexible growth function for empirical use. J Exp Bot 10(2):290–301

Roberts JW (2012) Control of underactuated fluid-body systems with real-time particle image velocimetry. PhD thesis, Massachusetts Institute of Technology

Scholz J, Wiersbinski T, Ruhnau P, Kondermann D, Garbe CS, Hain R, Beushausen V (2008) Double-pulse planar-lif investigations using fluorescence motion analysis for mixture formation investigation. Exp Fluids 45:583–593

Shimoda M, Sugano A, Kimura T, Watanabe Y, Ishiyama K (1990) Prediction method of unburnt carbon for coal fired utility boiler

using image processing technique of combustion flame. IEEE Trans Energy Convers 5(4):640–645

Smart J, Lu G, Yan Y, Riley G (2010) Characterisation of an oxy-coal flame through digital imaging. Combust Flame 157:1132–1139

Sun D, Lu G, Zhou H, Yan Y (2011) Flame stability monitoring and characterization through digital imaging and spectral analysis. Meas Sci Technol 22:1–9

Xiangyu Z, Qiang C, Chun L, Huaichun Z (2011) An improved colorimetric method for visualization of 2-d, inhomogeneous temperature distribution in a gas fired industrial furnace by radiation image processing. Proc Combust Inst 33:2755–2762

Xu C, Zhang J, Yang D, Zhou B, Tang G, Wang S (2009) Dense-phase pneumatically conveyed coal particle velocity measurement using electrostatic probes and cross correlation algorithm. J Phys Conf Ser 147:1–16. doi:10.1088/1742-6596/147/1/012004

Zhang J, Okerlund R, Eddings EG, Wendt JOL (2007) Ignition of axial pulverized coal jets in a specially designed 100kw oxy-fuel combustor. In: Proceedings of the 6th international symposium on coal combustion, pp 305–309

Zhang J, Kelly KE, Eddings EG, Wendt JO (2011) Ignition in 40 kw co-axial turbulent diffusion oxy-coal jet flames. Proc Combust Inst 33:3375–3382

CHAPTER 10

IMAGING OPTICAL DIAGNOSTICS OF 40 KW CO-AXIAL OXY-COAL FLAMES

10.1 Abstract

Oxy-firing is a promising technology for the clean combustion of pulverized coal, by which coal is combusted in an O_2/CO_2 environment. Retrofitting a burner for oxy-firing changes the ignition, heat flux profile, and soot production of the flame; furthermore, in oxy-firing, the combustion conditions are more freely alterable as the flow rate of O_2 becomes an independent variable. Therefore, a comprehensive understanding of flame stability, heat flux profiles, and pollutant emission is desirable for the optimal design of retrofit combustion systems. In this work, a 40 kW, Type 0, co-axially fired oxy-coal flame was studied by applying high-speed, simultaneous imaging optical diagnostics, consisting of two-color pyrometry, midwave infrared radiation imaging, and optical flow velocimetry. Flame temperature, soot volume fraction in terms of the KL factor, multiband radiant flux, flame liftoff, flame length, and flame velocity were extracted from image data. This study explores the effects of different O_2 injection schemes and coal type on the above mentioned parameters. Two bituminous coals and a subbituminous coal were tested.

10.2 Introduction

Oxy-coal combustion, the combusion of pulverized coal in pure O_2/CO_2 atmospheres, is known to provide potential benefits over conventional air-firing. These potential benefits include the complete capture and sequestration of emitted CO_2 and reduced NO_x emission by the recirculated flue gas [120–122].

Oxy-fired pulverized coal flames behave differently than air-fired ones in several ways. Altered particle ignition delay is one of the most well-known effects of oxy-firing. It has been hypothesized that the change in particle ignition is caused by the altered molecular diffusion rate of O_2 to the particle surface and also by the changed thermal properties of the surrounding gas [57, 96, 123–127]. Altered ignition and flame stability were observed

and quantified in flames larger than laboratory-scale as well [128–132]. It was generally found that when burning bituminous coals, increasing the local partial pressure of O_2 or the temperature of fed gases in the near-burner zone of the flame increases flame attachment and stability [128–130]. Flame stability is also greatly affected by the flue gas recycle ratio and secondary O_2 feeding [133]. Attempts were made to capture and explain flame liftoff caused by particle ignition delay in oxy-combustion in numerical simulations [134].

Oxy-fuel combustion changes the heat flux profiles of pulverized coal flames. Previous studies investigated heat flux profiles by analyzing flame temperature [101,133] or heat flux directly [135, 136]. Smart et al. showed that the flue gas recycle ratio inversely affects peak axial heat flux [136] and decreases flame temperature [133]. Draper et al. studied the effect of primary O_2 concentration, coal feed rate, and flame swirl on flame temperature and emissivity [101]. They report a decrease of flame liftoff and general increase of temperature as primary O_2 flow rate is increased up to a certain point, along with decreased soot production in more detached flames [101]. Stimpson et al. performed line-of-sight optical measurements of soot concentration in similar oxy-coal flames [137]. Their study looked at the effects of different coal types as well on soot production, but was unable to quantify significant differences between flames of a Utah bituminous and a PRB coal. They found that oxy-firing generally decreases soot concentration in the flames, compared to air-firing.

This paper aims to expand the results of Zhang et al. [128,129] by applying more comprehensive optical diagnostics measurements to similar, 40 kW co-axial, zero-swirl flames. The motivation behind this work is two-fold: first, we attempt to provide deeper understanding behind the dynamics and stability of co-axial oxy-coal jets; second, the long-term objective is to provide a canonical dataset for the validation of numerical simulations of oxy-coal combustion. To fulfill these objectives, the data set presented herein describes a broader experimental matrix, which is focused on studying the effects of O_2 injection schemes and coal type.

10.3 Materials and methods

10.3.1 The combustion system

The details of the construction of the oxy-coal combustor (OFC) have been reported previously [128]. In brief, the combustion system consists of a refractory-lined, cylindrical combustion chamber with an inner diameter of 0.61 m, a cylindrical radiative section with an inner diameter of 0.27 m, and a convective zone with installed heat exchangers (0.15×0.15 m, square cross-section). The flue gas leaving the convective zone passes through a bag

filter before being emitted. The furnace is controlled by an automated digital system that takes gas concentration, flow rate, and temperature information as the input in its control loop. The combustion chamber ("burner section") of the system has built-in electric wall heaters (each approximately 800 W) that allow for keeping wall temperature constant during experiments. This section also has four quartz windows set at 90 degree orientations (the area of each is approximately 5×100 cm^2) as optical access ports. The quartz windows allow for unobstructed optical access to most of the length of the flame along the flame axis. A collinear pair of windows was used for flame imaging in the experiments to minimize the radiation from the background, as suggested by [107]. Figure 10.1A and Figure 10.1B show the combustion system schematically.

In an attempt to simulate tangential-fired boilers, a co-axial zero-swirl burner was used in the experiments. The burner was a tube-in-a-tube construction (with pulverized coal and the primary gas stream in the inner tube and the secondary gas stream in the outer annulus). The diameter of the inner tube was 15.8 mm. The outer diameter of the primary tube was 21.34 mm, and the inner diameter of the secondary annulus was 35.05 mm. Figure 10.1C shows a rendering of the burner. More details on the burner can be found in [130].

A steady feed rate of pulverized coal was realized by using a twin-screw gravimetric coal feeder with automatic flow rate control. The twin-screw feeder was connected to the primary stream of the burner by a solid conveying pneumatic eductor, which mixed pulverized coal with the primary CO_2 stream. O_2 was added to the primary stream further downstream

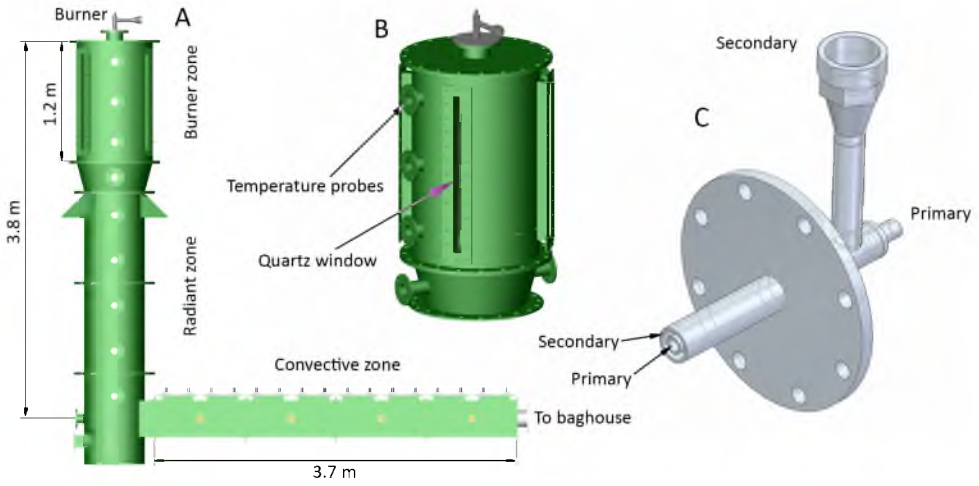

Figure 10.1: A schematic of the combustion system used in the experiments. (A) side view of the oxy-coal combustor with the combustion chamber and flue-gas disposal system. (B) a rendering of the combustion chamber. (C) a rendering of the co-axial burner.

of the conveying system. The coal feeding system provided a steady feed rate accurate to ±0.5% of the nominal feed rate.

The furnace was controlled by an OPTO 22-based system. Flue gas temperature and composition (O_2, CO_2, NO_x, and SO_x) was analyzed continuously during the experiments. Flue gas O_2 was kept constant at approximately 3.2% by volume by the slight adjustment of the coal feed rate. Controlled gas flow rates were accurate within ±0.1% of the set value.

10.3.2 Coals

The three tested coals were Utah Skyline bituminous, Illinois #6 bituminous, and PRB Black Thunder subbituminous coals. All three coals were pulverized and stored in supersacks before feeding into the furnace.

To characterize the chemical and physical properties of the coals, proximate, ultimate, ash, and ^{13}C Nuclear Magnetic Resonance (NMR) analyses were performed, along with laser diffraction particle sizing. Solid state ^{13}C NMR experiments provide insight into the molecular structure of coal. NMR analysis was conducted as described by Grant et al [138]. Laser diffraction sizing showed that the two bituminous coals had similar particle size distributions, with volume-mean diameters around 40 μm. The PRB coal had a higher fraction of fine particles—the mean diameter of the studied population was around 25 μm. Table 10.1 summarizes the results of proximate, ultimate, ash, and NMR analysis.

Proximate and ultimate analysis reveal, as expected, that among the three, the two bituminous coals are fairly similar, except for the higher sulfur-content of the Illinois #6. The PRB coal is a lower rank coal with significantly higher moisture and oxygen content than that of the other two. NMR results support the finding regarding the high oxygen content of the PRB coal. This is reflected in the fraction of the functional group f_a^C (carboxyl or carbonyl groups), along with groups f_a^O and f_a^{OO} and possibly the lattice parameters. The two bituminous coals have similar structures, with the exception of the slightly higher aromaticity of the Illinois #6 coal and the higher molecular weight and more pronounced branching and cross-linking in the structure of the Skyline coal.

10.3.3 Optical diagnostics

The design and assembly of the optical diagnostics system was motivated by the objective of producing high-fidelity and high-resolution data describing the analyzed flames. Since the studied combustion system was larger than laboratory-scale and was installed in a semi-industrial environment, applying the most detailed laser diagnostic techniques was impractical. For this reason, a combination of imaging diagnostics was realized. The

Table 10.1: Proximate, ultimate, ash, and ^{13}C NMR analysis of the three tested coals.[1]

	UT Skyline	Ill. #6	PRB BT		UT Skyline	Ill. #6	PRB BT
	proximate analysis				^{13}C NMR analysis		
HHV, MJ/kg	29.3	26.9	21.1				
moisture	3.18	9.65	23.69	f_a	0.65	0.71	0.68
ash	8.83	7.99	4.94	f_a^C	0.05	0.04	0.09
volatile	33.6	36.78	33.36	f_a^O	0.02	0.01	0.04
fixed C	49.39	45.58	38.01	f_a^{OO}	0.03	0.03	0.05
	ultimate analysis			$f_{a'}$	0.6	0.67	0.59
C	70.6	64.67	53.72	f_a^H	0.2	0.24	0.19
H	5.41	5.59	6.22	f_a^N	0.4	0.43	0.4
N	1.42	1.12	0.78	f_a^P	0.09	0.08	0.09
S	0.53	3.98	0.23	f_a^S	0.15	0.18	0.15
O	13.21	16.65	34.11	f_a^B	0.16	0.17	0.16
	ash analysis			f_{al}	0.35	0.29	0.32
Al	14.52	17.66	14.78	f_{al}^H	0.26	0.22	0.25
Ca	6.11	1.87	22.19	f_{al}^*	0.09	0.07	0.07
Fe	5.09	14.57	5.2	f_{al}^O	0	0.01	0.02
Mg	1.39	0.98	5.17	χ_b	0.267	0.254	0.271
Mn	0.02	0.02	0.01	C	12.8	12.2	13
P	0.59	0.11	1.07	σ+1	5.1	4.7	5.3
K	0.57	2.26	0.35	P^o	0.63	0.73	0.71
Si	60.89	49.28	30.46	$B.L.$	3.2	3.4	3.8
Na	1.41	1.51	1.94	$S.C.$	1.9	1.3	1.5
S	2.33	2.22	8.83	$M.W.$	319	279	352
Ti	0.88	0.85	1.3	M^δ	32	27	36

imaging system presented in this section is capable of providing simultaneous, high-speed, quantitative information regarding flame shape, length, liftoff, temperature, visible and infrared luminosity, and flame velocity, while being flexibly deployable and robust to nonideal measurement conditions.

The core of the imaging system was a synchronized pair of a high-speed visible camera (Photron APS-RX, 1Mpixel resolution) equipped with an in-house built stereo beam-splitter and a midwave infrared camera (FLIR SC6703, 0.3 Mpixel). For synchronization, a Stanford Research DG535 type digital signal generator was used. The syncing pattern was set so that synchronized dual-framing operation was realized with both cameras. Dual-framing operation means that the cameras alternated between two framing rates (FPS). In our case, two pairs of images (one visible, one infrared) were taken at 1000 FPS—the time between the frames was 1 ms. The second frame in the 1000 FPS event was followed by a longer interframe time, 100 ms, realizing 10 FPS recording. This frame was followed by another frame taken at 1000 FPS and the pattern was repeated. The purpose of the dual-framing operation was the acquisiton of an image sample that spanned a duration that was enough to be practically meaningful (5 minutes), while still allowing the extraction of high-speed

information, such as flame velocity. For each combustion condition, 3000×2 dual-frames were acquired by each camera.

By using a stereo beam-splitter and bandpass optical filters, imaging at three different wavelengths was realized. The three wavelengths consisted of two visible channels (550 nm and 676 nm) and one midwave infrared (MWIR) channel (3900 nm). The bandwidths were 25 nm for the visible channels and 150 nm for the infrared channel (full widths at half maximum). The blocking of unwanted frequencies was equivalent to a better than OD 6 optical density. The choice of visible bandpass filters allowed for extracting line-of-sight flame temperature and soot concentration, expressed as the KL factor. For this purpose, a methodology described elsewhere [101] was followed, with the exception of using real bandpass filters instead of Bayer filter arrays—better separated and narrower optical bands allows for the extraction of higher-fidelity pyrometric data [114]. Visible filter central wavelengths were chosen following the suggestions of [51]. The bandwidths of the visible filters were chosen as a compromise between total transmittance and monochromaticity—with the intermediate bandwidth, the signal-to-noise ratio of the images was significantly better than that achievable by true monochromatic filters. The single-wavelength form of the two-color pyrometric equation [99] was not assumed when computing temperature and the KL factor – the full integral form was used [101]. The infrared channel recorded a mixture of Planck radiation and the gas radiation of hydrocarbons [139]. It is reasonable to assume that the hydrocarbon radiation is dominated by the radiation of hot volatiles and intermediate combustion products in this wavelength range.

For computing two-color pyrometric information and visible and infrared fluxes, the cam-

---

[1]The aggregate molecular structure of coals are: $C_{100}H_{85}N_{1.7}S_{0.3}O_{11}$ (Utah Skyline), $C_{100}H_{83}N_{1.5}S_{2.3}O_9$ (Illinois #6), $C_{100}H_{79}N_{1.3}S_{0.2}O_{18}$ (PRB Black Thunder). The meaning of the ^{13}C NMR parameters are the following. str. denotes the approximate aggregate molecular structure, normalized by the carbon content. f_a, the fraction of carbon atoms that are sp^2 hybridized (aromaticity). f_a^C, the fraction of carbon atoms that are in carboxyl or carbonyl groups. f_a^O, the fraction of carbon atoms that are in a carbonyl group (aldehydes and ketones). f_a^{OO}, the fraction of carbon atoms that are in a carboxyl group (acids, esters, amides). f_a, the fraction of carbon atoms that are sp^2 hybridized excluding (corrected aromaticity). f_a^H, the fraction of carbon atoms that are protonated aromatics. f_a^N, the fraction of carbon atoms that are nonprotonated aromatics. f_a^P, the fraction of carbon atoms that are aromatic with an oxygen atom attached. f_a^S, the fraction of carbon atoms that are aromatic with a carbon chain attached (also includes biaryl carbons). f_a^B, the fraction of carbon atoms that are aromatic and a bridgehead carbon. f_{al}, the fraction of carbon atoms that are sp^3 hybridized (aliphatic). f_{al}^H, the fraction of carbon atoms that are aliphatic but not methyls. f_{al}^*, the fraction of carbons that are aliphatic and methyls. f_{al}^O, the fraction of carbon atoms that are aliphatic and attached to an oxygen atom. ξ_b, the mole fraction of bridgehead carbon atoms. C, the average aromatic cluster size. $\sigma + 1$, the average number of attachments on an aromatic cluster. P^O, the fraction of attachments that do not end in a side chain (methyl group). $B.L.$, the average number of attachments on an aromatic cluster that are bridges or loops (a loop is a bridge back to the same cluster). $S.C.$, the average number of side chains on an aromatic cluster. $M.W.$, the average molecular weight of an aromatic cluster including side-chains and bridges. M^δ, the average mass of a side chain or one-half of a bridge.

eras were calibrated. The visible camera was calibrated by using a NIST-calibrated tungsten ribbon lamp. The infrared camera was calibrated by using a temperature-controllable black-body furnace. The details of the calibration procedures can be found elsewhere [99,101]. Emissivity data for tungsten ribbon can be found in [112]. When calibrating both cameras, the quartz glass from the combustion chamber of the OFC was placed between the radiation source and the cameras to cancel out its effects on the obtained pyrometric data. This can be done by assuming that the quartz glass acts a neutral density filter in the selected optical channels, which is reasonable, given the reasonably narrow bandwidths. In all other aspects, the calibration conditions mimiced the measurement conditions.

The two cameras were registered spatially by an automatic multimodal intensity image registration procedure that maximized the cross-correlation metric between synhronized image pairs obtained by the two cameras. The initial guesses for the affine transformation parameters were provided manually, and the final registrations were manually checked for correctness. The two cameras were positioned similarly in space—the standoff between the visible camera and the flame was 4.5 m, while the infrared camera was placed 5.4 m away from the flame. Both cameras were on the same optical axis, and the whole setup was in-line with the collinear window pair through which the flame was imaged. The cameras were mounted on rugged tripods and were tilted slightly vertically so that the visible camera was avoided in the infrared image. A Tamron telephoto lens (18–270 mm, set at 65 mm) was used with the visible camera, and a 35 mm fixed focal-length MWIR lens was used with the infrared camera. The different lenses and slight tilting of the cameras made the spatial registration step necessary. Spatial referencing was also carried out in the registration step. Camera gain and lens aperture values were set such that the resulting images maximized signal-to-noise ratio, but avoided image saturation. In every case, the whole thickness of the flame was within the zone of acceptable sharpness. Camera integration times were chosen such that the images maximized signal-to-noise ratio without any smearing observed. Typically, f-numbers of 3.5 (visible) and 2.8 (infrared) and integration times of 1 ms (visible) and 0.06 ms (infrared) were used. For each set of imaging conditions, a different camera calibration was performed.

Flame liftoff was extracted from image data as described in [128]. By applying a very similar methodology, flame length was extracted as well. The methodology for extracting flame velocity is described elsewhere [140]. The velocity we extracted is the apparent "optical flow" velocity of the flame, which is a line-of-sight mixture of flamefront and particle velocity. We have recently shown that given a large enough sample, the mean velocities

extracted by the optical flow velocimetry (OFV) technique are well comparable to those obtained by planar particle image velocimetry (PIV) [140]. One of the drawbacks of the OFV method is that velocity extraction is only possible in areas of high luminosity. In the case of a detached flame, this means that velocity data are unavailable in the near-burner region; however, using the infrared channel for velocity extraction solves this problem by allowing the tracking of the motion of hydrocarbons that radiate in MWIR. Therefore, both visible and MWIR image data were used to compute optical flow velocity and the results are presented jointly.

The detection limits of the cameras were handled statistically in postprocessing. When computing time-averaged axial profiles, time-series of intensity data was treated as left-censored data sets. The log-normal distribution was fit over the censored intensity data by applying maximum-likelihood estimation [141]. The uncertainty of the estimation, along with calibration uncertainty and additional processing uncertainty (in the case of temperature and KL) were propagated into the final uncertainty by the Monte-Carlo method. Velocity uncertainty was handled differently by using the standard error measure. Axial profiles were created by time-averaging the intensities in the centerline of the flame images.

10.3.4 Experimental conditions

Table 10.2 summarizes the combustion conditions tested. The main purpose of this experimental matrix was to investigate the effects of coal type and O_2 feeding on the radiative properties and stability aspects of the flames. The overall chemistry of the flames were unaltered, but the feedings scheme of O_2 was changed by shifting a portion of the fed O_2 from the secondary stream to the primary stream. Generally, when more O_2 is introduced through the primary stream, a better mixing of fuel and oxidizer is expected in the near-burner region, whereas more O_2 put through the secondary stream is expected to delay ignition and combustion.

10.4 Results and discussion

Figure 10.2 shows band-integrated, mean axial fluxes. As can be seen, increasing O_2 concentration in the primary stream shifted luminous zones in the visible range towards the burner surface while affecting peak fluxes as well. In the case of the Illinois coal, the peak visible flux was the highest in the case of 0% primary O_2 and lowest in the case of 20% primary O_2. Peak locations were similarly shifted in the Skyline flame, but the peak flux was the highest in the 10% primary O_2 case. The PRB flame showed no significant effect of altered O_2 feeding, and the visible fluxes were the lowest of the three coals. It is worth

Table 10.2: Combustion conditions

Case	Coal	Primary Coal	Primary O_2	Primary O_2	Primary CO_2	Secondary O_2	Secondary CO_2	Wall T	Flue gas O_2
	type	kg/h	vol%	kg/h	kg/h	kg/h	kg/h	K	vol%
1	Ill. #6	3.5	0	0.0	6.8	7.8	9.1	1283	3.2
2	Ill. #6	3.5	10	0.5	6.2	7.3	9.8	1283	3.2
3	Ill. #6	3.5	20	1.0	5.4	6.7	10.5	1283	3.2
4	UT Skyline	3.3	0	0.0	6.8	7.8	9.1	1283	3.2
5	UT Skyline	3.3	10	0.5	6.2	7.3	9.8	1283	3.2
6	UT Skyline	3.3	20	1.0	5.4	6.7	10.5	1283	3.2
7	PRB BT	4.6	0	0.0	6.8	7.8	9.1	1283	3.2
8	PRB BT	4.6	10	0.5	6.2	7.3	9.8	1283	3.2
9	PRB BT	4.6	20	1.0	5.4	6.7	10.5	1283	3.2

noting here that the axial profiles show averages over time; thus flickering flame behavior lowers the mean flux values.

The MWIR fluxes were similar for the two bituminous coals, with similar shapes for all three coals; however, the MWIR flux profiles showed distinct differences compared to the visible fluxes. The reasonably high fluxes measured in the near-burner area indicate that hydrocarbon radiation was indeed captured in the infrared images. The initial portions of the curves thus contain information on the amount of volatiles locally present in the flame. As seen, in the cases of the bituminous coals, increased O_2 concentration in the primary stream increased MWIR intensity in the near-burner region. The effect is more pronounced in the Illinois coal flames. Again, the flames of the PRB coals were apparently unaffected by O_2 feeding in terms of MWIR flux profiles. The difference between the visible and MWIR flux profiles is the most pronounced in the case of the PRB flames, where the indetectible visible fluxes are contrasted with peaking MWIR fluxes in the near-burner region. This indicates a quick release of volatiles early in the flame. The early MWIR intensities of the PRB flame stayed lower than those of the bituminous coal flames.

Figure 10.3 shows mean axial profiles of line-of-sight averaged flame temperature and soot concentration expressed in terms of the KL factor. In the case of flames that were mostly attached, peak temperatures around 1800 K were observed near the burner surface (the burner surface itself was not visible; thus the axial coordinates do not start from zero in the figures). These temperatures dropped quickly as the flame expanded and lost heat to the furnace wall—flame temperatures approached the temperature of the wall downstream, close to the end of the radiative section of the OFC. O_2 feeding altered temperature profiles. Decreasing O_2 concentration in the primary stream lowered temperatures close to the burner while increasing temperature more downstream. Peak temperatures were shifted similarly to

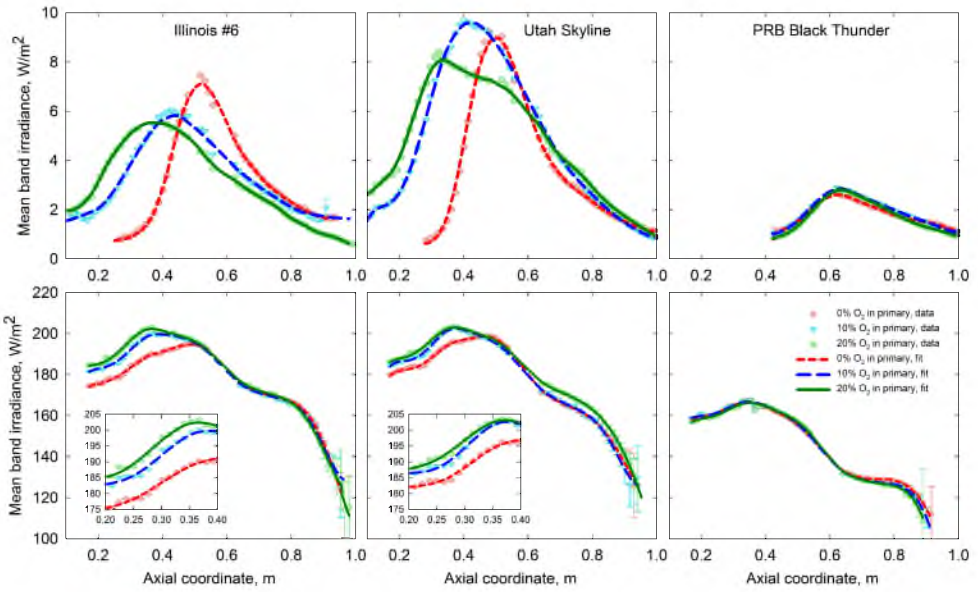

Figure 10.2: Mean axial fluxes of the studied flames. The top row shows visible fluxes at 676 nm, while the bottom row shows MWIR fluxes at 3900 nm. Every 10^{th} data point is plotted for clarity. Missing data occurs due to flame liftoff, the obstructed area between the two parts of the glass window, and in some cases, local ash deposition on the glass. Insets show zoomed-in portions of the profiles. Trendlines were obtained by LOESS fitting [142]. The statistical processing of the data is described in Section 10.3.3.

visible flux peaks. The overall temperature of the Skyline flame was the highest as expected based on its heating value (see Table 10.1). The temperature profiles of the PRB flame stayed similar without any significant trends. Weak trends suggest increasing temperature with primary O_2 concentration, implying that the overall location of the ignition zone in the PRB flame was shifted downstream, similarly to the 0% primary O_2 cases of the bituminous coal flames.

The trends in the mean axial KL profiles of the bituminous coal flames indicate that increased local O_2 concentration in the early flame leads to increased soot production more downstream in the flame. Previous studies [101, 143] proposed the existence of this effect. Our study provides further evidence, suggesting that a possible cause of the increased soot production is the increased volatile release caused by O_2 in the early flame. According to our observations, the amount of soot produced in the PRB flame was the lowest of the three coals, which is supported by the very low visible fluxes measured along the centerline in these flames and the high molecular O_2 content of this coal (see Table 10.1). The highest amount of soot was produced in the Skyline flame, which is also explainable by the heavier and more cross-linked molecular structure of this coal.

Measured axial flame velocity profiles are shown in Figure 10.4. As seen, flame velocities

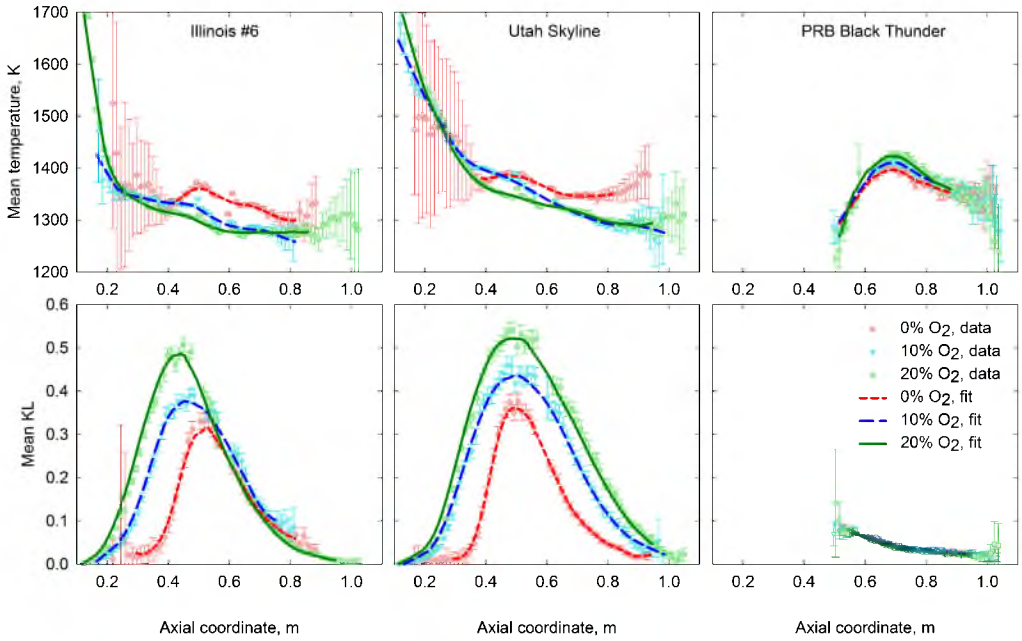

Figure 10.3: Mean axial profiles of temperature and soot concentration expressed as the KL factor of the studied flames. These results were extracted from the two-color visible images. The top row shows temperature profiles, while the bottom row shows KL profiles. Every 10^{th} data point is plotted for clarity. Missing data occurs due to flame liftoff, the obstructed area between the two parts of the glass window, and in some cases, local ash deposition on the glass. Trendlines were obtained by LOESS fitting [142]. The statistical processing of the data is described in Section 10.3.3. High uncertainties in the profiles are caused by insufficient luminosity in the visible band.

extracted from visible and infrared images show very good overlap, although MWIR imaging allows for the extraction of optical flow velocities in regions where visible imaging does not (in the liftoff area of detached flames). Flame velocity profiles show approximately monotonically decreasing velocities along the centerline in the cases of the bituminous coals for primary O_2 concentrations higher than 0%. O_2 feeding affected the velocities of the Illinois coal flame more than those of the Skyline coal flame. The 0% primary O_2 cases showed velocity profiles indicative of delayed ignition and flame liftoff. The velocities of the PRB flames always showed lifted flame behavior. The differences in velocities in the early flame were possibly caused by slight inaccuracies of the gas flow rates. It also seems that the peak locations in the velocity profiles were shifted downstream by increased O_2 flow rates in the primary stream.

The insets in Figure 10.4 show axial flame velocity probability distributions sampled at the axial coordinate of 0.25 m. This location represented a transitional region, where, based on visible luminosity, the flames were sometimes ignited and in other instances were

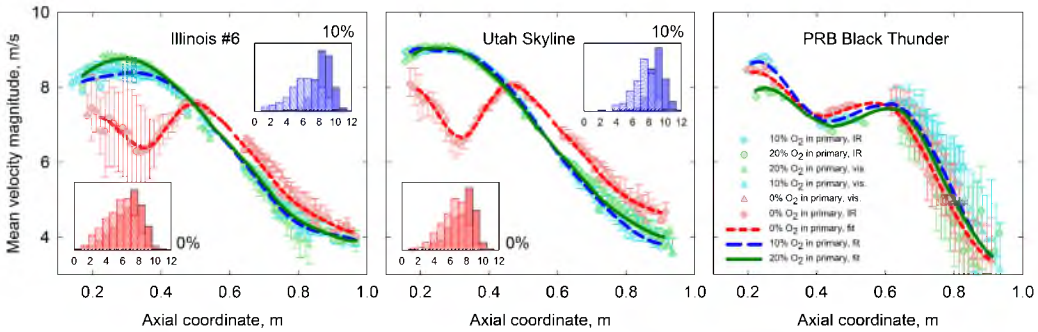

Figure 10.4: Mean axial profiles of flame velocity. These results were extracted from the red channel of the visible images and from the MWIR images. Every 10^{th} data point is plotted for clarity. Missing data occurs due to flame liftoff, the obstructed area between the two parts of the glass window and in some cases, local ash deposition on the glass. Insets show axial velocity probability distributions in the near-burner zone of the flames, for both attached (solid) and detached (dashed) conditions. The probability distributions were obtained from synced visible and MWIR image pairs. Attachment was detected by using the methodology presented in [128] and setting a best-separating threshold (0.3 m) on flame liftoff. Trendlines were obtained by LOESS fitting [142]. The statistical processing of the data is described in Section 10.3.3. Colors indicate O_2 feeding consistently in every subplot.

not. Careful observation reveals that the nonignited mean velocities were increased with increased O_2 concentration in the primary stream. Since the overal flow rate of gas was kept constant in the primary stream between cases (see Table 10.2), this is further evidence that a higher rate of volatile release may have occured in the near-burner zone with higher primary O_2 concentrations.

Figure 10.5 aims to clarify qualitative statements made on flame liftoff and length when discussing previous figures. As seen, the liftoff and stability of the Illinois coal flame was affected more by O_2 feeding than that of the Skyline flame. This result is consistent with previous reports [128, 129]. In the case of both coals, the 0% primary O_2 cases produced mostly always lifted flames—the mean liftoff distance was shorter in the case of the Skyline coal than in the case of the Illinois #6 coal. This may be caused by the higher soot concentration in the Skyline flame closer to the burner (see Figure 10.3) as the radiation from soot may contribute to flame stabilization. Looking at flame length histograms of the bituminous coals, it can be seen that length decreased with decreasing primary O_2 concentration. This is in agreement with the higher secondary peak temperatures observed in Figure 10.3. The length of the Skyline coal flame was less affected by shifting primary O_2 from 20% to 10%. Again, the stability of the PRB coal flame was not significantly affected by O_2 feeding.

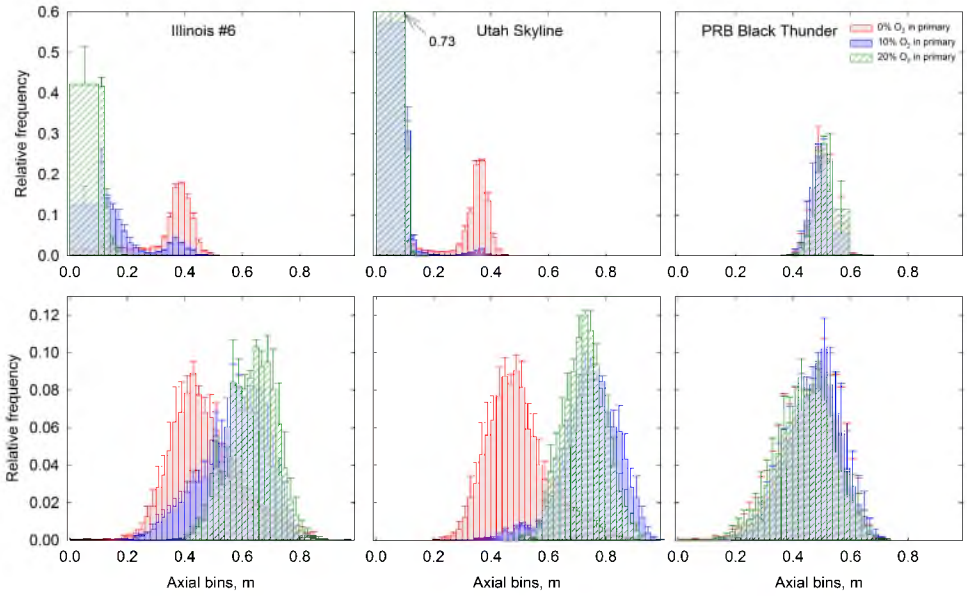

Figure 10.5: Flame liftoff and length probability distributions extracted from the red channel of visible images. See [128] for the details of the image processing methodology. The top row shows probability distributions of flame liftoff, while the bottom row shows those of flame length.

10.5 Conclusion

The comprehensive optical diagnostics of 40 kW co-axial turbulent coal jets was carried out. The experimental matrix tested focused on exploring the effects of coal type and O_2 injection schemes on flame temperature, soot production, heat flux profiles, flame velocity, and stability. The obtained results show self-consistency and good agreement with previous findings. Synchronized visible and MWIR imaging provided quantitative evidence suggesting that inreased local O_2 concentration in the early flames lead to a higher rate of volatile release, which in turn lead to inreased soot production downstream. Consequently, increased soot concentrations in the flames of the Utah Skyline coal resulted in better flame stability than that of the Illinois #6 flame. We were unable to quantify significant trends in the PRB flames caused by altered O_2 feeding; however, when compared to the other two coals, the PRB coal showed significant differences in terms of every studied parameter. PRB flames were colder, always lifted, and produced much less soot than the flames of the other two coals.

CHAPTER 11

SUMMARY

Digital imaging and image processing were applied to study different systems related to combustion. Although the studied problems were significantly different, the general applicability of the technique was demonstrated. This dissertation is a compilation of separate articles that each describe experimental and data processing approaches that originate in the field of optics, radiometry, imaging, and digital image processing.

The conclusions drawn in the separate chapters can be classified as either being connected to methodology development or new physical insights gained by applying the techniques developed.

In Chapter 2, it was demonstrated that the defined structural indices describing soot nanostructure as extracted by the developed technique were more robust than conventional parameters and well characterize and differentiate samples.

In Chapters 3 and 4, an image processing framework was described with which already defined structural parameters, such as interlayer spacing and symmetry of graphene layers can be extracted in a more rigorous way, and the obtained statistics of the extracted parameters are much more robust than those extracted by conventional methods.

In Chapter 5, the image processing framework described in Chapters 3 and 4 was extended by adding the capability of automating microscopes. This chapter thus also presented methodology development, although building on previously described fundamentals.

Chapter 6 yielded insight into the structural changes of soot under different oxidation pressures. It was found that with increasing oxidation pressure, the spacing between graphene lamellae becomes tighter and the structure becomes more symmetrical. This is new physical insight, which was made observable by the advanced image processing framework described in Chapters 3 and 4.

In Chapters 2–6, we demonstrated that by advancing and extending the current data processing methodologies by introducing concepts originally developed in different scientific fields (other than combustion), it is possible to extend the range of observable physical

phenomena and increase the fidelity of physical insight. We plan to apply the techniques presented in these chapters to a number of different problems in the area of sooting flames. The relevance and merit of the new methods were demonstrated; however, there is still ambiguity about the exact physical meanings of the structural parameters extracted by our techniques (and by conventional methods as well). For this reason, as future work, we plan to investigate the formation of electron micrographs of amorphous carbon nanostructures, such as soot, in the hope that understanding the process of image formation helps clarify the relationship between molecular structure and structural data obtained by quantitative electron microscopy.

In Chapters 7 and 8 we showed that the stereoscopic, particle streaking, emission imaging method is able to yield joint statistics of temperature, diameter, and velocity of combusting pulverized-coal particles at accuracies comparable to those obtainable by conventional methods. However, the presented method can provide these measurements by retaining the three-dimensional spatial information (location, velocity) of particles. Furthermore, the instrumentation required for our approach is less expensive than what is typically required for previously developed techniques.

The advantages of the stereoscopic diagnostics method were demonstrated in Chapters 7 and 8. However, for practical purposes, the applicability of this technique to larger-scale flames is desirable. For a number of reasons, it is advantageous to shift the spectral range of the stereoscopic imaging method towards the infrared, which requires slightly different instrumentation. This remains yet to be investigated.

Chapter 9 described a method of imaging-based flame velocity measurement. We showed that the developed method can be used to extract velocity information from images of a pilot-scale flame in an on-line fashion. This information can potentially be used for flame monitoring and control purposes.

Chapter 10 extended the velocimetry capability presented in Chapter 9 by simultaneous radiometric capabilities. A 40 kW, pilot-scale oxy-coal flame was studied with the combined methodology. Mean axial temperature, soot concentration, heat flux, and velocity profiles were extracted from image data. The physical insight gained supported literature data and provided further proof for more rapid devolatilization in the early flame as local oxygen concentration increased.

The real-time velocimetric and pyrometric capabilities of the combined method described in Chapter 10 are promising for the energy industry. In many cases, such as in the case of monitoring and controlling large, complicated boilers, it is desirable to have real-time,

three-dimensional diagnostic capabilities that can be implemented as rugged systems. We plan to investigate the economic feasibility and limits of the presented methodology in different industrial applications.

REFERENCES

[1] P. Delhaes, *Graphite and Precursors*. Amsterdam: Gordon and Breach Science Publishers, 1^{st} ed., 2001.

[2] R. L. V. Wal and A. J. Tomasek, "Soot oxidation: dependence upon initial nanostructure," *Combust. Flame*, vol. 134, no. 1-2, pp. 1–9, 2003.

[3] R. L. V. Wal and A. J. Tomasek, "Soot nanostructure: dependence upon synthesis conditions," *Combust. Flame*, vol. 136, no. 1-2, pp. 129–140, 2004.

[4] J. he Yang, S. hui Cheng, X. Wang, Z. Zhang, X. rong Liu, and G. hua Tang, "Quantitative analysis of microstructure of carbon materials by HRTEM," *Trans. Nonferrous Met. Soc. China*, vol. 16, pp. 796–803, 2006.

[5] T. Ishiguro, Y. Takatori, and K. Akihama, "Microstructure of diesel soot particles probed by electron microscopy: First observation of inner core and outer shell.," *Combust. Flame*, vol. 108, no. 1-2, pp. 231–234, 1997.

[6] R. L. V. Wal, "Soot nanostructure: Definition, quantification and implications," Tech. Rep. 2005-01-0964, SAE, 2005.

[7] A. Santamaria, N. Yang, E. Eddings, and F. Mondragon, "Chemical and morphological characterization of soot and soot precursors generated in an inverse diffusion flame with aromatic and aliphatic fuels," *Combust. Flame*, vol. 157, pp. 33–42, 2010.

[8] P. R. Lindstedt, "Simplified soot nucleation and surface growth steps for non-premixed flames," in *Soot formation in combustion mechanisms and models* (H. Bockhorn, ed.), pp. 417–441, Springer, 1994.

[9] C. W. Lautenberger, J. L. de Ris, N. A. Dembsey, J. R. Barnett, and H. R. Baum, "A simplified model for soot formation and oxidation in CFD simulation of non-premixed hydrocarbon flames," *Fire Saf. J.*, vol. 40, pp. 141–176, 2005.

[10] I. M. Kennedy, "Models of soot formation and oxidation," *Prog. Energy Combust. Sci.*, vol. 23, pp. 95–132, 1997.

[11] M. Frenklach and H. Wang, "Detailed modeling of soot particle nucleation and growth," *Symp. (Int.) Combustion*, vol. 23, no. 1, pp. 1559–1566, 1991.

[12] J. B. Howard, "Carbon addition and oxidation reactions in heterogeneous combustion and soot formation," *Symp. (Int.) Combustion*, vol. 23, no. 1, pp. 1107–1127, 1991.

[13] S. J. Harris and I. M. Kennedy, "The coagulation of soot particles with van der Waals forces," *Combust. Sci. Technol.*, vol. 59, pp. 443–454, 1988.

[14] I. M. Kennedy and S. J. Harris, "Direct numerical simulation of aerosol coagulation with van der Waals forces," *J. Colloid Interface Sci.*, vol. 130, no. 2, pp. 489–497, 1989.

[15] U. Wieschnowsky, H. Bockhorn, and F. Fetting, "Some new observations concerning the mass growth of soot in premixed hydrocarbon-oxygen flames," *Symp. (Int.) Combustion*, vol. 22, no. 1, pp. 343–352, 1989.

[16] J. Nagle and R. F. Strickland-Constable, "Oxidation of carbon between 1000-2000 C," in *Proc. Conf. Carbon*, pp. 154–164, Pergamon, 1962.

[17] R. H. Hurt, G. P. Crawford, and H. S. Shim, "Equilibrium nanostructure of primary soot particles," *Proc. Comb. Inst.*, vol. 28, pp. 2539–2546, 2000.

[18] A. B. Palotas, L. C. Rainey, C. J. Feldermann, A. F. Sarofim, and J. B. V. Sande, "Soot morphology: An application of image analysis in high-resolution transmission electron microscopy," *Microsc. Res. Tech.*, vol. 33, no. 3, pp. 266–278, 1996.

[19] A. Sharma, T. Kyotani, and A. Tomita, "A new quantitative approach for microstructural analysis of coal char using HRTEM images," *Fuel*, vol. 78, pp. 1203–1212, 1999.

[20] H. S. Shim, R. H. Hurt, and N. Y. C. Yang, "A methodology for analysis of 002 lattice fringe images and its application to combustion-derived carbons," *Carbon*, vol. 38, pp. 29–45, 2000.

[21] K. Yehliu, R. L. V. der Wal, and A. L. Boehman, "Development of an HRTEM image analysis method to quantify carbon nanostructure," *Combust. Flame*, vol. 158, pp. 1837–1851, 2011.

[22] P. Toth, A. B. Palotas, J. Lighty, and C. A. Echavarria, "Quantitative differentiation of poorly ordered soot nanostructures: A semi-empirical approach," *Fuel*, vol. 99, pp. 1–8, 2012.

[23] P. Toth, A. B. Palotas, E. G. Eddings, R. T. Whitaker, and J. S. Lighty, "A novel framework for the quantitative analysis of high resolution transmission electron micrographs of soot I. — improved measurement of interlayer spacing," *Combust. Flame*, vol. 160, no. 5, pp. 909–919, 2013.

[24] P. Toth, A. B. Palotas, E. G. Eddings, R. T. Whitaker, and J. S. Lighty, "A novel framework for the quantitative analysis of high resolution transmission electron micrographs of soot II. — robust multiscale nanostructure quantification)," *Combust. Flame*, vol. 160, no. 5, pp. 920–932, 2013.

[25] S. A. Saltykov, *Stereometric Metallography (in Russian).* 2^{nd} ed., 1958.

[26] A. Sharma, T. Kyotani, and A. Tomita, "Comparison of structural parameters of PF carbon from XRD and HRTEM techniques," *Carbon*, vol. 38, pp. 1977–1984, 2000.

[27] H. Aso, K. Matsuoka, A. Sharma, and A. Tomita, "Structural analysis of PVC and PFA carbons prepared at 500-1000 c based on elemental composition," *Carbon*, vol. 42, pp. 2963–2973, 2004.

[28] A. E. Karatas and O. L. Gulder, "Soot formation in high pressure laminar diffusion flames," *Prog. Energy Combust. Sci.*, vol. 38, pp. 818–845, 2012.

[29] D. Gabor, "Theory of communication. part 1: The analysis of information," *J. Inst. Electr. Eng., Part 3*, vol. 93, no. 26, pp. 429–441, 1946.

[30] J. Song, M. Alam, A. L. Boehman, and U. Kim, "Examination of the oxidation behavior of biodiesel soot," *Combust. Flame*, vol. 146, pp. 589–604, 2006.

[31] R. L. V. Wal and M. Y. Choi, "Pulsed laser heating of soot: morphological changes," *Carbon*, vol. 37, no. 2, pp. 231–239, 1999.

[32] W. Zhu, D. E. Miser, W. G. Chan, and M. R. Hajaligol, "Characterization of combustion fullerene soot, C_{60}, and mixed fullerene," *Carbon*, vol. 42, pp. 1463–1471, 2004.

[33] L. E. Murr and K. F. Soto, "A TEM study of soot, carbon nanotubes, and related fullerene nanopolyhedra in common fuel-gas combustion sources," *Mater. Charact.*, vol. 55, pp. 50–65, 2005.

[34] W. J. Griecoa, J. B. Howarda, L. C. Rainey, and J. B. V. Sande, "Fullerenic carbon in combustion-generated soot," *Carbon*, vol. 38, pp. 597–614, 2000.

[35] P. Hebgen, A. Goel, J. B. Howard, L. C. Rainey, and J. B. V. Sande, "Synthesis of fullerenes and fullerenic nanostructures in a low-pressure benzene/oxygen diffusion flame," *Proc. Comb. Inst.*, vol. 28, pp. 1397–1404, 2000.

[36] C. R. Shaddix, A. B. Palotas, C. M. Megaridis, M. Y. Choi, and N. Y. C. Yang, "Soot graphitic order in laminar diffusion flames and a large-scale JP-8 pool fire," *Int. J. Heat Mass Transfer*, vol. 48, pp. 3604–3614, 2005.

[37] W. Maier and A. Saupe, "Eine einfache molekularstatistische theorie der nematischen kristallinflussigen phase. teil i," *Zeitschrift Naturforschung A*, vol. 14, p. 882, 1959.

[38] W. Maier and A. Saupe, "Eine einfache molekularstatistische theorie der nematischen kristallinflussigen phase. teil ii," *Zeitschrift Naturforschung A*, vol. 15, p. 287, 1960.

[39] V. Fernandez-Alos, J. K. Watson, R. L. vander Wal, and J. P. Mathews, "Soot and char molecular representations generated directly from HRTEM lattice fringe images using Fringe3D," *Combust. Flame*, vol. 158, pp. 1807–1813, 2011.

[40] P. J. Wojtowicz, "Introduction to the molecular theory of nematic liquid crystals," in *Introduction to Liquid Crystals* (E. B. Priestley, P. J. Wojtowicz, and P. Sheng, eds.), New York: Plenum Press, 1974.

[41] G. R. Luckhurst and C. Zannoni, "Why is the Maier Saupe theory of nematic liquid crystals so successful?," *Letters to Nature*, vol. 267, pp. 412–414, 1977.

[42] L. D. Smoot and P. J. Smith, *Coal Combustion and Gasification.* New York: Springer, 1985.

[43] L. D. Smoot and D. T. Pratt, *Pulverized-coal combustion and gasification: theory and applications for continuous flow processes.* New York: Springer, 1985.

[44] J. Ballester and T. Garcia-Armingol, "Diagnostic techniques for the monitoring and control of practical flames," *Prog. Energy Combust. Sci.*, vol. 36, pp. 375–411, 2010.

[45] S. S. Penner, C. P. Wang, and M. Y. Bahadori, "Nonintrusive diagnostic techniques for measurements on coal-combustion systems," *Prog. Energy Combust. Sci.*, vol. 10, pp. 209–212, 1984.

[46] J. R. Fincke, W. D. Swank, C. L. Jeffery, and C. A. Mancuso, "Simultaneous measurement of particle size, velocity and temperature," *Meas. Sci. Technol.*, vol. 4, pp. 559–565, 1993.

[47] S.-M. Hwang, R. Kurose, F. Akamatsu, H. Tsuji, H. Makino, and M. Katsuki, "Observation of detailed structure of turbulent pulverized-coal flame by optical measurement (part 1, time-averaged measurement of behavior of pulverized-coal particles and flame structure)," *JSME Int. J., Ser. B*, vol. 49, no. 4, pp. 1316–1327, 1993.

[48] Y. Hardalupas, K. Hishida, M. Maeda, H. Morikita, A. M. K. P. Taylor, and J. H. Whitelaw, "Shadow doppler technique for sizing particles of arbitary shape," *Appl. Opt.*, vol. 33, no. 36, pp. 8417–8426, 1994.

[49] M. Maeda, H. Morikita, I. Prassas, A. M. K. P. Taylor, and J. H. Whitelaw, "Size and velocity measurement by shadow doppler velocimetry within a pulverized coal-fired furnace," *Part. Part. Syst. Charact.*, vol. 14, pp. 79–87, 1997.

[50] R. F. Cope, C. R. Monson, G. J. Germane, and W. C. Hecker, "Improved diameter, velocity, and temperature measurements for char particles in drop-tube reactors," *Energy Fuels*, vol. 8, pp. 925–931, 1994.

[51] J. J. Murphy and C. R. Shaddix, "Combustion kinetics of coal chars in oxygen-enriched environments," *Combust. Flame*, vol. 144, pp. 710–729, 2006.

[52] M. Queiroz, M. P. Bonin, J. S. Shirolkar, and R. W. Dawson, "Experimentally determined particle number density statistics in an industrial-scale, pulverized-coal-fired boiler," *Energy Fuels*, vol. 7, pp. 842–851, 1993.

[53] L. Zhang, E. Binner, Y. Qiao, and C.-Z. Li, "High-speed camera observation of coal combustion in air and O_2/CO_2 mixtures and measurement of burning coal particle velocity," *Energy Fuels*, vol. 24, pp. 29–37, 2010.

[54] J. D. Trolinger and M. P. Heap, "Coal particle combustion studied by holography," *Appl. Opt.*, vol. 18, no. 11, pp. 1757–1787, 1979.

[55] G. S. Samuelsen, J. D. Trolinger, and M. P. Heap, "Observation of the behavior of coal particles during thermal decomposition," *Combust. Flame*, vol. 40, pp. 7–12, 1981.

[56] Y. Wu, X. Wu, Z. Wang, L. Chen, and K. Cen, "Coal powder measurement by digital holography with expanded measurement area," *Appl. Opt.*, vol. 50, no. 34, pp. H22–H29, 2011.

[57] A. Molina and C. R. Shaddix, "Ignition and devolatilization of pulverized bituminous coal particles during oxygen/carbon dioxide coal combustion," *Proc. Comb. Inst.*, vol. 31, pp. 1905–1912, 2007.

[58] S. Niksa, R. Mitchell, K. Hencken, and D. Tichenor, "Optically determined temperatures, sizes, and velocities of individual carbon particles under typical combustion conditions," *Combust. Flame*, vol. 60.

[59] A. Molina, J. J. Murphy, C. R. Shaddix, and L. G. Blevins, "The effect of potassium bromide and sodium carbonate on coal char combustion reactivity," *Proc. Comb. Inst.*, vol. 30, no. 2, pp. 2187–2195, 2005.

[60] R. G. Racca and J. M. Dewey, "A method for automatic particle tracking in a 3-D flow field," *Exp. Fluids*, vol. 6, pp. 25–32, 1988.

[61] K. Nishino, N. Kasagi, and M. Hirata, "Three-dimensional particle tracking velocimetry based on automated digital image processing," *J. Fluids Eng.*, vol. 111, pp. 384–391, 1989.

[62] S. K. Sinha and P. S. Kuhlman, "Investigating the use of stereoscopic particle streak velocimetry for estimating the three-dimensional vorticity field," *Exp. Fluids*, vol. 12, pp. 377–384, 1992.

[63] A. Melling, "Tracer particles and seeding for particle image velocimetry," *Meas. Sci. Technol.*, vol. 8, pp. 1406–1416, 1997.

[64] R. Hartley and A. Zisserman, *Multiple View Geometry in Computer Vision.* New York: Cambridge University Press, 2011.

[65] J.-Y. Bouguet, "Camera calibration toolbox for Matlab." `http://www.vision.caltech.edu/bouguetj/calib_doc/`.

[66] Z. Zhang, "Flexible camera calibration by viewing a plane from unknown orientations," in *IEEE Proc. ICCV*, vol. 1, pp. 666–673, IEEE, 1999.

[67] J. Heikkila, "A four-step camera calibration procedure with implicit image correction," in *Proc. CVPR*, pp. 1106–1112, IEEE, 1997.

[68] R. Y. Tsai, *A versatile camera calibration technique for high accuracy 3D machine vision metrology using off-the-shelf TV cameras and lenses*, pp. 221–244. Jones and Bartlett Publishers Inc., 1992.

[69] J. Villa, I. D. la Rosa, G. Miramontes, and J. A. Quiroga, "Phase recovery from a single fringe pattern using an orientational vector-field-regularized estimator," *J. Opt. Soc. Am.*, vol. 22, no. 12, pp. 2766–2773, 2005.

[70] C. Leue, *Segmentierungsverfahren bei der stromungsvisualisierung.* PhD thesis, University of Heidelberg, Heidelberg, Germany, 1996.

[71] P. Geissler and B. Jahne, "A 3d-sensor for the measurement of particle concentration from image sequences," in *IEEE Proc. ISPRS Congr.*, vol. 31 B5, IEEE, 1996.

[72] R. O. Duda and P. E. Hart, "Use of the Hough transformation to detect lines and curves in pictures," *Commun. ACM*, vol. 15, no. 1, pp. 11–15, 1972.

[73] M. Kass, A. Witkin, and D. Terzopoulos, "Snakes: Active contour models," *Int. J. Comp. Vis.*, vol. 1, no. 4, pp. 321–331.

[74] R. Rodrigo, W. Shi, and J. Samarabandu, "Energy based line detection," in *IEEE Proc. CCECE/CCGEI*, pp. 2061–2064, IEEE, 2006.

[75] F. Rooms, M. Ronsse, A. Pizurica, and W. Philips, "PSF estimation with applications in autofocus and image restoration," in *IEEE Proc. BSPS*, pp. S02–1–S02–4, IEEE, 2002.

[76] M. E. Moghaddam and M. Jamzad, "Motion blur identification in noisy images using mathematical models and statistical measures," *Pattern Recognit.*, vol. 40, pp. 1946–1957, 2007.

[77] M. Rosenstiel and R.-R. Grigat, "Reconstruction of curved particle streak trajectories," *J. Flow Visualization Image Process.*, vol. 15, pp. 313–327, 2008.

[78] S. M. Choi, "Observation of volatile cloud formation during the early stages of pulverized coal combustion," *KSME Journal*, vol. 4, pp. 71–77, 1990.

[79] X. Liu, M. Tanaka, and M. Okutomi, "Noise level estimation using weak textured patches of a single noisy image," in *Proc. ICIP*, IEEE, 2012.

[80] J. P. Mathews, S. Eser, P. G. Hatcher, and A. W. Scaroni, "The shape of pulverized bituminous vitrinite coal particles," *KONA Powder Part. J.*, vol. 25, pp. 145–152, 2007.

[81] P. C. Carman, "Fluid flow through granular beds," *Trans. Inst. Chem. Eng.*, vol. 15, p. 150, 1937.

[82] B. C. Sakiadis, *Perry's Chemical Engineers' Handbook*. New York: McGraw, 1984.

[83] G. H. Spencer and M. V. R. K. Murty, "General ray-tracing procedure," *J. Opt. Soc. Am.*, vol. 52, no. 6, pp. 672–678, 1962.

[84] J. Heikkila and O. Silven, "Calibration procedure for short focal length off-the-shelf CCD cameras," in *Proc.* 13^{th} *Int. Conf. Pattern Recognition*, pp. 166–170, 1996.

[85] Joint Committee for Guides in Metrology, "Evaluation of measurement data supplement 2 to the guide to the expression of uncertainty in measurement," tech. rep.

[86] A. W. Bowman and A. Azzalini, *Applied Smoothing Techniques for Data Analysis*. Oxford: Clarendon Press, 1997.

[87] I. M. Sobol, "Global sensitivity indices for nonlinear mathematical models and their Monte Carlo estimates," *Math. Comput. Simulat.*, vol. 55, pp. 271–280, 2001.

[88] A. Saltelli, P. Annoni, I. Azzini, F. Campolongo, M. Ratto, and S. Tarantola, "Variance based sensitivity analysis of model output. design and estimator for the total sensitivity index," *Comput. Phys. Commun.*, vol. 181, pp. 259–270, 2010.

[89] K. L. Smith, L. D. Smoot, T. H. Fletcher, and R. J. Pugmire, *The structure and reaction processes of coal*. New York: Plenum Press, 1994.

[90] A. B. Ayling and I. W. Smith, "Measured temperatures of burning pulverized-fuel particles, and the nature of the primary reaction product," *Combust. Flame*, vol. 18, no. 2, pp. 173–184, 1972.

[91] D. W. Mackowski, R. A. Altenkirch, R. E. Peck, and T. W. Tong, "A method for particle and gas temperature measurement in laboratory-scale, pulverized-coal flames," *Combust. Sci. Technol.*, vol. 31, no. 3-4, pp. 139–153, 1983.

[92] T. H. Fletcher, "Time-resolved temperature measurements of individual coal particles during devolatilization," *Combust. Sci. Technol.*, vol. 63, no. 1-3, pp. 89–105, 1989.

[93] T. H. Fletcher, "Time-resolved particle temperature and mass loss measurements of a bituminous coal during devolatilization," *Combust. Flame*, vol. 78, pp. 223–236, 1989.

[94] S. M. Godoy and F. C. Lockwood, "Development of a two-colour infrared pyrometer for coal particle temperature measurements during devolatilisation," *Fuel*, vol. 77, no. 9/10, pp. 995–999, 1998.

[95] W. L. Grosshandler, "The effect of soot on pyrometric measurements of coal particle temperature," *Combust. Flame*, vol. 55, no. 1, pp. 59–71, 1984.

[96] P. A. Bejarano and Y. A. Levendis, "Single-coal-particle combustion in O_2/N_2 and O_2/CO_2 environments," *Combust. Flame*, vol. 153, pp. 270–287, 2008.

[97] P. J. van Eyk, P. J. Ashman, Z. T. Alwahabi, and G. J. Nathan, "Simultaneous measurements of the release of atomic sodium, particle diameter and particle temperature for a single burning coal particle," *Proc. Comb. Inst.*, vol. 32, pp. 2099–2106, 2009.

[98] C. R. Shaddix and A. Molina, "Particle imaging of ignition and devolatilization of pulverized coal during oxy-fuel combustion," *Proc. Comb. Inst.*, vol. 32, pp. 2091–2098, 2009.

[99] F. Payri, J. V. Pastor, J. M. Garcia, and J. M. Pastor, "Contribution to the application of two-colour imaging to diesel combustion," *Meas. Sci. Technol.*, vol. 18, pp. 2579–2598, 2007.

[100] Z.-W. Jiang, Z.-X. Luo, and H.-C. Zhou, "A simple measurement method of temperature and emissivity of coal-fired flames from visible radiation image and its application in a CFB boiler furnace," *Fuel*, vol. 88, pp. 980–987, 2009.

[101] T. S. Draper, D. Zeltner, D. R. Tree, Y. Xue, and R. Tsiava, "Two-dimensional flame temperature and emissivity measurements of pulverized oxy-coal flames," *Appl. Energy*, vol. 95, pp. 38–44, 2012.

[102] M. Brown, *Advanced Digital Photography*. Clontarf: Media Publishing Pty, Limited, 2004.

[103] J. J. Helble and A. F. Sarofim, "Influence of char fragmentation on ash particle size distributions," *Combust. Flame*, vol. 76, no. 2, pp. 183–196, 1989.

[104] L. L. Baxter, "Char fragmentation and fly ash formation during pulverized-coal combustion," *Combust. Flame*, vol. 90, no. 2, pp. 174–184, 1992.

[105] R. E. Mitchell and A. E. J. Akanetuk, "The impact of fragmentation on char conversion during pulverized coal combustion," in *Symp. (Int.) Combustion*, vol. 26, pp. 3137–3144, The Combustion Institute, 1996.

[106] D. A. Tichenor, R. E. Mitchell, K. R. Hencken, and S. Niksa, "Simultaneous in situ measurement of the size, temperature and velocity of particles in a combustion environment," in *Symp. (Int.) Combustion*, pp. 1213–1221, The Combustion Institute, 1984.

[107] T. Joutsenoja, J. Stenberg, R. Hernberg, and M. Aho, "Pyrometric measurement of the temperature and size of individual combusting fuel particles," *Appl. Opt.*, vol. 36, no. 7, pp. 1525–1535, 1997.

[108] T. Joutsenoja and R. Hernberg, "Pyrometric sizing of high-temperature particles in flow reactors," *Appl. Opt.*, vol. 37, no. 16, pp. 3487–3493, 1998.

[109] T. Reichelt, T. Joutsenoja, H. Spliethoff, K. R. G. Hein, and R. Hernberg, "Characterization of burning char particles under pressurized conditions by simultaneous in situ measurement of surface temperature and size," in *Symp. (Int.) Combustion*, pp. 2925–2932, The Combustion Institute, 1998.

[110] H. Lu, L.-T. Ip, A. Mackrory, L. Werrett, J. Scott, D. Tree, and L. Baxter, "Particle surface temperature measurements with multicolor band pyrometry," *J. AlChE*, vol. 55, no. 1, pp. 243–255, 2009.

[111] M. Sabet and B. T. F. Chung, "Radiation view factors from a sphere to nonintersecting planar surfaces," *J. Thermophys. Heat Transfer*, vol. 2, no. 3, pp. 286–288, 1988.

[112] J. C. D. Vos, "A new determination of the emissivity of tungsten ribbon," *Physica*, vol. 20, no. 7-12, pp. 690–712, 1954.

[113] J. R. Ehlert and T. F. Smith, "View factors for perpendicular and parallel rectangular plates," *J. Thermophys. Heat Transfer*, vol. 7, no. 1, pp. 173–174, 1993.

[114] K. I. Svensson, A. J. Mackrory, M. J. Richards, and D. R. Tree, "Calibration of an RGB, CCD camera and interpretation of its two-color images for KL and temperature," *SAE technical paper series, Combustion and Flow Diagnostics and Fundamental Advances in Thermal and Fluid Sciences (SP-1971)*, 2005.

[115] D. Lemire, "Streaming maximum-minimum filter using no more than three comparisons per element," *Nord. J. Comput.*, vol. 13, pp. 328–339, 2006.

[116] R. C. Gonzalez and R. E. Woods, *Digital Image Processing.* New Jersey: Prentice Hall, 2^{nd} ed., 2001.

[117] M. F. Modest, *Radiative heat transfer.* Elsevier, 2^{nd} ed., 2003.

[118] E. M. Sparrow, "A new and simpler formulation for radiative angle factors," *ASME J. Heat Transfer*, vol. 81, pp. 81–87, 1963.

[119] H. Hottel and F. Broughton, "Determination of true temperature and total radiation from luminous gas flames," *Ind. Eng. Chem. Res.*, vol. 4, no. 2, pp. 166–175, 1932.

[120] B. J. P. Buhre, L. K. Elliott, C. D. Sheng, R. P. Gupta, and T. F. Wall, "Oxy-fuel combustion technology for coal-fired power generation," *Prog. Energy Combust. Sci.*, vol. 31, no. 4, pp. 283–307, 2005.

[121] T. Wall, Y. Liu, C. Spero, L. Elliott, S. Khare, R. Rathnam, F. Zeenathal, B. Moghtaderi, B. Buhre, C. Sheng, R. Gupta, T. Yamada, K. Makino, and J. Yu, "An overview on oxyfuel coal combustion — state of the art research and technology development," *Chem. Eng. Res. Des.*, vol. 87, pp. 1003–1016, 2009.

[122] M. B. Toftegaard, J. Brix, P. A. Jensen, P. Glarborg, and A. D. Jensen, "Oxy-fuel combustion of solid fuels," *Prog. Energy Combust. Sci.*, vol. 36, pp. 581–625, 2010.

[123] D. Zeng, S. Hu, A. Mackrory, and A. Sayre, "Differences in chars formed from coal pyrolysis under N_2 and CO_2 atmospheres," in *25^{th} Int. Pittsburgh Coal Conf.*, University of Pittsburgh, 2008.

[124] S. Hu, D. Zeng, A. Mackrory, and A. Sayre, "Effects of co2 on char oxidation and ignition during oxy-coal combustion," in *26th Int. Pittsburgh Coal Conf.*, University of Pittsburgh, 2009.

[125] Y. Qiao, L. Zhang, E. Binner, M. Xu, and C. Li, "An investigation of the causes of the difference in coal particle ignition temperature between combustion in air and in O_2/CO_2," *Fuel*, vol. 89, pp. 3381–3387, 2010.

[126] J. Riaza, L. Alvarez, M. Gil, C. Pevida, J. Pis, and F. Rubiera, "Ignition and NO emissions of coal and biomass blends under different oxy-fuel atmospheres," *Energy Procedia*, vol. 37, pp. 1405–1412, 2013.

[127] J. Riaza, R. Khatami, Y. A. Levendis, L. Alvarez, M. V. Gil, C. Pevida, F. Rubiera, and J. J. Pis, "Single particle ignition and combustion of anthracite, semi-anthracite and bituminous coals in air and simulated oxy-fuel conditions," *Combust. Flame*, vol. 161, no. 4, pp. 1096–1108, 2014.

[128] J. Zhang, K. E. Kelly, E. G. Eddings, and J. O. Wendt, "CO_2 effects on near field aerodynamic phenomena in 40 kW, co-axial, oxy-coal, turbulent diffusion flames," *Int. J. Greenhouse Gas Control*, vol. 5S, pp. S47–S57, 2011.

[129] J. Zhang, K. E. Kelly, E. G. Eddings, and J. O. Wendt, "Ignition in 40 kW co-axial turbulent diffusion oxy-coal jet flames," *Proc. Comb. Inst.*, vol. 33, pp. 3375–3382, 2011.

[130] D. Rezaei, Y. Zhou, J. Zhang, K. E. Kelly, E. G. Eddings, R. J. Pugmire, M. S. Solum, and J. O. L. Wendt, "The effect of coal composition on ignition and flame stability in coaxial oxy-fuel turbulent diffusion flames," *Energy Fuels*, vol. 27, pp. 4935–4945, 2013.

[131] R. C. da Silva, T. Kangwanpongpan, and H. J. Krautz, "Flame pattern, temperatures and stability limits of pulverized oxy-coal combustion," *Fuel*, vol. 115, pp. 507–520, 2014.

[132] S. Khare, T. Wall, A. Farida, Y. Liu, B. Moghtaderi, and R. Gupta, "Factors influencing the ignition of flames from air-fired swirl PF burners retrofitted to oxy-fuel," *Fuel*, vol. 87, pp. 1042–1049, 2008.

[133] J. Smart, G. Lu, Y. Yan, and G. Riley, "Characterisation of an oxy-coal flame through digital imaging," *Combust. Flame*, vol. 157, pp. 1132–1139, 2010.

[134] J. Pedel, J. Zhang, P. J. Smith, J. Thornock, and J. Wendt, "Coal flame ignition mechanisms in oxy-combustion: A validation study using pilot-scale experiments and large eddy simulations," in *37th Int. Clearwater Clean Coal Conf.*, Coal Technologies Associates, 2012.

[135] K. Andersson, R. Johansson, S. Hjartstam, F. Johnsson, and B. Leckner, "Radiation intensity of lignite-fired oxy-fuel flames," *Exp. Therm. Fluid Sci.*, vol. 33, pp. 67–76, 2008.

[136] J. Smart, P. O'Nions, and G. Riley, "Radiation and convective heat transfer, and burnout in oxy-coal combustion," *Fuel*, vol. 89, pp. 2468–2476, 2010.

[137] C. K. Stimpson, A. Fry, T. Blanc, and D. R. Tree, "Line of sight soot volume fraction measurements in air- and oxy-coal flames," *Proc. Comb. Inst.*, vol. 34, pp. 2885–2893, 2013.

[138] D. M. Grant, R. J. Pugmire, T. H. Fletcher, and A. R. Kerstein, "Chemical model of coal devolatilization using percolation lattice statistics," *Energy Fuels*, vol. 3, pp. 175–186, 1989.

[139] H. Zhao and N. Ladommatos, "Optical diagnostics for soot and temperature measurement in diesel engines," *Prog. Energy Combust. Sci.*, pp. 221–255, 1998.

[140] P. Toth, Z. Zhan, Z. Fu, A. B. Palotas, E. G. Eddings, and T. A. Ring, "The potential of on-line optical flow measurement in the control and monitoring of oxy-coal flames," *Exp. Fluids*, vol. 55, no. 5, 2014.

[141] J. Pfanzagl, *Parametric Statistical Theory.* Berlin: Walter de Gruyter & Co., 1991.

[142] W. S. Cleveland, "Robust locally weighted regression and smoothing scatterplots," *J. Am. Stat. Assoc.*, vol. 74, no. 368, pp. 829–836, 1979.

[143] L. Bool, H. Kobayashi, K. T. Wu, D. Thompson, E. Eddings, R. Okerlund, J. Wendt, M. Cremer, and D. Wang, "Oxygen for NO_x control — a step change technology?," in *19^{th} Ann. Int. Pittsburgh Coal Conf.*, University of Pittsburgh, 2002.